The effect of cold spray coating parameters on the residual stress and fatigue performance of magnesium alloys

by

Bahareh Marzbanrad

A thesis
presented to the University of Waterloo
in fulfillment of the
thesis requirement for the degree of
Doctor of Philosophy
in
Mechanical and Mechatronics Engineering

Waterloo, Ontario, Canada, 2019

Examining Committee Membership

The following served on the Examining Committee for this thesis. The decision of the Examining Committee is by majority vote.

External Examiner	Bertrand Jodoin, Ph.D. Professor, University of Ottawa
Supervisor	Hamid Jahed, Ph.D. Professor, University of Waterloo
Supervisor	Ehsan Toyserkani, Ph.D. Professor, University of Waterloo
Internal Member	Adrian Gerlich, Ph.D. Professor, University of Waterloo
Internal Member	Mustafa Yavuz, Ph.D. Professor, University of Waterloo
Internal-External Member	Scott Walbridge, Ph.D. Professor, University of Waterloo

AUTHOR'S DECLARATION

I hereby declare that I am the sole author of this thesis. This is a true copy of the thesis, including any required final revisions, as accepted by my examiners.

I understand that my thesis may be made electronically available to the public.

Abstract

Global warming, dwindling fossil fuels, and the low efficiency of alternative energy sources such as batteries and solar panels compared to traditional carbon-based energy sources, have shifted the industrial design paradigm towards minimizing structural weight. In this scenario, employing low density grade metals is inevitable. Magnesium (Mg) alloys, such as AZ31B, are one of the lightest structural materials, and have been able to gain strong foothold in the industrial world due to their high "strength to weight ratio". However, the long-term performance of parts manufactured from Mg alloys are required for reliable structural applications. Hence, research on the methods to enhance the fatigue properties of Mg alloys is crucial.

Surface treatment, particularly surface coating of manufactured parts with a thin layer of high fatigue strength material is considered a versatile approach to address fatigue shortcomings of Mg alloys. Cold gas dynamic spray is an emerging technology that deposit metal powder with a supersonic velocity on substrate in a solid-state. The nature of this technology (peening) promotes compressive residual stress and results in a refined grain structure, which reinforces a material's surface and prolong crack initiation, thus enhancing the fatigue performance of materials like AZ31B alloy. Among all potential candidates for coating Mg parts, aluminum alloys are one of the best, due to their low density and strong fatigue performance. Hence, in this research, cold spraying is employed to deposit a thin layer of Al7075 on AZ31B-H24 Mg substrates in order to improve their fatigue performance. The complexity of the cold spray process requires some in-depth study through in situ measurements. For this, fiber Bragg grating (FBG) sensors is employed for monitoring and assessing the thermo-mechanical behaviour of Mg alloy during cold-spray coating. Furthermore, the hole drilling, X-ray diffraction and in situ FBG sensors residual stress measurement techniques are used to explore the effect of processing parameters and thermal mismatch on the residual stress distribution of coated Mg samples. In addition, SEM, TEM, CT scanning tomography, micro indentation hardness, surface topography and roughness measurements are utilized to identify the physical and microstructural characteristics of the coating, interface and substrate.

Based on the findings of this research, the common understanding that cold spray induced residual stresses are compressive is questioned. It is shown that the heat associated with the spraying, although much lower than melting temperature, can wash out the peening effect and result in tensile residual stress in the substrate. Hence, to customize the residual stress and for inducing compressive residual in the Mg substrate, the cold spray coating parameters were tuned to decrease the heat input to the

substrate. Moreover, a cooling system was designed that increased heat transfer from the substrate during the coating process. Another major factor affecting the state of the residual stress is the thermal mismatch of the coating and the substrate materials. The detrimental effect of thermal mismatch between the Al7075 coating and AZ31B substrate on the residual stress of substrate and coating was addressed by adding an interlayer of zinc, which has a higher thermal expansion coefficient than the substrate and coating material. Zinc is successfully deposited, and its coating parameters were selected in a way that resulted in inducing compressive residual stress in the substrate, coating and the zinc interlayer. However, detail characterization of the zinc and AZ31B substrate reveals that intermetallic phases have formed at the interface. Therefore, despite the induced compressive residual stress, cracking at the zinc magnesium interface restricts the application of this interlayer. Two extreme coating conditions that lead to induced tensile and compressive residual stress in the Mg substrate have been selected for the rest of this research. The quality of the coating is examined by CT-scan, which demonstrates that the compressive samples have less porosity than the tensile samples, although the densities of both samples are above 99%. The physical and mechanical properties of the compressive samples, including hardness and surface roughness, have also been significantly improved compared to tensile samples. Finally, the fatigue performance of the two types of coated samples (tensile and compressive) is investigated revealing that the compressive samples demonstrate exceptional fatigue life in high cycle regime compared to the bare AZ31B samples with 130% life enhancement.

Acknowledgements

I would like to express my sincere gratitude to my supervisors, Professor Hamid Jahed and Professor Ehsan Toyserkani, for their valuable support, advice, and encouragement over the past years.

I hereby express my gratitude to my thesis examining committee members, Professor Bertrand Jodoin, Professor Scott Walbridge, Professor Adrian Gerlich, Professor Mustafa Yavuz, for their reviews, valuable feedback, and suggestions.

Thanks, are also due to my colleagues, Siavash Borhan Dayani, Dr. Sugrib Kumar Shaha, Dr. Farzad Liravi, Sasan Faghih, Dr. Andrew Gryguć, Amir Yazdanmehr, Dr. Esmat Sheydaeian and particularly Dr. Seyed Behzad Behravesh, for their valuable advice and discussions. I am also thankful to Andy Barber, Henry Ma, Martha Morales, as well as to Dr. Yuquan Ding for his technical support.

I wish to thank Mary McPherson who offered her valuable help on proofreading this thesis.

I would like to acknowledge the Natural Sciences and Engineering Research Council of Canada (NSERC) through the Automotive Partnership Canada (APC), and the University of Waterloo and the Department of Mechanical and Mechatronics Engineering for financial support of the project.

I am especially grateful to my husband, Ehsan, for his assistance, collaboration and encouragement, which made this research possible. I am also extremely thankful to my lovely daughter, Vania, for her understanding and patience.

Finally, I must express my great appreciation of my parents for their sincere love, support and encouragement throughout my studies. I would also like to extend my deepest gratitude to my dear siblings for their continued support and motivation. This achievement would not have been possible without them. Thank you.

Dedicated to my adored Family

My Parents, My husband

And my lovely daughter

Table of Contents

List of Figures

List of Tables

Chapter 1

Introduction

1.1 Research Motivation

Today's severe environmental crises, including global warming, increased carbon footprints, and worldwide pollution, result from excessive use of carbon-based natural energy resources. The Intergovernmental Panel on Climate Change emphasizes that it is required to decrease the greenhouse gases emission to net zero by 2050 so as to limiting global warming to 1.5°C [1]. Hence, reducing fossil fuel consumption should be considered as a mission for industries, governments and people around the globe. Nowadays, burning fossil fuels produces most of the energy required for mobile structures such as vehicles. About 5% conservation of present fuel energy can be provided by 10% reduction of automotive weight [2]. Therefore, decreasing fuel consumption by optimizing vehicular designs, to the highest possible efficiency through weight reduction is crucial [3]. This new design paradigm is the driving force for transition from traditional structural materials towards lightweight ones.

Magnesium (Mg), the lightest structural metal, has superior properties, such as a high strength-to-weight ratio and low-energy consumption during the manufacturing processes, making it a good candidate to meet optimal design requirements [4]. Therefore, the trend is toward using mg alloys with a low density of 1.75 gr/cm^3, in place of steel or even aluminum of particular interest is wrought Mg alloys, which have superior mechanical properties to cast ones [5]. Hence, the use of wrought Mg alloys is dramatically on the rise in various industries, particularly those involving mass production, such as the automotive and aerospace ones [2]. Despite the stupendous performance of these alloys for use in load-bearing components, including suspension control arms, the application of Mg alloys is mainly restricted to non-load bearing components, such as casings, housing and trim parts [6][7]. The low fatigue strength, poor wear resistance and high corrosion susceptibility of Mg alloys confine their widespread use in load-bearing structures. The materials used for such structures are frequently subjected to cyclic loading, commonly leading to fatigue failure. Therefore, the processes needed to boost the fatigue limits and lifespan of Mg alloys are areas of substantial research interest.

A common method for increasing the fatigue strength and enhancing the lifespan of material structures is surface treatment that can generate compressive residual stresses and grain-refined microstructure, both of which can delay crack initiation and decelerate crack growth. Surface coating is one of the possible surface treatments that can be employed for this purpose. Among all available surface coating methods, high density and crack-free coating, produced by cold spray technique, seems to be a

relatively successful treatment in enhancing fatigue performance of Mg alloys [8][9]. Hence, high-quality cold spray coating may solve the aforementioned problems of Mg alloys and opens new windows for putting this interesting material in to service.

Cold spray coating is a new technology in which metal powders are accelerated to supersonic velocity by a relatively low temperature compressed gas stream through a de Laval nozzle, so as to forcefully impact a substrate. The solid-state bonding mechanism of cold spraying makes it ideal for thermally sensitive materials such as Mg alloys. The impingement-acceleration of the particles lead to their extensive plastic deformation and may induce compressive residual stresses as well as grain refinement at the substrate surface (peening process) as a result, crack initiation can be retarded. Moreover, applying a thin layer of ductile and stronger coating materials can also prevent crack initiation on material surfaces, increasing fatigue resistance. However, some contradictory results in the literature represent undesirable lower fatigue strength and life after cold spray coating [10]. Methods for optimizing the cold spray technique to achieve maximum fatigue performance are therefore highly desired.

Many studies have tried to improve the corrosion and wear resistance of Mg alloys through cold spray coating [11]–[14], and cold spray's positive role in enhancing corrosion and wear resistance has been declared unanimously. Furthermore, other research has investigated the role of processing parameters on the microstructure of the coating, bonding strength and coating quality [15]–[17]. However, less attention has been paid to another aspect of cold spraying: improving the fatigue characteristics of materials after coating, especially in case studies for Mg alloys [18], [19]. Since inducing compressive residual stress and creating a fine microstructure enhance the fatigue characteristic of Mg alloys, investigating the thermal and mechanical behaviour of material during the coating process is critical. Concerning the intricacies of the coating process, such as the high kinetic energy upon impact, heat generation during coating, and thermal mismatch, understanding the effect of the process on the induced residual stress seems to be difficult.

Careful control of the processing parameters as well as coating conditions is also essential, to maximize beneficial residual stress and coating integrity, to minimize porosities and surface roughness, to achieve high quality coated samples, and consequent increased of the fatigue life. Furthermore, the role of thermal mismatch in the attenuation or reinforcement of the residual stress of coated sample's induced by peening effect, should be considered, since the interaction between thermal and mechanical strain can release or even reverse residual stress. In addition, fractography and study of the locations of crack

initiation and propagation and the reason for crack formation during and after fatigue experiments can be crucial for obtaining the maximum fatigue performance with cold spray coating.

1.2 Research Objectives

The main goal of this research is to study the formation of residual stress due to cold spray process and to enhance the fatigue performance and mechanical properties of AZ31B-H24 by depositing a stronger material with higher fatigue strength, Al7075, using a modern coating technique, cold gas dynamic spray. In this process, various factors can affect the fatigue life of coated Mg alloys. The mechanical and physical properties, such as ductility, and the particle size of coating materials can significantly influence coating quality and bonding strength, thus influencing the fatigue performance. Moreover, the crucial role of processing-parameters on the thermo-mechanical behaviour of coated material, which causes residual stress as well as microstructural changes, are important in achieving longer fatigue life. For instance, the peening effect associated with cold spray is an important stimulus that can induce compressive residual stresses and cause grain refinement in the coating as well as the substrate near its interface. It can thus improve the fatigue strength and life of coated sample by retarding crack initiation and propagation in the substrate. However, the temperature of the carrier gas and rising temperature during severe plastic deformation of particles upon impact may relieve induced stress or/and change Mg alloys' microstructure during coating. In addition, the difference between the thermal expansion coefficient of coating material and substrate may also increase the chance of detrimental residual stresses after coating. Hence, cold spray might in fact function a "hot" coating process for Mg alloys due to their relatively low annealing temperature; a possibility that needs carful investigation. Selecting a proper coating material, increasing beneficial residual stress, and decreasing detrimental thermal effect are the focus of this research, which has the following objectives:

1.2.1 To successfully spray a layer of high fatigue strength material on Mg alloy

Material selection for cold spray deposition is critical, since the mechanical properties of coated material as well as the coating's quality strongly depend on the material chosen. Al7075 may be an appropriate coating material, because it has high ductility and high fatigue resistance. Particle size and shape, which affect particle velocity and impact temperature, should also be considered. Optimizing the processing parameters to create a relatively thin layer of coating material with low porosity and high bond strength should be a main target. Peening during the cold spraying may cause grain refinement of the substrate surface; this is highly dependent on the kinetic energy of particles and the

interaction of temperature with the substrate's microstructure. Therefore, the effect of cold spray coating on grain refinement needs to be evaluated through experiments and surface metallography and characterized by effective-parameters optimization.

1.2.2 To characterize the behaviour of Mg alloys during cold spray coating

The mechanical and thermal strain of substrates during cold-spray deposition need to be evaluated. In this regard, the use of fiber Bragg grating (FBG) sensors to measure the temperature and strain simultaneously during cold spraying to be explored for effective measurement of the material's behaviour.

1.2.3 To maximize compressive residual stress in Mg alloys

Regarding to the nature of cold spray deposition, the two sources of temperature (carrier gas and impact temperatures) and the peening process can interact with each other, and together may influence residual stress. Minimizing the effect of temperature by decreasing carrier gas temperature and gas exposure time, adding a cooling system during the cold spray coating process can increase the beneficial residual stress.

1.2.4 To study the effect of thermal mismatch

The effect of an undesirable thermal mismatch can be controlled through the coating material and condition. In addition, the effect of an intermediate layer of a material with a proper thermal expansion coefficient on residual stress and surface morphology will be studied.

1.2.5 To enhance the fatigue performance of Mg-alloy coated samples

Optimizing the coating parameters to create a thin layer of high strength material with the maximum density, hardness and beneficial residual stress of coating and substrate can facilitate Mg alloys' capacity to enhance fatigue resistance against cyclic loading, thereby increasing their potential for use in load-bearing components.

1.3 Thesis Structure

The content of this thesis has been organized in nine chapters. Introduction, this first chapter outlines the research motivation, and the research objectives.

In Chapter 2, a summary of relevant literature is presented to highlight the knowledge gap in this field and extract the research contribution. A background on mechanical properties, structure and fatigue

behaviour of Mg alloys are presented in the opening section of this chapter, followed by an introduction to the cold spray coating process. Then, the bonding mechanism and features of cold spray are reviewed in detail. Finally, the scientific background of Fiber Bragg Grating Sensors is discussed.

The remainder of the thesis comprises six journal articles, either published, submitted for publication in peer-reviewed, or to be submitted. Chapter 3 discusses the embedding methodology for FBG sensors, which is used qualitatively to monitor the strain behaviour, and includes a parametric study on residual stress evolution and microstructural changes of the substrate during cold spray coating. Chapter 4 is on the effects of multi-layer cold spray deposition on the residual strain formation in the coating and substrate. A method is proposed to separately measure the thermal and mechanical strains induced in cold spray. The FBG sensors are employed for in-situ monitoring and the measuring of the strain evolution during the cold spray of multi-layer coating. In addition, the effect of thermal mismatch on the inducing mechanical strain in the sample is uncovered during one pass and multilayer coating. Chapter 5 contains the results of investigating the deposition of a zinc layer on a Mg alloy substrate. Pure zinc was selected for this study because the thermal expansion coefficient of zinc being higher than that of AZ31B alloy and Al7075. In Chapter 6, the effects of processing parameters and coating setup on the residual stress development of the substrate are discussed. By this study, two sets of coating parameters and setups are chosen and designed to induce tensile and compressive residual stress in the substrate near the interface. Chapter 7 discusses and compares the microstructure of the interface and substrate near the interface for the coated samples with the different treated coating parameters and setups. Chapter 8 is on the fatigue life of coated samples with different coating parameters and compares their life with that of the uncoated AZ31B substrate. The fatigue failure of the samples in high and low cycle fatigue regimes is studied by fractography. Chapter 9 concludes the thesis by briefly summarizing the contributions and suggesting possible future work.

Chapter 2

Background and literature review

This section first provides background knowledge on Mg alloys, their fatigue behaviour, and cold spray technique, followed by details on the fatigue behaviour of cold spray coated materials, concentrating on the coating of Mg alloys. Then, residual stress measurement methods are discussed. Finally, the scientific background on the in-situ measurement method, based on use of the fiber Bragg grating sensors, is discussed.

2.1 Mg and its alloys

Magnesium, one of the world's lightest known metals, is abundant in seawater and the earth's crust and was first extracted and refined by Sir Humphrey Davy in 1808 [20]. About a century later, this metal started to be employed in the automotive industry, especially in the manufacture of the Volkswagen Beetle [2]. At that time, Mg was usually preferred for use as an alloying element in aluminum alloys, rather than as a structural material. However, some technical problems, and a demand for higher performance in the automotive industry, led to a decrease in the use of Mg alloys [6]. Since 1990, the drive to reduce fossil fuel consumption due to its environmental impact has caused renewed interest in employing Mg and its alloys in the automobile and aerospace industries and for other structural applications [4]. Currently, the use of Mg alloys, particularly wrought Mg given its specific characteristics, is expanding rapidly in North America and Europe [21].

Mg is the lightest commercial metal, with an atomic number of 12, a high strength to weight ratio of around 150 KNm/Kg, and a density of 1738 Kg/m^3. Its density is over 75% less than steel's and about 35% lighter than aluminum's [6][22][23]. Mg and its alloys also have good castability, weldabilty, forgeability [24] [25], damping capacity, and electrical and thermal conductivity [22][23]. These properties have persuaded manufacturers to use Mg and its alloys widely in the transportation industry. However, some of Mg's shortcomings such as inadequate strength at high temperatures, poor cold workability, relatively low fatigue strength, and weak corrosion resistance have restricted its use in many applications, particularly, those involving cyclic loading [6][26][27]. Moreover, the crystal structure of Mg is hexagonal-close-packed (HCP), which gives it specific and complicated mechanical properties such as asymmetric mechanical behaviour under tension and compression, and anisotropic properties related to the deformation history of the material. Two different mechanisms of plastic deformation, slip and twinning, are responsible for the complicated mechanical behaviour in HCP

structural materials that often leads to asymmetry in yield especially in wrought Mg alloys [23][26][28], which is different from hydrostatic pressure dependent yield asymmetry [29] and therefore requires pressure independent yield function [30][31][32]. For HCP crystal structures, four modes--basal <a>, pyramidal <a>, prismatic <a>, and pyramidal <c+a>--are possible under a slip mechanism [33]. Considering the high critical resolve shear stress of the slip modes in Mg alloys, only basal and pyramidal <c+a> planes can be activated during deformation at room temperature [34][35]. Therefore, another deformation mechanism, twinning, including tension and contraction, can be activated during the deformation of this alloy. According to the literature, only tension twinning on the (1012) plane can be observed at room temperatures during loading [36][37]. Activating tension twinning provides strain along the c axis of the HCP crystal structure. In contrast, contraction twinning can only be activated in Mg when the strain reaches above 8% in uniaxial tests [38].

Mg alloys are divided into two main groups: casting and wrought [39]. Wrought Mg alloys are manufactured by rolling or extrusion, or by a forging process carried out at a temperatures above 330ºC and followed by slow cooling to prevent crack initiation [40]. The different deformation modes and strong crystallographic texture present in HCP crystal structures lead to highlight certain features, such as high directional anisotropy in the monotonic tension and compression as well as the asymmetric behaviour under tension and compression in wrought Mg alloys [41]. Wrought Mg alloys have poor cold formability in comparison with cast alloys; therefore, the cast Mg alloys are used more in mass-production for mobile structure [39][42]. However, wrought Mg alloys have higher tensile yield strength and manifest mechanical properties that are preferable to those of cast ones [43][44][45].

To improve the mechanical and physical properties of Mg, various elements such as aluminum, zinc, manganese, zirconium and rare earths are added to pure Mg. For example, adding aluminum and zinc to Mg can provide solid solution strengthening, facilitate age hardening, increase tensile strength and hardness, and elevate corrosion resistance [40][46]. The combination of aluminum, zinc and Mg has produced the AZ group of alloys, which have greater mechanical strength, castability, workability, formability, weldability, and corrosion resistance than pure Mg. In addition, manganese is often added, usually at less than 1wt%, to refine the grain size of the alloy [47] and results in better ductility and castability, higher strength, and enhanced energy absorption. When zinc and zirconium are added to Mg to produce the ZK group of alloys, the hot workability of Mg is also improved. This enhancement is important to the manufacture of structural parts by hot working processes such as hot rolling and forging [48].

In this research, rolled AZ31B-H24, the selected test material, is an alloy with superior properties to those of pure Mg and has been recognized by the American Society of Testing Materials [49]. Based on the codification, this alloy contains about 3wt% aluminum and 1wt% zinc; the letter B was added to the AZ31 label as it was the second alloy developed under this qualification. The heat-treated or work-hardened conditions, i.e. tempers, of alloys are specified by a letter (F, O, W, H, or T), which is followed by one or more numbers. For example, H24 (in AZ31B-H24) indicates that it was strain hardened and then partially annealed to half hard [49][50].

Alloying Mg with aluminum, manganese, rare earths, thorium, zinc or zirconium increases the strength to weight ratio, resulting in useful materials for applications where weight reduction is important, and where it is essential to reduce inertial forces. However, it should be noted that conventional alloying techniques cannot eradicate all undesirable properties of Mg alloys, which restricts the possibility of improving their mechanical properties and chemical behaviour. Additionally, certain properties corresponding to the Mg hexagonal crystal structure limit its inherent ductility [6].

2.2 Fatigue Behaviour of Mg alloys

Fatigue in structural materials is a degradation process caused by cyclic loading that leads to irreversible damage. A large number of industrial structures and automotive components are usually subjected to cyclic loading, and even with low amounts of loading, failure of the components can occur after a period of time [51]. Therefore, fatigue characterization of load bearing components is of great importance for reliable mechanical design. The application of Mg alloys is currently limited to non-load bearing parts; investigating and improving their fatigue behaviour are essential to their wider use in the automotive and aerospace industries.

Many studies have investigated the effective parameters that influence the fatigue properties of Mg alloys. Tsushida et al. [52] investigated the effect of grain size on the fatigue behaviour of extruded AZ31B [52]. The fatigue tests were performed for the samples with the three different mean grain sizes: 4.7μm (fine), 15μm (medium) and 23μm (coarse). The fatigue limits of fine, medium and coarse samples were approximated as about 160MPa, 150MPa and 150MPa, respectively. The fatigue life in the low cycle region of the fine grain size specimen was shorter than those of the medium and coarse ones. Based on SEM images, twinning was not observed in the fine microstructure sample, but it was observed near the crack in the coarse grain specimen. Consequently, it can be concluded that twinning under fatigue loading depends on grain size and affects the fatigue life of AZ31B alloy [52]. Tokaji et al. [53] studied the fatigue and fracture behaviour of heat-treated AZ31 rolled plate Mg alloy in

comparison to Al7075, Al6063 and pure titanium [53]. The fatigue strength and fatigue crack propagation (FCP) characteristics were evaluated based on crack initiation, crack growth rate and fracture surface analyses. To compare the above-mentioned materials, a normalized stress intensity factor was defined as $\frac{\Delta k_{eff}}{E}$. Fig. **2-1**a demonstrates the FCP rate curves of these materials versus $\frac{\Delta k_{eff}}{E}$. FCP rates were characterized in terms of Δk_{eff}, where the slope change occurs at $\Delta k_{eff} = 2.5 - 3MPa\sqrt{m}$. At the lower range of the $\frac{\Delta k_{eff}}{E}$ region, AZ31B has a higher FCP rate, whereas after the transition in the high $\frac{\Delta k_{eff}}{E}$ region, the rates are almost the same, especially for AZ31B and Al7075. This finding reveals that the AZ31B has lower FCP resistance than other materials in this research. Tokaji et al. [53] concluded that the observed differences in FCP behaviour were attributable to the low corrosion resistance of the Mg alloy. The S–N curve of heat-treated rolled AZ31 Mg alloy is shown in Fig. **2-1**b. Fatigue failure did not occur at $\sigma = 50$ Mpa, and the cracks were not propagated on the specimen surface. The fatigue ratio ($\frac{\sigma}{\sigma_T}$) at high cycle, 10^7 cycles of 0.23, where σ_T is tensile strength, indicates that the rolled AZ31 has a relatively low fatigue ratio [53].

Complete monotonic and cyclic properties of AZ31B-H24 rolled sheet employed in this study can be found in [54][55].

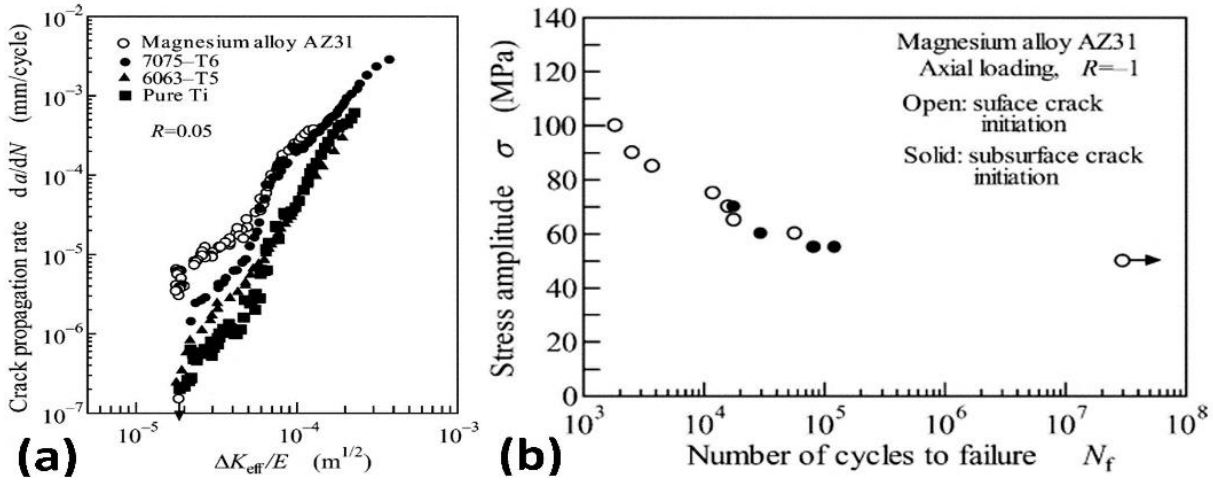

Fig. 2-1: a) Comparison of crack propagation behaviour between Mg alloy and other alloys; b) S-N curve for rolled AZ31 Mg alloy [53]**.**

To improve the fatigue behaviour of Mg alloys, two different main approaches are possible: 1) Improvement of the bulk material to decelerate crack initiation or to reduce the crack propagation rate through metalworking and modification of the manufacturing process, and/or adding certain alloying elements. 2) Surface modification to reduce surface defects and roughness and so improve fatigue resistance and /or corrosion resistance. Surface hardening can improve fatigue resistance by introducing compressive residual stresses in the surface layer. These can decelerate the process of fatigue crack initiation by reducing dislocation movement. Another possibility for decelerating fatigue crack initiation and enhancing fatigue strength, especially when the Mg components are exposed to a corrosive media, is the use of surface coating. Coating creates a high fatigue strength layer on the surface and reduces corrosive media attacks and consequent formation of corrosion-induced cracks and pitting, which often act as fatigue crack initiation sites [56].

2.3 Cold Spray Coating Technique

Cold spray (CS) is a solid-state material deposition technique, where micron-sized particles (1 to 50 µm) are accelerated to high velocity (300 and 1200 m/s) through a de Laval nozzle with a convergent-divergent geometry [57][58]. A pressurized and relatively low temperature carrier gas (below the particle material's melting point) is employed to accelerate particles to high enough velocities. The high kinetic energy of particles upon impact and associated severe plastic deformation provide the metallurgical bonding between particles and substrate, which is attributed to adiabatic shear instability [59]. Adhesion occurs between coating material and substrate when the powder particles exceed a critical impact velocity related to the material properties of the coating and substrate and process conditions. During the coating process, despite the existence of sufficient temperature to provide high acceleration and deformation of particles, the particles remain in the solid state. Hence, the process is known as "*Cold Spray*". This feature of cold spray makes it completely unique, with properties superior to those of conventional and traditional thermal coating techniques. Cold spray technique is usually used for coating, repair, welding [60] and also additive manufacturing at relatively high deposition rates, instead of the methods based on selective laser or electron beam melting [61]. Fig. **2-2**a and Fig. **2-2**b show a low-pressure cold spray machine and schematic view of our deposition system.

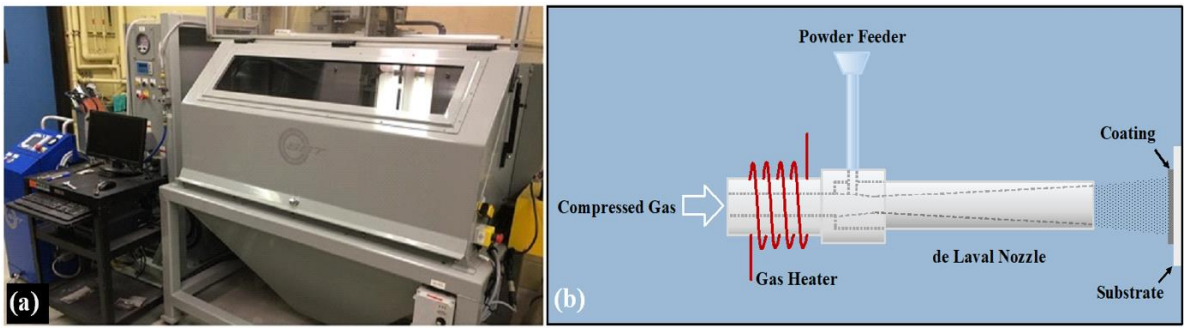

Fig. 2-2: a) cold spray system; b) schematic of low-pressure cold spray.

Cold spraying's main advantage over traditional thermal spray processes is alleviation of the problems associated with high temperature, such as oxidation, evaporation, melting, crystallization, thermal residual stresses and other common problems. Removing the deleterious effects of high temperature on coatings and substrates makes cold spray a suitable method for deposition on thermally sensitive surfaces, such as those Mg alloys [62]. Fig. 2-3 summarizes the advantages of cold spray. However, some shortcomings such as high gas consumption, restrictions about depositing on soft materials, and limitations related to hard and brittle coating materials like ceramics should be considered.

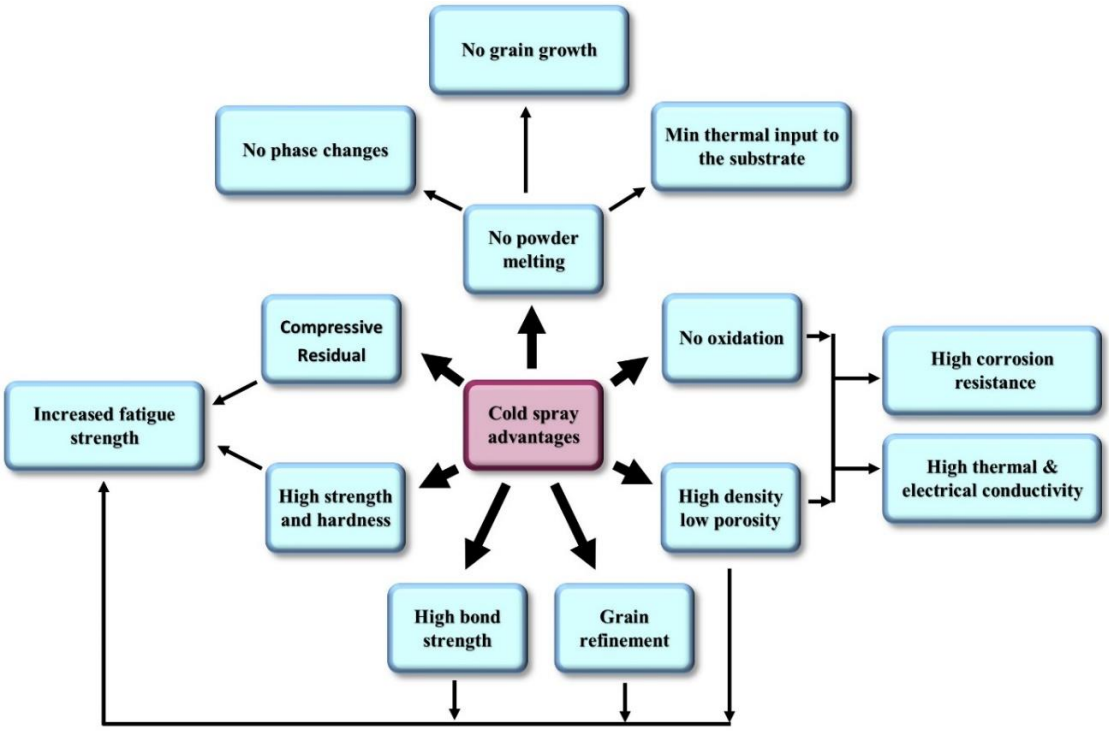

Fig. 2-3: cold spray coating advantages.

2.3.1 Bonding Mechanism

The bonding between particles and substrate happens rapidly (<100 ns related to particles' coating diameter), from the initial contact to the total transformation of the particles' kinetic energy and subsequently particle deformation. To better understand the bonding mechanism, numerical simulation of particle impact and experimental observations were performed [63]–[67]. Based on the simulation analysis, "*adiabatic shear instability*", occurs at the particle/substrate interface. Sufficient kinetic energy drives particles onto the substrate surface, plastically deforms them, puts the particles in direct contact with the substrate and causes their adherence. The high strain plastic deformation at the interface due to high velocity impact leads to work hardening and thermal softening as well. Ninety percent of total energy is dissipated as heat, which causes thermal softening. The thermal diffusion distance ($\sim\sqrt{\alpha t}$) is considerably less than the dimensions of the system; hence adiabatic deformation is assumed, and heat conduction is neglected. Moreover, less than 10% of total energy is stored within the material in the form of mechanical energy, which causes grain-structure distortion and increases the dislocation density and work hardening. However, thermal softening is more influential than work hardening, resulting in instability of a material at a certain point. Extra imposed strain accumulates in a narrow band. As a result of intense localization shear straining at the interface, an outward-moving layer of material is formed, which protrudes radially from the edge of the contact area. This layer is named the interfacial jet [58][68][69]. Fig. 2-4 shows the final deformed state of a 20-μm copper particle following 200, 400 and 600 m/s impacts on a copper surface, when simulation times were 38, 35 and 38 ns, respectively. Based on the simulation results, increasing the particle velocity to 600 m/s causes a material jet to form, involving both particle and substrate [68]. Hence, a minimum particle velocity (critical velocity) is required to form the localized shear strain. In some deposited material, the localized strain reaches a value of 10 [51].

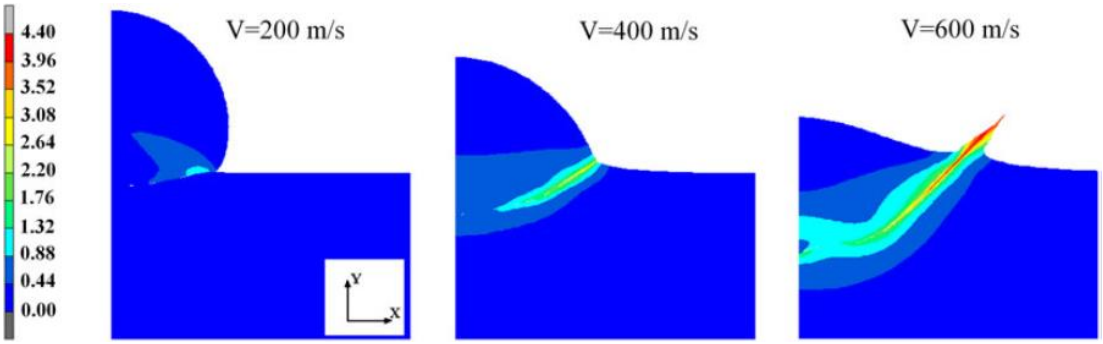

Fig. 2-4: Equivalent plastic strain of a copper particle's impact with a copper surface, when the initial impact velocities were 200 m/s, 400 m/s and 600 m/s [68]**.**

Li et al. [70] utilized the Lagrangian and Arbitrary Lagrangian Eulerian (ALE) methods in simulating the Cu particle deformation behaviour on Cu substrate during cold spraying. They observed that when a particle's impact velocity is increased, the effective plastic stain increases sharply, and also the flattening ratio and compression ratio of particles are increased [70]. On the other hand, Wang et al. [65] simulated the process of Al particles impacting a Mg alloy substrate, using ANSYS/LS-DYNA; the temperature distribution is shown in Fig. 2-5 [65]. Based on the simulation, increasing the particle impact velocity leads to more intensive particle–substrate deformation, and the temperature of the contact zone is locally increased and even exceeds the melting points of particles and/or substrate. Fig. 2-5 shows rising temperature at the periphery of the contact zone (in red), where the high effective plastic strain exists [65]. It is worth to mention that the plasticity theory behind these simulations has been developed for deformation at lower strain rate rather than being involved in cold spray; therefore, the limitation of these models should be considered.

In addition, for coating formation, the compaction effect or tamping effect of subsequent particles on previously deposited particles is beneficial, and thus can prevent the formation of voids and enhance the inter-particle bonding in cold spraying [71].

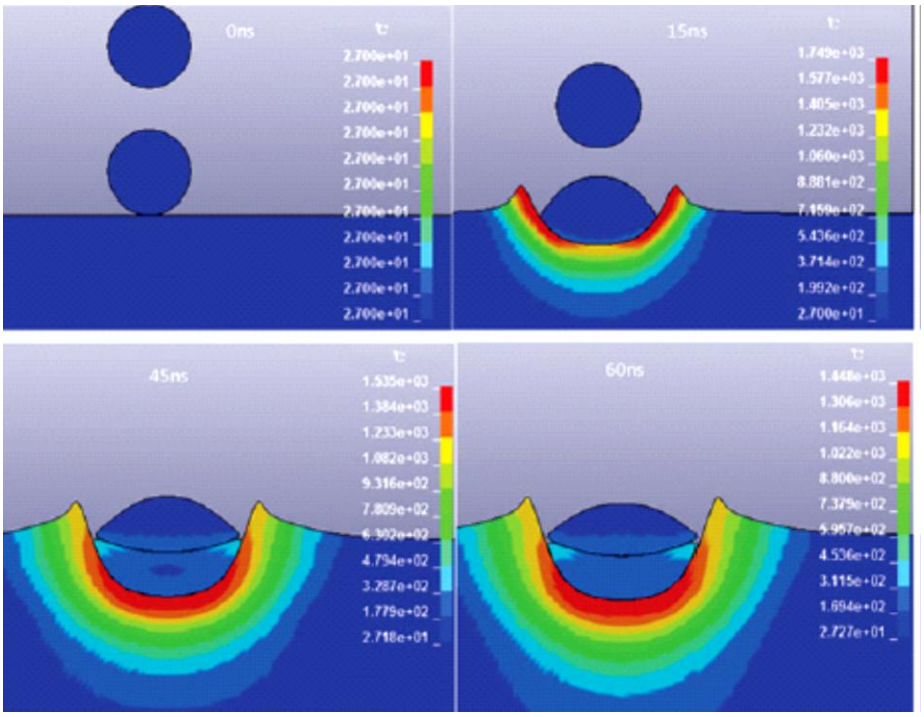

Fig. 2-5: Rising temperature (ºC) during the impingement of two Al particles on Mg alloy substrate (at impact particle velocity of 600m/s and initial temperature of 27ºC) [65]**.**

2.3.2 Coating Material

The physical and mechanical properties of coating material, such as melting point, hardness, density, mechanical strength, ductility, and particle size, which are the important factors in selecting a coating material, directly affect the quality and bond strength of coated materials. In particular, low melting point, low mechanical yield strength and high ductility materials, which are able to deform easily at relatively low gas temperature and exhibit softening, are ideal for coating. Among metal powders Al, Cu and Zn are suitable coating materials with respect to the aforementioned properties. There are quite a number of studies available in the literature, which have used Al, Cu, Zn and their alloys as coating materials [72]–[75]. Based on their findings, a stronger aluminum alloy such as Al7075, which has higher fatigue strength in comparison to other Al alloys, can be ideal in terms of fatigue improvement [76]; however, its low corrosion resistance compared to the aluminum alloy 5000 series should be taken into account. A summary of coating materials and coating parameters for Mg alloys is provided in Table 2-1. Considerable attention has been focused on improving the corrosion resistance of Mg alloys using Al and Al alloys coatings through the cold spray coating process.

Table 2-1: Summary of the most recently coatings on Mg alloys.

Substrate Material	Coating Material	Gas Type	Gas Pressure (psi)	Gas Temperature (°C)	Coating thickness (µm)	Surface roughness (µm)	Porosity	Comments	Ref
AZ31B(Ext)	Al	N_2	500	500	200-250	133-187	low	Corrosion and corrosion fatigue	[14]
AZ31B(Cast)	Al6061	N_2	435	350	200-300	-	0.4%	Effective protect from corrosion	[12]
AZ31(Cast)	Al-12Si	Air	200-260	200-400	3-2500	-	2%-12%	Study on microstructure, mechanical properties	[15]
AZ80 (wrought)	Ti	N_2	435	650	130	-	low	Combined with micro arc oxidation to enhance the corrosion resistance	[11]

Substrate Material	Coating Material	Gas Type	Gas Pressure (psi)	Gas Temperature (ºC)	Coating thickness (µm)	Surface roughness (µm)	Porosity	Comments	Ref
AZ31	Al-Zn-Ni-Al_2O_3	Air	90	500	400	-	low	Study on Corrosion and wear resistance	[13]
AZ31	Ti-6Al-4V	N_2	550	780	-	-	-	Study on particle deformation and bonding	[77]
AZ31	Al		260-320	280-340	-	-	-	Study on processing parameters	[16]
AZ91D	Al-Mg	Air	290	150	12	0.6	-	Combined with die-casting, high wear and corrosion resistance	[78]
AZ91(Cast)	Al	He	70-110	100-250	75-200	-	0.25%-1.75%	Study on processing parameters	[17]
ZE4A-T5Mg (Cast)	Al-Mg	N_2 He	300-500	He: 25 N_2: 300-500	380-700	-	0.5%	Study on corrosion resistance	[79]
AZ91D(Cast)	Al	Air	230	230	-	-	low	Study on microstructure of coating, corrosion resistance	[80]
AZ91E(Cast)	Al6061-Al_2O_3	He	90	125	500-1000	-	1%-1.5%	Study on tensile bond strength, corrosion, wear resistance	[81]

2.3.3 The influence of cold spray on fatigue strength and life

Cold spraying as a surface treatment significantly influences the fatigue strength of a material. It can create a densified coating layer of strong materials on the substrate surface, develop a fine microstructure at the interface or near the substrate surface, and induce compressive residual stress. It can also increase the corrosion resistance of a material when the coating material has a higher corrosion resistance than the substrate one.

Under cold spraying, when the particles impact the substrate surface (peening), severe tensile plastic deformation is formed on the surface layer, and the accumulation of numerous indentation expansions generates compressive stresses at the surface. The induced compressive stress can remain in a material after processing, even in the absence of external forces or thermal gradients, so it is defined as a compressive residual stress [82]. Fig. 2-6 depicts a schematic of particle impact and the distribution of residual stress at and near the surface.

In addition to inducing compressive residual stress, the intensive plastic deformation causes the densities of crystal lattice defects to increase, particularly dislocations, with consequent increased strain energy. To reduce the extra strain energy, the dislocations rearrange themselves and become grouped in the grains. Accumulation of dislocations in the grains makes them energetically unstable. When the number of dislocations in a crystalline grain increases and reaches a critical value, misorientation develops in the grain; hence the dislocations will align inside of the grain and create sub-grain boundaries or low-angle grain boundaries. Further deformation leads to rotation of the sub-grains on both sides of the low-angle grain boundaries; therefore, the sub-grains can rotate with high angle and form very small individual grains [83]. However, when the temperature of the substrate surface increases due to the heat transfer from the carrier gas, and more importantly from “impact temperature” the grain size may change, or even dynamic grain growth occurs. This grain refinement may occur after impact or during deposition and deformation of the interface, in what is called dynamic recrystallization. This dynamic recrystallization depends both on temperature and deformation, and occurs over a very short period of time while deformation is happening [84]–[88]. Therefore, the effect of cold spray on the microstructure of substrates should be considered since improving the fatigue life of coated materials is strongly related to the microstructure of those coated materials.

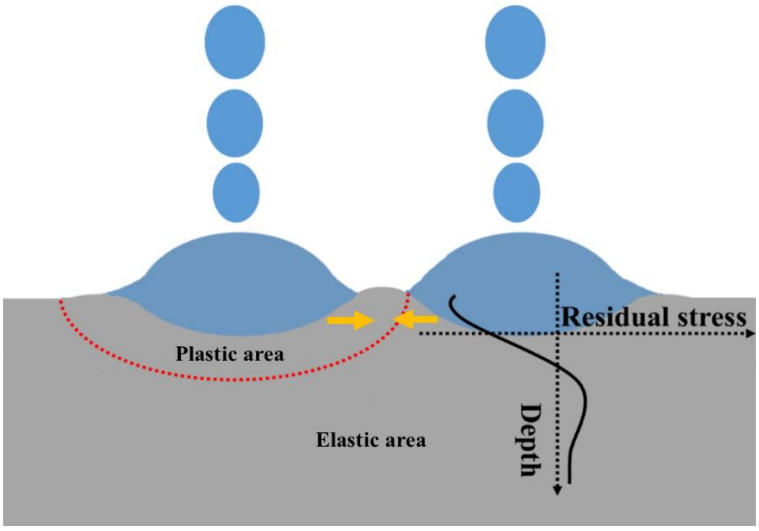

Fig. 2-6: Schematic of particle impact and formation of compressive residual stress.

Overall, the main factors influencing the fatigue strength of a material coated by cold spray are: a) the bond strength between substrate and coating, b) the coating material and quality (microstructure, porosity, and mechanical properties), c) surface roughness, and d) residual stress distribution. The role that bond strength plays in improving the fatigue strength is clear. A strong bond at the interface is required to prevent crack initiation from the substrate surface. Low bonding strength leads to coating delamination and increases surface roughness, resulting in decreased fatigue life. Ghelichi et al. [89] performed cold spray coating on Al5052 with two powdered materials: pure Al and Al7075. The poor adhesion of Al on Al5052 and the high bond strength between Al7075 and Al5052 can be observed in Fig. 2-7a, and Fig. 2-7b, respectively. The significant enhancement of the fatigue strength of a material coated with Al7075 occurs due to the noticeable bond strength and the strength of the coating material, as compared to pure Al [89]. To achieve higher bond strength, a surface pre-treatment (grit blasting) was performed by Ziemann et al. [90] prior to coating pure Al on Al2024. The fatigue behavior of the coated samples was significantly improved, up to 50% at 180 MPa (stress level) and up to 38% at 210 MPa, compared to bare samples. The authors mentioned that grit blasting induces compressive residual stress and increases the surface roughness, which can enhance the interaction between substrate and coating and facilitate removing or decreasing of the inherent oxygen layer from the substrate surface improving coating adhesion. Both inducing compressive residual stress and enhancing coating adhesion lead to the improvement of the fatigue strength at two stress levels. Comparisons between the results showed that the fatigue strength was strongly dependent on the surface preparation and cold spray parameters [90].

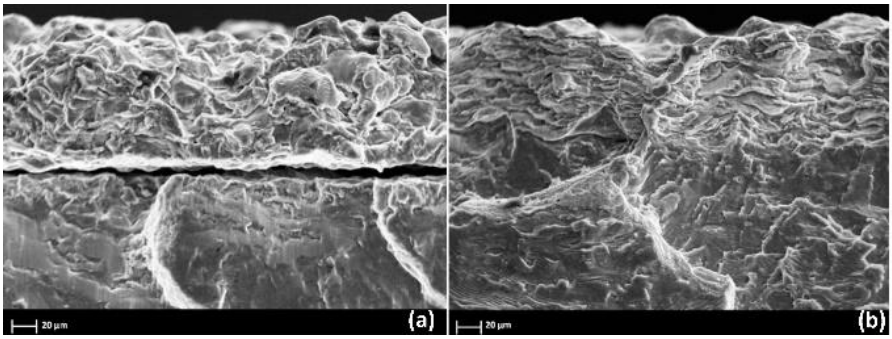

Fig. 2-7: SEM observation of cross section of deposited material (a) Al5052 coated with pure Al; (b) Al5052 coated with Al7075 [89]**.**

The processing parameters of cold spray also affect the bond strength. The relation between bonding ratio and particle velocity was determined by Wang et al. [17]. They demonstrated that increasing the carrier gas temperature increases particle velocity and leads to greater plastic deformation, resulting in a significant improvement in the adhesion of Al particles on AZ91Mg alloy. Moreover, increasing the gas temperature reduces coating porosity and enhances coating hardness, deposition efficiency and bond strength. Based on this report, increasing the carrier gas temperature more effectively enhances particle velocity than increasing the gas pressure [17]. In some cases, the impact of coating quality is greater than that of bond strength. When pure Ti was deposited on Ti6Al4V by Cizek et al. [91], there was good adhesion between the coating and the specimen substrate, but the fatigue strength decreased. Low coating quality (high surface roughness and relatively high porosity) allowed cracks to initiate in the coating and propagate vertically. Once a crack has formed, it will move toward the substrate due to the strength of the bond and lead to rapid sample deterioration, decreasing its fatigue life [91]. Hence, the integrity of the coating in terms of its compact microstructure and cohesive strength can significantly impact the mechanical properties of the coated material, enhancing or weakening its fatigue performance [92]–[94]. Moreover, the microstructure and mechanical properties of coating material can also play important roles in enhancing the fatigue strength of coated specimens. Materials with high ductility, such as pure materials, can be deposited with lower critical velocity and higher plastic deformation to create good quality coatings; however, these materials usually have lower strength compared to their alloys. Higher-strength material depositions show relatively higher fatigue strength compared to lower-strength materials with higher ductility. Xiong et al. [9] reported that by depositing Al+30% Al_2O_3 and Al+50% Al_2O_3 on AZ91 Mg alloy, the yield strength and high-cycle fatigue limit of AZ91 were increased significantly compared to uncoated Mg alloy [9]. These improvements were strongly related to the volume fraction of Al_2O_3 in the coatings. They claimed, by

strengthening the composite coatings and the bonding between the coating and substrate, the fatigue properties of AZ91 can be improved [9].

Besides bond strength and coating quality factors, surface roughness also affects the fatigue performance of a material. The presence of cavities, corners, edges and other topographic features can increase the stress concentration and promote crack initiation and propagation in coated material, diminishing its fatigue strength. To reduce the negative influence of surface roughness, the roughness must be minimized with post-deposition polishing and machining.

In addition to the abovementioned factors, peening, cooling or quenching, gas temperature and thermal mismatch due to differential coating-substrate material thermal expansion coefficients are factors that influence the residual stress of coated material [95]. Furthermore, increasing the impact velocity increases the kinetic energy, and as a consequence may induce more compressive residual stresses in coated material. The impact velocity can be increased by increasing the temperature and pressure of carrier gas and decreasing the particle diameter. Moreover, increasing the feed rate can enhance the number of particles impacts and affect the residual stress induced by peening. In addition, the dimension of the nozzle, the standoff distance and the spraying angle affect the velocity of particles [63]. However, increasing coating temperature impact and gradient temperatures can decrease the stress induced in materials.

The influence of pre-heated substrate temperature on the residual stresses was investigated by Rech et al. [95]. Pure Al was deposited on Al6061 at different temperatures in the range of 24º-375ºC. Coated samples were quenched in water and then residual stresses were measured. The compressive residual stress in the substrate, which began at -500 Mpa at 24º C, was decreased to -50 Mpa at 292ºC, due to the higher substrate temperature and the greater time required for reaching and stabilizing the temperature. The researchers concluded that the presence of tensile residual stress at the interfaces between sequential passes balanced the compressive residual stress in the coating [95]. Luzin et al. [62] studied the residual stress profiles (determined using neutron diffraction) of Al and Cu as coating and substrate materials in the configurations Al/Al, Al/Cu, Cu/Cu and Cu/Al [62]. They employed Tsui and Clyne's progressive model [96] and demonstrated that the residual stresses were strongly dependent on the plastic deformation due to the impact velocity, whereas the thermal effects did not play an important role in altering the residual stress profile for these coating and substrate materials The residual stress profiles of Cu/Cu and Al/Cu represented the tensile residual stresses at the interfaces of both coating samples ; however, at the surface of coated samples, compressive residual stress can be observed. The role of processing parameters on the residual stress and fatigue performance of coated samples such as

Al7075/Al7075, Al2024/Al7075 and Al2024/AZ91 was investigated by Cavaliere et al. [19]. They demonstrated that by increasing the gas pressure and decreasing the temperature, the compressive residual stress at the interface near the substrate was increased for Al alloys coated on Al7075; however, increasing the gas pressure had a greater influence on the resultant residual stress of AZ91 coated samples. Furthermore, the extent of compressive residual stress induced in the Al-alloy coated samples was significantly higher than that in AZ91-coated samples due to the greater hardness of Al-alloy substrates over Mg-alloy substrates [19].

The effect of particle impact on substrate residual stress was simulated by Shayegan et al. [97]. They employed an asymmetric material model that considered the strain rate effect to simulate the deposition of pure Al on an AZ31B extrusion substrate with asymmetric behaviour. A parametric study on a single particle model demonstrated that the maximum compressive residual stresses developed under high particle velocity, the right impact angle and large particle size. However, concluding that the modeling results showed a direct relation between particle size and increased beneficial residual stresses is somewhat controversial; increasing the particle size leads to a rise in the average impact temperature and increases the cooling rate at the identical velocity impact [93]. This fact may influence the residual stress profile, decreasing the compressive stress or completely releasing the beneficial stress. In addition, they proposed a second model for multiple particles in terms of size and shape that was in good agreement with experimental observation for a depth >100 μm. Based on their observations, the compressive residual stress at the surface of the substrate had better agreement with the XRD results, when the diameter of the particles was different (second model) [97]. Ghelichi et al. [89] performed coating deposition of pure Al and Al7075 on Al5052. The compressive residual stresses in both series were increased, and as a consequence the fatigue strength improved; however, the deposition of pure Al resulted in greater compressive residual stress in the substrate. Since higher temperatures are required to reach sufficient impact velocity for coating Al alloys versus pure Al, the substrate temperature increased more during cold spray coating with Al7075 powder and thus relieved the induced stress and decreased the compressive stress [89]. Moridi et al. [69] studied the effect of cold spraying on the fatigue behaviour of similar materials using Al6082/Al6082. Based on the results, the fatigue strength of the coated material was enhanced by about 15%. They concluded that the increased compressive residual stresses in the coating and substrate were the main reason for the improved fatigue limit of the coated material [69].

Dayani [98][99][100] investigated the fatigue behaviour of AZ31B cast Mg alloy after cold spray deposition with Al7075. The residual stresses profiles of the coated samples were determined through

XRD and hole-drilling. The results showed significant compressive residual stress in the coating, while tensile residual stress was induced in the substrate [98]. Based on the observation, the fatigue limit of the coated samples had considerably improved (25%), compared to the bare samples. Dayani reported that the higher hardness and higher fatigue strength of the coating material over the substrate and the induced compressive residual stresses of the coating were what led to the enhanced fatigue limit of the AZ31B cast samples [98]. The strength of the coating material and the significant compressive residual stresses in the coating served as an obstacle, retarding crack initiation at the surface; hence, the coated material could tolerate higher levels of stresses before any crack initiated; therefore, the number of cycles to failure increased [98]. Fig. 2-8 shows cross-sectional fractography observation of the coated AZ31B cast. No signs of delamination or cracking in the interface or coating regions can be observed. However, cracks initiated and propagated in the AZ31B cast substrate [98], and can be attributed to the lower strength substrate material and to the induced tensile residual stresses in the substrate. After the cold spray process, the substrate and coating are usually cooled to room temperature; hence, a thermal misfit strain may emerge and influence the residual stress.

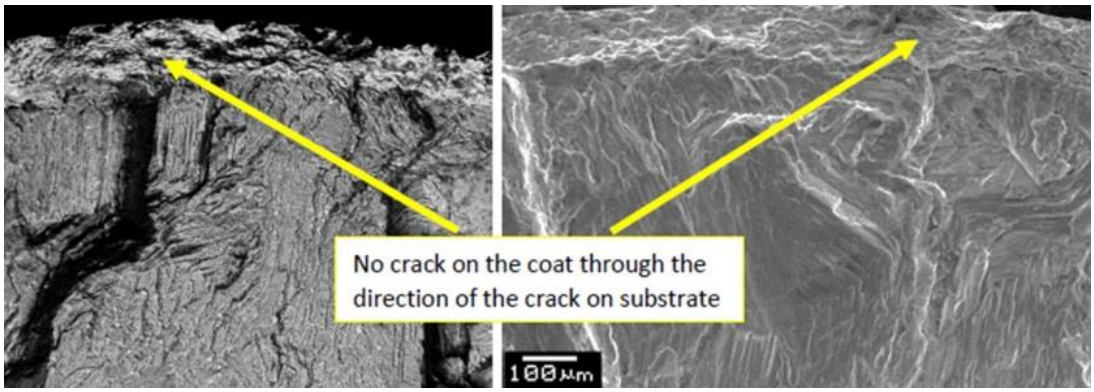

Fig. 2-8: SEM observation of cross section of deposited material Al7075 on AZ31B cast [98]**.**

The overall fatigue performance of different cold-spray coated materials from the literature is summarized in Table 2-2. As mentioned above, some of the conclusions reached about fatigue life based on the reported results should be taken with caution given how many factors can contribute to the fatigue behaviour of cold spray deposition.

Table 2-2: Summary of reported fatigue tests results for different coated samples.

Material	Gas type	Gas pressure (psi)	Gas temperature (ºC)	Coating thickness (µm)	Fatigue type specimen	Surface roughness (µm)	Fatigue life	Ref
Ti on Ti6Al4V	He	435	27	120	Hourglass	8.6	Decreased (15%)- Delamination	[101]
Ti on Ti6Al4V	He	232	260	700 (2pass)	Flat	11.28	Decreased (9%)- Delamination	[10]
Al6082 on Al6082	N_2	435	350	100	Hourglass	-	Increased (14.7%)-No delamination	[94]
Al on Al5052	N_2	232	350	115	Flat	9.5	Slightly increased - Delamination	[89]
Al7075 on Al5052	N_2	232	500	50	Flat	5.5	Increased (30%)-No delamination	
Al on AZ31B Extrusion	N_2	500	500	225	Hourglass	-	Increased (~10%)-No delamination	[14]
Al+xAl_2O_3 (x=30, 50 vol.%) on AZ91	He	90	204	500	Flat	-	Increased (~20%)	[9]
Al2024 on AZ91	-	60-400	250-400	500	Flat	-	Increased	[19]
Al7075 on AZ31B Cast	N_2	200	400	175	Hourglass	~1	Increased (25%)-No delamination	[98]

2.4 Residual Stress Measurement

Since inducing residual stress during cold spraying can significantly influence the fatigue resistance of coated materials, determining the residual stress before and after the process is essential. In addition, the beneficial residual stress associated with peening is influenced by factors such as rising temperature

during the process and thermal mismatch. Therefore, measuring the residual stress during the cold spray process and finding the influential parameters are both highly relevant.

Residual stress measurement techniques are divided into two categories: destructive/semi-destructive methods (relaxation methods) such as hole-drilling, sectioning, ring core, crack compliance and layer removal [102]; and non-destructive methods (physical determination) such as X-ray diffraction, neutron diffraction, magnetic, ultrasonic and Raman [103]. In the following sections, hole-drilling (semi-destructive) and x-ray diffraction (non-destructive) methods, commonly used approaches in residual stress measurement, are briefly described. A new in situ measurement technique, Fiber Bragg Grating sensor, is then introduced.

2.4.1 Hole-drilling

Hole-drilling is a relatively simple and fast method and one of the most popular residual stress measurements techniques [104]. The distribution of residual stress across the thickness of a sample can be measured in both magnitude and direction with this method. The technique is based on the principle of strain relaxation. A highly sensitive strain gauge rosette is installed on the sample surface where the residual stress is to be measured. A small shallow hole (about 1.8 mm diameter and up to about 2.0 mm depth) is mechanically drilled at the rosette's center with a high-speed turbine (400,000 rpm) that prevents inducing undesirable stresses during hole-drilling. Drilling and removing the material relieves the residual stresses in the locality around the circular hole. Corresponding released strains are measured with a three-element strain gauge at three different directions, and then the related residual stress profile can be calculated through the depth. There are a number of analytical solutions for calculating the residual stress that are corroborated with finite elements (e.g., [105]), such as ASTM E837-13 [106], ASTM E837-08 (used to determine the uniform constant stress field and non-uniform stress through depth), and the integral method [107][108]. Among these, the non-uniform and integral methods are the most suitable for measuring depth-varying residual stresses such as are found in coated Mg alloy samples, by using incremental hole-drilling steps. In these methods, the number and distribution of the depth increments are selected so as to calculate the residual stresses through the thickness while respecting the strains acquired at each drilling step.

2.4.2 X-Ray Diffraction

The X-ray method is a non-destructive technique with relatively high accuracy for the measurement of residual stresses on a material's surface. In this method, the stored stress in the material is obtained by

examining the elastic strains resulting from changes in the distance between crystallographic planes [109]. A crystalline material consists of many crystal grains, in which the atoms have been arranged in a periodic pattern in three dimensions. The interactions between the X-ray beam and the crystal lattice through diffraction can cause constructive and/or destructive interference patterns. Any changes in the lattice spacing due to applied mechanical loading and residual stress causes changes in the diffraction angle [110]. The fundamental interference pattern with respect to the diffraction angle is defined with Bragg's Law:

$$n\lambda = 2d \sin \theta \quad \textbf{(2-1)}$$

where n is an integer denoting the order of diffraction, λ is the X-ray wavelength, d is the lattice spacing of the crystal planes, and θ is the diffraction angle. The reflected X-ray from the lattice plane can be detected as two conic sections. In X-ray diffraction, data collection and analysis are conducted based on one-dimensional, and more recently two-dimensional (2-D), diffractions. Two-dimensional diffraction with a 2D detector focuses on the direct relationship between the stress tensor and the diffraction conic section distortion. In 2D method, it is possible to collect more information and data in shorter time and provides a 2D frame as a diffraction ring.

2.5 Fiber Bragg Grating Sensor

In situ mechanical and thermal strain measurements taken during cold spraying are essential for identifying the roles that critical parameters play in inducing mechanical and thermal strain. Moreover, the in-situ optimization of processing parameters would save time and energy. The FBG is a new generation of sensor, which can be embedded into or installed on a material to detect a variety of quantities such as strain, temperature, pressure, and vibration due to its fundamental nature and structure [111][112]. The general advantages of FBG sensors over conventional strain gauges include their ability to be embedded into the material, insensitivity to electromagnetic fields, suitability for use in harsh conditions such as cold spray (i.e., high vibration media) [113][114], small mass of the connecting leads and as a consequence small influence of this mass on the sample. However, FBG sensors have some shortcomings, such as being sensitive to temperature changes, brittleness, and conflation of thermal and mechanical strain results.

A fiber optic is a filament made of fused silica (SiO_2) that consists of two parts, a core and cladding. The core is a very thin, with a diameter of 4 to 9 μm, and is surrounded by cladding with the greater diameter of 125 μm. These two main parts are coated with acrylate, polyimide, or organic modulated

ceramic to enhance mechanical stability and prevent fiber cracking [115]. Fig. 2-9a and Fig. 2-9b depict the structure of an FBG sensor schematically and an actual FBG sensor, respectively. To create an FBG sensor, germanium is doped into the core using an intense ultraviolet light; afterward Bragg grating is written into the germanium doped core. A set of high intensity and narrow wavelength band peaks is created in the inner part of the fiber, after the Bragg grating is inscribed into the core. Therefore, the light (a broadband spectrum of electromagnetic wave) travels only inside the core, due to the higher refractive index of the core compared to the cladding [111].

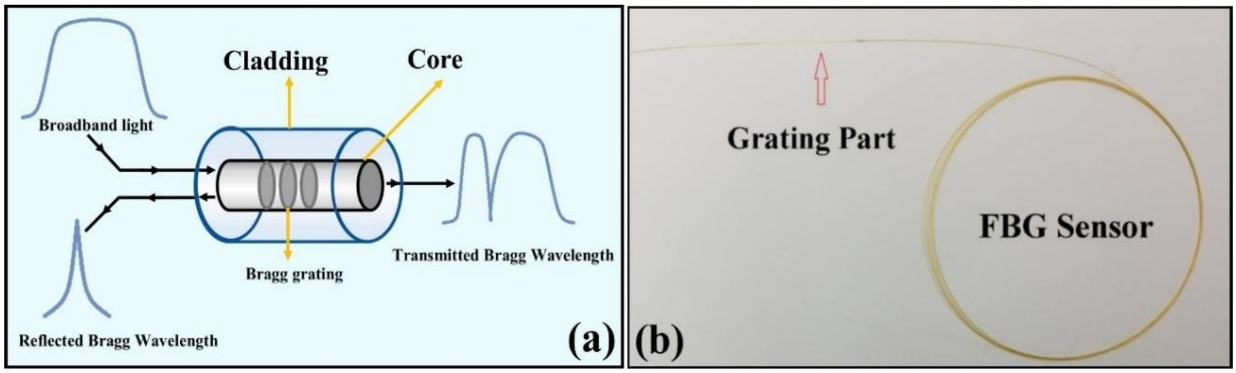

Fig. 2-9: a) Schematic of FBG sensor and wavelengths; b) FBG sensor.

The incoming light can be transmitted and reflected after it travels inside the core. The results of constructive and destructive interference can create a strong reflection peak and/or refraction, respectively [116]. According to Bragg's law, λ_B is the reflected wavelength or the Bragg wavelength, which is defined by the following equation:

$$\lambda_B = 2 n_{eff} \Lambda_G \quad \textbf{(2-2)}$$

where, n_{eff} is the effective refractive index of the grating in the core and Λ_G is the periodicity of the grating. If the effective refractive index of the grating or the periodicity of the grating is changed due to any external force and/or temperature changes, the Bragg wavelength is altered, and the FBG reflection main peak shifts to the right or left depending on the tension and compression and /or thermal expansion or contraction. Therefore, when the FBG is attached as a sensor on the structure, temperature changes and external force can shift a Bragg wavelength, which identifies the mechanical strain and temperature changes of a material sample. The Bragg wavelength changes can be recorded by an interrogator during the measurements that illustrate the changes in the periodicity of the grating. The

relation between the wavelength shifts, strain, and temperature changes is specified according to the following equations:

$$\frac{\Delta \lambda}{\lambda_0} = k \times \varepsilon + \alpha_\delta \times \Delta T \quad \textbf{(2-3)}$$

where, $\Delta\lambda$ is the wavelength shift, λ_0 is the initial wavelength, k is the gauge factor, ε is the total strain mechanical (ε_m) and thermal (ε_T), α_δ is defined by the change of the refractive index, and ΔT is the temperature change (K) [115].

The FBG sensors can be employed for multiple purposes in wide dynamic and temperature ranges as well as for strain/deformation and temperature measurement in different applications and situations such as monitoring the fatigue crack growth rate during fatigue testing [117]. Various mechanical packages have been introduced to provide good conditions for the sensors, which may have to stay in place for a long time in harsh environments. Since the FBG sensors use light instead of electrical conductors, they are immune to electromagnetic interference and high voltage. The sensor can be exposed to various temperatures, such as in cryogenic environments, due to its low thermal conductivity.

Recently, FBG sensors were used to measure the strain during rotating bending tests while the temperature was supposed to be constant [116], [118], [119]. In the current research, the ability to embed the sensors in a material is employed to characterize the thermo-mechanical strain behaviour induced in the substrate surface during cold spray tests. Fiber Bragg grating (FBG) sensors have been employed to study the thermo-mechanical behaviour of the substrate during the cold spray coating process.

2.6 Summary

According to the literature reviewed in this chapter, the cold spray technique has the capability to boost the fatigue characteristics of materials by creating a dense layer of high fatigue strength coating, inducing compressive residual stress and refining the microstructure of material. However, despite the role of cold spray coating on the fatigue life enhancement of materials, there are a few studies in this context with contradictory results. Among them, only few of the studies involved Mg alloys. Due to this lack of knowledge in the literature, and the importance of thermal effects on the physical and mechanical properties of Mg alloys, investigation into the thermomechanical behaviours of these alloys during cold spray coating is essential. In this regard, research would benefit from a comprehensive study on the effect of processing parameters (particularly carrier gas temperature), thermal energy

balance and thermal mismatch on the mechanical and thermal strain evolution of the Mg alloy substrate during the coating process.

Chapter 3

On the Evolution of Substrate's Residual Stress during Cold Spray Process: A Parametric Study[1]

3.1 Abstract

A comprehensive study was undertaken to determine the effects of carrier gas temperature, pressure, and nozzle speed on the residual stresses induced by cold spray coating of aluminum 7075 powder onto AZ31B-H24 magnesium (Mg) substrate. Embedded Fiber Bragg Grating sensors and thermocouples were employed for simultaneous in-situ measurements of strain and temperature during cold spray process. A statistical model was then developed based on the significance and interactions of the cold spray parameters on the residual stress field. This model demonstrated that the induced temperature is the most significant parameter to the final formation of residual stress. It is also shown that the peening effect plus the temperature resulted from the cold spray yields to the dynamic recrystallization of the substrate near the surface, and generates Nano-size grains at the interface. This research validates that the final size of the refined grains and the level of induced residual stress depend heavily on the process' thermal energy.

3.2 Introduction

Developing effective approaches to extending the life of aging structural materials is a major challenge, particularly for load-bearing components. Since majority of structural failure is attributable to fatigue, research focused on the enhancement of fatigue strength in structural materials has become significant [120]. For this purpose, inducing beneficial residual stresses at critical locations, where fatigue cracks nucleate, is shown to be a successful approach to postponing the fatigue crack failure of mechanical components during service [121][122]. Moreover, strengthening the material surface with the coating of high fatigue resistance material is a technique for increasing the life of a low fatigue strength material [123]. "Cold Gas Dynamic Spray" technology, a solid-state coating process, creates both mentioned benefits [124]. This coating method can be used to deposit micron-sized metal particles that have been accelerated to a high velocity (300-1200 m/sec) onto a material's surface via a de Laval nozzle [58]. The particles and substrate are severely deformed upon impact, resulting in mechanical/metallurgical

[1] This chapter was published as a paper in the journal of Materials and Design, 138 (2018), pages 90-102.

bonding between the substrate and coating [59]. On the other hand, the surface hardening treatment result of a peening effect can induce compressive residual stress as well as grain refinement in the coated material. Up to now, numerous studies involving cold spray technique have shed light on the bonding mechanism, coating quality, and applications toward corrosion and wear resistance. However, in spite of the important role of cold spray in improving the fatigue life of materials [89][18][19], this topic has been addressed in only a few cases, with some contradictory results regarding the effectiveness of cold spray in enhancing fatigue life [101][10].

To date, a few studies have attempted to evaluate the impact of the cold spray on the fatigue behaviour of materials through consideration of four main factors: 1) the properties and quality of a coating material [10][9][125], 2) bond strength [89][101][126], 3) surface roughness [90] and, 4) residual stress induced by the coating process [94][127]. The first three certainly have essential roles in enhancing the fatigue performance of coated samples, while detrimental residual stress distribution can remove all benefits and decrease fatigue strength [89][101]. Despite reports on minimal effect of residual stress on the fatigue life of coated materials [127][62], research on controlling residual stress distribution in both coating and substrate are necessary and critical [101][128]. However, there is little published data addressing the formation and distribution of residual stress induced during cold spray process.

Compressive residual stress may be generated in a substrate and/or coating due to high impact energy associated with the particles' mass and velocity. A particle velocity that is high enough to achieve the best quality of coating without interface delamination is provided through tuning the effective parameters, pressure and temperature, of the carrier gas [65][129][130]. However, there have been mixed findings about the carrier gas pressure and/or the temperature contribution to the final coating characteristic as well as to induced residual stress and fatigue performance of coated samples [89][19][62]. Cavaliere et al. [19] investigated the role of processing parameters on the residual stress and fatigue performance of coated samples: Al7075/Al7075, Al2024/Al7075, and Al2024/AZ91 coating/substrates. They found that with increasing the gas pressure and decreasing gas temperature, the compressive residual stress at the interface near the substrate was increased for coated Al alloys on the Al7075. However, gas pressure changes had more noticeable beneficial effects on the variation of residual stress of AZ91 coated sample compare to the other ones [19]. They further reported that in both Al/Al and Al/Mg cases the coating lead to increase in fatigue life with surface residual stresses playing a major role. Luzin et al. [62] studied the residual stress profiles of Al/Cu as coating and substrate materials at different conditions. They revealed that the residual stresses were strongly depending on the plastic deformation due to the impact velocity; whereas thermal effects were not

playing an important role in changing the residual stress profile [62]. Ghelichi et al. [89] studied Al/Al cold spray coating and observed that despite Al7075 higher hardness as compared to pure Al, the residual stress induced by Al7075 powder were lower than the ones induced by pure Al. They attributed this to the higher temperature in Al7075 coating. The difference between the studies is strongly related to the material property of coatings and substrates [89]. Moreover, it is reported that the strength of the substrate and coating material [131][132] as well as the substrate temperature [95] affect the residual stress of the coating and substrate. Hence, the effect of cold spray coating parameters on the residual stress and, as a consequence, the fatigue life of coated sample, can be accurately explained when the substrate and coating materials are both considered.

Due to the high demand for reducing greenhouse gas emissions, light weighting of transportation vehicles have recently received major attention [133]. In particular, the application of magnesium (Mg) alloys, as the lightest commercially available structural metals with superior properties (e.g., a high strength-to-weight ratio), for use in auto and aerospace industries has risen dramatically [22]. However, low corrosion, wear and fatigue resistances have restricted their widespread use in structural applications, particularly in load-bearing components [6][134]. Based on the nature of cold spraying, cold deposition of a fatigue-resistance metal powder on Mg substrate can be an ideal solution to boost the fatigue performance of the Mg alloy [18][97]. However, the induced residual stress of Mg substrates after cold spraying has been reported to range from compressive to tensile, corresponding to processing parameters and coating materials [19][127][62]. On the other hand, since high thermal sensitivity and low-strength of Mg alloys are more susceptible to residual stress changes, a comprehensive study of the residual stress evolution during cold spraying of these materials is of more interest in identifying the role of different coating parameters in the formation of residual stresses. Determination of the parameter most significant to optimal coating conditions will lead to increased beneficial residual stress and improved Mg alloy microstructure, thereby enhancing fatigue life.

To better understand the interaction between thermal and mechanical strains induced during cold spray coating, we present the in-situ thermo-mechanical behaviour of Mg alloy substrate undergoing cold spraying. Embedded Fiber Bragg Grating (FBG) sensors and thermocouples are simultaneously employed to monitor strain and temperature changes during the cold spray process. The effect of cold spraying on the substrate's microstructure and interface is investigated under various carrier gas temperatures and pressures. A set of experiments has been designed to study the role of carrier gas pressure, temperature, and nozzle travelling speed on a substrate's residual stress. The residual stresses of as-received and cold spray-coated Mg alloy substrates are measured by X-ray diffraction and hole

drilling methods. The effect of coating parameters and their interactions on residual stress are statistically analyzed to identify the most significant parameter.

3.3 Materials and Methods

3.3.1 Material characterization

In this study, for in-situ strain and temperature observation, 4mm thick AZ31B-H24 Mg alloy sheets were used as the substrate. The chemical composition of the substrate is reported in **Table 3-1**. The dimensions and shape of the samples are shown in Fig. 3-1a and Fig. 3-1b, respectively. Where applicable, stress relief heat treatment (260ºC/15min) was carried out on the as-received sheets based on the ASM-recommended procedure [135] to remove any manufacturing related residual stresses. In addition to examining different coating processing parameters on measured residual stress, 12 rectangular pieces of as-received AZ31B-H24 samples (50×30×3.16mm) were prepared.

Spherical-shape commercial Al7075 powder (supplied by Centerline Ltd., Windsor, Canada) was the material deposited in the experiments. The SEM image of particles and particle size distribution with a mean value of 23μm (measured by Retsch technology, Camsizer XT) are depicted in **Fig. 3-2**a and **Fig. 3-2**b, respectively. **Table 3-1** lists the chemical composition of the Al7075 powder.

Table 3-1: Chemical compositions of AZ31B-H24 Mg alloy [23] **and Al7075 coating powder.**

Materials	Aluminum (Al)	Zinc (Zn)	Manganese (Mn)	Iron (Fe)	Nickel (Ni)	Silicon (Si)	Copper (Cu)	Chromium (Cr)	Magnesium (Mg)	Other Elements
AZ31B-H24	2.5-3.5	0.60-1.40	0.2 Min	0.005 Max	0.005 Max	0.10 Max	0.05 Max	_	Bal.	_
Al7075	90	5.2	_	0.35	0.005	_	1.55	0.25	2.35	0.3

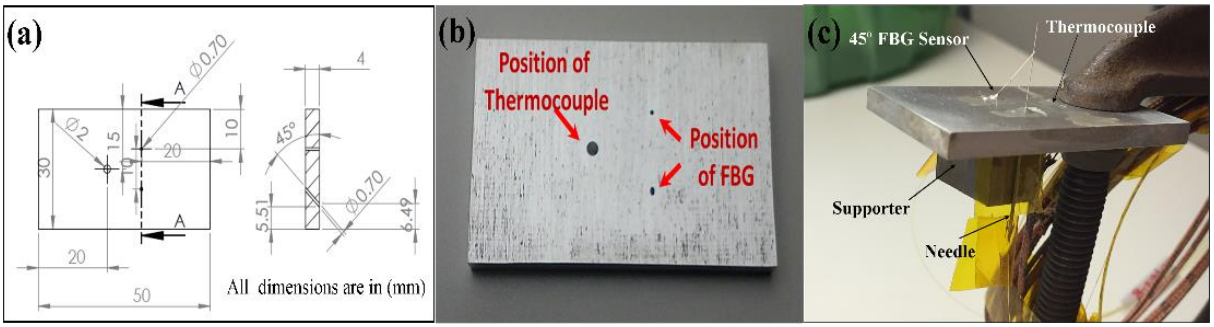

Fig. 3-1: a) Drawing and geometry of AZ31B-H24 samples; b) position of thermocouple and FBG sensors; c) test sample setup for embedded sensors and thermocouple.

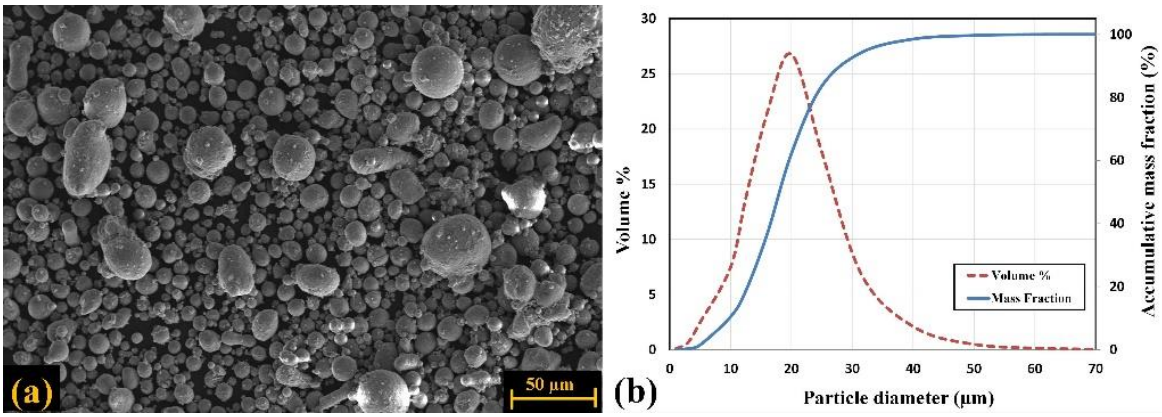

Fig. 3-2: a) SEM image of Al7075 powder; b) particle size distribution for Al7075.

3.3.2 In-situ strain and temperature measurement

FBG sensors are a class of optical sensors made of hair-thin filaments of fused silica that are able to detect and quantify external stimuli, such as load and temperature, by reflecting wavelength changes [111][112]. Strain evolution can be calculated through a simple equation that considers wavelength changes. The capacity of FBG sensors to measure mechanical (at a constant temperature) or thermo-mechanical strain locally with respect to changes in wavelength has been studied extensively, and shows high accuracy and good agreement with alternative measurement methods [118][136].

Corning SMF-28 FBG sensors with polyimide coating and a reflectivity of 90% were employed for in-situ measurements of strain. The FBG initial wavelength was 1560nm and the grating length was 10mm. To achieve a higher measurement accuracy, the sensor's polyimide protective layer was removed from the grating by dipping the sensor into hot sulfuric acid (98%) for 20 minutes followed by rinsing with deionized water [118].

The relationship between the wavelength shifts, strain, and temperature changes is specified according to the following equations:

$$\boldsymbol{\varepsilon = \frac{1}{K}\left(\frac{\Delta\lambda}{\lambda_0} - \alpha_\delta \times \Delta T\right)} \quad \textbf{(3-1)}$$

$$\boldsymbol{\varepsilon = \varepsilon_m + \varepsilon_T} \quad \textbf{(3-2)}$$

$$\boldsymbol{\varepsilon_T = \alpha_{sp} \times \Delta T} \quad \textbf{3-3)}$$

$$\boldsymbol{\alpha_\delta = \frac{\delta n/_n}{\delta T}} \quad \textbf{(3-4)}$$

where, $\Delta\lambda$ is the wavelength shift, λ_0 is the base wavelength at test start, k is the gauge factor, ε is the total strain caused by force (ε_m) and temperature (ε_T), α_δ is defined by the change of the refractive index with temperature, α_{sp} is the expansion coefficient of the sample (1/°K), and ΔT is the temperature change (°K). For measuring temperature, a type K thermocouple (300µm wires) was attached to each sample in such way that it would be able to detect the substrate surface temperature. The temperature of substrate was recorded during one pass coating treatment with a frequency of 1Hz. Experiments and numerical simulations have shown that during the coating process, stress in a substrate is faded as it approaches 1 mm depth [127][62][97][137]. Therefore, the depth and alignment of the grating of FBG sensor as well as thermocouple were selected carefully to ensure that the maximum strain and temperature changes at and under the substrate surface could be observed during the cold spray coating. Stress-relieved AZ31B-H24 samples were prepared with 90° and 45° aligned 700 µm diameter holes for embedding the FBG sensors, and with a 1 mm diameter hole for the thermocouple (Fig. 3-1b and Fig. 3-1c). Then, the sensors and thermocouple were embedded in the holes and adhered by a thin layer of thermal epoxy (353ND EPO-TEK) that was cured at 150°C [138].

3.3.3 Cold-spray process

A commercial Supersonic Spray Technologies (SST) Series P Cold Spray System, manufactured by Centerline, Windsor, Canada, was used to coat the as-received samples. In this process, Al7075 powders are accelerated through a converging–diverging de Laval UltiLife TM nozzle to supersonic velocities in a low-pressure system. **Table 3-2** lists the typical processing parameters required for high coating quality. Sample thicknesses were between 300-350µm, with a high hardness of 139.6 ± 19.4 HV.

Table 3-2: Cold spray coating parameters.

Carrier Gas	Gas Temperature	Gas Pressure	Powder Feed Rate	Nozzle Speed	Step Over	Stand-off Distance	Nozzle Type	Nozzle Length	Nozzle Orifice Diameter	Nozzle Exit Diameter
N_2	400 °C	200 psi (1.38 MPa)	8 gr/min (5 rpm)	2 mm/s	1.2 mm	12 mm	De Laval UltiLife TM	120 mm	2 mm	6.3 mm

3.3.4 Microstructural analysis

Microstructural analysis was performed using transmission electron microscopy (TEM, JEOL-2010F) and scanning electron microscope (SEM, model: Zeiss Leo UltraPlus FESEMs) equipped with an Oxford energy-dispersive X-ray spectroscope. X-ray spectroscopy determined the chemical composition and surface coverage of the coated surfaces. Treated samples were cross sectioned in the plane perpendicular to the rolling directions, mounted, and polished with a series of graded abrasive papers from ~ 400 to 1200 grit, followed by fine polishing using diamond paste from 6 μm to 0.1 μm on Leco paper. Samples were then etched for 10 seconds in a reagent composed of 35 mL ethanol, 5 mL acetic acid, 2.1 g picric acid and 5 mL water to reveal the grain structure of the Mg alloy samples.

3.3.5 Residual stress measurement

The hole-drilling and X-ray diffraction methods were used to measure the induced residual stress in the coating and substrate samples. A hole-drilling machine (Sint technology, Restan MTS-3000) was used to evaluate the distribution of residual stresses through the depth of coated samples by measuring the relaxation strain. For this, conventional HBM three-element strain gauge rosettes were installed on the samples surface in the inspected area. The equipment's air turbine incrementally drilled a 2mm diameter shallow hole in the middle of the strain gauge rosette, at a speed of 400,000 RPM. The relieved strains were measured through the strain gauge rosette in three different directions. The measured incremental strain data were used to calculate the stress gradient through the depth of the sample by using the integral method [108]. This method is capable of calculating residual stresses corresponding to a highly non-uniform residual stress distribution up to 1mm depth. In addition, a Bruker D8-Discover equipped with a VÅNTEC-500 area detector with a radius of 135 mm, using Cu-Kα radiation at 40 kV and 40 mA, was used for X-ray residual stress measurements. During the measurement, the incident

beam and the detector were placed at a fixed 2θ angle of 99.22°. The collimator size was 1.0 mm. The sample was mounted on the motorized stage, which was oscillated at amplitudes of 1.5 mm and 2.5 mm at speeds of 3.5 mm/s and 5.5 mm/s for the X and Y axes, respectively. The samples were tilted between 0° and 50° with a step of 25° considered as the Ψ-scan, while the sample rotation known as Φ-scan was between 0° and 360° with a step size of 45°. The sample was scanned for 60s at each orientation. The Debye–Scherrer diffraction rings were collected using the area detector in a two-dimensional diffraction image. The complete residual stresses were then calculated using Leptos software in average depth of 50-100 μm corresponding to the penetration coefficient of Mg alloys [110].

3.4 Results and Discussion

3.4.1 In-situ strain and temperature monitoring

In-situ monitoring of mechanical and thermal strain was implemented during cold-spray coating deposition process through the FBG sensors embedded in the Mg alloy substrates. The response of the FBG sensor to extension or contraction of the gratings due to thermal and/or mechanical loads is a linear change in the reflected wavelength[2] [118][139]. Fig. 3-3 shows an example of some critical spectrums obtained at different nozzle positions during cold spraying, and schematically illustrates the relative positions of the nozzle and sensor. The response of the sensor after the embedding process but before coating is depicted in Fig. 3-3a. The spectrum of the sensor was asymmetrical because of the non-uniform strain along the grating (a part of the grating was embedded and attached into the substrate while another part was suspended outside of the substrate). In this case, the spectrum is expanded from the right side, emphasizing an initial elastic strain accumulation close to the substrate surface. When the nozzle approached the sensor (Fig. 3-3b), pick broadening and shifting to the right of the spectrum happened concurrently. In this condition, thermal strain due to the carrier gas temperature caused the shifting and broadening of the spectrum. When the distance between the nozzle and sensor is decreased, more stretching and shifting of the spectrum is expected. However, by placing the nozzle exactly above the sensor (see schematic Fig. 3-3c) the temperature is higher and as a consequence more peak shift and widening would be predicted. However, peak narrowing was observed, although the peak still showed more transition to the right (Fig. 3-3c). This change of spectrum shape illuminates a significant compressive strain induced by peening and severe plastic deformation during deposition decreasing the

[2] Further explanations have been provided in Appendix A.

effect of thermal expansion. This observation clarified the contrast between peening effect and increasing temperature. After passing the nozzle (Fig. 3-3d), the peak became broader and transmitted further to the right than before; thus, signs of compressive strain cannot be detected. This is evidence that the induced compressive stress of the substrate can be relieved in a few seconds. Fig. 3-3e shows the spectrum changes after the cold spraying and the Mg alloy sample reached room temperature. The shape of the spectrum has become narrower; however, the peak has shifted to the right as compared to the first recordings (Fig. 3-3a). Significant wavelength changes after cold spray coating (equivalent to 0.06% tensile strain) highlighted the effect of temperature arising from carrier gas and severe plastic deformation as an important factor on the strain evolution during the cold spray process. It is of note that the stress relief process releases the residual elastic energy of the material—in this case not only the compressive stress due to peening was relieved, but also tensile residual strain was resulted in the substrate. This can be explained by considering the thermal mismatch of the Al7075 coating and the AZ31B-H24 substrate. This mismatched strain created tensile residual strain during the cooling process (after the coating was completed). Variation in the residual stress remaining in the system, alternating from compressive to tensile, was also reported in the case of copper deposition on steel via analytical and numerical modelling [140].

In addition to in-situ FBG measurements, simultaneously the temperature at the substrate surface during the cold spray deposition was measured by embedding a thermocouple in the sample. Fig. 3-4 depicts the temperature gradient of the substrate sample during a single pass coating. When the nozzle was directly above the thermocouple, the thermal conductivity attributable to the carrier gas temperature in addition to the impact temperature raised the substrate surface temperature to 330ºC. In-situ temperature measurements also revealed that the interface experienced a temperature higher than 260ºC for 46 seconds. It is well known that increasing the temperature of a metallic crystalline material may cause annealing, which includes recovery, recrystallization and grain growth processes. These processes are both time and temperature dependent. Recovery happens at a lower temperature than the other processes and involves the realignment of dislocations leading to a significant decrease in dislocation density and, as a consequence, reduction of the residual stress even though the crystal structure of the sample is not changed. Recrystallization and grain growth are thermally activated diffusional processes that require more thermal energy. The annealing process of AZ31B-H24 takes only 20 seconds at 260ºC [141]. This fact, along with the measured temperature during coating (Fig. 3-4), can explain the in-situ strain observation reported in Fig. 3-3. The high velocity Al7075 powder had sufficient energy to deform the substrate and induce compressive residual stress within it. However,

the temperature of the carrier gas accompanied by a rapid temperature rise due to the conversion of kinetic energy into the strain energy increased the substrate temperature in a way that activated the temperature-dependent mechanisms and released the residual stress.

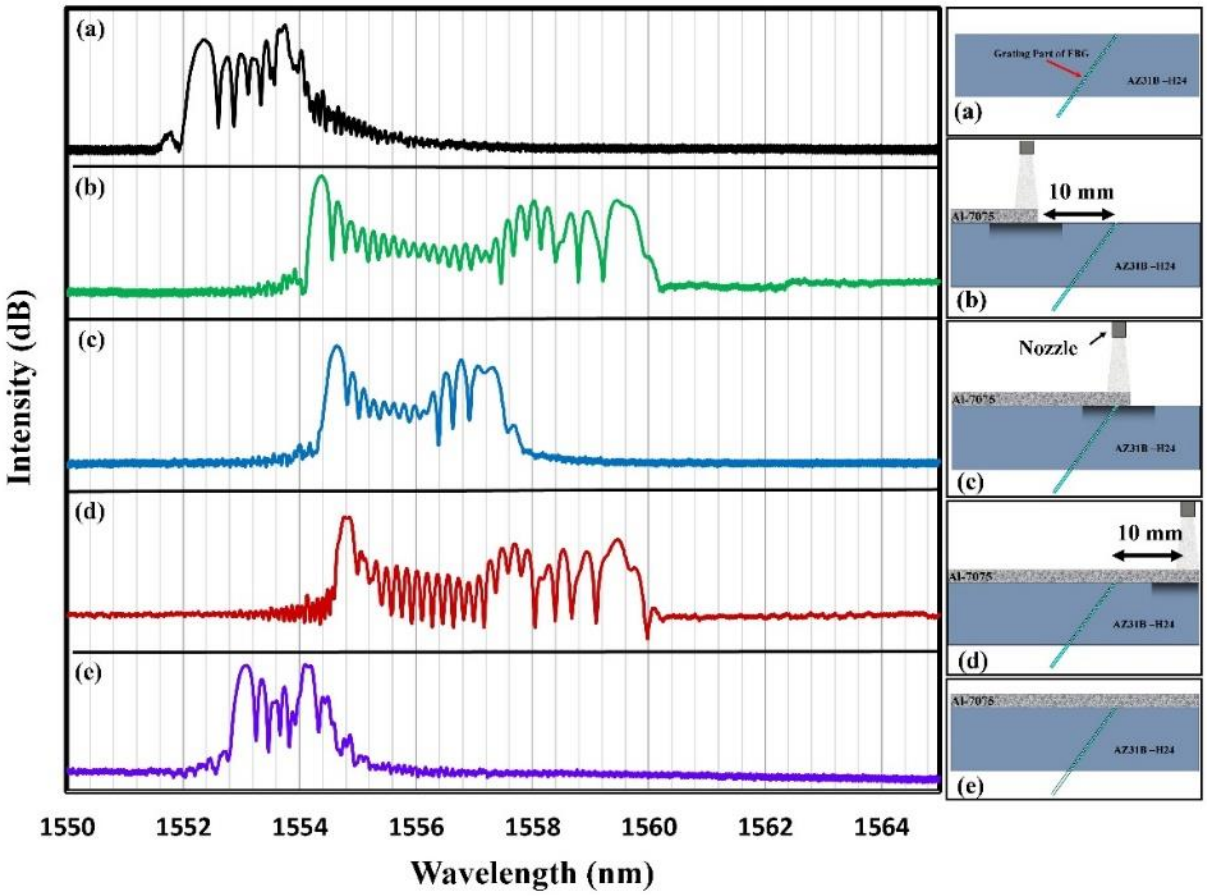

Fig. 3-3: Schematic of the coating process (right) and spectrum of FBG sensor response (left): a) after embedding the sensor and before the coating process; b) during coating at a location 10mm away from the sensor; c) coating on the sensor; d) at 10 mm away from the sensor; e) after coating and substrate reach room temperature[3].

[3] Vide Appendix A for further information.

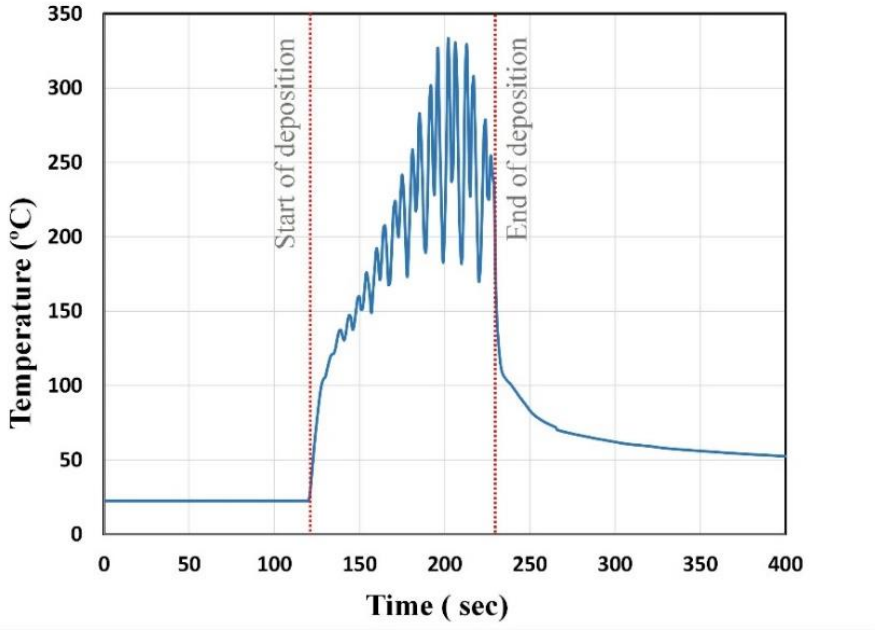

Fig. 3-4: Temperature of substrate measured by thermocouple during coating process.

3.4.2 Microstructure of the interface

The microstructure of coated samples, which were treated under the processing parameters from **Table 3-2** with the high nozzle velocity (V=10 mm/s) was investigated by TEM. **Fig. 3-5**a demonstrates three distinct zones that are visible in the bright field image. A continuous layer of ~200-300nm is clearly noticeable between the coating and substrate. Grain refinement is observed adjacent to the interface of the substrate. The dark field image (**Fig. 3-5**b) shows that the bright spots obtained near the interface are refined grains of ~200 nm. **Fig. 3-5**c shows the magnified bright field STEM-HAADF image, enclosed by red box in **Fig. 3-5**b, also more visible recrystallized grains. The EDX line scan confirms the mixture of Al and Mg elements with Zn. The microstructure of the coating of Al7075 alloy shows elongated grains with ladder-like morphology. The grain refinement and diffusion of Al in Mg were the effect of impact temperature. The induced high impact and severe plastic deformation at higher strain rate causes the dynamic recrystallization of Mg, which enhances the refinement of grains, resulting in nano grains at the interface.

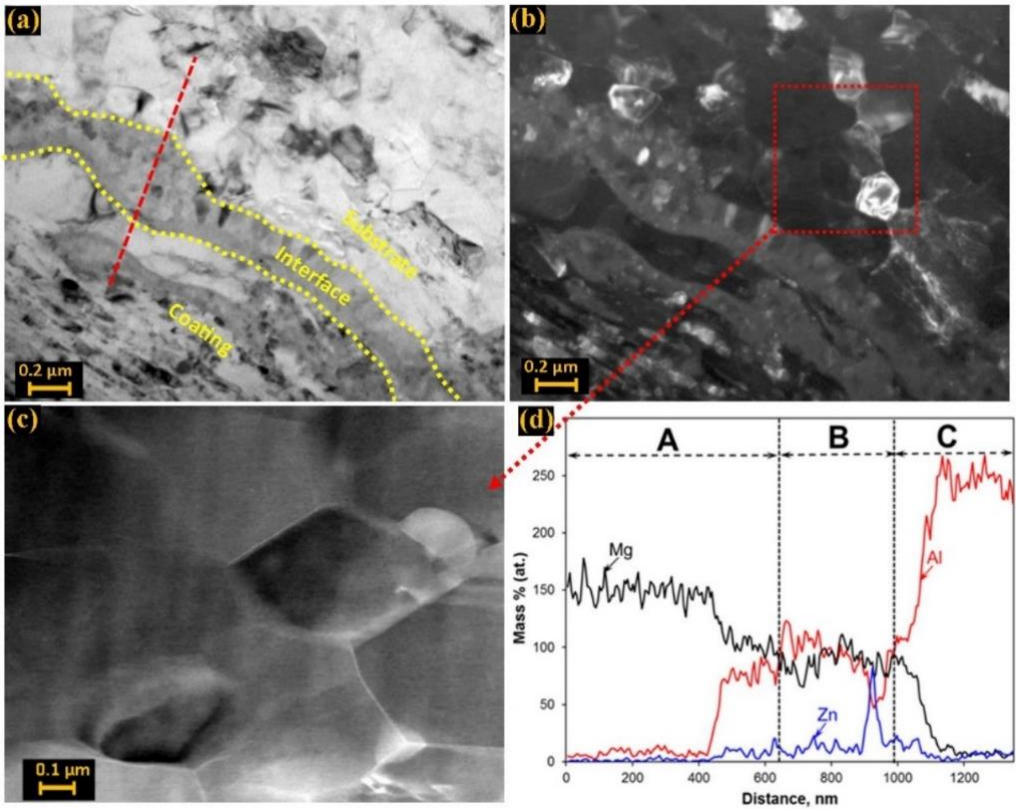

Fig. 3-5: Typical TEM micrograph lines show the microstructure at different zones: substrate (A), interface (B) and coating (C) of AZ31B alloy coated with Al7075 alloy in different modes, (a) bright field image, (b) dark field image, (c) STEM-High-angle annular dark-field (HAADF) image and (d) EDX line scan.

3.4.3 Microstructure of the substrate

To study the effects of carrier gas temperature and carrier gas temperature exposure time on the microstructure of AZ31B-H24 substrate samples, grain structure evaluations of sample cross-sections were conducted before and after coating deposition. For the sake of comparison, the cold-spray coating experiments were conducted with different nozzle velocities (V=2 mm/s and V=10 mm/s). Low and high magnification microstructure images of the as-received samples are shown in **Fig. 3-6**a and **Fig. 3-6**b. These images reveal that the microstructure of the sample close to the surface was uniform, and no significant differences are observable on the surface or in the bulk close to the surface. After the cold spray coating, in the sample with high nozzle velocity (V=10 mm/s), the grain size of the Mg near the interface was decreased, as clearly seen in the low and high magnification SEM images of the cross-section (**Fig. 3-6**c and **Fig. 3-6**d). It is well known that plastic deformation of a crystalline material

increases the densities of crystal lattice defects, particularly resulting in dislocations. An accumulation of dislocations in the deformed grains leads to local misorientation in the grains that increases the energy of the crystal; hence, the dislocations will align inside of the grain and make sub-grain boundaries to reduce this excess energy. Further deformation of these grains would produce more rotation in the sub-grains, forming high angle grain boundaries and dividing the grains into smaller individual grains [142]. Based on this explanation, greater deformation should result in smaller grains. To evaluate this hypothesis, another coating was done with low nozzle velocity (V=2 mm/s). This would result in more peening time and hence more deformation in the substrate was expected. However, as seen in **Fig. 3-6**e and **Fig. 3-6**f, the grain size of the substrate at the interface is larger than the former case (V=10 mm/s). This can be attributed to the grain growth during the latter process. Decreasing the nozzle travel speed not only increased the peening time by 60%, but also exposed more heat to the substrate over a longer period of time as the coating process time took longer and hot gas flow exposure to the substrate increased. Therefore, beside the grain refinement due to the peening effect, the excessive heat associated with longer exposure time facilitated grain growth. While, grain refinement was still observable when the coated samples with lower nozzle velocity were compared to as-received samples, grain growth due to higher heat resulted in larger grain sizes when compared to the coating with higher nozzle velocity. To compare the microstructure evolution in the samples, the grain size of each sample was measured at the interface to 30 μm below the surface (**Fig. 3-7**). Based on this measurement, the average grain size of the as-received sample was 3.2 μm. For the cold spray with high nozzle travel speed (V=10 mm/sec), the minimum grain size was not only 60% smaller than that seen after cold spraying at low nozzle travel speed (2 mm/sec), but the effect of peening was observable in deeper areas (**Fig. 3-7**).

To eliminate the effects of carrier gas temperature on the substrate, the coating was done at room temperature with two different gas pressures: P=96 psi (0.66MPa) and P=200 psi (1.38MPa). The surface was peened by Al particles; however, no deposition occurred. **Fig. 3-8**a and **Fig. 3-8**b illustrate the microstructure of the substrate after peening at P=96 psi at room temperature. These images clearly show grain refinement near the substrate's surface when compared to the coated samples shown in **Fig. 3-6**c to **Fig. 3-6**f. **Fig. 3-8**c and **Fig. 3-8**d demonstrate that increasing the gas pressure to 200 psi dramatically reduced the grain size of the substrate surface beyond that of the sample coated at P=96 psi, while the grains below the surface layer were deformed to lamellar grains. By comparing the peened samples (**Fig. 3-8**) and coated samples (**Fig. 3-6**) it would be hypothesized that the temperature of the cold spray was high enough to not only relax the induced residual stress during cold spraying but to

allow grain growth. Microstructure observations reveal that the peening of the AZ31B-H24 substrate by Al7075 powder, in the condition of experiments, has enough energy to aggressively deform the grains near the substrate surface and lead to dynamic recrystallization and grain refinement. However, the average grain size of substrate near the surface for the peened samples is smaller than the coated samples. In cold spray, two sources of thermal energy are available: 1) thermal energy from the hot carrier gas and 2) thermal energy of the local plastic deformation due to high impact of particles with substrate. While the severe plasticity due local deformation of particle and substrate and released heat upon impact results in grain refinement near surface, the exposure of carrier gas over the deformed zone after collision lead to grain growth, which results in larger grain in coated samples as compared to only-peened samples.

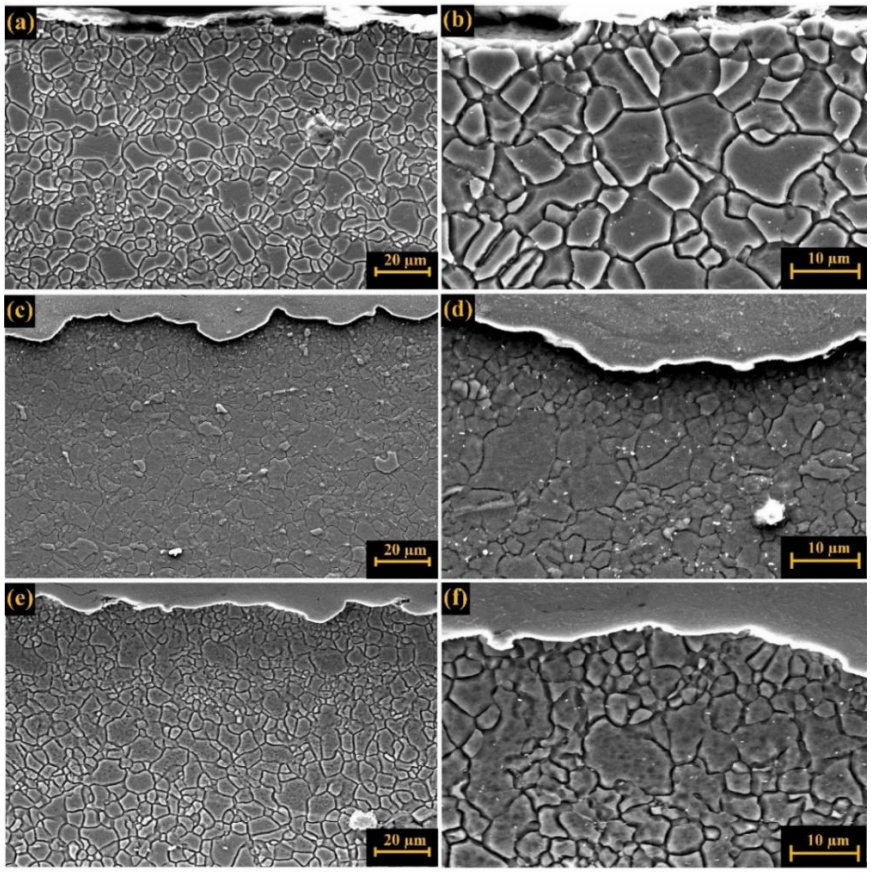

Fig. 3-6: a) and b) low and high magnification SEM images of the as-received sample; c) and d) low and high magnification SEM images of the sample after cold-spray coating (V=10 mm/sec); e) and f) low and high magnification SEM images of the sample after cold-spray coating (V=2 mm/sec).

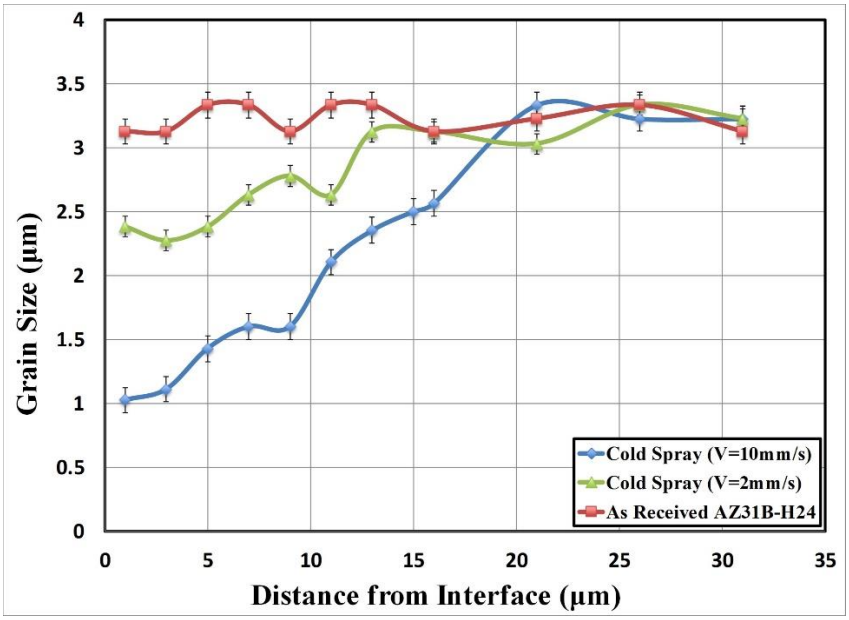

Fig. 3-7: Changes in substrate's grain size for three samples adjacent to the interface: as received, coated with low nozzle velocity, and coated with high nozzle velocity.

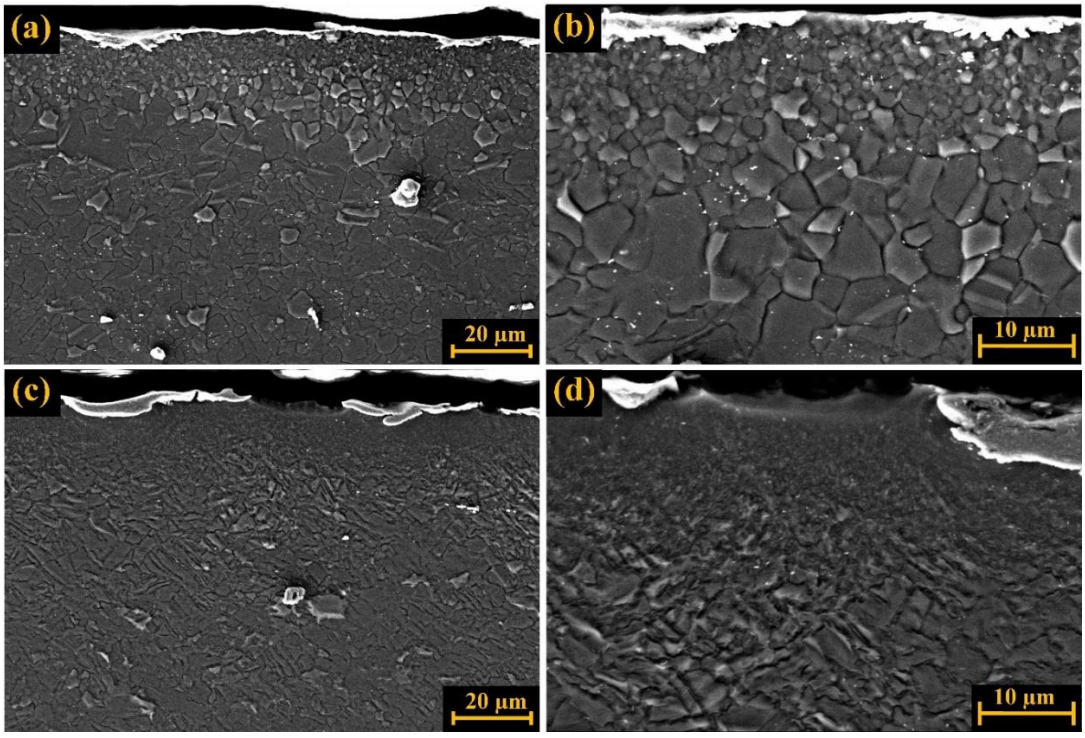

Fig. 3-8: Microstructure of the peened sample by aluminum particles, a) and b) P=96 psi at low and high magnifications SEM; c) and d) P=200 psi at low and high magnifications SEM images.

3.4.4 Residual stress measurement

The influence of relevant cold spray parameters on inducing compressive residual stress in Mg alloy substrate samples was further investigated by conducting individual experiments and measuring the residual stress. The processing parameters used in the four experiments are listed in **Table 3-3**. First the cold spray test was carried out without spraying Al7075 powder, while the gas temperature and pressure were 400°C and 200 psi, respectively (sample 1). The residual stress measurements were conducted using the hole-drilling method. **Fig. 3-9** a shows the stress profile of the Mg alloy substrate sample before and after the test. The stress measurements illustrate that the compressive residual stress decreased 83% near the substrate surface due to temperature effects. As the test was done without powder no deposition occurred, hence, the results were not affected by rising localized temperature due to impact. In sample 2, the effect of nozzle temperature was controlled with conducting the test at room temperature, imposing the peening process. In this condition, the cold spray test was conducted with 200 psi pressure of flow gas with a powder feed rate of 8 gr/min. Examination of the sample revealed that the peening effect increased 27% the compressive residual stress of the substrate (**Fig. 3-9**b) as expected from the microstructure evolution findings of the peened sample. By increasing the carrier gas temperature to create a relatively high quality of coating in sample 3, not only was the stress of the Mg alloy substrate relieved, but the stress was also released near the surface of the Al coating (**Fig. 3-9**c). Finally, the influence of sample carrier gas temperature exposure time on the residual stress was studied by increasing the velocity of the nozzle to 10 mm/s in sample 4 (i.e., decreasing the exposure time). The stress relaxation measurement demonstrated that increasing the nozzle travelling speed during the coating of the sample did not provide high enough thermal energy to relieve the residual stress of the Al coating, but the time was sufficient to release the residual stress of the Mg alloy substrate (**Fig. 3-9**d). Based on these observations, inducing residual stress in Mg substrate is a function of several variables.

Table 3-3: Cold spray parameters for hole-drilling measurements.

Sample number	Gas pressure (psi)	Gas Temperature (°C)	Nozzle speed (mm/sec)	Powder feed rate (gr/min)
1	200	400	2	0
2	200	23	2	8
3	200	400	2	8
4	200	400	10	8

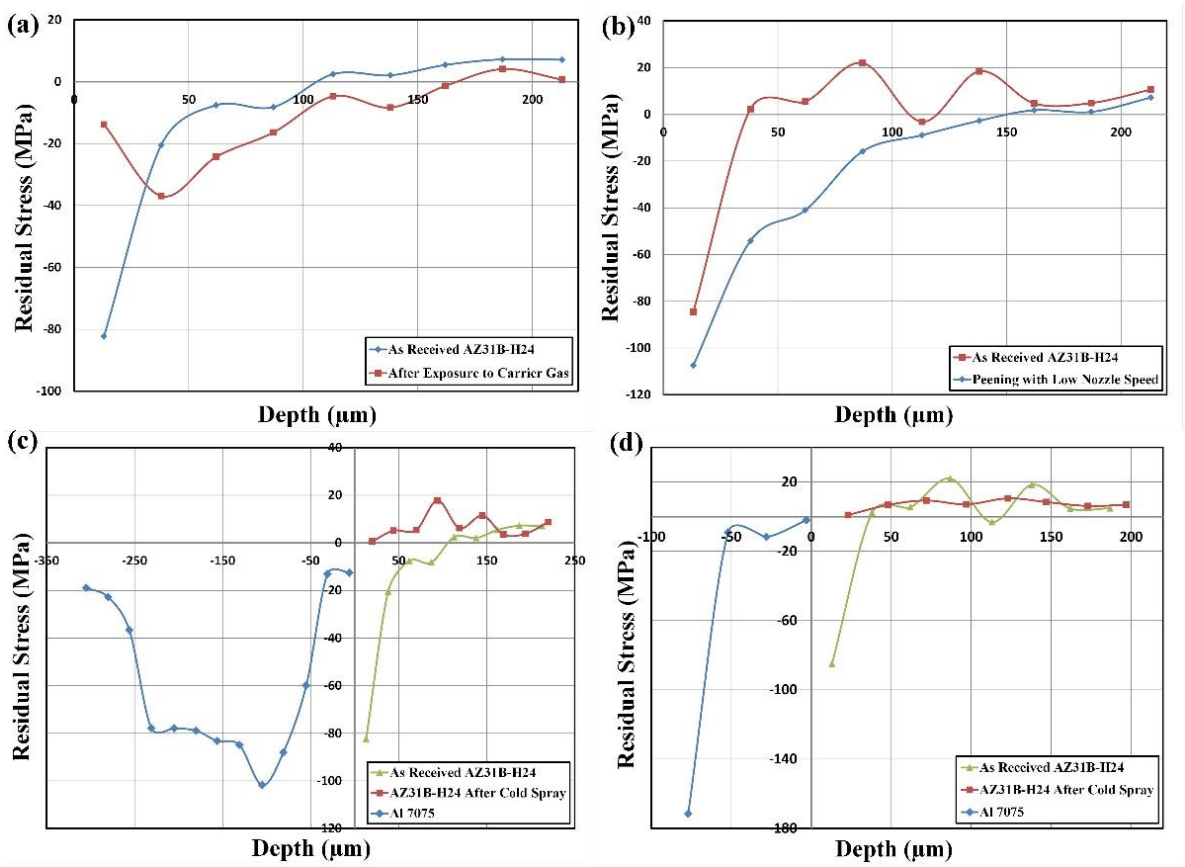

Fig. 3-9: Residual stress measurement by hole drilling: a) cold spray without spraying powder (exposure to carrier gas); b) cold spray at room temperature (peening effect); c) cold spray test (V=2 mm/s); d) cold spray test (V=10 mm/s).

By comparing the residual stress change variations across samples 1 to 4 following observations are made: 1) the heat transfer from 400°C carrier gas to the Mg alloy substrate was not able to provide enough thermal energy to completely relieve the stresses of the Mg alloy substrates; 2) the peening process was able to induce high level of residual stress in the Mg alloy substrates; 3) the thermal energy released during deformation due to Al7075 deposition, in addition to the thermal energy from the carrier gas, provided sufficient energy to anneal the Mg alloy substrates (compatible with the microstructural observations made above); and 4) the travelling speed of the nozzle was an important parameter that could affect the residual stress of the Al7075 coating while not affecting the residual stress of Mg alloy substrate (as far as the current examination extended).

3.4.5 Design of experiment

The design of experiments method was employed to evaluate the contribution of significant processing factors on the substrate's residual stress [143]. This design had three factors (2^3 full factorial): pressure of carrier gas, temperature of carrier gas, and velocity of the nozzle. All three factors play considerable role in successful coating. The temperature and pressure of carrier gas provide the required velocity that the particles need for a high impact collision. Moreover, the temperature of carrier gas generates thermal energy for the particles to have the required ductility for successful deposition on the substrate. The nozzle velocity influences the thickness of the coating and the exposure time to carrier gas temperature. Each of these factors had two levels of high and low. Based on the full factorial design, eight trials were planned. The responses for each trial included residual stress measurements were repeated at three different points on each sample, before and after applying the cold-spray process. Hence, a total of 48 residual stress measurements were made under different conditions. STATISTICA software was employed to analyze the results with a confidence level of 95%. Since only residual stresses at the surface were of interest, all of the residual stress measurements were conducted using the X-ray diffraction method.

First, the low level of gas pressure was determined with respect to the coating deposition condition. For this purpose, the cold-spray coating process was done for different levels of pressure while the temperature of gas flow was kept at 400ºC. The substrate weight was measured before and after the coating process, for each gas pressure. The weight change of the substrate samples versus pressure is shown in **Fig. 3-10**. As the pressure increased, up to a pressure of 92 psi, the weight of substrate decreased due to the abrasion of the substrate. At around 96 psi, the sample weight change was essentially zero and above that weight was added to the substrate indicating successful coating. Based on this observation, it was considered that coating deposition occurred after the critical value of 96 psi of pressure was reached.

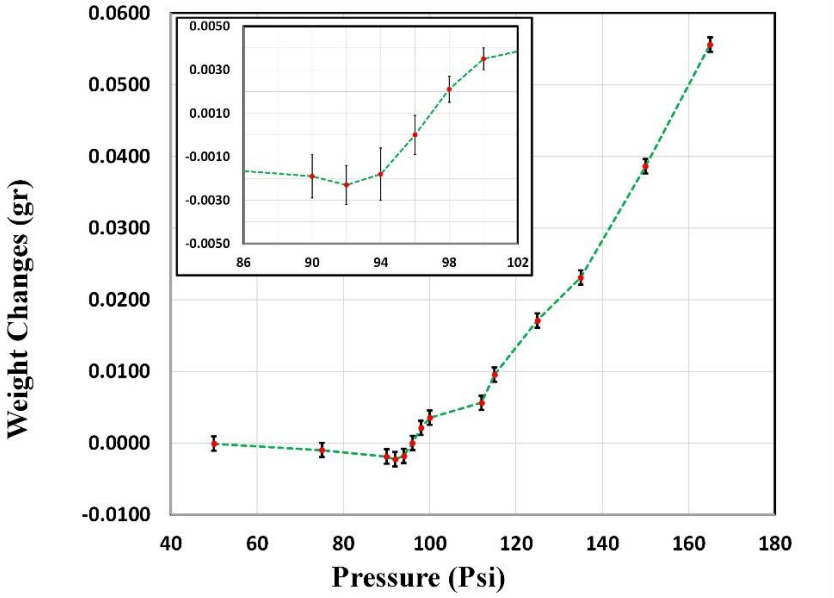

Fig. 3-10: Change in the weight of substrate at different pressures.

The microstructure of a sample coated at a pressure of 100 psi, and a map of the alloying distribution are shown in **Fig. 3-11**a and **Fig. 3-11**b. The SEM results revealed that 64% of the sample was coated by Al7075 powder at a pressure of 100 psi, confirming that Al particles were deposited onto the Mg substrate at pressures above 96 psi.

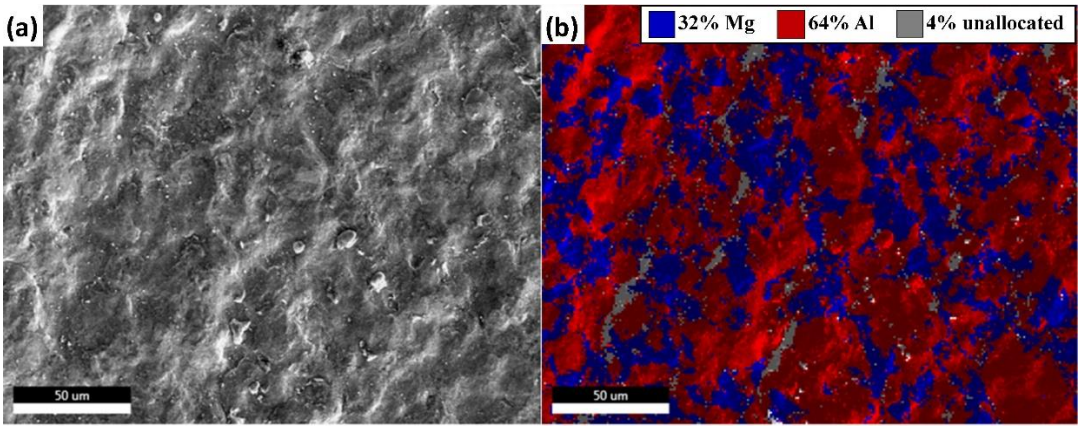

Fig. 3-11: a) Surface of coated sample and b) map of alloying distribution at pressure of 100 psi.

Based on the experimental design, four experiments were performed at low carrier gas temperatures (room temperature) with two different levels of gas pressure and nozzle speed. Al alloy powder impinged the substrate with high speed and produced dimples on the surface. At room temperature,

coating deposition did not occur; however, the role of the peening process in increasing the compressive residual stress could be highlighted. **Fig. 3-12**a shows the average measurement of residual stress for AZ31B-H24 samples before and after cold-spray coating tests. The green bars represent the average residual stress measurements for as-received samples before conducting the experiment, and the brown bars specify the residual stress values obtained after cold-spray tests were conducted under the different processing parameters. The differences between the initial induced residual stresses of as-received AZ31B-H24 samples and the generated residual stresses after cold-spray tests are presented in **Fig. 3-12**b. The results reveal that cold-spray processing at a low temperature of carrier gas increases the compressive residual stress, irrespective of the gas pressure value or nozzle speed level. However, as the carrier gas temperature increased, the results were completely dependent on the gas pressure and nozzle speed. In this situation, at low gas pressure, the compressive residual stress was reduced in the specimen surface when the nozzle speed was 2mm/s. Since increasing the nozzle speed decreases the exposure time of the Mg substrate during which it can obtain energy from the carrier gas temperature, the reduction in compressive residual stress was negligible with a nozzle speed of 10 mm/s (see **Fig. 3-12**a, **Fig. 3-12**b). In contrast, increased gas pressure in conjunction with high gas temperature boosted the kinetic energy of the particles. During impact, the kinetic energy is transformed to internal energy in the particles and substrate surface grains. This phenomenon happens over a very short impact time; hence, there is not enough time for the heat to transfer to the substrate and environment. The localized temperature generated at the interface increases dramatically, leading to softening of the crystalline material. Rising temperature allows the particles and substrate surface grains to deform and enables metallurgical bonding at the interface. The mechanism of coating deposition, severe particle and substrate deformation, along with carrier gas temperature provides enough energy to release the compressive residual stress of the substrate. The results obtained at high gas pressure and temperature demonstrate that the residual stresses of the samples are completely released, and the original compressive residual stresses of the as-received samples are replaced by tensile stresses (**Fig. 3-12**a, **Fig. 3-12**b). This observation is compatible with the in-situ observation data gathered by the embedded FBG sensor. However, based on the progressive coating deposition model and corresponding literature, residual stresses are strongly related to kinetic energy rather than thermal effects in copper/Al coated samples. Also, it has been claimed that the effects of thermal mismatch on stress relaxation have been neglected, and that these could be extended to all coating materials and substrate selections [62].

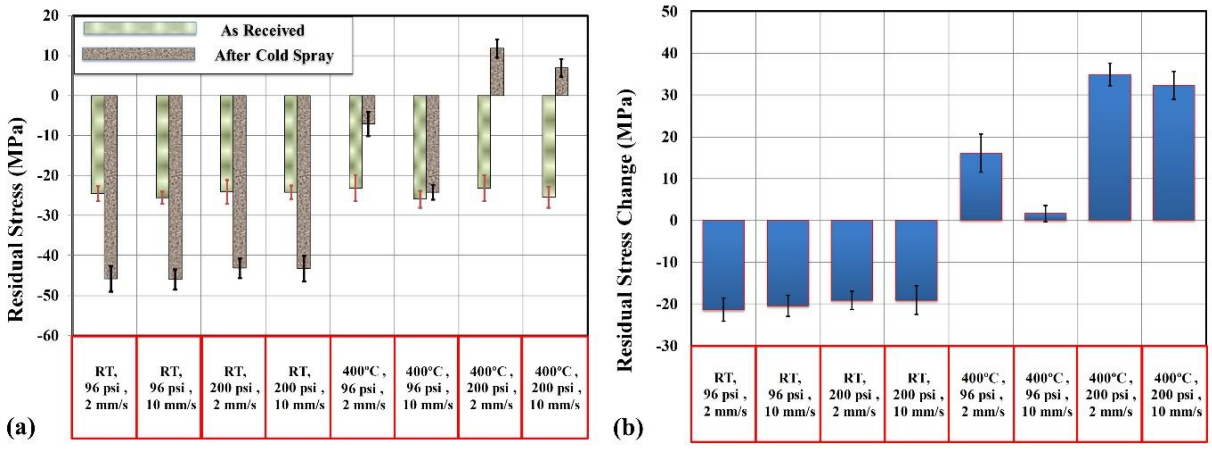

Fig. 3-12: Residual stress measurement by X-ray diffraction: a) for Mg AZ31B-H24 substrate before and after different processing parameters of cold-spray coating; b) difference between residual stresses of as-received substrate and after different conditions of coating.

To recognize the effects of significant factors on the substrate residual stress changes, an analysis of response variance was made using ANOVA (**Table 3-4**) [143]. The results demonstrate that there exist statistically significant relationships between the sources of variation and the residual stress change responses. Indeed, the results reveal that the temperature and pressure of carrier gas have more significant effects than other variables, although all of the identified factors are strongly related to the residual stress response (p-value <0.05). Furthermore, based on the coefficients of determination squared R (0.989) and adjusted R^2(0.984) were calculated by (3-5) and (3-6). As these values are both very close to one, it is clear that the regression line model almost perfectly fits the data.

$$\boldsymbol{R^2 = \frac{SSR}{SST}} \qquad \textbf{(3-5)}$$

$$\boldsymbol{R^2_{Adj} = 1 - \left[\frac{(1-R^2)(n-1)}{n-q-1}\right]} \qquad \textbf{(3-6)}$$

where SSR (sum of squares regression) is the sum of the squared differences between the prediction for each observation and the population mean, which is equal to SST-SSE. In equation (3-6), n is the number of observations, 24, and $q = 7$ is the number of significant parameters, considering the error.

Table 3-4: ANOVA results

Source of Variation	Sum of Squares (SS)	Degree of Freedom	Mean Squares	F Ratio	p-value
Temperature of carrier	10201.45	1	10201.45	1385.374	0.000000
Pressure of carrier gas	1054.60	1	1054.60	143.216	0.000000
Speed of the nozzle	96.42	1	96.42	13.095	0.002121
Temperature*pressure	790.14	1	790.14	107.303	0.000000
Temperature*speed	121.20	1	121.20	16.460	0.000819
Pressure*speed	44.81	1	44.81	6.085	0.024556
Error	125.18 (SSE)	17	7.36		
Total SS	12433.81(SST)	23			

To further confirm that the data fit the model reasonably well, the residual plots (the most valuable regression diagnostic tools) were extracted (see **Fig. 3-14**). Residual terms refer to the difference between the observed value of the dependent variable and the predicted value of the regression analysis. Based on the residual plots obtained, the relationships between the dependent variable (residual stress change) and independent variables (gas temperature, gas pressure and nozzle speed) were linear, and the residual was distributed normally around the predicted dependent variables (**Fig. 3-14**a). Moreover, **Fig. 3-14**b shows that the data was statistically independent, because the magnitudes of the residuals were completely random. The independent variables had almost equal variance around the regression line, meaning that the variance is a deviation from the best-fit line. Therefore, this model had enough validity to be used to predict the change of residual stress in the substrate in relation to the identified significant processing parameters. However, based on observations made from two random combination tests, the regression equation could behave non-linearly, especially around the area where coating occurs. The following predictive stress relaxation equation was obtained from the linear regression analysis of the identified processing parameters:

$$\boldsymbol{Residual\ Stress\ Change} = -17.98 + 0.0406T - 0.0357P - 0.8430V + 0.0006TP - 0.003TV + 0.0066PV \quad \textbf{(3-7)}$$

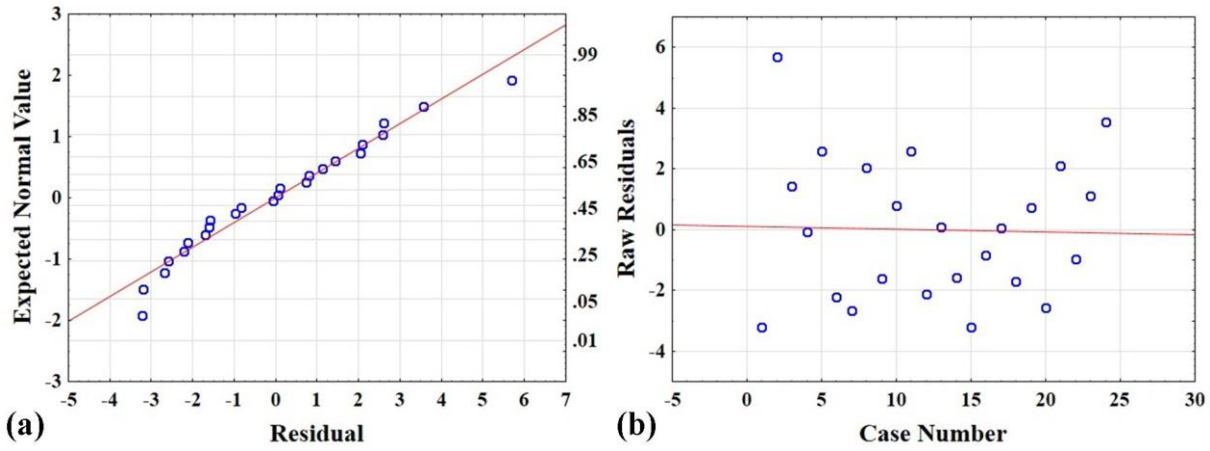

Fig. 3-13: a) Normal probability plot; b) selected raw residual values against the case numbers for each case or run.

Using the generated statistical model, three-dimensional (3D) fitted surface plots were created to explore the relationships between the significant processing parameters of cold-spray coating and residual stress variation in the Mg alloy substrate samples. **Fig. 3-14** indicates the relationship between two independent parameters, carrier gas pressure and nozzle velocity, and the residual stress variation, at two different levels of temperature. According to the obtained surface plots, the parameter having the biggest effect on residual stress change is carrier gas temperature, as it has the biggest variation domain (-23ºC to 400ºC). This is compatible with the ANOVA results. At room temperature, a high compressive residual stress change (less than -23 MPa) is observed in the conditions of high gas pressure and low speed of nozzle (**Fig. 3-14**a). At high gas pressure and high speed of nozzle, a significant compressive residual stress change (more than -17 MPa) was achievable (**Fig. 3-14**a); however, no deposition occurred at room temperature. After increasing the carrier gas temperature to 400°C, the change varied between -2 MPa and 40 MPa, corresponding to low gas pressure and high nozzle speed, and high gas pressure and low nozzle speed, respectively (see **Fig. 3-14**b). This range of residual stress variation is not sufficient to improve fatigue life. It is of note that at a high carrier gas temperature, increasing the nozzle speed does not significantly improve the compressive residual stress in the substrate, nor does decreasing the gas pressure. However, at a low gas pressure, increasing the nozzle speed helped to boost the compressive residual stress in the substrate.

The variety of residual stress changes can be predicted with a 3D surface plot when the carrier gas pressure was kept constant at low and high levels (see **Fig. 3-15**). At both levels of pressure, 96 psi and 200 psi, when the carrier gas temperature is below 150ºC, the maximum changes of compressive

residual stress can be predicted at any level of nozzle speed. However, at high carrier gas pressure, a greater slope of response surface can be observed, which includes a bigger domain of residual stress changes in the substrate while compared with the low carrier gas pressure results. In this situation, the effect of nozzle speed is not significant at low temperature at either level of pressure. The effect of nozzle speed is specified in **Fig. 3-16**. Based on the prediction model, the ranges of residual stress variation at low and high levels of nozzle speed are the same, although increasing the nozzle speed can lead to better predictions of compressive residual stress changes at higher temperatures. Employing the results of this research to induce maximum possible residual stress along with grain refinement of the substrate toward enhancing fatigue performance of Mg alloy will be examined in future.

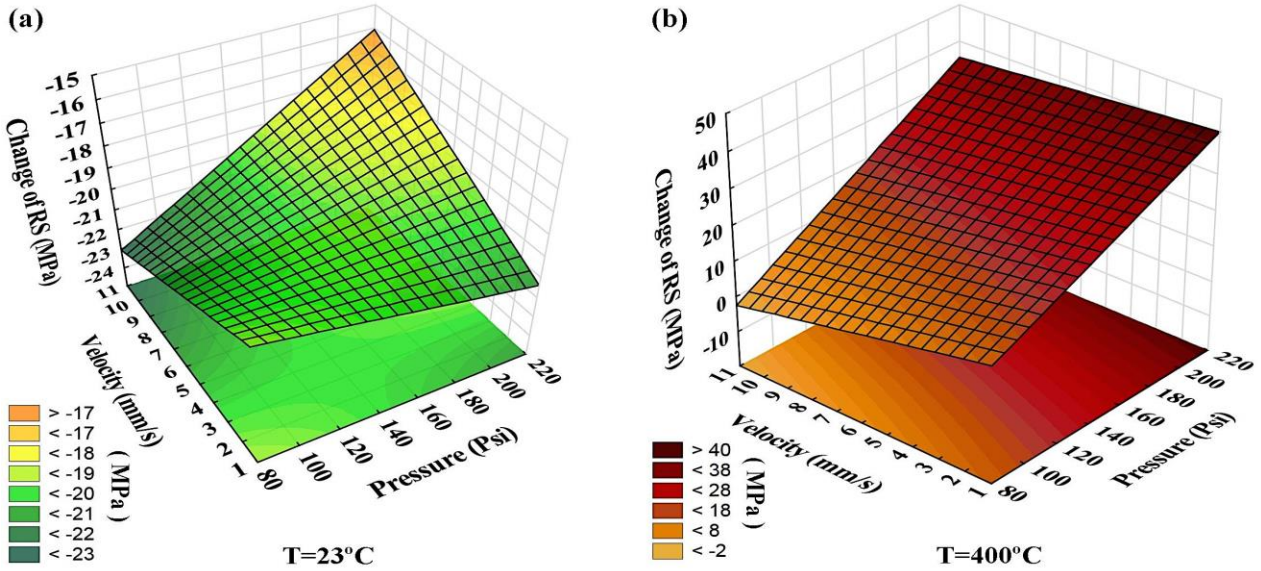

Fig. 3-14: 3D surface plot at a) T=23°C and b) T=400°C.

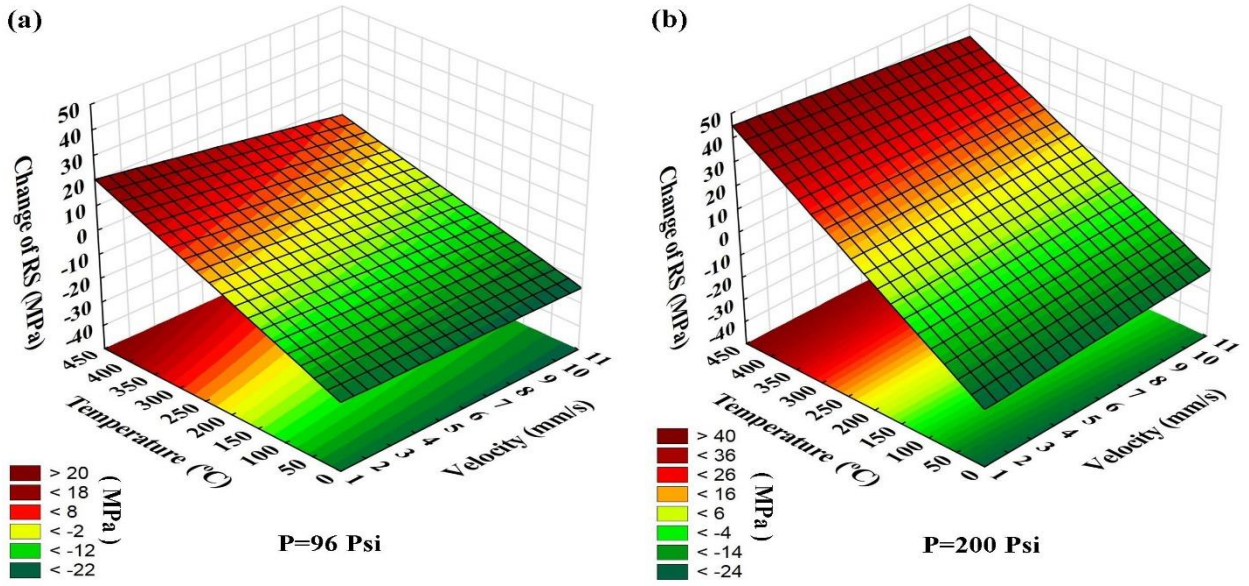

Fig. 3-15: 3D surface plot at a) P=96 psi and b) P=200 psi.

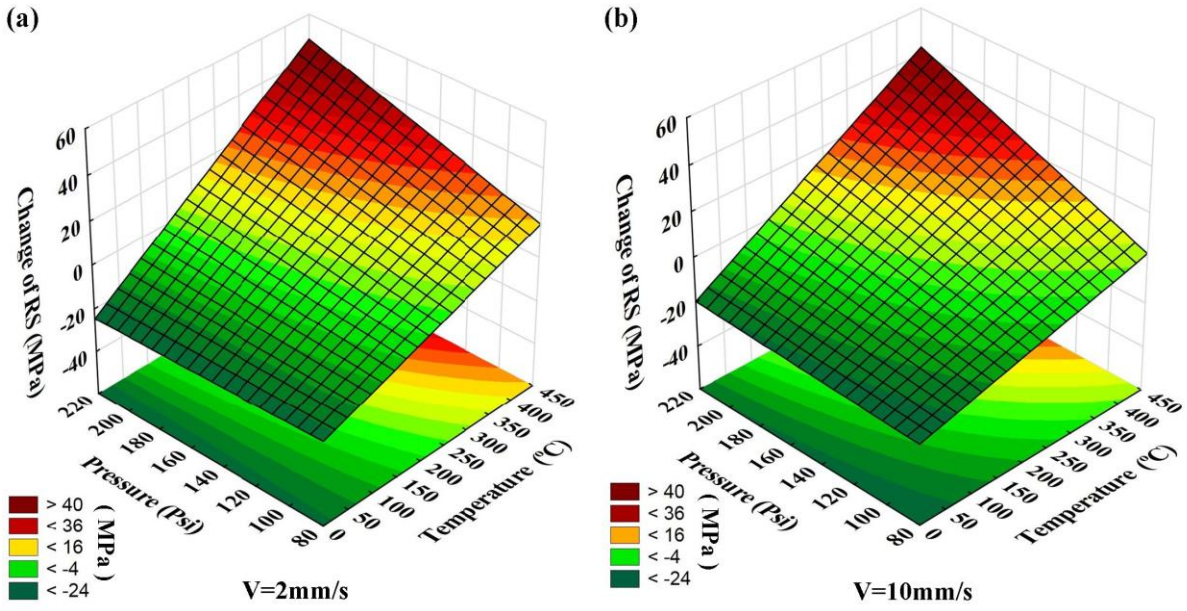

Fig. 3-16: 3D surface plot at a) V=2mm/s and b) V=10mm/s.

3.5 Conclusion

The effect of cold-spray deposition processing parameters on the residual stress induced in Mg alloy substrates was investigated. Thermo-mechanical strain evolution and interaction effects were monitored in situ through embedded FBG sensors under the optimum cold-spray coating condition. The following conclusions can be drawn from the results obtained in this study:

1) The embedded FBG sensors were able to monitor the thermo-mechanical strain evolution of samples during the cold-spray coating process. The in-situ observations uncovered that the compressive strain created in the substrate during cold-spray coating was released after a few seconds. Thermocouple data recorded during coating revealed that the substrate was warmed up to 330°C for a short period.
2) The substrate grain size was found to be a function of the absorbed thermal energy; more transferred heat to the substrate led to larger grains.
3) The consistency of the results obtained from in-situ strain and temperature measurements during coating, microstructural changes of the sample and residual stress measurements lead to the conclusion that the high energy generated by Al7075 particles during the peening process led to grain refinement of the substrate surface and induced higher compressive residual stress in the sample. However, the temperature of the cold gas spray was sufficient for the AZ31B Mg sample to not only recover the residual stress of the substrate but also provide enough energy for recrystallization and partial grain growth in the substrate close to the interface.
4) Based on the statistical analysis, the temperature and pressure of the carrier gas had the most significant impact on the residual stress variation of the examined parameters; and, the interaction of the carrier gas pressure and the speed of nozzle had minimal effect.

Chapter 4

Multi-Layer Cold Spray Coating: Strain Distribution[4]

4.1 Abstract

In this paper, we report the effect of multi-layer cold spray deposition on the residual stress formation in the coating and substrate. A method is proposed to separately measure the thermal and mechanical residual stresses induced in cold spray coating. Fiber Bragg Grating (FBG) sensors were employed for in situ monitoring of the strain evolution during the cold spray of multi-layer coating Al7075-Zn on AZ31B Mg substrates. Utilizing the capability of the FBG sensors in recording both thermal and mechanical strain gradients, first the effect of temperature on the substrate was investigated when the sample was only treated under carrier gas temperature. Then, the sensors were employed to evaluate the mechanical strain behaviour of substrate during the coating process and cooling. Therefore, the effect of thermal mismatch on inducing mechanical strains was observable during the process. Finally, the interaction between the peening process of cold spray and thermal mismatch after cooling was studied. It is shown that the thermal expansion coefficient (CTE) plays a critical role in residual stress development in the substrate and consequently affects the mechanical properties of the coated sample. Hence, careful selection of layers in multilayer deposition can provide desired residual stress in the coating and substrate.

4.2 Introduction

Cold spray is an emerging solid-state deposition technique with promising applications from surface modification and corrosion mitigation to restoration and build of structures. In this process, the high kinetic energy of particles is transferred to cause severe plastic deformation in the particles and substrate leading to a mechanical/metallurgical bonding. Upon impact, a localized heat is generated in fractions of seconds, much faster than the heat transfer in the substrate, resulting in thermal softening. This may lead to severe shear deformation at the interface, which has been introduced as the most prevailing bonding mechanism in this process [63]. Recently, hydrodynamic plastic effect development at the interface during impact, which leads to material jetting and bonding has shown to be a competitive

[4] This chapter was published as a paper in the journal of Key Engineering Materials, 813 (2019), pages 411-416.

bonding mechanism [144]. This illustrates uncertainty in the bonding mechanism and mechanisms in developing thermal and mechanical strain in the coating and substrate. Furthermore, and after coating, the thermal mismatch, as a significant factor on the final residual elastic strain of the substrate, interferes with the developed strains during the coating. Therefore, this process is a complicated localized high temperature and fast deformation phenomenon that needs to be studied in more details. In-situ measurements of the thermo-mechanical behaviour of materials during and after deposition is amongst methods for further investigations.

Fiber Bragg grating (FBG) sensor has been employed to monitor the strain changes of the substrate during coating and cooling [145]. FBG sensor is made of a hair thin filament of fused silica consisting of core and cladding, which is usually coated with acrylate, polyimide, or organic modulated ceramic. The grating is written into the germanium-doped core to produce refractive index difference [139]. The deformation of grating part in regarding to external stimulus is represented by wavelength shifts, which can be recorded by a data acquisition (interrogator). Based on the nature of FBG, it has the capability for responding to temperature changes and axial loadings that can measure the mechanical and thermal strain, simultaneously. The use of optical mechanism instead of electrical (strain gauge) leads to a fast response and a safe approach in a wide range of applications even in harsh environments [118]. Therefore, the specification of the FBG sensor makes it an ideal sensor for measuring the localized area under high temperature and high strain rate such as cold gas spraying [146].

In this research, we investigate the capability of FBG sensor for revealing the thermo-mechanical strain changes during the cold spray of multi-layer coating pure Zn and Al7075 on AZ31B magnesium alloy substrates. The mechanical strain evolution happens over a few hundred microns below the substrate surface while the temperature changes occurs in the entire substrate. The FBG sensors can record the wavelength shifts resulted from both thermal and mechanical strains. We first extracted the temperature calibration results and accordingly, the effect of temperature on the substrate when the sample was only treated under carrier gas temperature. Then, the mechanical strain behaviour of the substrate during the coating process and subsequent cooling was evaluated by deduction of the thermal strain. The goal of this study is to monitor and distinguish between the dynamic deformation of substrate (mechanical strain) and temperature changes (thermal strain), which is induced during the coating of the multi-layer Al7075 and pure Zinc on AZ31B. In addition, the effect of thermal mismatch during cooling is studied.

4.3 Experimental Procedure

In this study, three AZ31B-H24 Mg alloy samples with 3.16mm thickness were employed for in-situ strain and temperature measurements. Details of the substrate properties is found in [147]. The drawing of samples is shown in Fig. 4-1a. The specimens were finely polished and then, three 300µm diameter holes were drilled into the samples at a 45º angle. This angle is chosen to be able to monitor the maximum planar strain, which is induced about 100µm below the substrate surface. After drilling the holes, all samples were heat treated at 260°C (500°F) for 15 minutes, followed by air-cooling to relieve residual stress of the samples.

For preparing smart samples, nine acrylate-coated, Corning SMF-28, FBG sensors with an initial wavelength of around 1550nm and a grating length of 10mm with the reflectivity of 90% were utilized. After cleaning the holes, the three of as-received FBG sensors with acrylate coating were embedded into each sample. For this, the sensors were dipped into the high temperature EPO-TEK 353ND adhesive and accommodated in such a way that the 3 mm of grating parts were placed inside the holes and the rest of the grating parts were out of the samples. To cure the epoxy resin, the samples were heated at 150ºC for an hour using a hotplate (Torrey Pines Echo Therm HS40). After embedding the sensors and curing the resin, the 7mm protruding extra parts of the grating were cut and gently polished with 800-grit sandpaper. Fig. 4-1 shows the shape and dimension of the sample and the positions of the embedding sensors and eventually, the prepared sample for coating.

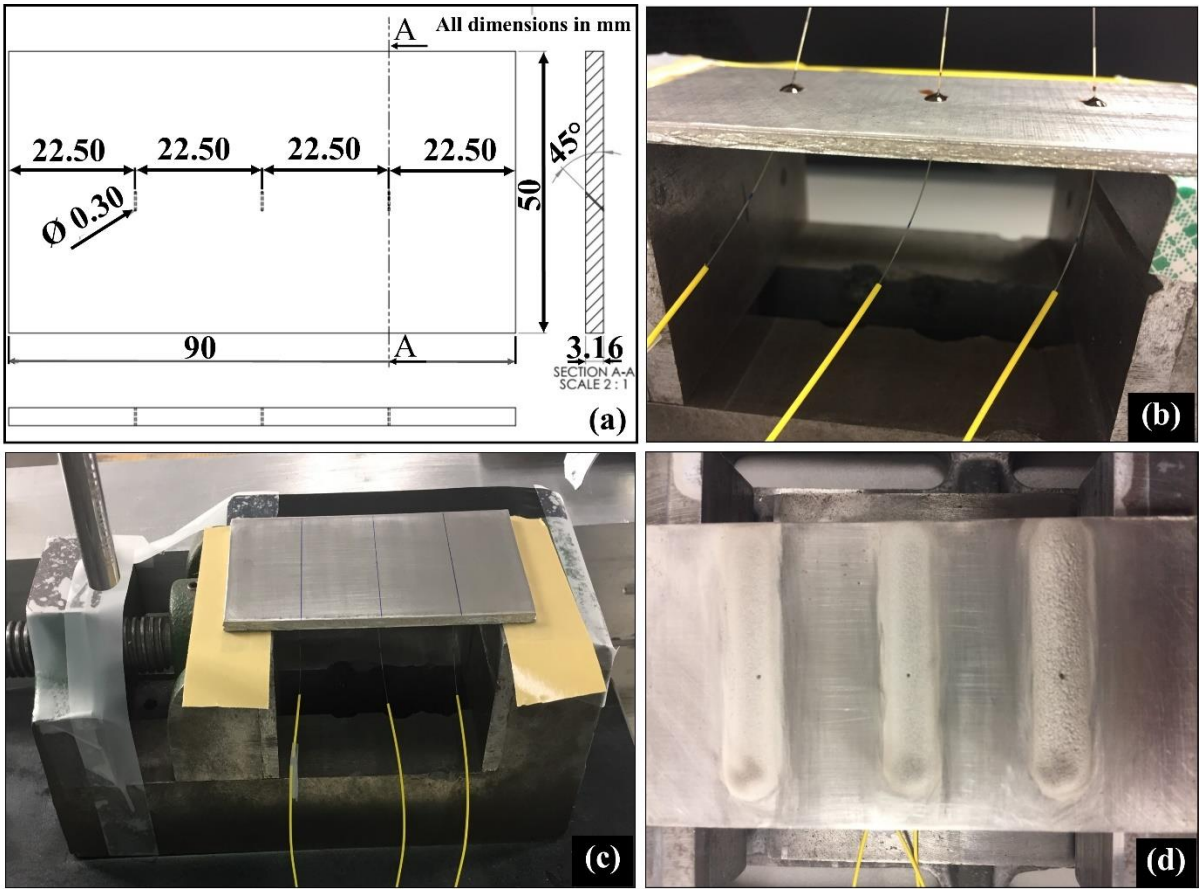

Fig. 4-1: a) Geometry of the AZ31B-H24 Magnesium alloy samples; b) embedding three sensors with thermal epoxy; c) prepared sample for coating; d) coated sample

For the temperature calibration tests (See Appendix B), one of the samples was employed for recording the responses of the three embedded FBG sensors at 23 different temperatures, from room temperature (24°C) to 280°C. To control the temperature changes, a thermocouple was attached on the sample surface. For increasing the temperature, the hotplate was used. During the hotplate temperature increase, the thermocouple and the interrogator (Hyperion, Si155) recorded the sample temperature and wavelengths changes, respectively. The temperature was increased incrementally and kept constant for a sufficient time until it stabilized at a certain temperature, and then the responses of the sensors and temperature of the sample were recorded.

A commercial Cold Spray system (SST Series P) manufactured by Centerline was used to deposit pure Zinc and spherical commercial Al7075 powder (supplied by Centerline) with the mean particle size of 35µm and 23µm (measured by Mastersizer 2000 and Camsizer XT) on the smart Mg alloy samples,

respectively (Fig. 4-2). All requirement parameters for conducting the relatively high quality of coating by cold spray deposition are listed in Table 4-1. **Fig. 4-1**d shows one of the coated samples, which was one cycle treated on each sensor with different materials and processing parameters.

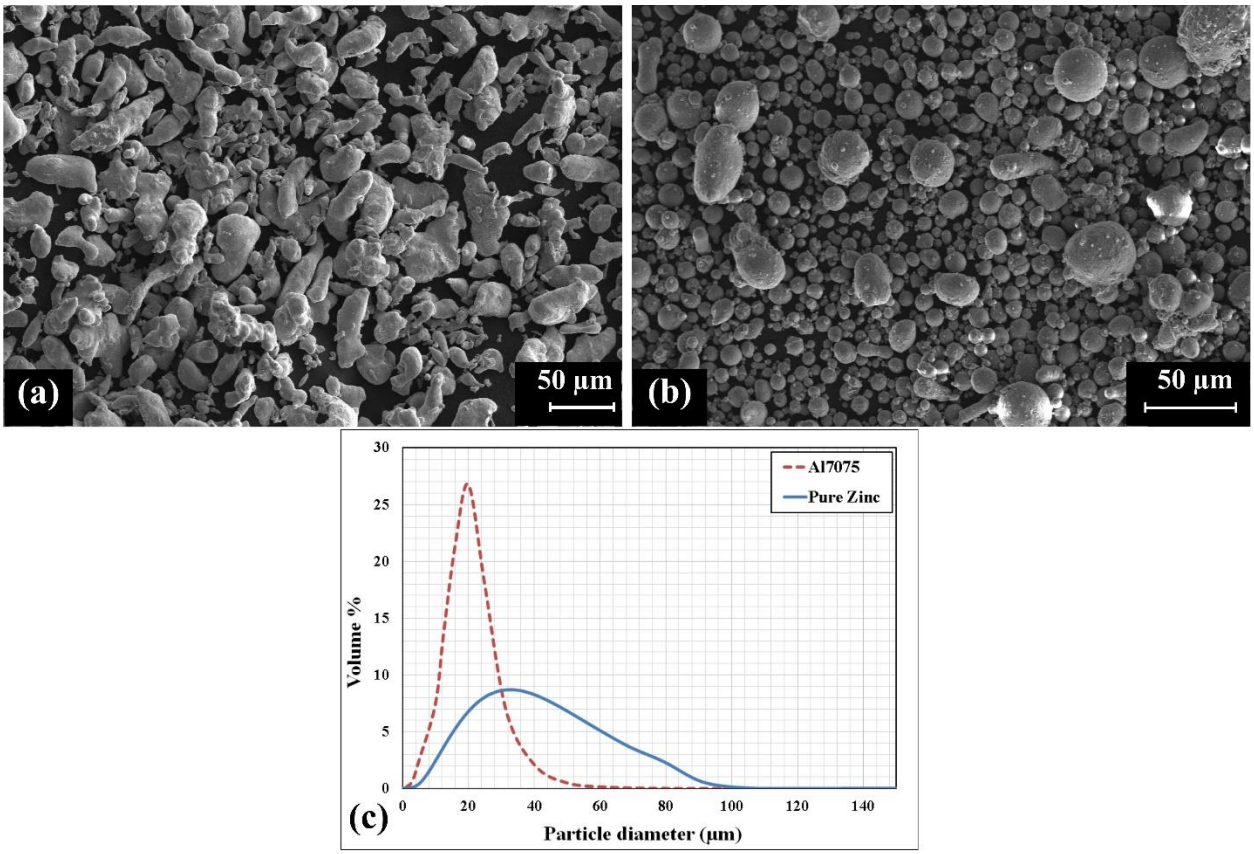

Fig. 4-2: a) SEM image of pure Zn; b) SEM image Al7075; c) Particle size distribution for Zn and Al7075.

Table 4-1: Cold Spray Coating Parameters.

Coating Materials	Flow Gas	Gas Temperature (°C)	Gas Pressure (MPa)	Powder Feed Rate (gr/min)	Nozzle Speed (mm/s)	Step Over (mm)	Stand-off Distance (mm)	Nozzle Length (mm)	Nozzle Orifice Diameter (mm)	Nozzle Exit Diameter (mm)
Al7075	N_2	400	1.38	8	2, 15	1.2	12	120	2	6.3
Zn	N_2	100, 250	1.38	8	5, 10	1.2	14	120	2	6.3

4.4 Results and Discussion

The response of the FBG sensor to thermal and/or mechanical loads is specified by the wavelength shifts related to the extension and contraction of the gratings. The calibration temperature experiments revealed the relation between the temperature changes and the wavelength shifts of the three embedded FBG sensors in an Mg alloy substrate (See Appendix B). Fig. **4-3**a depicts the positive spectrum shifts for one of the sensors when the temperature was increased from RT to 287°C. With increasing the temperature, all three sensors demonstrate the linear trend of wavelengths shifts, which is shown in Fig. **4-3**b. The slope of the three FBG sensors at different embedding positions are almost the same and can be considered as the coefficient of the temperature changes ($k \times \alpha_{Sp} + \alpha_{\delta}$) in the following equation in the absence of mechanical strains [115].

$$\frac{\Delta\lambda}{\lambda_0} = \left(k \times \alpha_{Sp} + \alpha_{\delta}\right)\Delta T + k\,\varepsilon_m \qquad \textbf{(4-1)}$$

where, $\Delta\lambda$ is the wavelength shift, λ_0 is the initial wavelength at the beginning of the experiment, k is the gauge factor, ε_m is the mechanical strain, α_{δ} is defined by the change of the refractive index with temperature, α_{sp} is the expansion coefficient of the sample (1/°K), and ΔT is the temperature change (°K). Considering Eq 4-1, the wavelength changes are included the mechanical and thermal changes. When the sample was only exposed to the carrier gas, the mechanical strain during the coating process is zero; therefore, the temperature changes can be simply obtained during the treatment. However, the temperature variation during the coating process is more complicated. By installing the thermocouple and recording the temperature changes and comparing the recorded data with the sensors, when the spectrums had the maximum shifts, the maximum temperature changes were recorded and listed in Table **4-2**. Then the thermal strains for different treatments were calculated by using the CTE of the sample. The presented data is an average of three repeated trials including standard deviations (Table **4-2**). Fig. 4-4a and Fig. 4-4b are the examples of the sensor's wavelengths changes, when the samples were treated with carrier gas at 100°C and 250°C and the Zn deposition with the same temperatures of gas. During the coating process, the maximum temperature was increased between 8% and 23% compared to the same carrier gas temperature. This extra temperature can be generated from the solid-state bonding during coating process. The thermal strain of impact can be determined by subtracting the effect of carrier gas temperature from the total measured thermal strain. Interestingly, the coating temperature is not comparable with the predicted temperature in the literature [65]. In these measurements, the 3mm grating length along the sample can be affected by the temperature changes,

hence the measured wavelengths changes are the average of the temperature distribution in the entire substrate. In addition, with knowing the first term of Eq 4-1 and wavelengths changes from the recorded data, the mechanical strain during the coating was calculated for each treatment and is listed in Table **4-2**. Based on these data, the significant amount of negative mechanical strain can be calculated during the coating process showing the severe plastic deformation of particles impact. However, these values will be reduced after the coating process due to the induced positive thermal strain during the coating and the effect of thermal mismatch (see Fig. 4-4b). It is noted that the mechanical strain after coating process at room temperature was obtained from the Eq 4-1, when the temperature changes were considered to be zero; hence the first term of the equation was omitted.

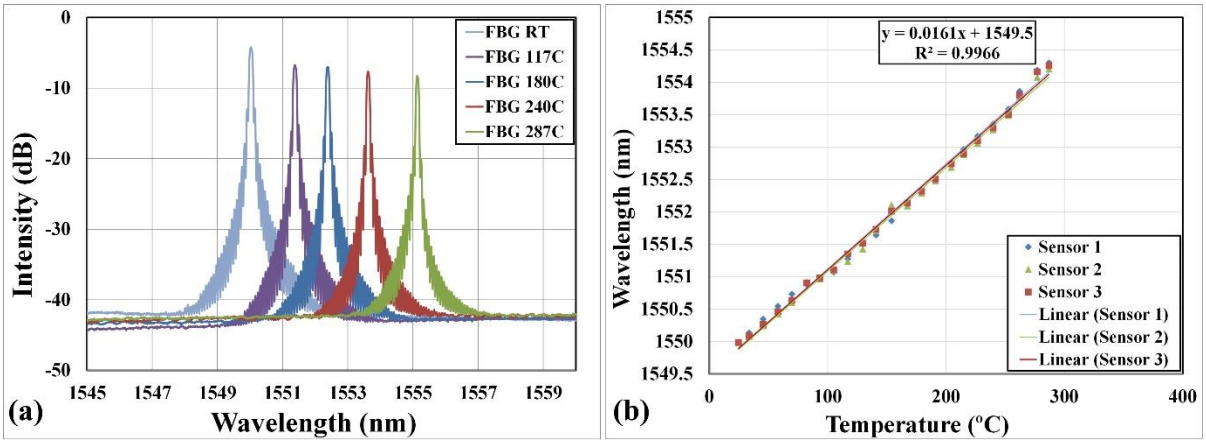

Fig. 4-3: a) The changes of spectrum with raising the temperature of the sample; b) wavelengths changes vs temperature for three FBG sensors.

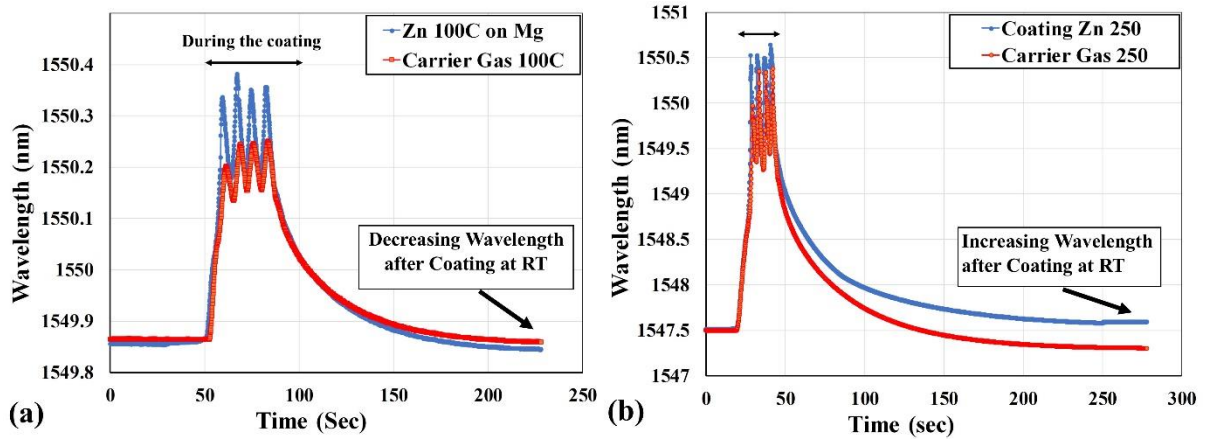

Fig. 4-4: a) wavelengths changes during coating and gas temperature of 100°C; b) wavelengths changes during coating and gas temperature of 250°C.

Table 4-2: In situ measurements of thermal and mechanical strain before, during and after coating.

Coating Treatments	Mechanical Strain Before Coating (με)	Maximum ΔT (°C)	Maximum Thermomechanical strain During Coating (με)			Mechanical Strain After Coating (με)
			Thermal strain		Mechanical Strain	
			Carrier Gas	Impact		
Gas 100ºC on Mg (5mm/s)	Stress Relief	26±1	680±21	0	0	-1.65±0.94
Gas 250ºC on Mg (10mm/s)	Stress Relief	179±9	4657±198	0	0	-19.05±5.87
Gas 400ºC on Mg (2mm/s)	Stress Relief	193±10	5009±220	0	0	38.05±1.84
Gas 400ºC on Mg (15mm/s)	Stress Relief	145±9	3777±190	0	0	2.48±0.65
Zn on Mg (100ºC, 5mm/s)	-1.65±0.94	32±4	680±21	155±78	-1070±120	-16.54±1.58
Zn on Mg (250ºC, 10mm/s)	-19.05±5.87	194±10	4657±198	392±26	-6473±280	61.31±3.81
Al7075 on Mg (400ºC, 2mm/s)	38.05±1.84	215±12	5009±220	581±52	-7167±340	25.64±0.97
Al7075 on Mg (400ºC, 15mm/s)	2.48±0.65	167±8	3777±190	557±26	-5556±270	-3.31±1.06
Al7075 on Zn 100ºC on Mg (15mm/s)	-16.54±1.58	135±5	3245±106	265±104	-4502±370	-17.37±2.04
Al7075 on Zn 100ºC on Mg (2mm/s)	-16.54±1.58	170±9	4072±165	589±26	-5667±305	-133.47±2.74

To improve the beneficial mechanical strain after coating Al7075 on AZ31B, first, the effect of nozzle speed on the heat generation was studied. Based on the FBG results, the thermal strain during coating process was decreased to about 20% with increasing the speed of the nozzle from 2mm/s to 15mm/s, hence, the residual strain was change from tensile to compressive strain. To investigate the effect of thermal mismatch on the inducing of final strains, a thin layer of pure Zn was coated on Mg substrate at 2 different gas temperatures (100°C, 250°C). Since the CTE of Zn is higher than Mg, developing tensile residual strain in Zn coating and compressive strain in the substrate is expected. However, the obtained results demonstrated that it is completely corresponded to the processing temperature. Unlike the high temperature, the low temperature of carrier gas for coating Zn on Mg could retain the negative

mechanical strain about -16.54±1.58με, which was produced from impact deformation (see Fig. 4-4a and Fig. 4-5). Finally, coating a thin layer of pure Zn as an intermediate layer between Al7075 and Mg substrate with the relatively higher CTE than both Al7075 and AZ31B could reduce the effect of thermal mismatch and increase the significant amount of beneficial residual strain in Mg substrate. As the results demonstrated, coating Al7075 with the lower nozzle speed illustrated a huge reduction in compressive residual strain (-116με) leading to the negative strain of -133.47±2.74με in comparison with the higher nozzle speed (Fig. 4-5). It can be addressed by considering the higher deposition rate corresponding to the lower nozzle travel speed, which causes the impact of more particles compared to the higher nozzle speed.

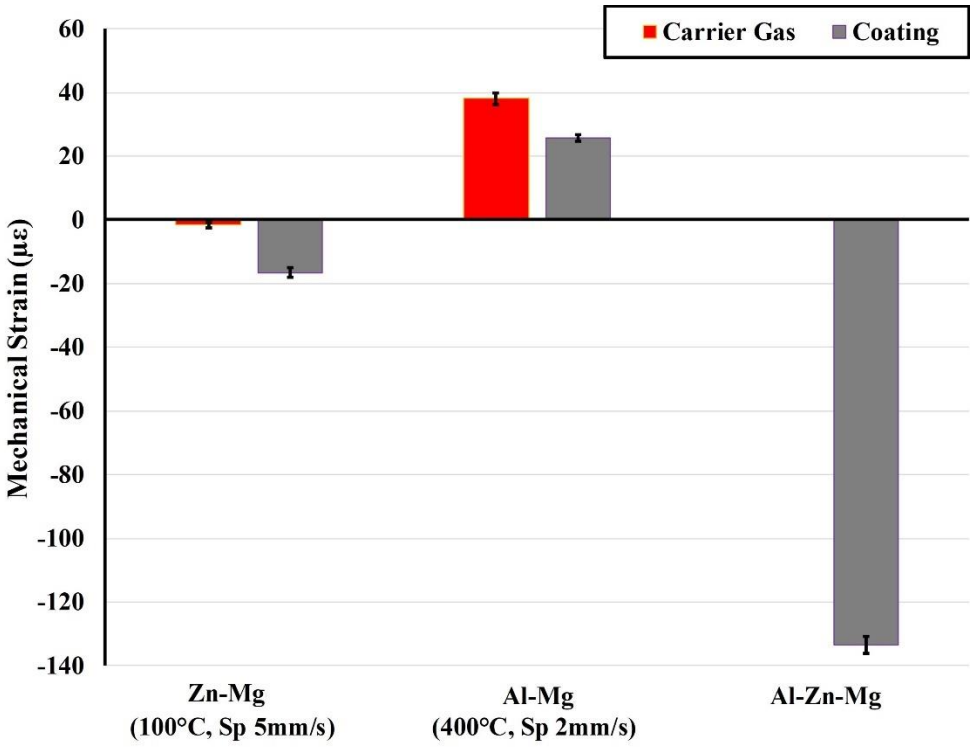

Fig. 4-5: Comparison between mechanical strain under different coating materials and parameters.

4.5 Conclusions

The strain development in the AZ31B-H24 Mg substrate during the multi-layer cold spray coating of Zn and Al7075 was successfully investigated by using FBG and thermocouple sensors. The following conclusions can be drawn from the results obtained in this study:

1) The localized effect of carrier gas temperature and coating impact was successfully separated by employing FBG sensors for in situ measurements.
2) The mechanical strain for different cold spray treatments associated with the particles impact was calculated and separated from the total strain.
3) In the case of Al7075 coating and for the coating parameters of this study, the thermal mismatch created a positive elastic strain of 26με in the substrate and eliminated the effect of impact strain because of the lower CTE of Al7075 compared to Mg substrate.
4) Depositing a zinc interlayer between AZ31B substrate and Al7075 coating enabled the control over distribution of residual stress by thermal mismatch. The tensile residual stress in the substrate near the coating due to Al7075 coating was changed to a negative residual stress when Zn interlayer was introduced.

Chapter 5

Effects of Cold Spray Coating Parameters on the Characteristics of Interlayer Zinc Deposited on Magnesium alloy

5.1 Abstract

Zinc, a soft material with a low melting point and high corrosion resistance, was deposited on AZ31B magnesium alloy through the cold spray coating. The physical and mechanical properties of the resulting Zn/AZ31B coated samples were then investigated to explicate the role of coating parameters on the microstructural and mechanical characteristics of these samples. The results clarified that the intermetallic phases were formed at the interface of the Zinc/AZ31B even at low carrier gas temperatures. The observation of spherical droplets on the zinc coating confirm that zinc particles melt during impact, leading to the formation of intermetallic phases during solidification. A thin layer of dense zinc coating was used to create an intermediate layer between Al7075 coating and an AZ31B substrate, forming a multi-layer coating of Al7075/Zn/AZ31B. Because of the higher thermal expansion coefficient of zinc in comparison with Al7075 and AZ31B, beneficial, compressive residual stress was developed in the coated samples. However, without a zinc interlayer, Al7075 coating on AZ31B substrates under the same coating parameters showed tensile residual stress in the substrate.

5.2 Introduction

Cold gas dynamic spray is an innovative solid-state material deposition method and a pioneering technology in the surface modification, repair, and even build-up of structures without melting the materials involves; unlike with thermal spraying. A convergence-divergence de Laval nozzle supersonically accelerates micron-sized particles through a pressurized and relatively low temperature gas. The high velocity particles impact a substrate with high kinetic energy, consequently being intensely deformed [57]. This intensive plastic deformation of particles produces a significant amount of localized heat upon impact, resulting in mechanical and metallurgical bonding with the substrate [63]. Since the heat generation during particle impingement is greater than the heat dissipation, and because of high interfacial strain and shear bonding under solid state, adiabatic shear instability is designated as one of the possible bonding mechanisms [148][63]. Considering the thermal energy released under the bonding mechanism and the thermal energy input through the carrier gas, a temperature increase in coated samples is inevitable. When the coated samples drop to room

temperature, the discrepancy between the thermal expansion coefficient (CTE) of the coating and substrate materials develops thermal strain in both. On the other hand, bombarding the substrate with high velocity particles privileges the substrate and coating to attain compressive residual stress. However, the thermal expansion mismatch between coating and substrate can completely or partially neutralize the induced compressive stress. This phenomenon for materials such as magnesium with a high sensitivity to temperature is more probable and problematic. For instance, when a high strength and relatively good corrosion resistance aluminum alloy, Al7075 powder, which is one of the most attractive coating materials, was coated on magnesium alloy structures, the thermal mismatch affected the compressive residual stress that developed under the peening effect, turning it into the tensile residual stress [146]. To address the issues, having an intermediate layer of a material with a greater CTE than aluminum and magnesium such as zinc might be a practical approach to controlling the destructive effects of thermal mismatch.

Zinc, as a highly corrosion-resistant metal, is used to chemically protect ferrous and magnesium alloys from corrosion and surface degradation [149]. Moreover, the use of zinc as a biodegradable material for medical applications has been considered due to its corrosion resistance and compatibility with the human body [150][151]. Zinc, with its hexagonal closed packed structure, have a few slip systems resulting in low plasticity and deformability; however, the low mechanical strength and low melting point of this soft material provide good ductility and a low critical velocity-in the cold spray temperature range. Therefore, a dense layer of zinc with a low critical velocity can be easily deposited using a solid-state cold spray process with a low-pressure system. However, only a few successful studies have explored cold spraying of zinc coating layers on mild steel to improve its corrosion resistance, and investigated the characteristic of the zinc coating [152][153][154]. Li et al. [155] deposited pure zinc on stainless steel using two different carrier gas temperatures, 320°C and 410°C, with the nozzle travel speed of 80 mm/s. A dense microstructure of zinc coating layer was reportedly created on the steel. Nanocrystalline grains formed in the coating near the interface, severely deforming the particles, and leading to recrystallization of elongated grains. Moreover, spherical particles was observed as a result of the jetting of melted particles, which can occur in soft materials with a low melting point and intensive deformation during cold spraying [155]. In another study, Maledi et al. [153] investigated the effect of processing parameters on the mechanical and microstructural properties of mild steel coated with zinc. They performed the zinc coatings in the temperature range between 450°C to 550°C and pressures of 0.69 MPa and 0.8 MPa, with different stand-off distances of 15mm/s and 25mm/s. Based on their observations, they found that increasing the temperature and pressure of a carrier gas could

improve the bond strength between zinc and steel, and decrease the residual stress; however, in terms of hardness, no significant changes occurred with increasing these parameters [153]. The trend of these limited studies into cold spray deposition on zinc was toward increasing the temperature to achieve successful coating. High-temperature coating is reasonable when the process is conducted on high strength and high melting point substrate materials such as steel. However, in the case of low melting point substrates such as magnesium, increasing the coating temperature can be problematic and affect the mechanical properties and the microstructure of coated samples (Chapter 6&7).

This research has studied the cold spray deposition of pure zinc on AZ31B-H24 magnesium sheet. The aim of this research is to investigate the possibility of using zinc as an interlayer between a magnesium substrate and Al7075 coating to minimize the detrimental effect of thermal mismatch and develop residual stress. Using a theoretical model, the critical velocities and particle-impact velocities of zinc powder are calculated for different carrier gas temperatures to select the coating parameters. Regarding the negative impact of coating temperature on the magnesium substrate [146] (Chapter 6&7), minimizing the coating temperature with respect to a high quality of coating and maximizing the compressive residual stress has been considered. Then, the Zn/AZ31B coated samples have been examined to uncover appropriate physical coating properties such as thickness and surface roughness. The phase identifications of coated samples conducted by x-ray diffraction technique are analyzed to investigate the probable intermetallic phases at the interface area for different treated samples. The effects of zinc coating on the microstructure and residual stress formation in magnesium substrate are also studied. Finally, the effect of a zinc interlayer on the residual stress development in Al-7075/Zn/AZ31B coated samples is investigated to determine the role of thermal mismatch in coating temperature-sensitive materials.

5.3 Experimental Procedure

5.3.1 Materials and Methodology

In this research, several 30×50 mm rectangular specimens of AZ31B-H24 Mg alloy sheet, 3.16 mm thick, were used as the substrate. The substrate samples were heat treated based on the ASM-recommended procedure (260ºC/15min) to release any initial residual stresses [135]. The feedstock powders used in the experiments were an irregular-shaped commercial pure zinc powder (supplied by Centerline Ltd., Windsor, Canada) with an average value of 35μm (measured by Mastersizer 2000, Malvern, UK) and a spherical-shaped Al7075 powder (supplied by Centerline Ltd., Windsor, Canada)

with an average value of 23μm (measured by Retsch technology, Camsizer XT). The morphology of the zinc powder and the size distribution of zinc and Al7075 powders are shown in Fig. 5-1a and Fig. 5-1b. A commercial low-pressure Supersonic Spray Technologies (SST) Series P Cold Spray System (Centerline, Windsor, Canada) was used to conduct the coating process. To create a coating layer of zinc on Mg substrate, the zinc particles were accelerated by nitrogen (N2) propellent gas under the low pressure of 1.38 MPa and a standoff distance of 15mm. The experiments were performed under the a constant feedrate of 8gr/min, whereas the carrier gas temperature and nozzle speed varied. Table **5-1** lists the various gas temperatures and nozzle speeds as the most significant parameters to study the effect of parameters on the physical and mechanical properties of coating and substrate. In addition, after selecting an optimum condition for depositing zinc on magnesium, Al7075 powder was coated on the Zn/Mg samples. The standoff distance was reduced to 12mm, and the carrier gas temperature increased to 400°C with the low nozzle speed of 2 mm/s. The feedrate was 8 gr/min, and the carrier gas pressure was 1.38 MPa in this series of experiments. For sake of comparison, the same processing coating parameters were also used to deposit Al7075 on AZ31B substrates.

5.3.2 Residual Stress Measurement

For measuring the distribution of residual stress through the depth of coated samples, a hole-drilling machine (Sint technology, Restan MTS-3000) was used to measure the relaxation strain during drilling. Then the obtained strains were calculated based on the non-uniform method using the EVAL software to extract the residual stress of the coated samples.

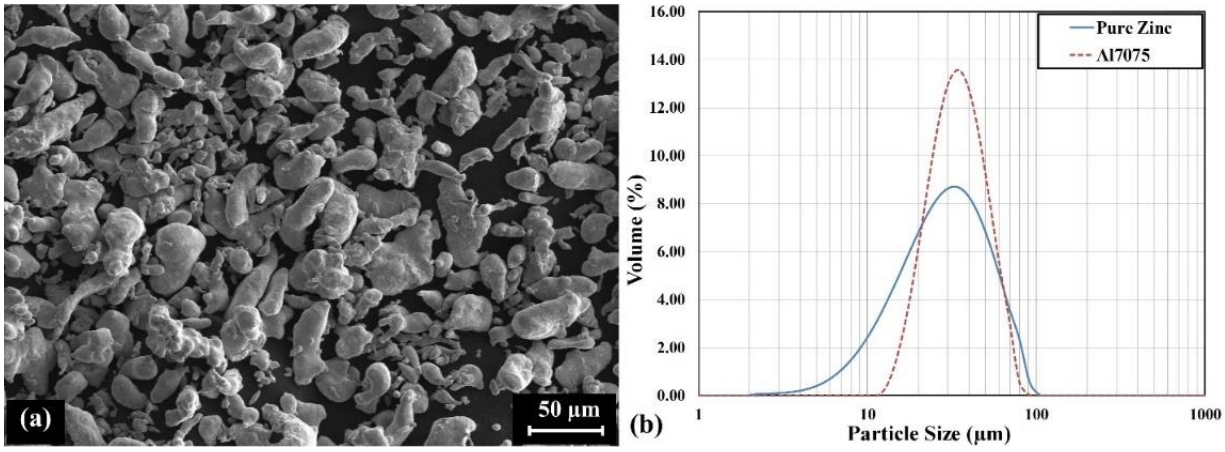

Fig. 5-1: a) SEM image of pure zinc powder; b) particle size distribution for pure zinc and Al7075.

Table 5-1: Design of experiments

Test #	Pressure (MPa)	Feedrate (gr/min)	Temperature (ºC)	Nozzle Speed (mm/s)
1	1.38	8	250	5
2	1.38	8	200	5
3	1.38	8	150	5
4	1.38	8	100	5
5	1.38	8	250	10
6	1.38	8	200	10
7	1.38	8	150	10
8	1.38	8	100	10
9	1.38	8	250	15
10	1.38	8	200	15
11	1.38	8	150	15
12	1.38	8	100	15

5.3.3 Microstructural Analysis

A scanning electron microscope (SEM, model: Zeiss Leo UltraPlus FESEMs) equipped with an Oxford Energy Dispersive X-ray spectroscopy (EDX) and TESCAN VEGA3 electron microscope were employed to analyze the microstructure and chemical composition of the interface. For this work, the cross-sectioned samples were polished and etched to reveal the grain structure of the Mg alloy samples. Details of sample preparation have been described in [146]. To study the phase identification at the interface of the Zn/Mg coated samples, a Bruker D8-Discover equipped with a VÅNTEC-500 area detector and using Cu-Kα radiation at 40 kV and 40 mA was employed. During the measurement, a 300 μm collimator scanned the area in 2θ angle mode from 20° to 95°, with an increment of 15° and exposure time of 60s. Then, the obtained data were analyzed using Bruker's Diffrac.Eva software. A Keyence VK-X250 confocal laser microscope (manufactured by Keyence Corporation, Osaka, Japan) was used for measuring the surface roughness (Sa) and the thickness of the coating. In addition, the micro-hardness of the samples in three different locations- the coating, interface and substrate-was determined on cross-sections of coated samples, using Clemex Technologies (Inc, Longueuil, Canada). Several micro indentations with 10 gr loads for 10 s were applied on the polished surface of the coated samples, which were treated with different carrier gas temperatures and nozzle speeds.

5.3.4 Three-Point Bending Fatigue Test

Three-point bending fatigue tests were conducted using an Instron 8872 servo-hydraulic axial test machine equipped with a 3-point bending system. The load capacity of the machine is 25KN, and the tests were conducted at ambient temperature. Several rectangular coated samples with dimension of 12.7×120×6.2 mm were prepared for performing the bending fatigue tests. Based on the ASTM D5947 test method, the distance between supporting spans was adjusted to (16±1) times the thickness, which was about 100 mm; however, this span distance was not appropriate to carry out the tests, resulting in a large bending radius and failure. Therefore, the snap distance was decreased to 80 mm, and the bending tests were conducted with the R ratio of 0.1 and the frequency of 1Hz for low cycle and 3Hz for high cycle fatigue tests. These series of tests were run for AZ31B-H24 Mg alloy samples as well as the coated samples.

5.4 Results and Discussion

Controlling certain pivotal processing parameters that critically affect the particle velocity in order to exceed the critical velocity is a fundamental part of the coating process. Having an appropriate level of particle velocity compared with the critical velocity can directly affect the coating creation or substrate surface erosion. To obtain the impact velocity and critical velocity of the particles, related equations were extracted from the literature [92][156][93][63]. Moreover, the relation between the shock waves effect and the standoff distance was found from the literature prepared by Pattison J. et al. [157]. They used computational fluid dynamics, Particle Image Velocimetry and Schlieren imaging to show the negative influence of bow shock on the deposition efficiency and observe the relation between standoff distance and the thickness of bow shock.

After the material properties of zinc as well as the processing parameters used in these experiments were altered, particle velocities at different carrier gas temperatures were calculated for various particles size. Fig. 5-2a depicts the impact velocity of the zinc particle at different carrier gas temperature versus the particle size calculated from the above-mentioned mathematical models. Based on this graph, at a constant temperature, the impact velocity is more sensitive to particles size when the particles are smaller than 40 µm. Fig. 5-2b shows the impact velocity for the particles size of 35µm versus the carrier gas temperature. This curve illustrates that the impact velocity increases nonlinearly with an increase in the temperature. This increase can be attributed to the drag coefficient factor changes, which are influenced by a particle's Mach number [92]. The impact and critical velocities of zinc particles with the average value of 35 µm were calculated for the nozzle temperature range of 50-

400°C (Fig. 5-2c). Since critical velocity is determined based on the properties of particles as well as the particles' temperatures, with a rising carrier gas temperature, the particles' temperatures are increased, decreasing the critical velocity (Fig. 5-2c). Equation (5-1) expresses the critical velocity, and K_1 as a fitting parameter is obtained with respect to the existing experimental data from Equation (5-2):

$$\boldsymbol{v_{cr} = K_1\sqrt{C_p(T_m - T_p) + 16\frac{\sigma_{UTS}}{\rho_p}\left(\frac{T_m - T_p}{T_m - 293}\right)}} \quad \textbf{(5-1)}$$

$$\mathbf{K_1 = 0.64\left(\frac{d_p}{d_p^{ref}}\right)^{-0.18}} \quad \textbf{(5-2)}$$

where C_p is a particle's specific heat capacity, T_m is a particle's melting temperature, T_p is the particle's impact temperature, σ_{UTS} is the ultimate tensile strength, ρ_p is the particle's density, and d_p is the particle's diameter. The Particle impact temperature for this calculation was extracted based on a the mathematical equation reported by Mauer et al. [158]. Based on the results, the range of carrier gas temperatures was considered to be from 100 to 250°C for the cold spray experiments, because at the lowest temperature of 50°C only a very thin layer of Zn coating could be formed with the low deposition deficiency.

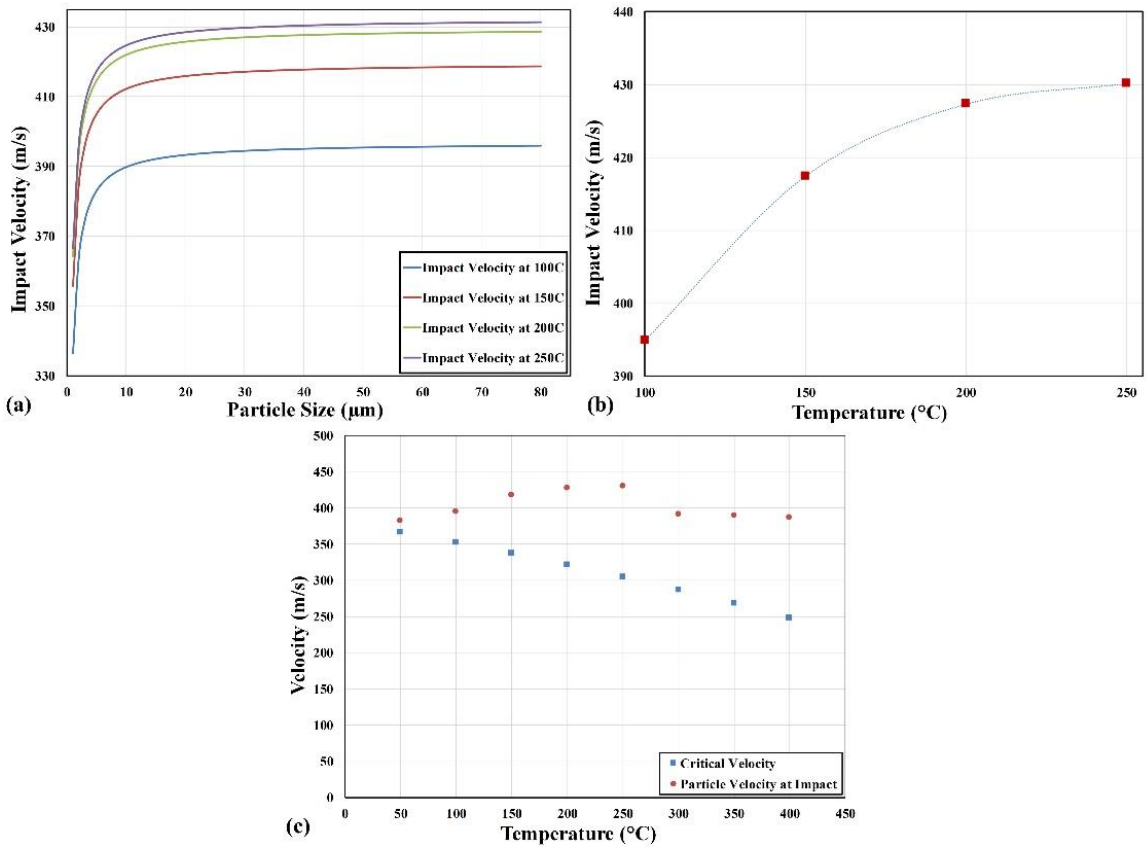

Fig. 5-2: a) Impact velocity vs particle size for different temperatures; b) the impact velocity of the 35 µm zinc particles vs temperature; c) the critical and impact velocities of pure Zn particles with an average size of 35µm at different temperatures.

5.4.1 Surface Roughness and Thickness

The relations between carrier gas temperature, coating thickness and surface roughness are shown in Fig. 5-3. By increasing the carrier gas temperature for all nozzle speeds, particularly for a nozzle speed of 5 mm/s, the surface roughness was linearly increased (Fig. 5-3a). The same trend can be seen in the relation between temperature and thickness (Fig. 5-3b). This phenomenon can be attributed to the critical velocity of particles, which decreases with an increase in temperature, resulting in more particles being able to exceed the critical velocity and thus create a thicker coating. On the other hand, increasing the carrier gas temperature and so enhancing the coating thickness leads to an increased temperature of the substrate and particles. In consequence, more ductility and intensive deformation occur upon impact, causing more material jetting and increasing the surface roughness (Fig. 5-3c).

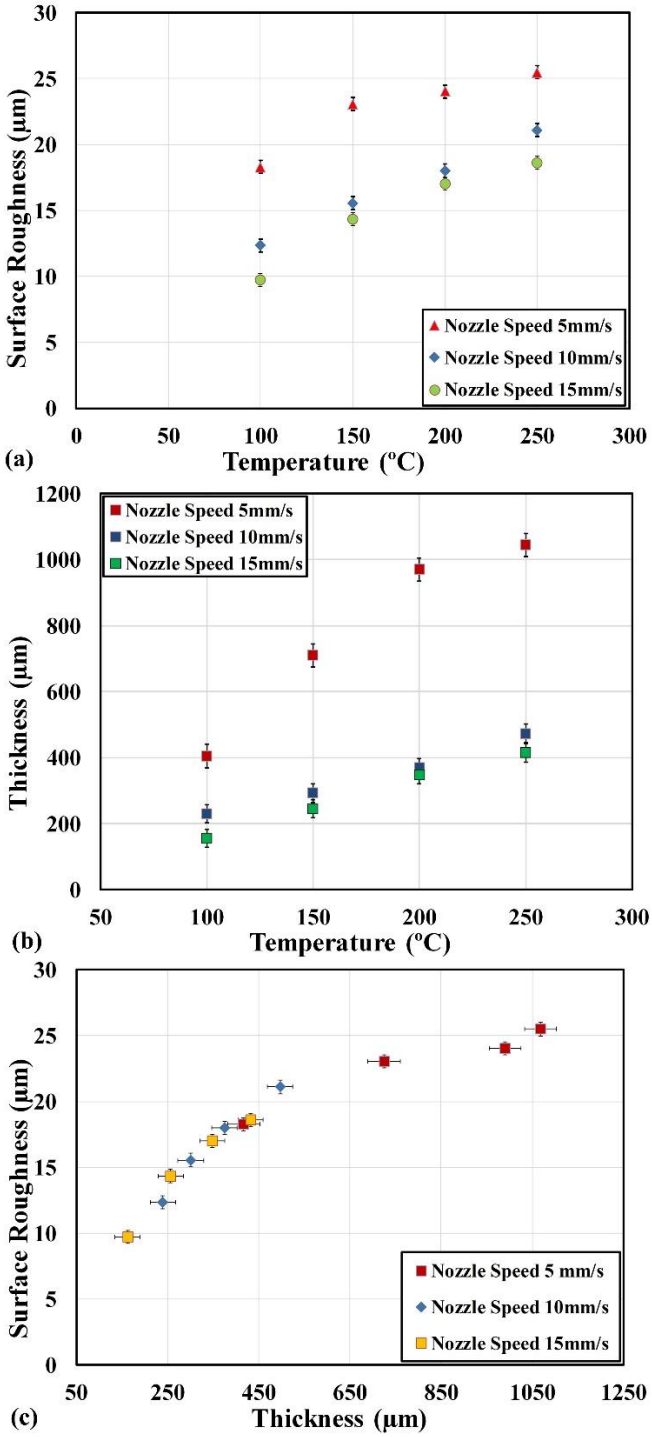

Fig. 5-3: The relation between; a) the average of surface roughness and carrier gas temperature; b) the average of coating thickness and carrier gas temperature; c) the average of surface roughness and the average of coating thickness for different nozzle speeds (5mm/s, 10mm/s, 15mm/s).

5.4.2 Phase Identification

Fig. 5-4a depicts an example of the interface SEM image when the sample was treated at a carrier gas temperature of 250°C with the nozzle speed of 5 mm/s (Test#1), and Fig. 5-4b shows the chemical composition analysis of the coating, interface, and substrate detected by EDS line scan. This SEM image and chemical analysis clearly affirm the mixing of the magnesium and zinc, and formation of a distinguishable interface region. The interface between the coating and substrate of all 12 samples, listed in **Table 5-1**, were examined by x-ray diffraction technique to determine the structure of the interface region. Fig. 5-5 depicts typical X-ray diffraction patterns of the interface for Zn/Mg samples, coated with a constant nozzle speed of 10 mm/s under various carrier gas temperatures. The conclusion of this study is presented in **Table 5-2**. The results demonstrate that different intermetallic phases have formed under various combinations of temperature and nozzle travel speed. These results are compatible with those from EDS line scans. For instant, the ratio of Mg/Zn at the interface region for test #1 (Fig. 5-4b) is around the ratio of these elements for the intermetallic $Mg_{51.04}Zn_{19.8}$, detected by x-ray (**Table 5-2**). Since the coating temperature increases with an increase in the carrier gas temperature and\or decrease of the nozzle travel speed, the ratio of carrier gas temperature to nozzle speed was considered as an index for coating temperature. To evaluate the relation between the coating temperature index and the synthesized intermetallic phases, the Mg/Zn ratio of the intermetallic phases formed at the interface of each coating condition was plotted versus the coating temperature index (Fig. 5-6). This graph indicates a specific trend for creating the intermetallic phases at the interface of Mg/Zn coated samples. When coating temperature is low, a metastable intermetallic phase of Mg rich $Mg_{0.97}Zn_{0.03}$ is formed. However, when the coating temperature index is greater than about 16ºCs/mm, zinc-rich phases have been detected at the interface. Fig. 5-6 reveals that both carrier gas temperature and nozzle travel speed are decisive factors playing crucial roles in the phase formation. For example, when the carrier gas temperature is 100°C, although this is the minimum temperature of this study, and the nozzle speed is 5mm/s, a high temperature intermetallic phase ($Mg_{51.04}Zn_{19.8}$) is formed. In contrast, during coating at a carrier gas temperature of 200°C and nozzle travel speed of 15 mm/s, a low temperature intermetallic phase of $Mg_{0.97}Zn_{0.03}$ phase is developed.

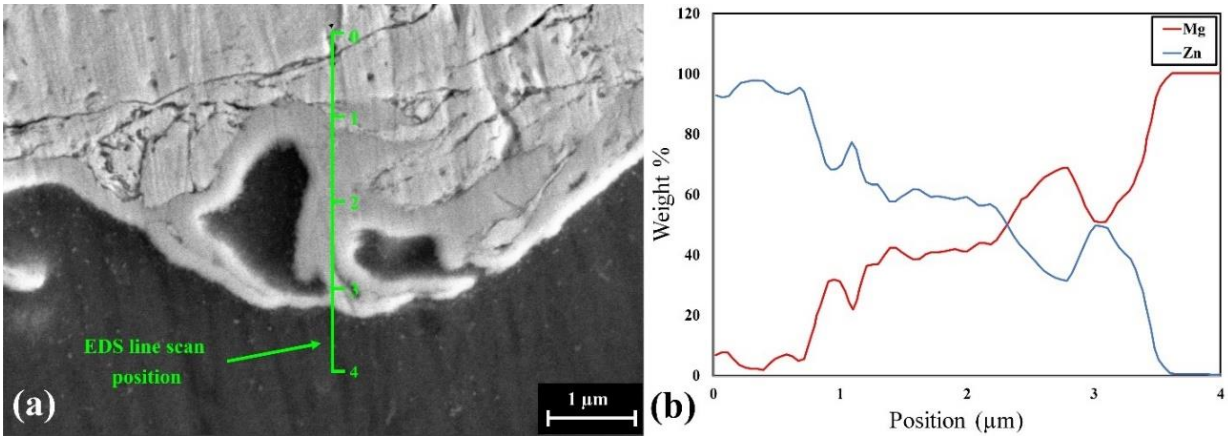

Fig. 5-4: a) SEM image of the interface showing formation of an interface region between coating and substrate; b) the chemical composition changes across the interface, analyzed by line scan EDS.

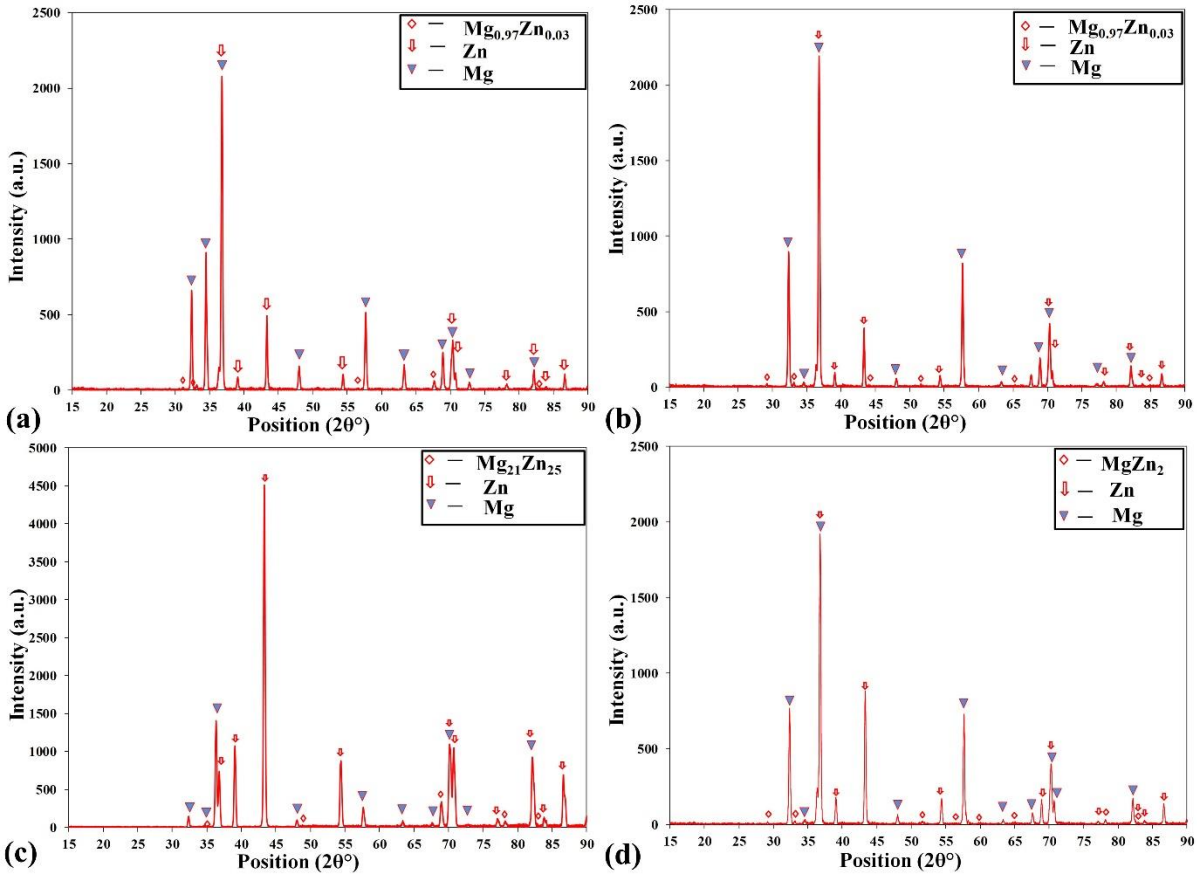

Fig. 5-5: X-ray diffraction pattern for the interface of Zn coating on AZ31B at a constant nozzle speed of 10mm/s, and under various carrier gas temperatures of a)100°C; b)150°C; c)200°C; d)250°C.

Table 5-2: Phase Identification at the interface

Temperature (°C)	Nozzle Speed (mm/s)	Phase	Crystalline Structure	Mg/Zn
100	5	$Mg_{51.04}Zn_{19.8}$	Orthorhombic	2.58
100	10	$Mg_{0.97}Zn_{0.03}$	Hexagonal	32.33
100	15	$Mg_{0.97}Zn_{0.03}$	Hexagonal	33.48
150	5	Mg_2Zn_{11}	Cubic	0.18
150	10	$Mg_{0.97}Zn_{0.03}$	Hexagonal	32.33
150	15	$Mg_{0.97}Zn_{0.03}$	Hexagonal	32.33
200	5	$MgZn_2$	Hexagonal	0.50
200	10	$Mg_{21}Zn_{25}$	Trigonal	0.84
200	15	$Mg_{0.97}Zn_{0.03}$	Hexagonal	32.33
250	5	$Mg_{51.04}Zn_{19.8}$	Orthorhombic	2.58
250	10	$MgZn_2$	Hexagonal	0.50
250	15	$Mg_{51.04}Zn_{19.8}$	Orthorhombic	2.58

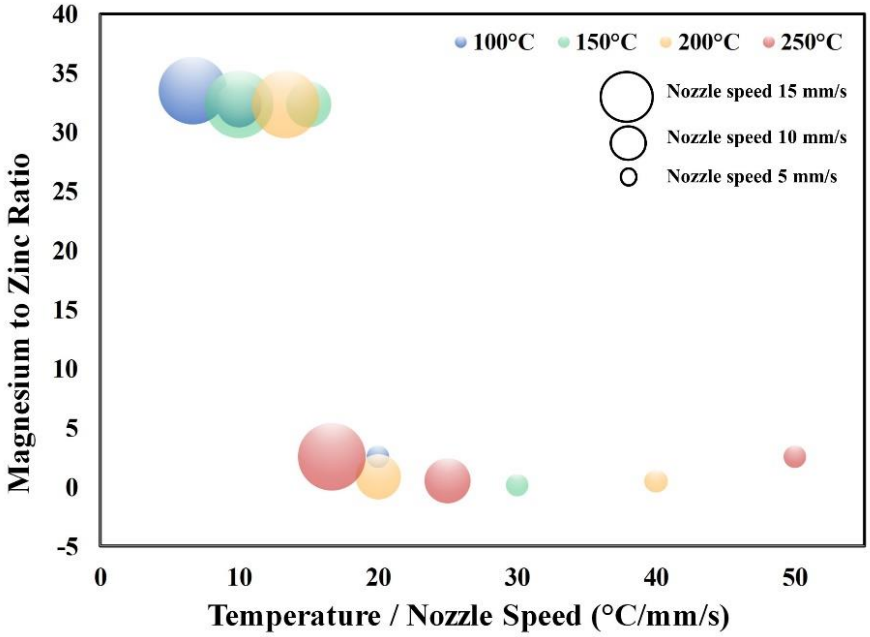

Fig. 5-6: The ratio of Mg/Zn in the intermetallic phases formed at different temperatures versus the ratio of carrier gas temperature to the nozzle speed (The bubble sizes represent the nozzle speeds).

In the solid-state cold spray condition with the temperature process far from the particles melting point, there are insufficient thermal energy and time for intermetallic phases to be synthesized by a solid-state diffusional process. In contrast, mixing the substrate and coating material in liquid-state is a fast process, and intermetallic phase nucleates and grows during solidification, the probable mechanism for coating zinc on Mg. To evaluate the intermetallic phase formation through melting and solidification mechanisms, the surface of the coating at different coating conditions was observed. Fig. 5-7a and Fig. 5-7b show the small spherical droplets on the surface coating, formed at 250°C with a nozzle speed of 5mm/s at two different magnifications. When the coating temperature drops to 100°C with the nozzle speed of 15 mm/s, the same spherical droplets occurred; however, their sizes and the numbers are significantly reduced (Fig. 5-7c). Similar the literature has claimed the existence of spherical particles on a zinc surface as evidence for partial melting during the coating process [155].

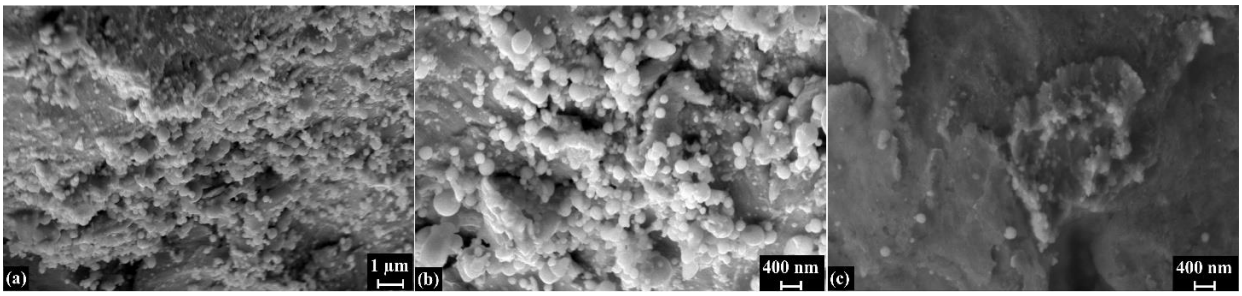

Fig. 5-7: SEM morphology of zinc coating surface at temperature of 250°C and nozzle speed of 5mm/sec, a) low and; b) high magnifications of melting particles during jetting; c) melted particles at the surface of coating at 100°C and nozzle speed of 15mm/s.

Together, SEM observations and x-ray diffraction analysis provide important insights into the formation of intermetallic phases at the zinc/Mg interface during cold spray coating. A sufficiently high thermal energy of particles, created during the impact of soft material with a low melting temperature, can spatter the melted particles from the edge of the material jetting zone and form spherical droplets on the surface. Based on the x-ray diffraction analysis, under low temperatures, the chance of mixing magnesium and zinc is low; therefore, the metastable magnesium rich $Mg_{0.97}Zn_{0.03}$ devitrifies from the liquid during solidification. By increasing the coating temperature index, the impact energy becomes sufficient for mixing the magnesium and zinc; hence, different intermetallic phases grow at the interface.

5.4.3 Hardness measurements

Fig. 5-8 shows the hardness of the coating, interface and substrate in the vicinity of the interface for the Zn/Mg coated samples at the constant nozzle travel speed of 10mm/s and different coating temperatures. Comparing the interface hardness for different carrier gas temperatures reveals the similarity of the hardness for temperatures of 100°C and 150°C, which can be attributed to the same intermetallic $Mg_{0.97}Zn_{0.03}$ phase formation (Table **5-2**). To the best of our knowledge, the metastable $Mg_{0.97}Zn_{0.03}$ crystal structure and its mechanical properties might be similar to those of magnesium [159], resulting in the hardness of the interface under low carrier gas temperature to be similar to that for the magnesium substrate. However, increasing the carrier gas temperatures to 200°C and 250°C increases the hardness of interface, and as mentioned above, $Mg_{21}Zn_{25}$ and $MgZn_2$ have been detected at the interface, respectively. $Mg_{21}Zn_{25}$ has a trigonal crystal structure with a hardness of 4.66GPa, and $MgZn_2$ has a hexagonal C14 Laves crystal with a hardness of 5.08GPa [160], while the respective hardness of the interface of the coating at 200°C and 250°C are 113HV and 124HV equal to 1.1GPa and 1.2Gpa. Decreasing the hardness of the interface in comparison with the intermetallic hardness can be related to the intermetallic compounds, embedded in the matrix of zinc and magnesium. Moreover, a higher carrier gas and coating temperature of 250°C leads to increased melting, and thus more chance for intermetallic phase formation of $MgZn_2$ with a higher hardness. In addition, the effect of carrier gas temperature on the coating and substrate hardness, shown in Fig. 5-8, can be justified by considering the two competitive processes; peening and annealing. Increasing the temperature leads to increased particle kinetic energy, resulting in improved peening effect as well as greater hardness. On the other hand, a rise of temperature can reduce the hardness due to annealing and stress relief effects. Based on the data presented in Fig. 5-8, the carrier gas temperature of 200°C seems to be the optimum deposition condition and the point at which maximum hardness was measured in the coating; however, under 150°C the substrate is at maximum hardness.

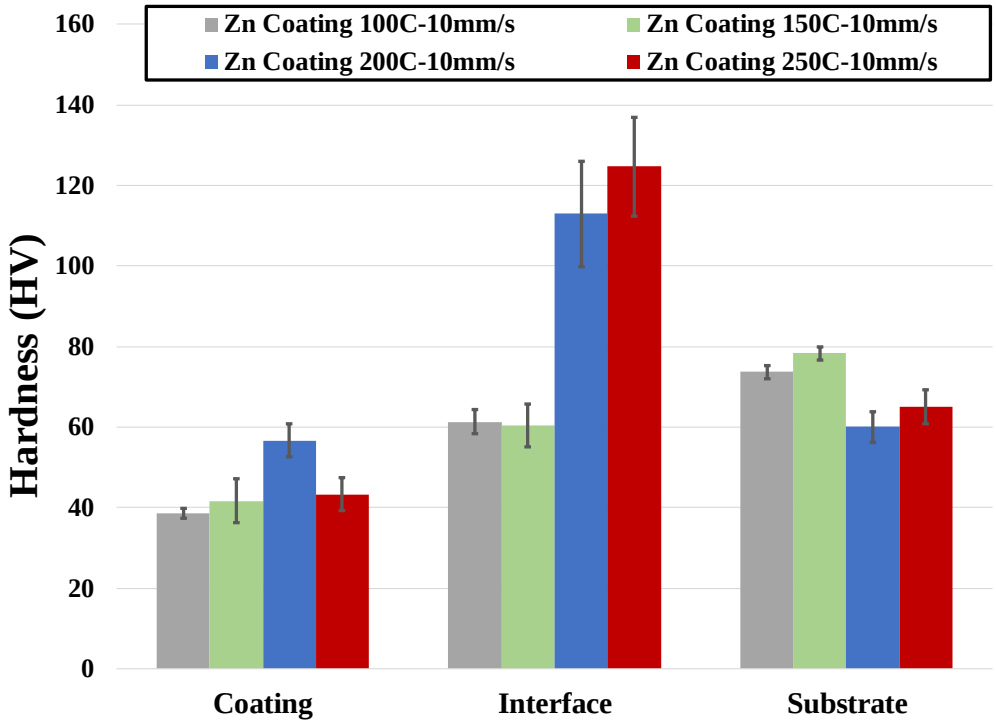

Fig. 5-8: Change in hardness of coating, interface, and substrate exactly below the interface with increasing temperature at the constant nozzle speed of 10 mm/s.

The intermetallic phases are usually brittle, which can be considered a weakness for zinc coating on AZ31B samples in long term service. To evaluate the performance of the coated samples, the fatigue life of the stress relieved Mg alloy samples and coated samples under temperatures of 100°C and 250°C was investigated by the 3-point bending method. The fatigue failure of the coated samples in low cycle and high cycle regimes occurred at a lower number of cycles compared with the stress relieved Mg alloy samples. Fig. 5-9 shows the fatigue results of uncoated AZ31B and zinc coated samples under temperature of 250°C. The lower fatigue strength of zinc and the brittle intermetallic phase formation at the interface cause earlier crack nucleation at the interface than in the stress relieved Mg samples. Fig. 5-10a shows the fracture surface of coated samples, revealing fatigue cracks initiated from the interface and propagated in the coating; however, there is no evidence of coating delamination. Fig. 5-10b shows a high-resolution image of the interface with a crack in it. Moreover, the other crack seen in this figure nucleated at the interface and grew in the magnesium perpendicular to the crack at the interface. Hence, it seems, in the range of the coating parameters of this study, depositing a layer of zinc on the AZ31B magnesium sample can deteriorate the fatigue performance of coated samples.

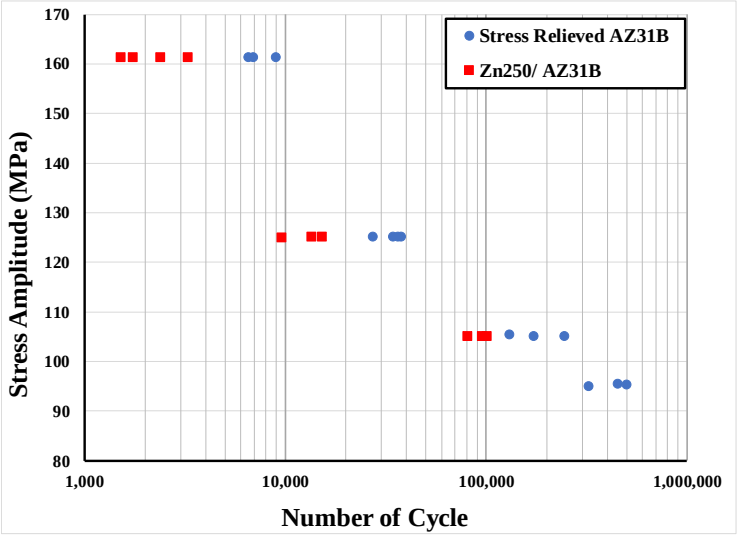

Fig. 5-9: Fatigue test results for magnesium AZ31B and Zn coated samples with a carrier gas temperature of 250°C.

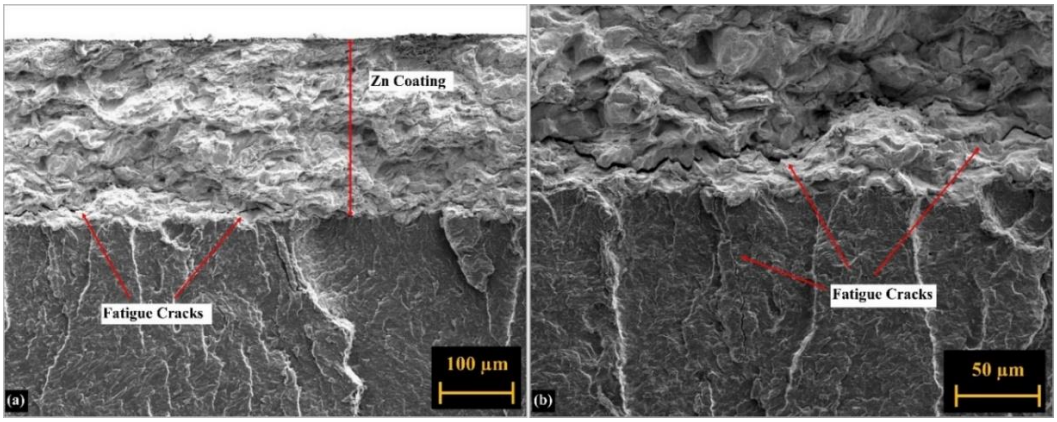

Fig. 5-10: Fracture surface of the 3-point bending fatigue of the coated sample, showing propagation of the cracks at the interface.

5.4.4 Microstructural Observations

Fig. 5-11 shows the microstructure of coating deposited at the constant nozzle speed of 10mm/s and carrier gas temperatures of 100°C and 250°C. At the lower temperature, the coating structure mainly consists of lamellar grains formed by intensive deformation of the zinc particles during coating (Fig. 5-11a). However, the coating deposited at the higher temperature (Fig. 5-11b) shows less elongation of grains as well as trapped particles along with lamellar microstructure. The trapped particles can be considered as a source of defects in the coating, because free spaces remain around these particles due to their structures. One of the magnified trapped particles is seen in Fig. 5-11c. In this case, the particles

were deposited successively over the trapped particle while some space still remains below the particle in the coating.

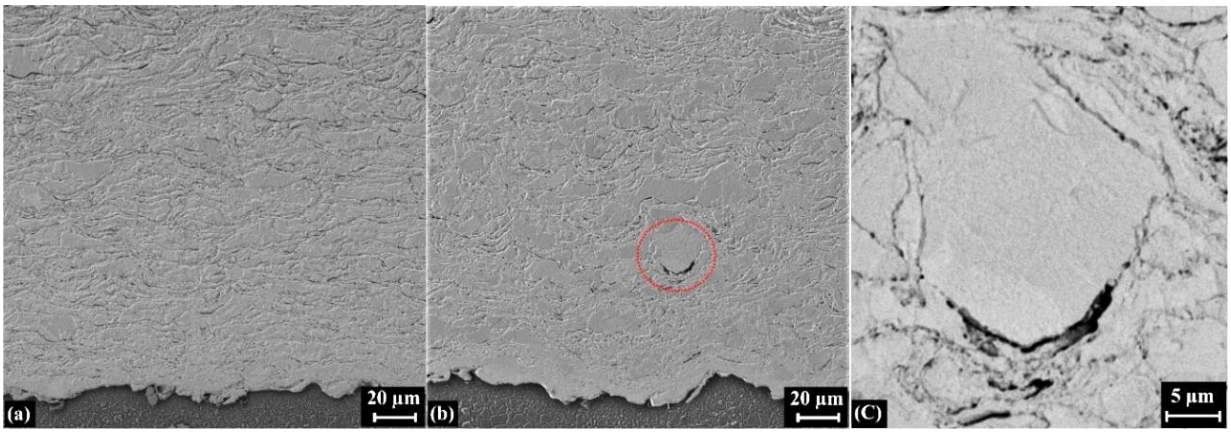

Fig. 5-11: Microstructure of zinc coatings at the constant nozzle speed of 10mm/s and carrier gas temperatures of; a) 100°C; b) 250°C; c) High-resolution image of defect in zinc coating at 250°C.

Fig. 5-12 shows the microstructure of the magnesium substrate in the vicinity of the interface in which two regions are distinguishable: the first area, with very fine grains just below the interface, is contiguous with the second zone consisting of coarser grains. The row and the column of the images represent various temperatures and different nozzle speeds, respectively. In the first row, at temperature of 100°C, increasing the nozzle speed decreases the width of the fine-grain area, and the coarser grains are formed in the second zone as a result of reducing the number of impact particles. This trend is repeated for all temperatures. Moreover, in a certain column at a constant nozzle speed, the fine-grain area is reduced by increasing the carrier gas temperature. In the coarse-grain zones, two types of grain structure are formed. For the higher temperature process, dynamic grain growth is a predominant grain structure exactly after the grain refinement zones, as can be seen in Fig. 5-12g, Fig. 5-12j, and Fig. 5-12k, while with decreasing the thermal energy, the prevailing peening effect causes a decrease in the grain size in the second zone (Fig. 5-12d). The size of the grains in the second area is changed by changing the coating parameters and depends on the interaction between thermal and peening effects. The maximum grain size of this region can be seen in the case of 100°C-15 mm/s, which has the minimum coating temperature and minimum material deposition (Fig. 5-12c). In contrast, the minimum grain size for this region can be observed in the sample coated at 150°C-5mm/s, as the velocity of particles is high enough to produce the maximum peening effect and the temperature is not sufficient to change the microstructure (Fig. 5-12d).

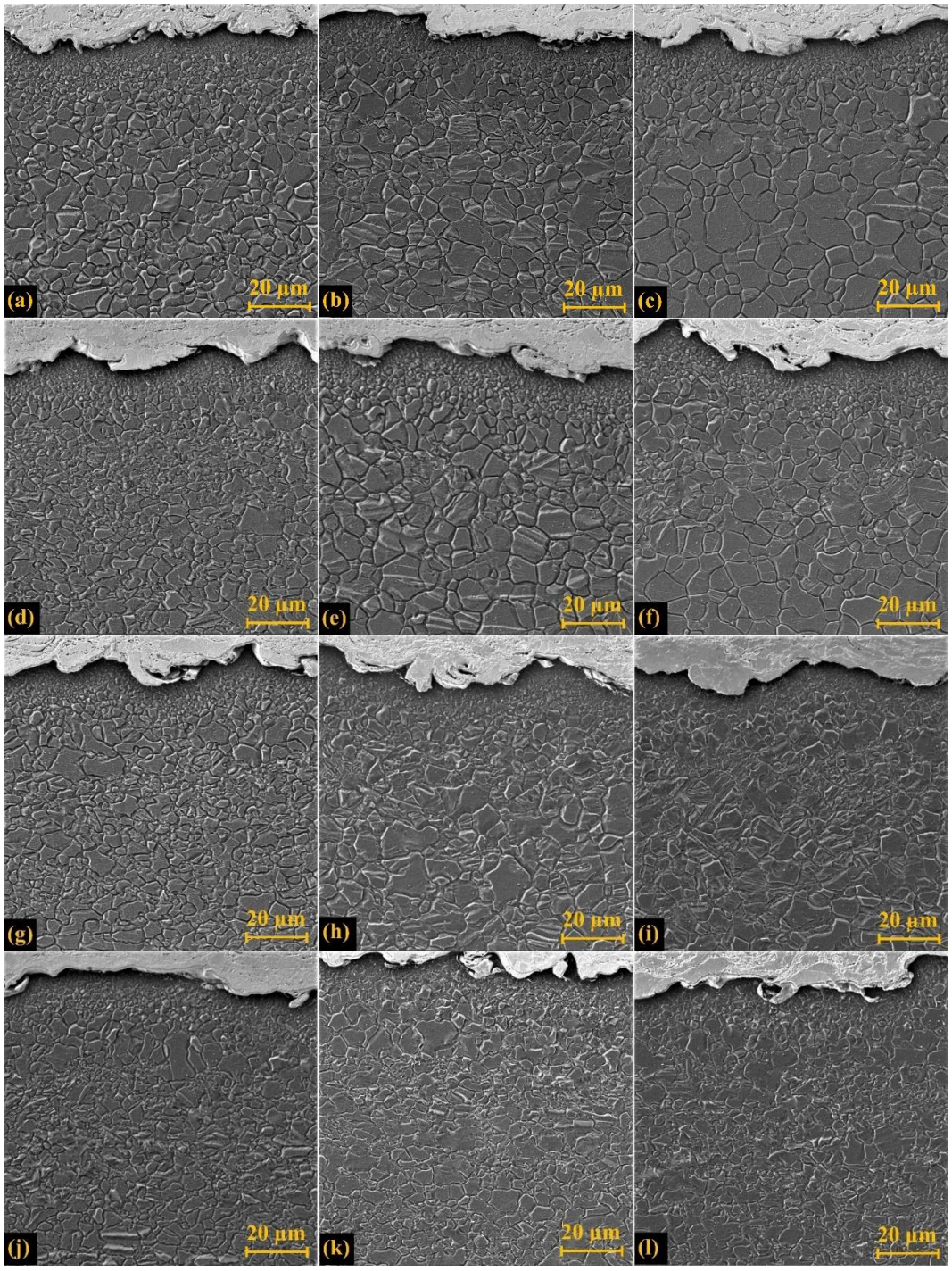

Fig. 5-12: SEM images of magnesium alloy coated samples at temperature and nozzle speed of; a) 100°C, 5mm/s; b) 100°C, 10mm/s; c) 100°C, 15mm/s; d) 150°C, 5mm/s; e) 150°C, 10mm/s; f) 150°C, 15mm/s; g) 200°C, 5mm/s; h) 200°C, 10mm/s; i) 200°C, 15mm/s; j) 250°C, 5mm/s; k) 250°C, 10mm/s; l) 250°C, 15mm/s showing the microstructure of Mg alloy substrate.

5.4.5 Residual Stress Profiles

Based on the observations, some experiments were designed to assess the processing parameters, listed in Table **5-3**. Various nozzle speeds were considered to build up a constant coating thickness of 350±1 at the specified range of temperatures. A rising carrier gas temperature enhanced the coating thickness, while feedrate and carrier gas pressure were constant; therefore, the nozzle speed was increased to achieve a specific coating thickness. Then the residual stress was measured for different coating treatments.

Table 5-3: processing parameters for residual stress measurements

Temperature (°C)	Pressure (MPa)	Feedrate (g/min)	Nozzle Speed (mm/s)	Coating thickness (µm)
100	1.38	8	6.5	350±1
150	1.38	8	8.5	350±1
200	1.38	8	12.5	350±1
250	1.38	8	20	350±1

Fig. 5-13 depicts the residual stress distribution of the Mg substrate coated with zinc. Decreasing the thermal energy of the system by reducing the gas temperature induced more compressive residual stress on both the Mg side and Zn side of the interface. These residual stress changes for the temperature of 100°C (about -41.1 MPa) are similar to those at 150°C (-35.5 MPa) that significantly enhance compressive residual stress development compared to the higher temperatures of 200°C and 250°C with the similar compressive residual stresses of -17.8 MPa and -15.2 MPa, respectively. The enhancement of residual stress at the interface can be justified by three different phenomena, which occur simultaneously; thermal mismatch, the interface temperature, and the peening effect. The nozzle travel speed for coating at 100°C and 150°C were almost the same and this range of temperature is not critical for magnesium alloy; hence, the higher compressive residual stress is expected compared to the coating treatments at the higher temperature. However, the nozzle travel speed of the coating at 250°C was notably higher than coating at 200°C that partially compensates the high temperature of carrier gas for the selected coating parameters at this critical temperature range. Therefore, similar residual stress can be observed for these two coating conditions (at the carrier gas temperature of 200°C and 250°C). The coating at lower temperature reduces the destructive thermal mismatch effect and the chance for microstructural relaxation of magnesium substrate. On the other hand, increasing the temperature of gas transformed the residual stress on the coating surface into tensile residual stress, despite the

existence of peening effect. Development of tensile residual stress on the coating surface can be attributed to the thermal mismatch, which occurs at the higher coating-temperature situations.

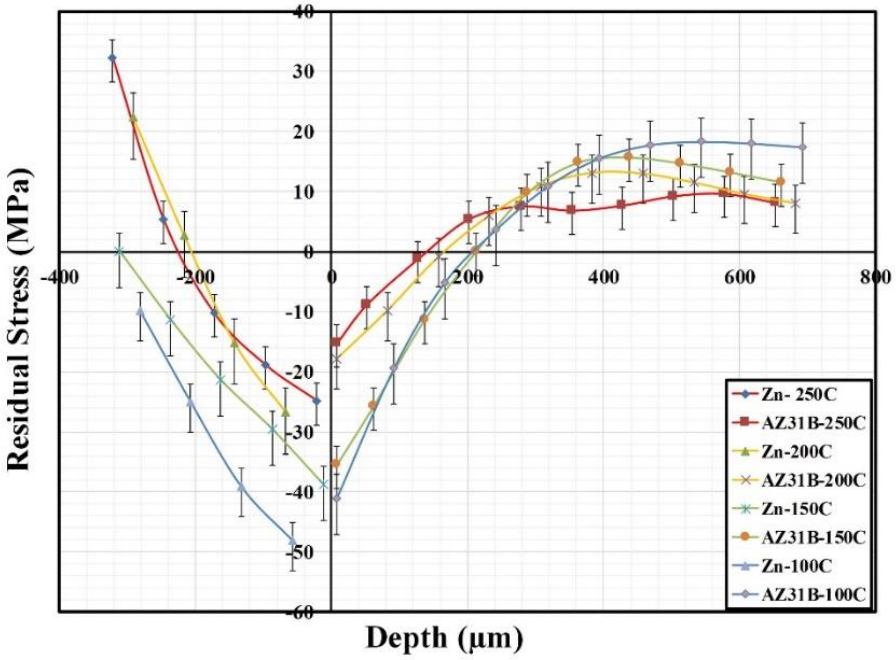

Fig. 5-13: Hole drilling residual stress measurements for Zn-AZ31B-H24 coated samples at; 100ºC, 150ºC, 200ºC, 250ºC carrier gas temperature.

5.4.6 Residual Stress Distribution in Multi-Layer Coating

Fig. 5-14a depicts the residual stress developed in Al7075 coated on magnesium AZ31B samples. Comparing the distribution of residual stress in Al7075/AZ31B and Zn/AZ31B samples reveals that coating aluminum alloy that has a lower thermal expansion coefficient than Mg alloy changes the residual stress of the interface from compressive to tensile stress. However, when pure zinc was coated at a low gas temperature of 100°C as an interlayer between Al alloy and Mg alloy, the three layers of Al alloy, Zn and Mg alloy up to about 400 µm experienced compressive residual stress in relation to the thermal expansion coefficient and an appropriately low level of thermal energy of the system (Fig. 5-14b). It is noted that the processing parameters for coating Al7075/Zn/AZ31B were like the coating parameters used for Al7075 on a Mg alloy substrate in Fig. 5-14a (see the Table 5-4). The same observation was reported when fiber Bragg grating sensors were embedded in Mg alloy samples and multiple layers of the coating materials Zn and Al7075 were deposited on the embedded samples [161]. Because the thermal expansion coefficient of the zinc coating is higher than Al7075 and AZ31B, zinc

coating should experience tensile residual stress, whereas compressive residual stress develops in Al7075 and AZ31B substrates with the coating process. However, the peening effect of Al7075 coating on the zinc coating overcame the thermal mismatch impact and induced significant compressive residual stress in the zinc coating as well as in the Al7075 and AZ31B.

Table 5-4: processing parameters for multi-layer coating.

Coating Treatment	Temperature (°C)	Pressure (MPa)	Feedrate (g/min)	Nozzle Speed (mm/s)
Al7075 on AZ31B	400	1.38	8	2
Zn on AZ31B	100	1.38	8	6.5
Al7075-Zn-AZ31B	400	1.38	8	2

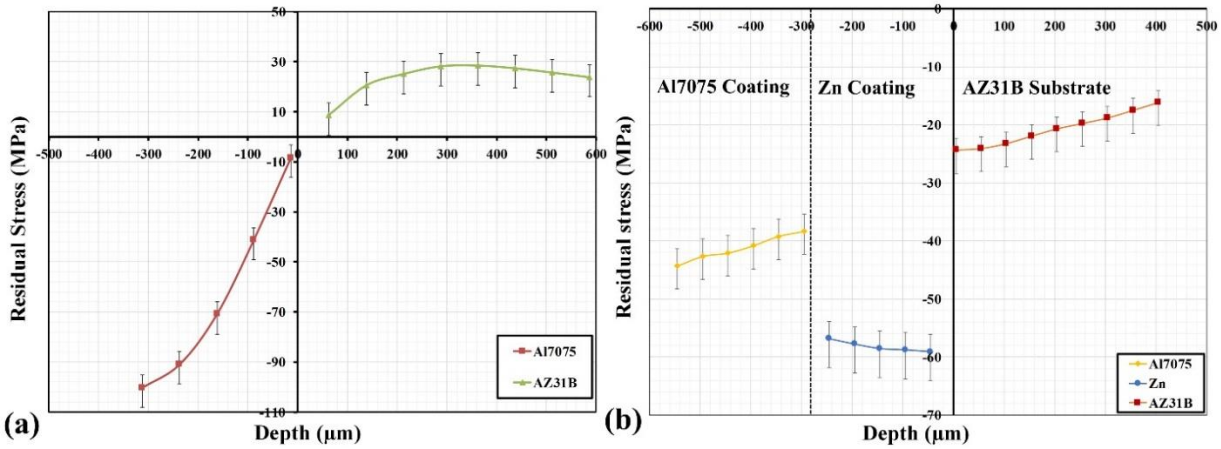

Fig. 5-14: Hole drilling residual stress measurements for a) Al7075-AZ31B; b) Multi-layer of Al7075-Zn-AZ31.

Fig. 5-15 demonstrates the hardness of different parts of the multi-layer coated samples. Based on these results, the Al7075 coating has the highest hardness, whereas the zinc has the lowest hardness in the coated samples, as expected. The interface between the zinc and magnesium AZ31B is harder than that between Al7075 and zinc. This high hardness of the zinc and magnesium interface can be attributed to the intermetallic phases that form in these regions during multilayer coating of Al7075/Zn/AZ31B.

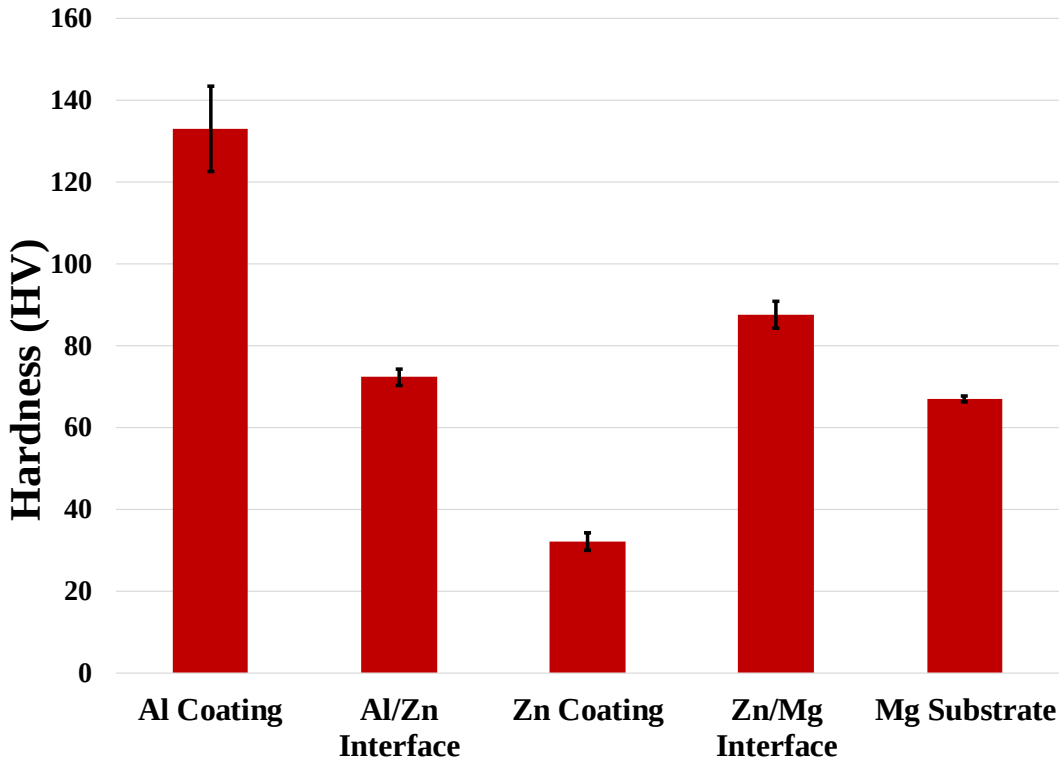

Fig. 5-15: Hardness changes of multi-layer coated samples.

5.5 Conclusion

In this research, the cold spray technology was utilized to deposit pure zinc on AZ31B-H24 magnesium sheet. The effect of processing parameters (carrier gas temperature and nozzle travel speed) on the physical/mechanical properties, and the microstructural changes in the coating and substrate have been investigated. Moreover, the possibility of using zinc as an interlayer between a magnesium substrate and Al7075 coating was evaluated in an effort to minimize the effect of thermal mismatch on residual stress development in coating and substrate. The following conclusions can be drawn from the results:

1) The coating thickness and surface roughness of the zinc coating were directly related to using a carrier gas temperature in the range of 100°C to 250°C at different nozzle speeds of 5 to 15 mm/s. Moreover, the surface roughness of the zinc coating was a function of the coating thickness; increasing the coating thickness leads to increased surface roughness.
2) Various intermetallic phases were formed at the interface of the magnesium AZ31B substrate and zinc coating under different coating conditions. We found a relation between the type of

intermetallic phase formation at the interface and the coating temperature index, which has been defined as the ratio of carrier gas temperature to the nozzle travel speed. When the coating temperature index is below 16°Cs/mm, a metastable phase of $Mg_{0.97}Zn_{0.03}$ can grow at the interface. However, increasing the coating temperature index leads to different zinc rich phases forming at the interface.

3) The intermetallic phases crystallized during the solidification of the melted magnesium and zinc mixture at the interface. Spherical droplets observed on the surface of the coated samples were evidence for melting at the interface.
4) The microhardness of the coating, interface and substrate was measured. The hardness of the interface was dependent on the intermetallic phase of the interface. In addition, the fractography of the fatigue samples reveals that the cracks were nucleated at the interface, propagated along the interface, and continued through the substrate perpendicular to the surface.
5) The cold spray processing parameters influenced the microstructure of the zinc coating. At low coating temperature, the microstructure of the coating consisted of lamellar grains creating an integrated dense coating. However, with an increase in carrier gas temperature, undeformed particles are more likely to be trapped in the coating, creating defects such as porosity in the coating.
6) The interaction between the peening and thermal effects affected the microstructure of AZ31B by developing grain refinement near the interface and various grain structures further away in response to the coating conditions.
7) Residual stress observations showed that the compressive residual stress was developed at the interface of the zinc coating and AZ31B substrate in the carrier gas temperature range of this study. However, increasing the gas temperature induced detrimental residual stress at the zinc coating surface due to thermal mismatch effect.
8) Depositing zinc coating as an interlayer between Al7075 coating and AZ31B magnesium substrate improves the formation of compressive residual stress in the three layers.

Chapter 6

Controlling Thermal Energy in Cold Spray Process to Maximize Induced Residual Stress and Improve Coating Quality of Magnesium Alloy

6.1 Abstract

This article investigates the effect of variables such as coating and substrate temperature on the physical and mechanical properties of cold spray coated materials Al7075/AZ31B. Parameters such as thermal mismatch, substrate temperature, feedrate, and nozzle speed as the effective stimuli have been optimized to improve feedback, including residual stresses induced in the coating and substrate, coating thickness, surface roughness, mechanical properties, and the density of coating. This study determines that running the cold spray coating under a low temperature condition in the coating and interface will result in high-quality deposition (e.g., high density, strong interface, and proper coating hardness). In addition, this condition will enhance the induced compressive residual stress in the coating and substrate; improving the long-term service performance of coated samples under the cyclic loading.

6.2 Introduction

Coating formation in solid-state is materialized through the promising cold gas spraying process whereby micron-size particles are accelerated to a high velocity (300-1200m/s) towards the substrate by a pressurized and relatively-low-temperature carrier gas through a de Laval nozzle [57][162]. Mechanical and metallurgical bonding with the substrate is produced by intensive plastic deformation and the localized heat generation upon impact resulting from the high kinetic energy of particles [59]. This solid-state bonding mechanism, which occurs as a result of the lower process temperature (much less than the particles' melting point) and the higher velocity of particles, makes it distinctive from other types of thermal spray coating processes. Continuous bombarding of the substrate with high velocity particles generates high local stress in the coating and in the vicinity of the interface and contributes to the development of a compressive residual stress in the coating and substrate. However, the induced residual stress in coated materials is influenced by thermal features, including, but not limited to, the temperature gradient, cooling rate and thermal mismatch in dissimilar coating and substrate materials [163][164]. These factors have the capability of relieving the stress or converting it from the expected compressive stress to tensile stress, depending on the coating and substrate materials

involved and the processing parameters. Since the residual stress might have destructive effects on the integrity of coating, adhesion strength, peeling and delamination, it should be carefully assessed in order to enhance the coating performance [163]. Additionally, the coated material with destructive residual stresses can be susceptible to early fatigue crack initiation, reducing the fatigue life of the coated part. It is, therefore, imperative to evaluate the residual stress of cold spray coated samples, both in the coating and substrate parts.

Only a limited number of experimental studies, numerical simulations and empirical approaches have explored the residual stress distribution developed by cold spraying. For instance, Matejicek et al. [165] used the micro-diffraction approach to measure the residual stress in cold-sprayed copper particles. Compressive residual stresses were observed in all coated samples, despite the use of different particle velocities. It was concluded that even though particle velocity significantly affects deposition efficiency, it has no effect on the residual stress development in cold-sprayed splats [165]. In a different study, Song et al.[166] employed numerical simulation and direct measurement technique (FIB-DIC) to measure and evaluate the micro-residual stress in a single particle. They identified a correlation between compressive residual stress at the interface with the impact velocity for Ti-6Al-4V particles [166]. Luzin et al. [62] measured the residual stress on Al/Cu coating and substrate materials using neutron diffraction method and then compared the results with those from Tsui and Clyne's progressive model [96]. They concluded that the residual stress was affected by plastic deformation, the kinetic parameters of the coating process, and the coating material properties, while the thermal effects were neglected [62]. In another study, Suhonen et al. investigated the role of different material combinations—Al, Cu, and Ti coatings and carbon steel, stainless steel, and aluminum substrate materials—on residual stress formation. Using a curvature-based approach to determine the deflection of the coated materials during coating deposition, they measured the residual stress. Based on their results, they observed that pre-treatment of a substrate (grit blasting) as well as the features of coating and substrate materials can shift the residual stress arising with cold spraying from compressive to neutral and tensile stresses [167]. Boruah et al. [168] evaluated the residual stresses induced by cold spraying of Ti-6Al-4V on a Ti-6Al-4V substrate. They employed neutron diffraction and contour methods to measure the residual stress through the depth, and investigated the effect of the number of cold spray layers, the thickness of the substrate and coating, and the track pattern on the magnitude and distribution of residual stress in the coated samples. The magnitudes of the residual stress were found to be dependent on the geometrical values, but all had the same trend. The maximum compressive residual stress was induced at the interface, while high tensile residual stress was formed near the free

surface of the Ti-64 coating and towards the bottom of the substrate[168]. They concluded that rising temperature and a fast cooling rate were the main factors affecting residual stress distribution rather than the peening effect [168]. However, Singh et al. [169] claimed that the compressive residual stress, induced in cold sprayed IN 718 coatings, is strongly influenced by peening effect even though the thickness of a coating can also affect the magnitude of the compressive residual stress [169]. In another study, Ghelichi et al. coated Al5052 substrates with pure Al and Al7075 to investigate the role of coating materials and deposition parameters on the fatigue life of the coated samples [89]. They showed that coating materials and processing parameters have strong effects on the fatigue strength improvement of the substrate materials, whereas compressive residual stress can be observed in all sets of experiments independent of the coating parameters and materials [89]. In a recent work, Marzbanrad et al. [146] coated Al7075 on AZ31B magnesium alloy sheets, and measured the residual stress of the coated samples under different deposition parameters. The strain evolution during the cold spray process was monitored with embedded fiber Bragg grating sensors. The results revealed that the development of compressive residual stress in Mg coated samples is strongly influenced by thermal energy as a predominant factor rather than the peening effect; hence, the residual stress could be restored as tensile or neutral stress in the temperature sensitive substrate materials[146]. Considering the possible harmful effects of tensile residual stress and the mechanical performance of the cold spray coated Mg substrates, optimizing the deposition parameters seems necessary to sustain the beneficial residual stress in coated parts.

In this research, AZ31B magnesium alloy, one of the lightest commercial metals with a high strength to weight ratio, is considered as a substrate material on which Al7075 aluminum powder is deposited. Because of the great interest in using Mg alloys for light weighting in the automotive and aerospace industries[54], even though AZ31B has shown promising fatigue strength [25][147], it would be valuable to more improve its fatigue performance. To do so, surface treatment with a cold spray process is carried out to induce beneficial residual stresses. The effect of thermal mismatch on the residual stress of the Al7075/AZ31B samples is simulated. The influence of substrate temperature on the final residual stress formation of the coated parts is also investigated. To measure the substrate temperature, a thermocouple is embedded into it to monitor the temperature during the different heat transfer scenarios. Then, the coating parameters are optimized, and the heat transfer is accelerated to evaluate the effectiveness of reducing the coating temperature in manipulating the induced stress in the substrate. Finally, the quality of coating, such as coating defects, coating thickness, surface roughness and hardness, is examined under the various processing parameters and conditions.

6.3 Experimental Procedure

6.3.1 Materials and methodology

In this study, 3.16 mm thick AZ31B-H24 magnesium alloy sheet was cut into several 30×50 mm rectangular coupons as the substrate samples. Heat treatment (260ºC/15min) [135] was carried out on the as-received samples based on the ASM-recommended procedure to ensure the identical mechanical state for all specimens. Before spraying, the substrate surface was polished using 1200 SiC grit paper and cleaned with ethanol. The feedstock powder used in the experiments was a spherical-shaped commercial Al7075 powder supplied by Centerline Ltd., Windsor, Canada, with an average value of 23μm measured by Retsch technology, Camsizer XT [146]. **Table** 6-1 lists the chemical compositions of AZ31B-H24 and Al7075 powder. A 300 μm diameter hole was drilled parallel to the surface for embedding a thermocouple where it could be accommodated 100 μm from the substrate surface in the middle of the coating zone. After the thermocouple was embedded in the hole, it was fixed in place with a thin layer of thermal epoxy 353ND EPO-TEK cured at 150°C [138]. The low-pressure cold spray system used for conducting these experiments was a commercial Supersonic Spray Technologies (SST) Series P Cold Spray System (Centerline, Windsor, Canada). The propellant gas was nitrogen (N_2) streamed at the low pressure of 1.38 MPa.

Table 6-2 lists the processing parameters employed for depositing Al7075 on the Mg alloy substrates in order to improve the residual stress distribution in the coating and substrates. The coating parameters, which were kept constant for all experiments except for the feed rate and nozzle speed. The main characteristics of cold spray coating, including mechanical and thermal properties, are known to intensely affect the residual stress. The mechanical effect introduced by peening and thermal effect are divided into thermal mismatch and coating temperature, including carrier gas temperature and deformation temperature. The role of thermal mismatch has been studied by a simple simulation to assess the influence of the material properties and coating geometries. However, the effect of coating temperature and peening effect can be evaluated by changing the most effective processing parameters such as feedrate and nozzle speed. Based on these parameters, several experiments have been designed to study the residual stress formation in the coating and substrate. Then in two extreme situations, where the tensile and compressive residual stress can be developed in the sample (which are named “tensile sample” and “compressive sample”), the quality of the coating and characteristics of the deposited material including surface roughness and hardness are investigated.

Table 6-1: Chemical composition of AZ31B-H24 magnesium alloy [170] **and Al7075 coating.**

Composition (Weight %)	Aluminum (Al)	Zinc (Zn)	Manganese (Mn)	Iron (Fe)	Nickel (Ni)	Silicon (Si)	Copper (Cu)	Chromium (Cr)	Magnesium (Mg)	Other Elements
AZ31B-H24	2.99	0.95	0.2	0.005	-	0.05	0.05	-	Bal.	-
Al7075	90	5.20	-	0.35	0.005	-	1.55	0.25	2.35	0.30

Table 6-2: Cold spray coating parameters

Carrier Gas	Gas Temperature	Gas Pressure	Powder Feed Rate	Nozzle Speed	Step Over	Stand-off Distance	Nozzle Type	Nozzle Length	Nozzle Orifice Diameter	Nozzle Exit Diameter
N_2	400 °C	1.38 MPa	25% (8gr/min), 50% (16gr/min)	2-5-10-20 mm/s	1.2 mm	12 mm	De Laval UltiLife TM	120 mm	2 mm	6.3 mm

6.3.2 Residual stress measurement

A hole-drilling machine (Sint Technology, Restan MTS-3000) was used to measure the relaxation strain through the depth of coated samples. For this, conventional Fras-2 three-element strain gauge rosettes were installed on the coated surface. Before installing the strain gauges, the coated surface was polished to reduce surface roughness and increase the bonding strength between the strain gauges and the coating surface. This surface treatment reduces the thickness of coating by at most 200 µm. During drilling, strain relief was measured incrementally through the strain gauge rosettes in three different directions. Then, the ASTM E837-13 [108] (non-uniform stress field) method with the Tikhonov regularization algorithm was employed to calculate the residual stress up to 1mm through the depth of the coated structure.

6.3.3 Surface roughness and hardness measurements

Surface roughness (Sa) for all coated samples was measured using a Keyence VK-X250 confocal laser microscope manufactured by Keyence Corporation, Osaka, Japan. The scanning areas for the surfaces of all coated samples had the same dimensions of 4×6mm. The coating's thickness was measured using the Keyence microscope with 0.5µm precision. In addition, Vickers micro hardness testing was performed on cross-sectioned of the various coated samples with different processing parameters by using Clemex Technologies (Inc, Longueuil, Canada). Several indentations with a 50gr load were

applied on the polished surface in three different regions of the samples: the coating, interface and substrate.

6.3.4 Tomography of the coating

A non-destructive method, X-ray computerized micro-scale tomography (CT) scanning, was performed using a ZEISS Xradia 520 Versa 3D X-ray microscope (ZEISS, Oberkochen, Germany) to study and compare the integrity of the coating when different processing parameters were used [171]. A volume with dimensions of 5.6×4.7×3.26 mm was specified for the scanning to identify the distribution of pores/defects close to the surface of the coated samples. A total of 2001 2D projections were recorded, with a voxel size of 3.5 µm for each sample. Table **6-3** lists the parameters used for the CT scan. After scanning, for image processing and analysis of the pores sizes and distributions, 2D projections were recreated using Dragonfly Pro v3.1 software (Object Research Systems (ORS), Montreal, Canada).

Table 6-3: CT scanning parameters

Voxel size (µm)	Source-to-detector distance (mm)	Field of view (µm)	Voltage (kV)	Power (W)	Source filter Exposure time (s)	Optical magnification	Camera binning	Number of projections
3.5	35.064	3472.694	80	7	1	4.0021	2	2001

6.3.5 Numerical simulation

Thermal stress development in the cold spray coated sample was simulated by a two-dimensional numerical isotropic and linear elastic finite element models coupled with a heat transfer model using COMSOL Multiphysics software. The deformation was assumed to be plain strain. The coefficients of thermal expansions are assumed to be constant at different temperatures. The temperature of the plates is considered to be homogenous. To avoid any external stress on the plates, only the bottom left corner of the simulation domain in each step was fixed. In each step, the temperature was adjusted to its determined temperature. In this simulation, the system was meshed by using square adoptive meshing of COMSOL Multiphysics. This model consists of three layers: 1) Al7075 coating as a top layer with variable thicknesses between 100 to 1000 µm and temperatures in the range of 200-600°C, and the substrate was divided into two layers 2) a 220 µm thick middle layer, and 3) 3000 µm thick bottom layer as a substrate. The material of the middle layer and substrate was AZ31B, and it was assumed that the Mg and aluminum alloys did not mix during the coating. The middle layer was defined as a thin layer that would warm up very fast during the deposition of the coating material. The initial lengths of all three layers were equal (30 mm) and the initial temperature of the middle layer and substrate was

set at 20°C. However, the temperature of the top layer was changed, which will be explained for each case in the result section. In first part of the simulation, the top and the middle layers were considered for modeling. In this situation, the length of the top layer and the middle layer were equal. The coating was set at a high temperature, while the middle layer was cold. After running the simulation, when the middle layer and substrate reached equilibrium, the residual stress was developed in these two layers due to the thermal mismatch between Mg and aluminum alloys. Then, the bottom layer (substrate) was added to the model. After adding the substrate, the residual stress in the three-layer system was calculated when the system was cooled to room temperature.

6.4 Results and discussion

6.4.1 Simulation results

The role of thermal stress on the dissimilar metals joined in the Aluminum/Magnesium sample was simulated by finite element method. This model only demonstrated the effect of temperature evolution during cooling of the coated part, while the stress induced by peening effect was neglected. The primary results were extracted to reveal the impact of coating thickness on thermal stress distribution in the coating and substrate. For this, the maximum temperature was kept at 400°C for the top layer (coating) and then reduced within the middle layer to 190°C and reduced to room temperature of 20°C for the substrate. Coating-layer thicknesses ranging from 100 μm to 500 μm were selected for this thermomechanical simulation. Fig. 6-1 a shows the thermal stress distribution of the coated samples at the various coating thicknesses. Obvious discrepancies appear between the thermal stress of the coating and substrate, especially at the interface region. This finding can be attributed to the thermal expansion coefficient (CTE) differences of aluminum and Mg alloys. The CTE of aluminum alloy is less than that of Mg; hence, the thermal strain of aluminum alloy would be less than Mg alloy's when they experience similar temperature changes. Since they are bonded together, both are subjected to stress from each other depending on their mechanical properties and thickness. Because aluminum alloy coating experiences less dimensional change than Mg alloy does, the coating exerts tensile stress on the substrate and the substrate imposes compressive stress on the coating during cooling. Fig. 6-1a shows the magnitude of residual stress at the interface, revealing considerable changes from negative to positive ranges. With an increase in the thickness of the deposited layer, the slope of the residual stress curve in coating area as well as the absolute value of thermal stress on the coating-free surface decrease, as a result of the bending stress distribution in the composite beam and thermal stress (see Fig. 6-1c).

However, the thermal stress of the substrate surface near the interface underwent no significant changes when the coating thickness was changed (Fig. 6-1a).

Since coating tends to be more affected by thickness changes, its thermal stress of coated parts was investigated at different coating temperatures ranging from 200-600°C. Fig. 6-1b shows the distribution of the stress through the coating thickness when the maximum coating temperature is increased to the specified temperatures. Thermal residual stress distribution in the coating is changed from a negative value to a positive one, with increasing the coating temperature or increasing the thickness at the constant temperature (see Fig. 6-1b). Therefore, the coating thickness and temperature have the critical role in inducing thermal stress in the substrate and coated parts. On the other hand, a minimum carrier gas temperature is required to feed the nozzle to accelerate the particles to supersonic velocity, beyond the critical velocity, and create bonding with the substrate. However, increasing the gas velocity decreases the temperature and pressure of the carrier gas in the nozzle, resulting in decreased particles temperature. Nevertheless, the temperature of particles upon impact, and the deformation temperature, which is induced in a few nanoseconds, can still affect the residual stress of the substrate and overcome the peening effect.

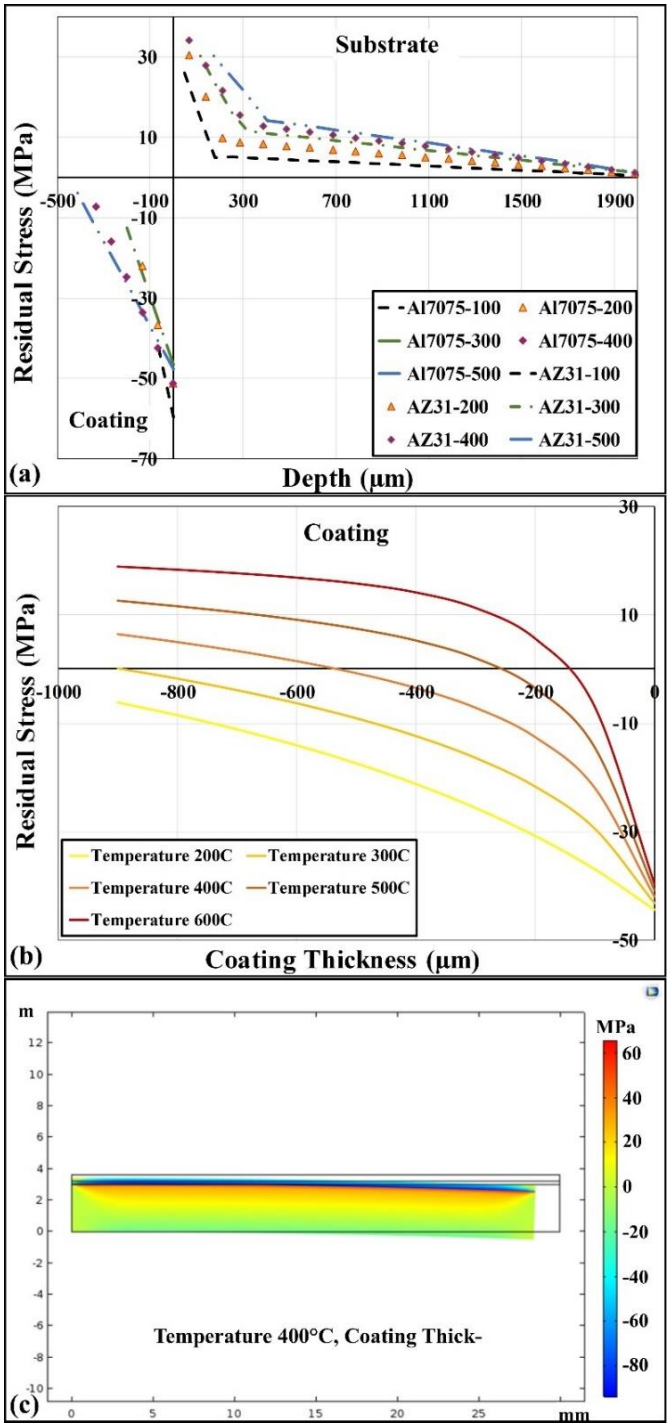

Fig. 6-1: a) Thermal stress distribution in coating with different thicknesses of 100-500 µm, and the substrate at the constant temperature of 400°C; b) The stress distribution of the coated aluminum at different coating temperatures; c) An example of induced residual stress in the simulated part at room temperature.

6.4.2 Substrate temperature measurements

For better evaluation of the substrate temperature, temperature changes were monitored by the embedded thermocouple during the process (see Fig. 6-2a). The coating process was conducted for several samples in two different situations: with and without spraying powder (Fig. 6-2b). For all experiments, the carrier gas temperature and pressure were set at 400°C and 1.38MPa, respectively. Furthermore, different setups-- with an insulated fixture and a fast cooling rate fixture (an aluminum plate) underneath the Mg substrate--were designed to study the effect of heat transfer during the coating process. First, the substrates were placed on the thermally insulated fixture and the process was performed with and without powder deposition. The embedded thermocouple enabled recording of the substrate's temperature 100 μm below the surface. It is well known that the basis of existing theories of cold-spray bonding mechanisms is the local softening of particles and substrates due to the local heat induced by impact. However, because of the embedded thermocouple position, the measured temperature was far from the deformation temperature range, which is generated at a few hundreds of nanometers of the interface (Chapter 7). Based on this observation and using the insulated fixture, the temperature was elevated to 190°C when the nozzle was exactly over the thermocouple. Fig. 6-2c demonstrates that no significant changes occurred between the temperature changes with and without depositing powder. These experiments were repeated several times, and the same results were observed. However, when an aluminum plate, with much higher heat transfer than the former case, was situated under the substrate, there was about a 10°C discrepancy between the two coating procedures (spraying carrier gas with and without powder). This observation can be explained by considering the heat transfer difference in the two cases. Using the insulated substrate, the temperature change between the hot top surface and cold bottom side of the substrate is less than in the other case. Therefore, the thermocouple recorded less difference where it was accommodated (below the substrate surface). Furthermore, in the aluminum fixture, the maximum temperature of the substrate reached 160°C for the coating process, whereas this temperature was about 30°C less than the maximum temperature of the substrate with the insulated fixture. In addition, the cooling rate of the substrate with the aluminum fixture was considerably faster than that with the insulated fixture (see Fig. 6-2c). The most obvious finding to emerge from the temperature monitoring study is that the temperature of the substrate dropped by about 16% when the aluminum fixture was replaced, with relatively good thermal conductivity.

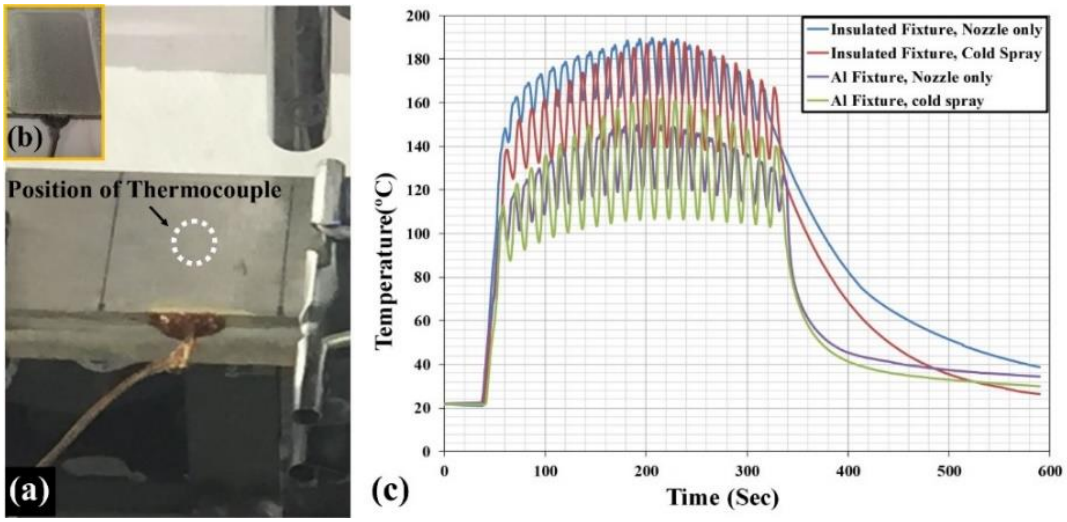

Fig. 6-2: The temperature measurements of fixed substrates on the aluminum and insulated during cold spray process.

6.4.3 Residual stress measurements

To examine the effect of this temperature reduction on the residual stress formation in the cold spray coated samples, various experiments were carried out. The processing parameters used in all experiments are listed in Table 6-2. Residual stress measurements were conducted using the hole-drilling method on the stress relieved Mg alloy samples to disclose the residual stress resulting from peening\hammering and thermal effects. Fig. 6-3a shows the stress profiles of the coated samples under two different heat transfer boundary conditions--a) fast cooling at the boundary and b) insulated boundary condition--at the constant and relatively low nozzle speed of 2mm/s. These measurements illustrate that no substantial difference exists in the substrate residual stress, especially close to the interface. In contrast, the dissimilar trends of stress distribution in coated parts are greatly affected by the substrate fixtures (Fig. 6-3a). A considerable compressive residual stress value can be observed for the coated surfaces of samples placed on the Al fixture compared with the other samples that were on the insulated fixture during the process. Moreover, the coating thickness of Al fixture samples is about 30% less than that of the insulated fixture samples, despite the same processing parameters being used (see Fig. 6-3a). This amount of temperature reduction due to heat conduction through the substrate influences only the stress development in the coated part. However, for high temperature sensitive materials like Mg, a greater temperature decrease is required to eliminate the impact of thermal energy on the properties of the sample. Since decreasing the carrier gas temperature from the specified value

of 400°C leads to reduced velocity of the Al7075 particles with no deposition, or poor coating quality; hence, reduction of the exposure time by increasing the nozzle speed was considered. Fig. 6-3b depicts the stress relaxation measurements for the coated samples with the nozzle speed of 5mm/s for two different fixtures. The results demonstrate that increasing the nozzle travelling speed during sample coating greatly improved the beneficial residual stress of the coating surface for the coated samples with the insulated fixture; however, the thermal energy was sufficient to release the residual stress of the Mg alloy substrates (Fig. 6-3b). For the samples that were situated on the Al plate fixture treated with 5mm/s nozzle speed, the exposure time was not adequate to relieve the peening stress induced in the substrate; therefore, significant compressive residual stress was developed in the Mg substrate at the interface as well as the coated parts.

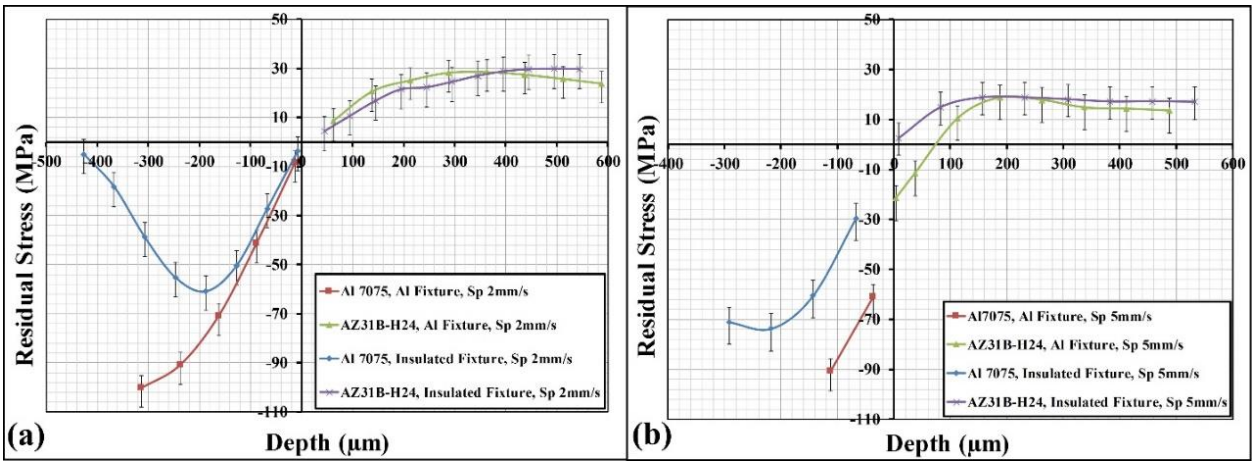

Fig. 6-3: Residual stress distributions for cold spray coated samples with different fixtures for placing the substrates, when the nozzle speed is a) 2mm/s; and b) 5mm/s.

For the rest of the study, the Al plate was considered as a fixture under the Mg alloy substrates during the coating process to decrease the substrate temperature. Then, the effect of reducing the exposure time on the residual stress distribution in coating and substrate was studied for various nozzle speeds from 2-20mm/s, with two different feedrates of 25% (8gr/min) and 50% (16gr/min). Fig. 6-4a and Fig. 6-4b comparatively illustrate the residual stress distributions for different nozzle velocities at a constant feedrate low and high of 25% and 50%, respectively. However, the two combinations (feedrate=25% and nozzle speed=20mm/s) and (feedrate=50% and nozzle speed=2mm/s) were not considered, because in the former case the coating thickness was too low to be utilized for the residual stress measurements and in the latter case the deposited material was very thick and the quality of coating was not good

enough to be considered for residual stress measurements. Decreasing the coating thickness by increasing the nozzle speed inherently leads to reducing the number of particles impacting the surface. This trend can be observed in the results reported in Fig. 6-4a and Fig. 6-4b. By increasing the nozzle speed and, as a consequence, reducing the thermal input to the system, the compressive residual stress was enhanced in the coating as well as in the substrate materials at the interface. Moreover, the compressive residuals stress on the coating surface decreases in response to an increase of the coating thickness and decrease of the nozzle speed. This trend is observable for all cases except for the feedrate=50% and nozzle speed=20mm/s. In this case, the peening was less effective because of the smaller number of impacting particles despite the higher feedrate. Therefore, the nozzle speed needs tight control to prevent negative effects on peening residual stress. In addition, comparing the effects of two feedrates with the same nozzle speed, increasing the feedrate means increasing the number of particles with effective impact, thereby increasing the beneficial residual stress due to peening effect.

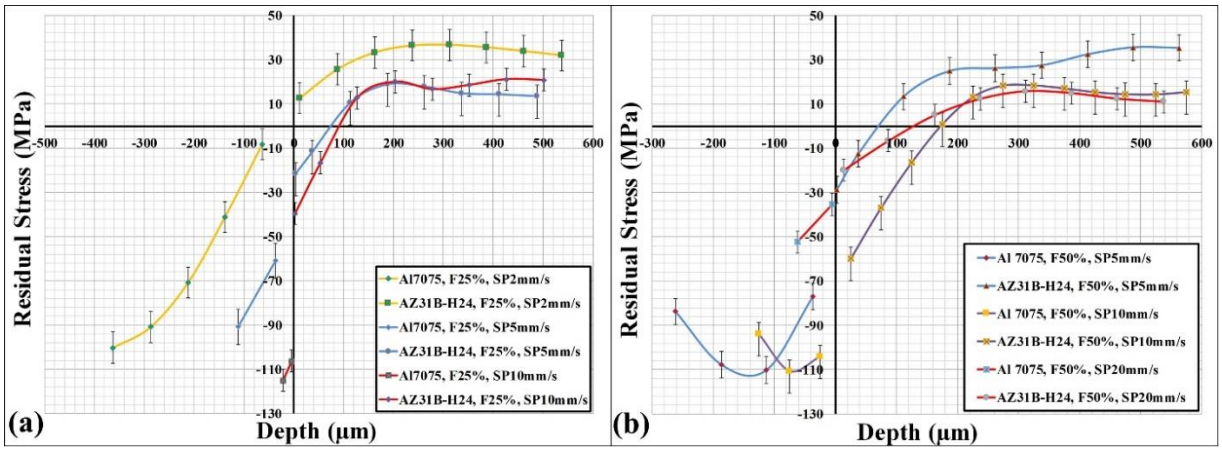

Fig. 6-4: Residual stress distributions for cold spray coated samples with different nozzle speed and feed rate; a) 25% (8gr/min); and b) 50% (16gr/min).

To study the effect of temperature gradient in multi-pass deposition on the residual stress induced in Mg and coated surfaces, the cold spray coating was performed for different samples at the constant processing parameters of feedrate=50%, and nozzle speed= 20mm/s. Fig. 6-5 shows through-the-depth residual stress distribution for different 1, 3, 5 passes. The residual stress was developed in a higher compressive amount at the substrate interface by increasing the number of passes, as a result of increasing number of impacts and improving the peening/hammering effect. However, the effect of thermal mismatching was predominant and reduced the compressive residual stress at the coating

surface and even turned to the tensile for the 5 number of pass (Fig. 6-5). Therefore, even though increasing the number of passes promotes compressive residual stress at the interface,it can induce destructive tensile residual stress in the coated surface. The results confirm the simulation observations, especially for the coating surface with the high thickness, where the peening effect was influenced by the rising temperature and fast cooling for dissimilar materials, highlighting thermal mismatch effect.

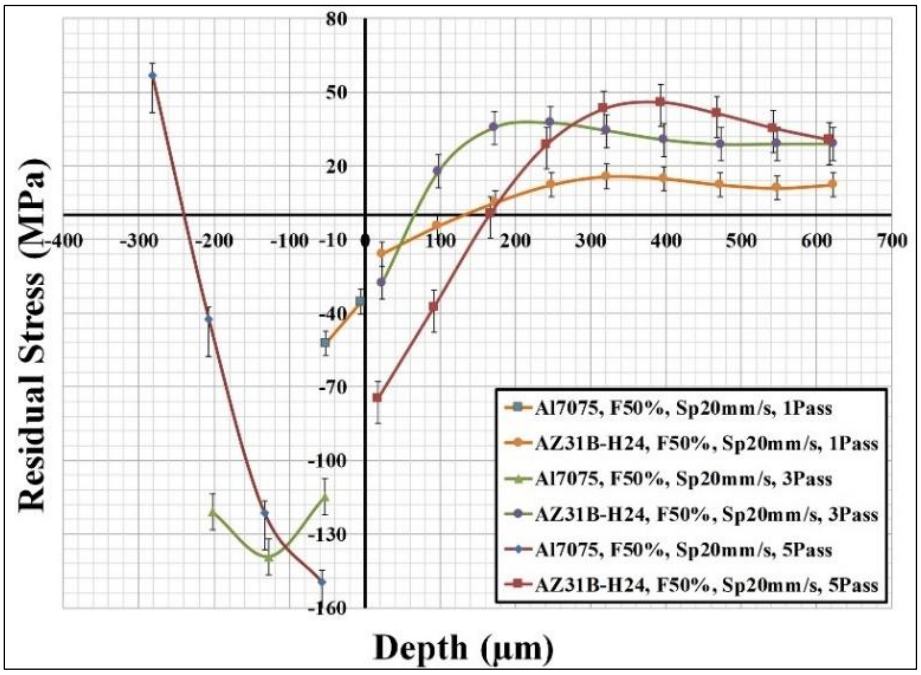

Fig. 6-5: Residual stress distributions of the cold spray coated samples with different numbers of passes.

6.4.4 Surface morphology

To evaluate the effect of a coating's thickness on its surface roughness, coating thickness and surface roughness were measured for several coated samples, each treated with different process variables. Fig. 6-6a depicts the coating thickness and surface roughness for the samples coated with low and high feedrates of 25% and 50% and low and high nozzle speeds of 5mm/s and 10mm/s. The results show that the surface roughness increased by 24% when the coating thickness was doubled. The same trend is also observed in -multi-pass experiments (Fig. 6-6b). Fig. 6-7 demonstrates the high-resolution topography images of two different coating surfaces with the minimum and maximum thicknesses among these experiments. In these figures, the maximum level of the peak for the samples with the lowest and highest surface roughness are shown. The minimum surface roughness of about 10.9 µm is

obtained for the thinnest coating, and the maximum roughness of 22.7 µm belonged to the thickest coating in these series of experiments. Increasing surface roughness by increasing the coating thickness has been reported in the literature for cold sprayed Ti6Al4V coatings on Ti6Al4V substrates [172]. To explain this observation, the authors claimed that increasing the thickness raised the accumulation of heat generation during coating formation at the coating surface; hence, low speed particles with a less than critical velocity have a chance to be partially deformed and attached to the surface as a result of the increased surface roughness. However, Fig. 6-7a and Fig. 6-7b show that the surfaces of both samples are covered with shallow indents with raised edges instead of hemispherical bumps, indicating partially deformed particles on the surface. This surface feature could represent the fingerprint of particles that impact the surface, are deformed and joined to the coating. These observations can be explained by considering the heat generation during coating deposition. Thicker coating generates higher temperature per unit time and as a result, the particles are exposed to higher temperatures upon impact. Therefore, more softening, more deformation, and bigger indentations occur in the thicker coating materials during impact, as can be seen in Fig. 6-7b.

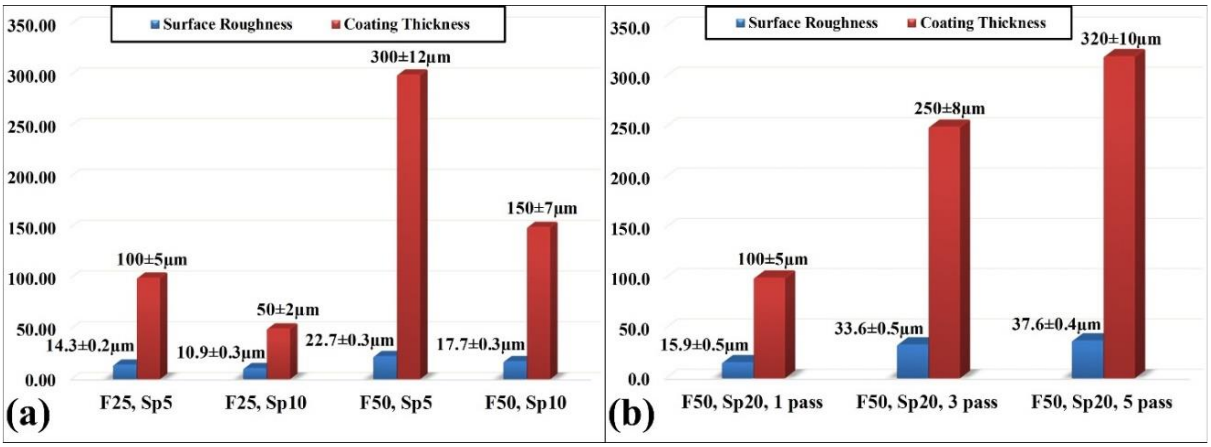

Fig. 6-6: comparison between the coating thickness and the surface roughness of cold spray coated samples; a) for different feedrates and nozzle speeds; b) for different numbers of passes.

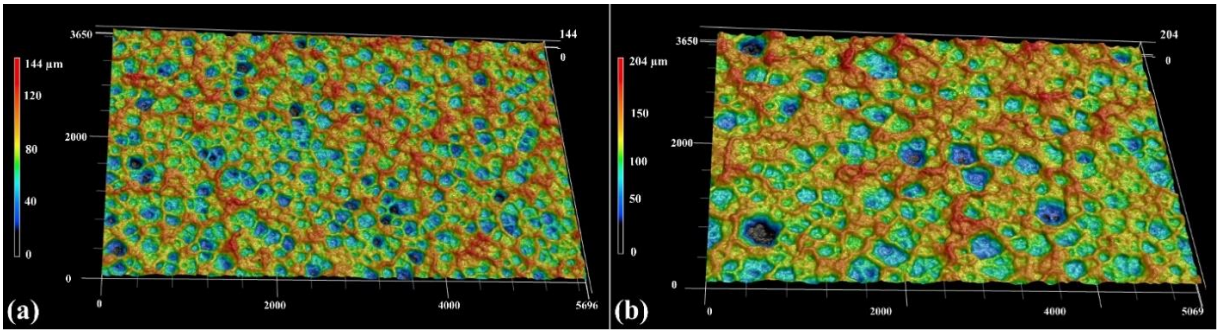

Fig. 6-7: Surface roughness images of coated samples with; a) F=25% and Sp=10mm/s; b) F=50% and Sp=5mm/s (All dimensions are in µm).

6.4.5 Computerized tomography (CT) analysis

The computerized tomography (CT) is utilized to investigate the integrity of the deposited material in the samples with tensile and compressive residual stress. The processing parameters for preparing the samples in these two extremes are listed in Table 6-4. The coating parameters to achieve the maximum compressive residual stress were assigned based on the minimum value of the surface roughness.

Table 6-4: Processing parameters for inducing tensile and compressive residual stress in coated samples

Coated Samples	Gas Temperature	Gas Pressure	feedrate	Nozzle Speed	Fixture
Tensile	400°C	1.38 MPa	25% (8gr/min)	2mm/s	Insulated
Compressive	400°C	1.38 MPa	25% (8gr/min)	10mm/s	Fast cooling rate

The CT scan results presented in Fig. 6-8 uncover the quality of coating for the tensile and compressive samples. Based on the presented data, the pore density in the tensile sample was much greater than that in the compressive sample, and the pores were uniformly distributed throughout the cross section of the sample (Fig. 6-8b). Fig. 6-9 depicts the pores size distribution of the tensile and compressive samples, and demonstrates that not only was the number of the pores in the tensile sample drastically more than that in the compressive sample, but also that the average of the pore sizes were greater in the former than in the latter. To address the exact densities of the coated samples, the equivalent solid fraction was calculated based on the pore and part voxels, which are listed in Table **6-5**. It is concluded that 94% reduction of the porosity in compressive samples, representing the coating quality of the compressive samples was much better than that of the tensile ones. This observation contradicts results reported in the literature claiming that increasing the temperature of the substrate improves the bond strength and

the quality of coating [173]. It is obvious that only a portion of the particles is accelerated to a specific velocity in the gas stream sufficient for successful impact and bonding, depending on their geometry and size. However, there is a chance for the other particles to sit on the surface, even partially deformed, and become trapped between the other particles, especially by the material jetting of their neighbors. Because of the trapped particles' geometry, the area around them is susceptible for pore formation. Moreover, increasing the temperature of the substrate provides more surface ductility, which promotes more material jetting and hence trapping of the low kinetic energy of particles during unsuccessful impact. When the substrate is cold, it has higher yield strength; hence the substrate stores more elastic energy, which is released by springing back effect, shooting the particle out. The strong spring back breaks the weak bond between the trapped particles and the surface, thus releasing the particles. On the other hand, the coating efficiency is less for the cold substrate. In this case, in comparison with the higher temperature substrate at the constant feedrate, fewer particles consume their kinetic energy for deformation toward deposition. The rest of the particles have an elastic impact and so help increase the density of the coating, and close the pores by hammering effect. Combinations of these effects work to increase the coating density when the substrate is kept cold.

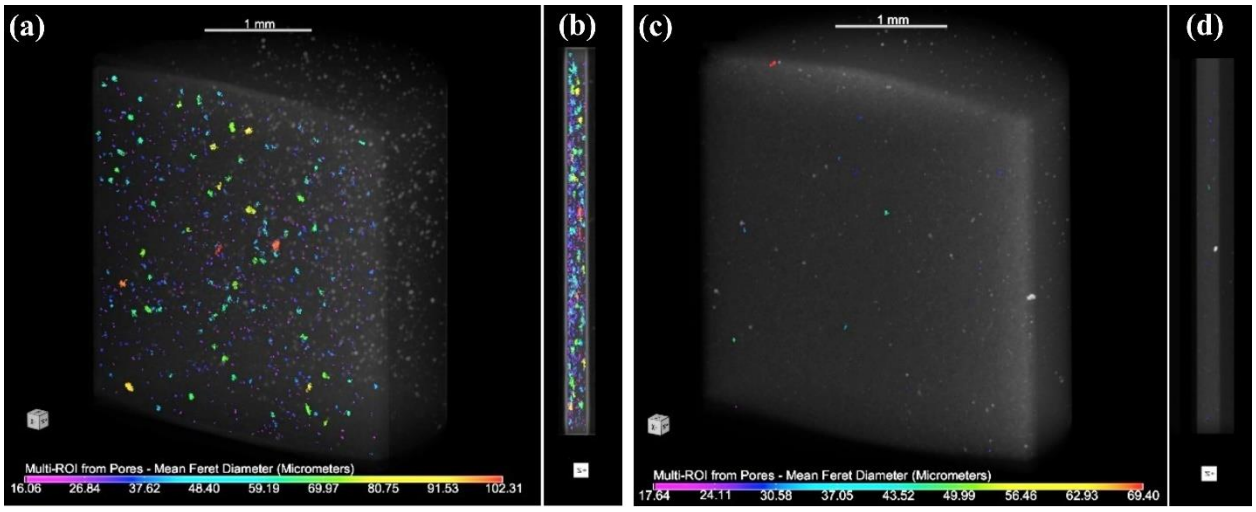

Fig. 6-8: Micro-scale tomography (CT) scanning: a) 3D image of the tensile coated sample; b) distribution of the pores in the thickness of the tensile sample; c) 3D image of the compressive sample; d) distribution of the pores in the thickness of the compressive sample.

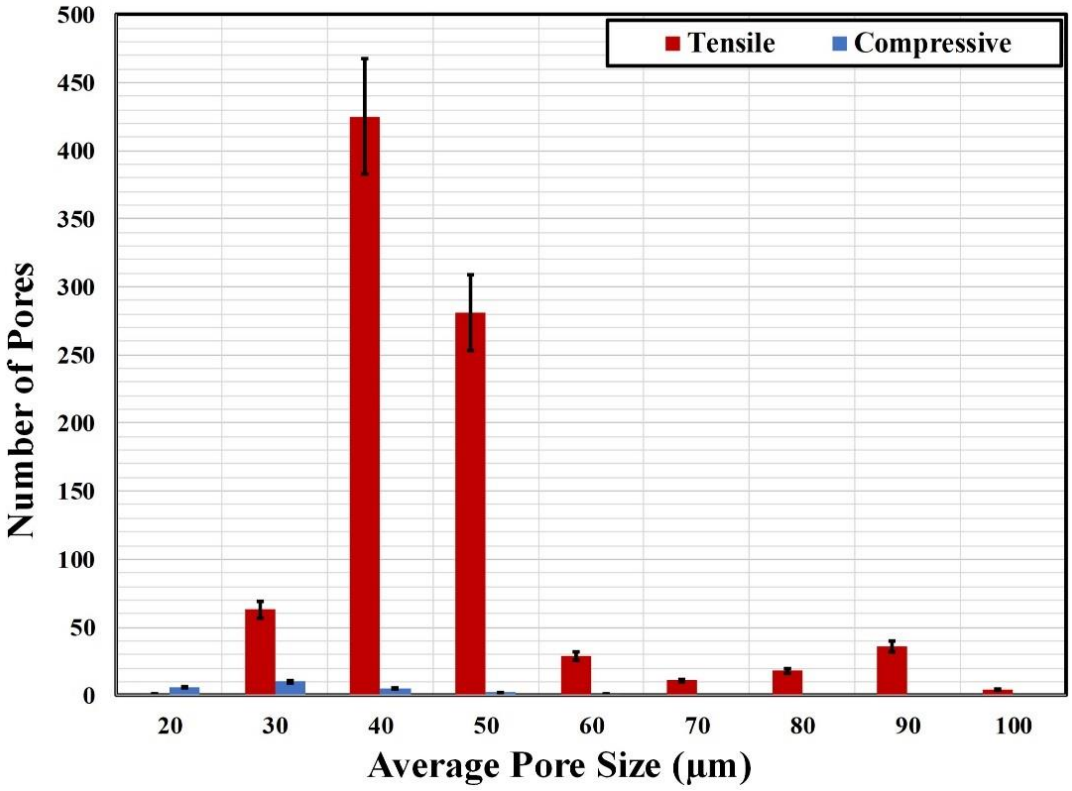

Fig. 6-9: Pores size population in the coating of the tensile and compressive samples.

Table 6-5: The density of coated samples

Coated Samples	Pore Voxels	Part Voxels	Equivalent Solid Fraction
Tensile	235,574	43,591,534	**99.4596%**
Compressive	14,997	44,609,663	**99.9664%**

6.4.6 Hardness analysis

Microhardness tests were conducted for the two types of coated samples: tensile and compressive samples. Fig. 6-10 shows that the microhardness of all AZ31B magnesium substrates is unchanged in the two samples and stays around 70 HV. However, the hardness of coating and interface differed. The compressive samples show an interface microhardness that is about 53% greater and a coating microhardness that is 13% greater than those of the tensile samples. This may be due to two reasons: 1) compressive residual stress at the interface region and in the coating of compressive samples

increases the hardness; 2) the compressive samples were kept cool, making the material less ductile and more work-hardening. Therefore, peening effect is more effective in hardening the substrate and coating.

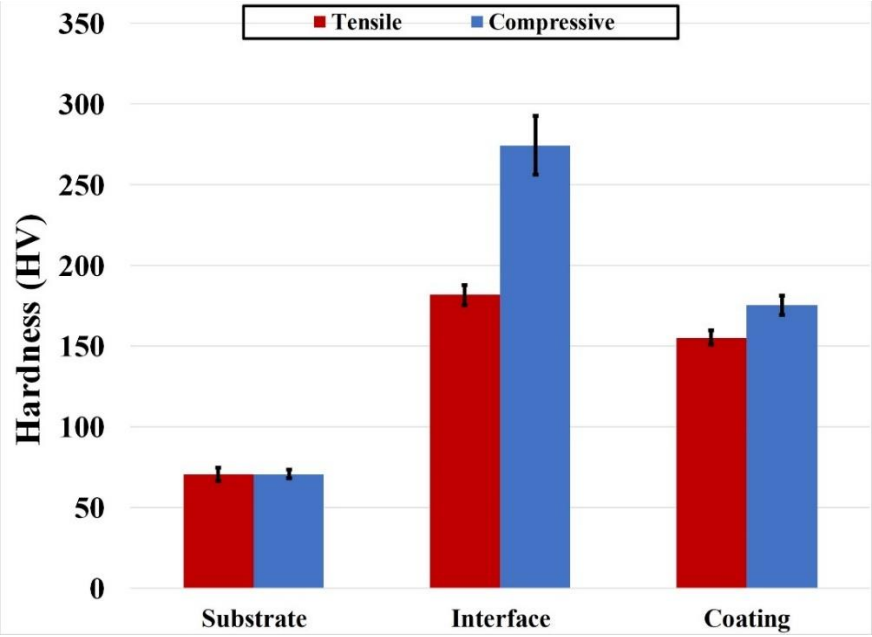

Fig. 6-10: Microhardness of the coated samples in three different regions (substrate, interface, and coating) for compressive residual stress and the samples with tensile residual stress at the substrate interface.

6.5 Conclusions

The effect of substrate temperature and exposure time on residual stress formation in the coated Al7075 on AZ31B was investigated. Tensile and compressive residual stress were induced in the substrate near the interface, and at the coating surface depending on the coating conditions and substrate temperature. The physical and mechanical properties and the quality of coating were influenced by the coating parameters corresponding to these two types of residual stress. The results support the following conclusions:

1) Reducing the coating thermal energy by decreasing the exposure time and reducing the substrate temperature by using a heat sink to cool the substrate during coating could significantly influence the state of residual stress in the coated samples. For this, a nozzle speed

of 10 mm/s was selected as an optimum velocity for inducing the compressive residual stress in the Mg substrate at the vicinity of the interface as well as in the coating surface.

2) By decreasing the nozzle speed to 5 or 2 mm/s and raising the substrate temperature by employing an insulated fixture, thermal effect can overcome the peening effect, consequently inducing a detrimental residual stress in the Mg substrate.
3) At a constant nozzle speed, increasing the feedrate (for example from 25% to 50%) can manipulate the peening effect to impose beneficial compressive residual stresses in the coated samples. However, increasing the powder feedrate had less impact on increasing the coating temperature compared to the nozzle speed.
4) The thermal mismatch between the Al7075 coating and AZ31B substrate had a negative impact on the Mg substrate because of the tensile residual stress induced in the substrate. Reducing the coating temperature is essential to minimizing the detrimental effects of thermal mismatch. In addition, based on the results of this research, reducing the coating temperature and using a heat sink to cool the substrate during coating decreases coating surface roughness, which in turn reduces the risk of fatigue crack initiation.
5) A successful strategy for increasing coating thickness and maintaining compressive residual stresses in the substrate involves increasing of the number of passes at a high nozzle speed. This approach maintains the compressive residual stress and even increases it due to the extra hammering effect. Similarly, increasing the powder feedrate and maintaining a constant nozzle speed leads to a higher coating thickness with the compressive residual stress.
6) The surface roughness was directly related to the coating thickness of the deposited layer. The powder impact indented the surface and produced the raised edges that the surface topography revealed to be the origin of surface roughness. This observation was justified by the coating and substrate temperature. The greater coating thickness increased the coating temperature, making the coated material softer, which promotes bigger indentations and higher impact edges.
7) The coating quality and the coating density of the compressive samples were higher than those of the tensile samples. Moreover, the size of pores in the compressive samples was smaller than of those in the tensile samples.
8) Forming the coating at a lower coating temperature increases the hardness of the interface and coating.

Chapter 7

Role of Coating Temperature on the Microstructure of Magnesium Alloy Coated by Cold Gas Spray Technique

7.1 Abstract

A promising solid-state coating mechanism based on cold spray technique provides highly advantageous conditions on thermal-sensitive magnesium alloys. A defect-free coating of a high strength material, Al7075 aluminium alloy, on a magnesium alloy substrate, creates the potential to boost the substrate's mechanical and metallurgical properties. However, the temperature of the cold spray process is enough high to change the residual stress and microstructure of magnesium alloys. These changes are resulted from the accumulation of thermal energy from particle impacts accompanied by a carrier gas, consequently tensile stress induces in coating and substrate. Therefore, by controlling the heat input, the residual stress in the substrate can be tailored to desirable pattern. To investigate the effect of coating temperature on the microstructure of magnesium alloy and the interfaces of coated samples, SEM, TEM and phase identification were conducted on samples with high- and-low temperature inputs. No intermetallic phase was detected at the interface under either high or low temperatures. Moreover, the interface of the Al7075 coating and magnesium alloy substrate under both temperature conditions consists of a narrow-band layer with very fine grains, followed by columnar grains of magnesium that have grown perpendicular to the interface. At higher temperatures, this layer became wider. In addition, the microstructure of the substrate was affected by coating temperature, leading to stress relief, dynamic recrystallization and even dynamic grain growth of magnesium under high temperature. In contrast, reducing the heat input and heat generation by using coating parameters minimizes microstructural changes in the substrate during coating.

7.2 Introduction

Motivated by environmental concerns, there is an increasing trend towards lighter-weight mobile structures in both the automotive and aerospace industries [174]. The lightest commercially available structural metals, magnesium and its alloys, are valued for their high strength-to-weight ratio and low energy consumption during manufacturing processes, and are thus of interest to researchers designing lighter vehicles [22]. However, the application of magnesium and its alloys is mainly restricted to non-

load bearing components. Weaknesses such as the poor corrosion resistance and low fatigue strength of magnesium alloys are obstacles in growing market and are a major barrier to extending their application to load-bearing components. One approach to overcoming the durability drawbacks is to coat the surface of magnesium-made parts with a relatively high fatigue strength material.

The promising coating approach, cold gas spray technique, is a versatile method in which particles moving at supersonic speed impinge on a surface and deform, creating a dense coating layer [175][57]. Due to the particles' relatively low temperature during the process (significantly lower than their melting point) and because they impact with high kinetic energy, compressive residual stress and grain refinement develop in the coating and substrate parallel and near to the surface [176][97].Thus, crack initiation from the coated surface as well as the interface are retarded, and crack propagation into a material's substrate is postponed (Fig. 7-1a)[123]. These desirable goals can be achieved in magnesium alloys by coating them with a dense layer of high fatigue strength material such as Al7075. Despite the expectation of induced compressive residual stress, the cold spray coating process was found to be susceptible to tensile residual stress in the magnesium alloy substrate near the interface [146], which might have a detrimental impact on the fatigue life of magnesium parts. Increased temperature of the substrate during coating, and thermal mismatch during cooling for temperature-sensitive materials such as magnesium may be responsible for inducing unfavorable stress in the substrate. On the other hand, the temperature gradient during the process and after can influence the microstructure of a substrate, especially near the interface. Therefore, the likelihood of microstructural changes due to temperature and residual stress changes, including stress relief, dynamic recovery, recrystallization or even dynamic grain growth, needs to be carefully investigated.

To address the possibility of microstructural changes and reversal of the beneficial residual stress in substrates during coating, we proposed and confirmed a technique for controlling the heat balance of the system to decrease the target surface's interface temperature (Chapter 6). The heat input and output of such a system (highlighted by dashed-line) is summarized in Fig. 7-1b. In the system, the heat balance occurs between the heat energy input to the system, including heat input from the carrier gas (Q1), heat generation due to the particles' impact (Q2), and heat dissipation to the surroundings (Q3), and especially, through heat conduction to the substrate. Increasing the spray nozzle's travel speed at a constant feedrate decreases the time, which the system is exposed to the gas temperature, thereby lowering Q1. At the same time, it causes less material to be deposited on the substrate, which reduces Q2. Based on results reported for Al7075-AZ31B coated samples, increasing the nozzle speed decreases the tensile residual stress, but not enough to induce compressive residual stress, when Q3

(heat dissipation) cannot happen adequately [146] (Chapter 6). However, by maximizing Q3 and optimizing Q1 and Q2, the substrate residual stress turns into compressive stress (Chapter 6).

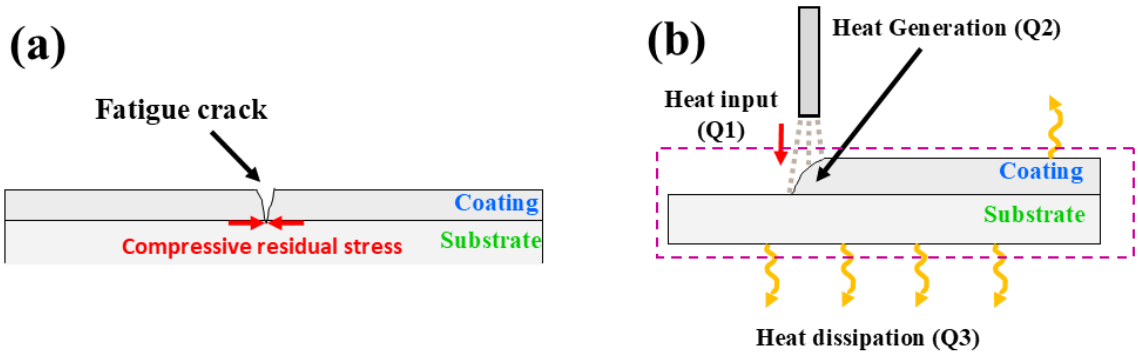

Fig. 7-1: a) Compressive residual stress at the interface with potential to postpone fatigue crack propagation; b) Heat balance of the cold spray coating system.

The aim of this research is to investigate the microstructural evolution of the interface and substrate when tensile and compressive residual stress have been induced in the substrate. To conduct this research, two sets of cold spray parameters are used to develop the tensile and compressive residual stress in the substrate. The respective samples are hereafter called either the tensile or the compressive sample. The residual stress in the coating and substrate are measured using a hole drilling machine. Then, the crystal structure of the interface is analyzed by XRD. SEM and TEM techniques have been employed to evaluate the difference between the bonding and microstructure of the substrate and interface for the two samples, tensile and compressive, which have experienced different coating conditions.

7.3 Experimental procedure

7.3.1 Material

Six rectangular pieces of as-received AZ31B-H24 samples (50×30×3.16mm) were prepared, and then the samples were stress relieved based on the ASM-recommendation procedure (260ºC/15min). Spherical-shape commercial Al7075 powder (supplied by Centerline Ltd., Windsor, Canada) with an average particle size of 23µm (measured by Retsch technology, Camsizer XT) was deposited on the magnesium alloy samples. The chemical composition of Al7075 powder are listed in Table 7-1.

Table 7-1: Chemical composition of Al7075 coating powders.

Composition	Aluminum (Al)	Zinc (Zn)	Iron (Fe)	Nickel (Ni)	Chromium (Cr)	Copper (Cu)	Magnesium (Mg)	Other Elements
Weight %	90	5.20	0.35	0.005	0.25	1.55	2.35	0.30

7.3.2 Coating parameters

A low-pressure cold spray system (SST) Series P, manufactured by Centerline, Windsor, Canada, was used to coat the stress relieved magnesium alloy samples. In this process, Al7075 powders are accelerated to supersonic velocities by a pressurized nitrogen gas (N_2) through a convergence–divergence de Laval UltiLife TM nozzle. Table 7-2 lists the processing parameters required for preparing two types of sample. In this process, the nozzle stand distance was 12mm and the compressive samples were fixed on the copper water-cooling system to increase the heat transmission by increasing the temperature difference between the hot and cold sides. Moreover, the insulated fixture was used for the tensile samples to prevent heat loss during the coating process. The coating thickness of the tensile samples (350µm) was significantly higher than that of the compressive samples (100 µm) with the same step-over of 1.2 mm.

Table 7-2: The processing parameters of cold spray coating for inducing tensile and compressive residual stress in magnesium alloy samples.

Parameters	Tensile samples	Compressive samples
Carrier Gas Temperature (°C)	400	400
Carrier Gas Pressure (psi)	200	200
Speed of Nozzle (mm/s)	2	10
Feed Rate (gr/min)	8	8

7.3.3 Characterization

To evaluate the distribution of residual stresses through the depth of coated samples, a hole drilling machine, Sint technology, Restan MTS-3000, was used to release strain by drilling a hole and measure the relaxation strain and calculate the stress with non-uniform method [40]. Phase identification was performed by employing the X-Ray diffraction, Bruker D8—Discover equipped with a Cu-Kα x-Ray tube (40 kV and 40 mA) and VÅNTEC-500 area detector to study the phase development of the

interface for tensile and compressive samples (Chapter 5). Microstructural analysis was conducted using a high-resolution Keyence optical microscope (VHX6000 manufactured by Keyence Corporation, Osaka, Japan), and SEM (TESCAN VEGA3) for the cross-sectioned cold spray samples. For this, the polished samples were etched using an appropriate etchant, which was mentioned in [146]. In addition, transmission electron microscopy (TEM, JEOL-2010F) was employed to investigate the structure of the interface between the coating and substrate. The TEM sample was prepared by focused ion beam (FIB, Zeiss NVision40) combining a Schottky field emission SEM. The operating voltage of the SEM was 200KeV.

7.4 Results and Discussion

Fig. 7-2 shows the distribution of residual stress for the compressive and tensile coated samples through the coating thickness and substrates. In the tensile samples, under the lower nozzle speed and higher temperature process, the residual stress of the Al7075 coating is parabolic. Near the coating surface, the residual stress has a lower negative value (about -20Mpa) compared to the middle of the coating thickness, which reaches a maximum level of -80MPa. Then, at the interface, the deterioration trends are observable again. This trend continues and can even be exacerbated in the temperature sensitive magnesium substrate. The distribution may be dependent on the heat transfer between two adjoining materials with different thermal expansion coefficients that have different thicknesses. Therefore, tensile residual stress has developed in the magnesium substrate coated with Al7075. However, decreasing the thermal energy of sample, which is coated by high nozzle travel speed, results in a compressive residual stress of around -50MPa at the interface It is important to mention here that increasing the nozzle speed decreases the thickness of the coating. It has been demonstrated that recoating the sample can increase the coating thickness while the compressive residual stress is maintained in the substrate (Chapter 6).

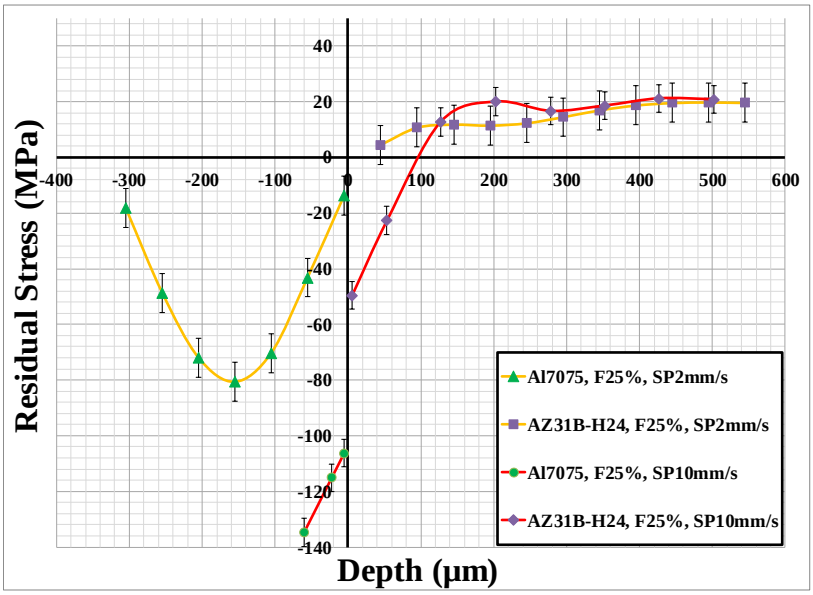

Fig. 7-2:Residual stress measurements for coated samples with different processing parameters.

Phase identifications of two coated samples, tensile and compressive, are shown in Fig. 7-3. The XRD patterns of these samples were collected over a longer period of time to increase the chance of detecting any phases at the interface. However, analyzing the XRD patterns detected only Al (card number: COD 9012428) and $Mg_{0.971}Zn_{0.029}$ (Card Number: COD 1523360) for both samples and no difference can be observed for detecting peaks. The development of intermetallic phases including $Al_{17}Mg_{12}$ has been reported at the interface of aluminum and magnesium, when the coated samples were heat treated at the temperature range from 360°C to 430°C for 24h [177]. In another research, the post processing was done by annealing at 200 °C for 1 h after fabricating Al/Mg/Al laminate by four-pass rolling and they identified two intermetallic phases of $Mg_{17}Al_{12}$ and Al_3Mg_2 at Mg/Al interface [178]. To the best of our knowledge, only one study reports in situ formation of $Al_{17}Mg_{12}$ during multi-pass cold spray coating. They coated AZ31B with Al7075 under a carrier gas temperature of 400°C and a pressure of 200 psi, with the nozzle speed of 5 mm/sec, and a feed rate of 8 gr/min [179]. However, based on the XRD patterns and in the resolution range of the experiments, no intermetallic phase was formed at the interface during coating in this research. Intermetallic phase formation during solidification is a relatively fast process. However, solid-state intermetallic phase formation is a diffusional process, and requires 1) enough thermal energy, and 2) ample time for diffusion [180]. Mixing of aluminum and magnesium at the interface is probable during solid-state bonding. Depending on the concentration of this mixture, solid solution or intermetallic phases have a chance to develop at the interface through diffusional mechanisms. However, during cold spray coating, the interface experiences high

temperature for a short time, which is a few orders of magnitude less than the time required for diffusion of the atoms. This situation is very far from thermodynamic equilibrium condition. Therefore, in situ formation of intermetallic phases during the short time of cold spray coating will most likely not occur.

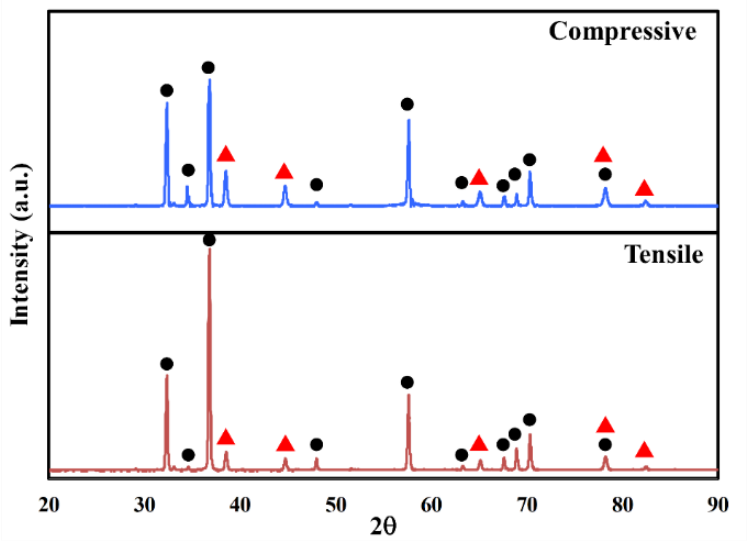

Fig. 7-3: XRD pattern of the tensile and compressive sample (●: $Mg_{0.971}Zn_{0.029}$, ▲ Aluminum).

A transmission electron microscope (TEM) was performed to reveal the grain structures at the interface. Fig. 7-4a and Fig. 7-4b show the TEM image of the interface for the tensile sample at two different magnifications. Based on the observations, at the interface of aluminum and magnesium, a very fine grain zone has been formed, labeled in the image by 1 in the magnesium side of the interface, a ladder shape structure consisting of columnar grains has been developed (marked by 2). TEM images of the compressive sample are shown in Fig. 7-4c and Fig. 7-4d, and have the same magnification of the tensile sample. Based on the TEM images, the grain structures of the interface for compressive samples are similar to the tensile ones. However, the interface features of the compressive sample are smaller than the tensile ones. The fine grain zone of the tensile sample has a thickness of around 220 nm (1), but this zone in the compressive sample is around 48 nm (3) (Compare Fig. 7-4b and Fig. 7-4d). The thickness of the ladder grains region of the tensile sample is also greater than that of the compressive sample. The columnar grains in the tensile sample is about 300 nm (2), while this size in compressive sample is only about 87 nm (4). Since the structure of the interface is not changed by altering the coating condition from the tensile sample to compressive samples, it may be concluded that the bonding mechanism and the impact effects on both samples are similar. However, the effect of excess thermal energy in the tensile sample can clearly be observed in the size of the interface features.

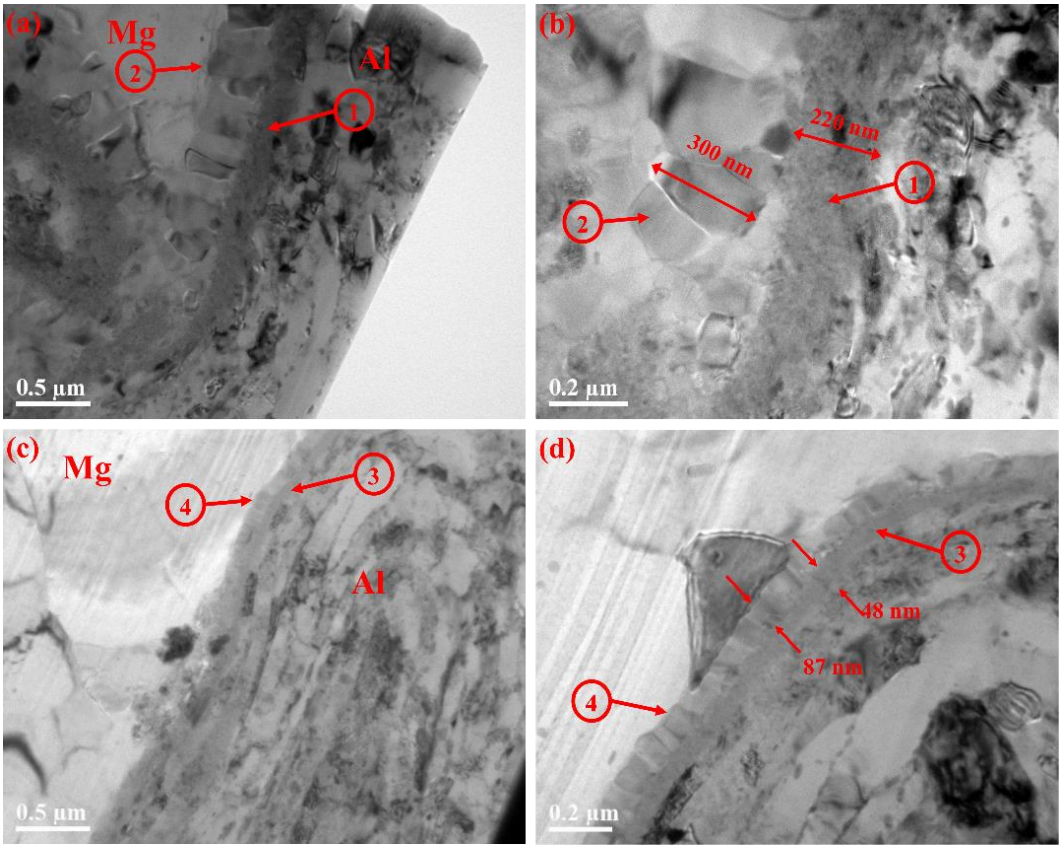

Fig. 7-4: TEM image of the: a and b) tensile sample; c and d) compressive sample, showing the interface of the coating and substrate including a region of fine grains follows by columnar grains in magnesium side of the interfaces.

To clarify the structure of the columnar grains and fine grain interfacial zones, these areas have been studied in detail. Fig. 7-5a shows a TEM image of the interface. Fig. 7-5b demonstrates a high-resolution TEM image of these columnar grains. As marked on the image, the distance between the atomic planes of this grain are equal to 0.236nm, which is close to the interplanar distance of $(\bar{1}011)$ plane of magnesium alloy. This high-resolution TEM image reveals that the ladder shape feature on the magnesium side of the interface consists of the crystalline magnesium grains, which nucleated at the interface and grew perpendicular to the small grain zone interface region, in the direction of heat transfer from the hot interface to the cold substrate. Fig. 7-5c depicts the selected area diffraction or SAD pattern of the fine grain interface zone. According to the ring pattern and bright spots on the rings, this area consists of very fine crystalline grain. This feature is a sign of a highly deformed pattern and a solid-state mixing of the two materials at the interface, formed during particles' impact and the extensive deformation of particles and the substrate surface upon impact. Based on the TEM study, a

rather large crystal grain of intermetallic phases is not formed during coating and bond formation. This observation is compatible with XRD results presented in Fig. 7-3. The intermetallic phases formation of the fine grains' interface zone is probable; however, the TEM and SAD patterns do not provide clear evidence for the formation of the intermetallic phases. More investigation is necessary to confirm the intermetallic phases of the fine grains in the interface zone.

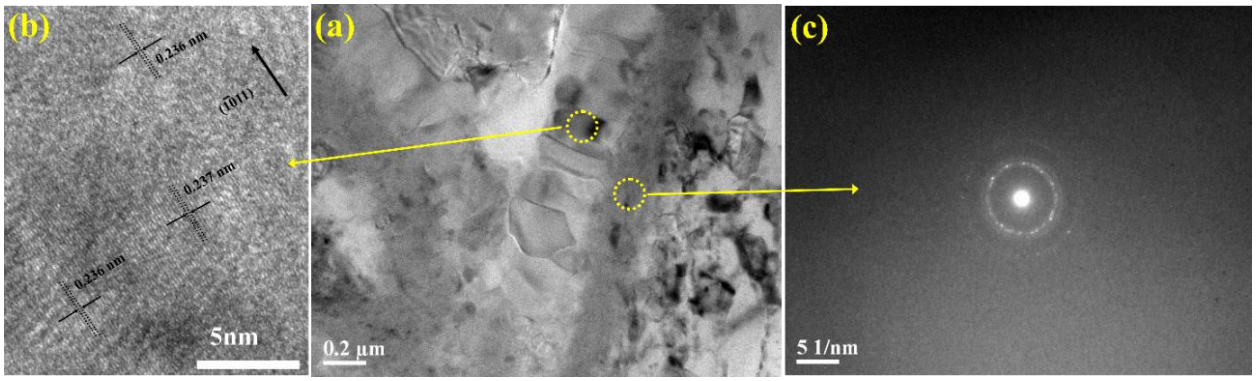

Fig. 7-5: a) TEM image of the interface; b) high resolution TEM image of the columnar interfacial grains; c) Selected area diffraction (SAD) pattern of the nanocrystalline grains at the interface region.

Fig. 7-6a and Fig. 7-6b show the microstructure of the magnesium alloy substrate near the interface for tensile and compressive samples, respectively, over a wide range. High-resolution SEM images of tensile and compressive samples are depicted in Fig. 7-7a and Fig. 7-7b. The optical and SEM images of the microstructure of the tensile sample (Fig. 7-6a and Fig. 7-7a) demonstrate grain refinement formation adjacent to the interface, followed by a region of large grains. Fig. 7-7c provides a zoomed picture of one the large magnesium grains in this region, surrounded by relatively small gains. After this region, grain sizes decrease again, as can be observed in Fig. 7-6a and Fig. 7-7a. Comparing the microstructure of the compressive sample (see Fig. 7-6b and Fig. 7-7b) to that of the tensile sample reveals that the grain size of the compressive sample adjacent to the interface (Fig. 7-7e and Fig. 7-7f) is smaller than tensile samples. Moreover, Fig. 7-6b, Fig. 7-7b and Fig. 7-7e show that around 25 µm below the interface of the compressive sample, there is a band in which high intensity twin boundaries are observed inside their grains. Comparing the optical microscopy images of Fig. 7-6a and Fig. 7-6b reveals that the accumulation of twin boundaries in the tensile sample happened around 140 µm below the interface. The SEM image of Fig. 7-7d confirms the existence of twinning in the tensile sample grains at the specified area.

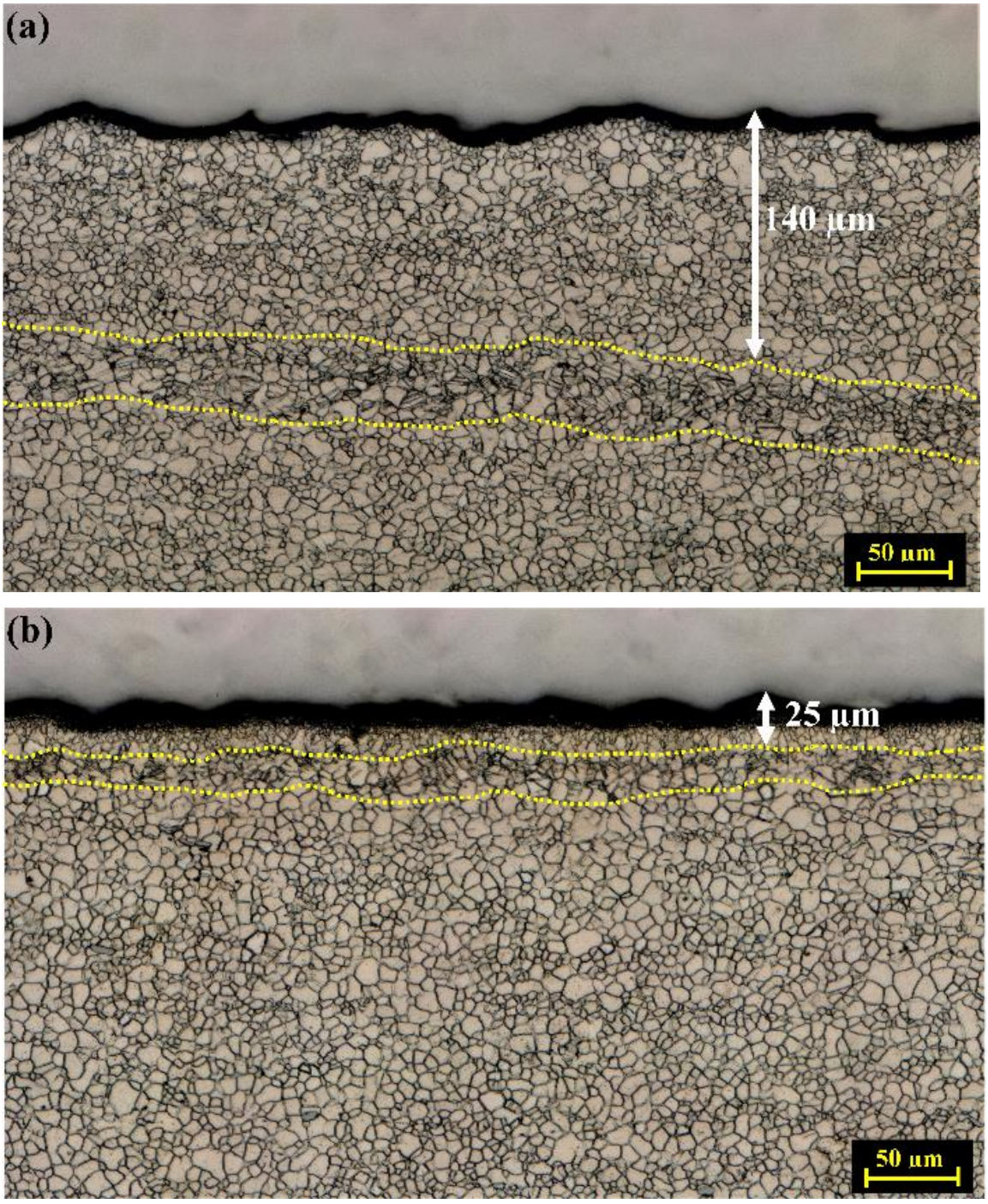

Fig. 7-6: Microstructure of: a) tensile sample; b) compressive sample showing the grain refinement near the interface and the accumulation of twinning in a narrow band parallel to the interface.

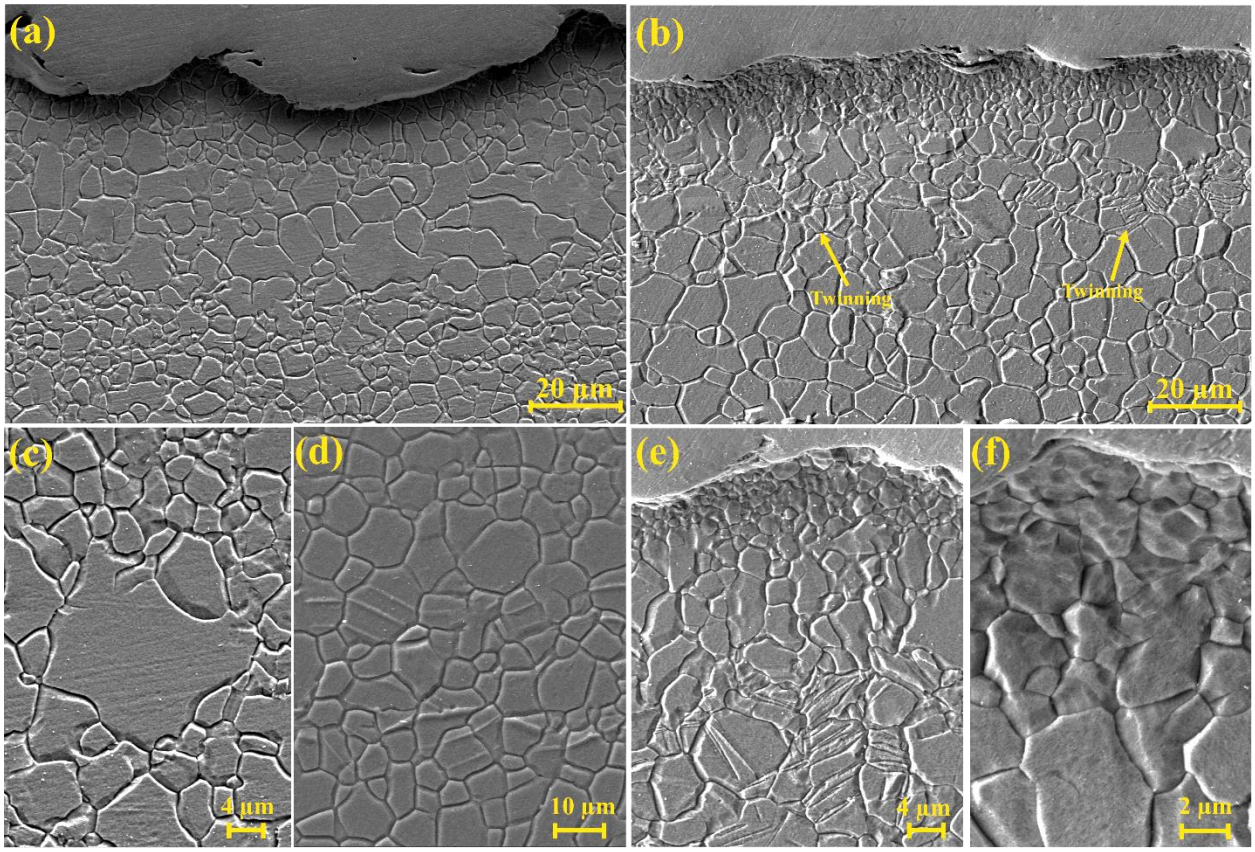

Fig. 7-7: The SEM images of substrate microstructures: a) tensile sample; b) compressive sample showing the microstructure of the magnesium substrate near the interface; c, d) tensile sample with high resolution showing dynamic grain growth in magnesium substrate and twining in the grains of the twin band region, respectively; e, f) compressive sample with high magnification showing the twin band region of the compressive sample and fine grain structure of magnesium substrate at the interface, respectively.

The deformation mechanism of AZ31B-H24 magnesium alloy is highly dependent on temperature and strain rate. It is well known that the deformation modes of AZ31B alloy are: basal <a> slip {0001} <1120>, prismatic <a> slip {1010} <1120>, pyramidal<a> slip {1011} < 1120>, pyramidal <c +a> slip {1122} <1123> and tensile twinning mode {1012} <1011> [181][182][183][184] . The AZ31B alloy sheet has a strong basal texture with a c-axis perpendicular to the surface of the sheet [184][42]. During cold spray deposition, a compressive stress is applied on the top of the surface along the c-axis by particle impact. At low temperatures, a combination of basal slip and tension twinning is necessary for deformation [184][181][185][186]. The critical resolve shear stresses (CRSS) predicted for these mechanisms at different temperatures are listed in Table 7-3 [187]. These data and other results reported in the literature [188] illustrated that the CRSS of the twinning deformation mechanism increases with

an increasing temperature, while the CRSS of the other deformation mechanisms such as pyramidal <a+c> decreases. Looking at Table 7-3 shows that up to 150°C, Basal slip and twinning have the lowest CRSS compared to other mechanisms. However, at 200°C, Prismatic slip and pyramidal <a+c> have lower CRSS than twinning and, as a consequence, from a temperature between 150°C to 200°C, the deformation mode changes and the chance for twinning to contribute to the deformation of AZ31B will be very low. Looking at the microstructure of the AZ31B sprayed substrate, Fig. 7-6a and Fig. 7-6b reveal that both tensile and compressive samples have a narrow band parallel to the interface in which the accumulation of twinning can be observed. However, twinning deformation is not seen in the grains between the interface and twin band. These special microstructures represent high temperature deformation of the substrate in the area between the interface and twin band. Comparing the tensile and compressive samples (Fig. 7-6a and Fig. 7-6b) demonstrates that the twin band in the tensile sample is around 140 µm from interface, while in the compressive sample, the width of this area is about 25 µm. In other words, the high temperature deformation zone in the tensile sample is 5.6 times bigger than that of the compressive sample. The substrate of the tensile sample experiences more peening than does the compressive sample, because of the increasing number of particles impact; however, the hot deformation area of the tensile samples consists of relatively larger equiaxed grains than are found in the compressive sample (compare Fig. 7-6a and Fig. 7-6b). Considering the duration and temperature of the cold spray process, larger equiaxed grains may happen through dynamic recrystallization and grain growth. The microstructure of the tensile sample shows abnormal grain growth in the hot deformation region, which is additional evidence for dynamic grain growth in this condition. Dynamic recrystallization and dynamic grain growth have been reported for AZ31B alloy under a high strain rate and high temperature deformation [185][189][190]. Therefore, the observations of this research seem to be compatible with those in the literature. Comparing the microstructure of the tensile and compressive samples confirms that the proposed strategy for controlling the thermal input (Q1) and heat generation (Q2) during coating and maximizing of the thermal output of the system (Q3) can successfully decrease the temperature of the interface. The temperature optimization process can minimize the dynamic recrystallization and eliminate dynamic grain growth in the compressive sample, providing suitable conditions for improving magnesium's microstructure as well as enhancing its mechanical properties.

Table 7-3: Critical resolve shear stress (CRSS) of different deformation modes for AZ31B at different temperatures [187]**.**

Temperature (°C)	Deformation mode	CRSS (MPa)
100	Basal slip	1.3
	Prismatic slip	75
	Pyramidal <c +a>	85
	Tension twin	63
150	Basal slip	1
	Prismatic slip	65
	Pyramidal <c +a>	72
	Tension twin	63
200	Basal slip	0.8
	Prismatic slip	44
	Pyramidal <c +a>	56
	Tension twin	82

7.5 Conclusion

The structure of the interface and substrate next to the interface have been studied to clarify the effect of heat balance on the microstructural evolution and residual stress development of AZ31B substrate coated with Al7075 alloy through the cold spray process. For this study, two sets of high and low thermal energy coating conditions were selected for the deposition. The residual stress of the coating and substrate were measured for these types of samples. Tensile and compressive residual stress were induced under high and low thermal energy of the system, respectively. The following conclusions can be drawn from the results:

1) The phase identifications of the tensile and compressive samples reveal that no intermetallic phase is developed by the coating process at the interface of the samples. Since cold spraying is a fast and low temperature coating method in which a solid-state bonding mechanism is dominant, nucleation and growth of intermetallic phases within the cold spray temperature range are unlikely.
2) TEM microscopy uncovered that for both high and low thermal energy coating situations, a fine grain region followed by a columnar grain on magnesium were created, and grow

perpendicular to the fine grain zone in the magnesium side of the interface. High thermal energy leads to a thicker interfacial area and bigger columnar grains.

3) The selected area diffraction pattern of the fine grain interfacial zone illustrates that this area of the interface consists of fine crystalline embryos, but no significant intermetallic phases development could be detected in this region. Moreover, high resolution TEM study of the columnar grains proved that these grains are magnesium, and no other phases developed in this area.
4) Optical microscopy and SEM study of the magnesium substrate near the interface uncovered that equiaxed grains were formed near the interface by dynamic recrystallization. High thermal energy coating leads to a higher temperature at the substrate near the interface. In this situation, not only dynamic recrystallization but also dynamic grain growth is observed in the substrate near the interface. Decreasing the temperature resulted in smaller grains being observed in the compressive sample due to the predominant peening effect.
5) The accumulation of twins in a band parallel to the interface was observed in both tensile and compressive samples. Twinning is an indispensable part of low temperature deformation mechanism for magnesium under this loading condition. Therefore, the existence of the twin band was considered as an evidence for the substrate temperature at this region. The higher thermal energy of the coating leads to formation of the twin band in an area around 140μm from interface. However, decreasing the heat input pushes the twin band toward the interface, making the interface temperature in the compressive sample less than that of the tensile sample and inducing compressive residual stress in the former.

Chapter 8

Effect of Cold Spray Coating of Al7075 on the Fatigue Performance of Magnesium Alloy

8.1 Abstract

Cold spray coating technique, a surface modification approach, was performed to improve the fatigue properties of AZ31B-H24 magnesium alloy. For this, Al7075 powder with a high fatigue strength was deposited on the AZ31B-H24 to enhance the substrate's fatigue resistance by increasing its surface strength and inducing beneficial residual stress. By controlling the coating parameter different residual stress state was achieved. The role of tensile and compressive residual stress in the substrates and how that affects the fatigue behaviour of coated samples were explored. Inducing tensile residual stress in the magnesium alloy substrate decreased the fatigue life of coated samples in comparison with the stress-relieved AZ31B-H24 samples, despite the compressive residual stress developed in the coating. However, when compressive residual stress was in the substrate as well as the coating; hence, the fatigue life of coated samples was increased compared to the AZ31B-H24 fatigue life in high cycle regime.

8.2 Introduction

Phenomena such as climate change, global warming, and shrinking energy resources are driving research into reducing fuel consumption. Since a big portion of fuel energy is directly consumed in the transportation sector, minimizing mobile structures' weight is now a major priority in the automotive and aerospace industries. Recently, magnesium and its alloys have become a source more interest, as the lightest structural materials, with the highest strength-to-weight ratio among all commercially available metals [40]. However, the use of magnesium alloys is tightly restricted to non-load bearing components due to shortcomings such as low fatigue strength, and poor corrosion and wear resistance [191]. To enhance the surface strength and durability of magnesium alloys, coating the surface of manufactured parts with a thin layer of a higher corrosion-and fatigue-resistant material can be an effective surface-modification approach [56]. Among all possible techniques, solid-state cold spray coating can facilitate a dense coating layer without encountering the deleterious effects of high temperature, such as oxidation, evaporation, melting, and detrimental residual stresses [58][57]. Coating is created by the high kinetic energy of micron-sized coating particles, accelerated

supersonically using a relatively low temperature and pressurized gas through a de Laval nozzle, rather than high temperature. The intensive plastic deformation of particles upon impact creates mechanical and metallurgical bonding [63]. Unlike thermal spray, particles' impingement at high kinetic energy induces compressive residual stress in coated samples due to the low-temperature process. However, increase in the thermal energy of the system from the carrier gas and particle deformation upon impact, as well as thermal mismatch, can provide a destructive condition that reverses the residual stress for temperature-sensitive materials, such as magnesium alloys. Therefore, apart from the development of beneficial residual stress, a means of achieving a coating with low porosity and good bonding strength is required to improve the fatigue properties of magnesium coated samples. Since fatigue cracks can be initiated from the interface area due to discontinuities being formed, the mechanical and microstructural characteristics of an interface should be studied [175].

Despite the advantages of cold spraying to enhance the fatigue resistance of materials, few researchers have investigated the fatigue behaviour of magnesium alloy coated samples [14][19][192][18]. Cavaliere et al. [19] investigated the role of processing parameters in the residual stress and fatigue performance of Al2024/AZ91coated samples. The role of carrier gas pressure and temperature, and particle speed in the coating microstructure, porosity, bonding strength and residual stress formation were studied. They demonstrated that increasing the carrier gas temperature and pressure increased the surface compressive residual stress and improved the mechanical properties and fatigue limit of the coated samples. Dayani et al. [18] studied the fatigue behaviour of samples in which Al7075 was used to coat AZ31B cast magnesium alloy substrates. The residual stress profiles of the coated samples showed the development a significant amount of compressive residual stress in the coating, while the tensile residual stress of 12 MPa was induced at the substrate interface. The higher hardness and higher fatigue strength of the coating material over the substrate, and the induced compressive residual stress of the coating led to 25% enhancement of the fatigue strength at 10^7 cycles in the coated samples compared to as-received samples. Cross-sectional fractography showed delamination and cracks at the interface; the authors showed that primary cracks were initiated and propagated from the substrate due to pores and casting defects [18]. Although pores and casting defects may be factors for primary crack initiation, the existence of tensile residual stress in the substrate due to thermal mismatch, as well as the substrate microstructural changes because of the sufficient thermal energy can also cause crack initiation from the substrate [9]. It has been reported that residual stress of a substrate near the interface can be turned from tensile to compressive stress when Al7075 is deposited on AZ31B-H24 substrate samples with optimized coating parameters, particularly coating temperature [146][18]. Based on our

observations, the magnesium coated samples with compressive residual stress showed better mechanical properties, such as higher hardness in the coating and interface, lower porosity and surface roughness, and finer grain microstructure compared to the samples with tensile stresses (Chapter 6&7).

The aim of this research is to study the effect of substrate residual stress on fatigue resistance in Al7075/AZ31B-H24 coated samples. To conduct this study, different coating setups and parameters have been used to prepare the coated samples with tensile and compressive residual stress at the substrate interface. Three-point bending fatigue tests are employed to determine the fatigue life of the tensile and compressive samples. The locations of crack initiation in the tensile and compressive samples before failure are compared. Finally, fractography of the failed samples is employed to clarify the differences in fracture surfaces.

8.3 Experimental procedure

8.3.1 Materials

Several 70×12.5 mm rectangular samples of AZ31B-H24 magnesium alloy sheet, 3.16 mm thick, were stress-relieved at 260°C/15min based on the ASM procedure and used as substrates [135]. The dimensions of the samples were determined based on the ASTM D5947 test method. A spherical-shaped commercial Al7075 powder (supplied by Centerline Ltd., Windsor, Canada), with an average value of 23μm (measured by Retsch technology, Camsizer XT) was selected as a coating material. Fig. 8-1a and Fig. 8-1b show the SEM image of spherical powders and the particle size distribution, respectively. The chemical compositions of AZ31B-H24 magnesium alloy and Al7075 coating material are listed in Table 8-1.

Table 8-1: Chemical composition of AZ31B-H24 [170]**, and Al7075**

Composition (Weight %)	Aluminum (Al)	Zinc (Zn)	Manganese (Mn)	Iron (Fe)	Nickel (Ni)	Silicon (Si)	Copper (Cu)	Chromium (Cr)	Magnesium (Mg)	Other Elements
Al7075	90	5.20	-	0.35	0.005	-	1.55	0.25	2.35	0.30
AZ31B-H24	2.99	0.95	0.2 Min	0.005	-	0.05	0.05	-	Bal.	-

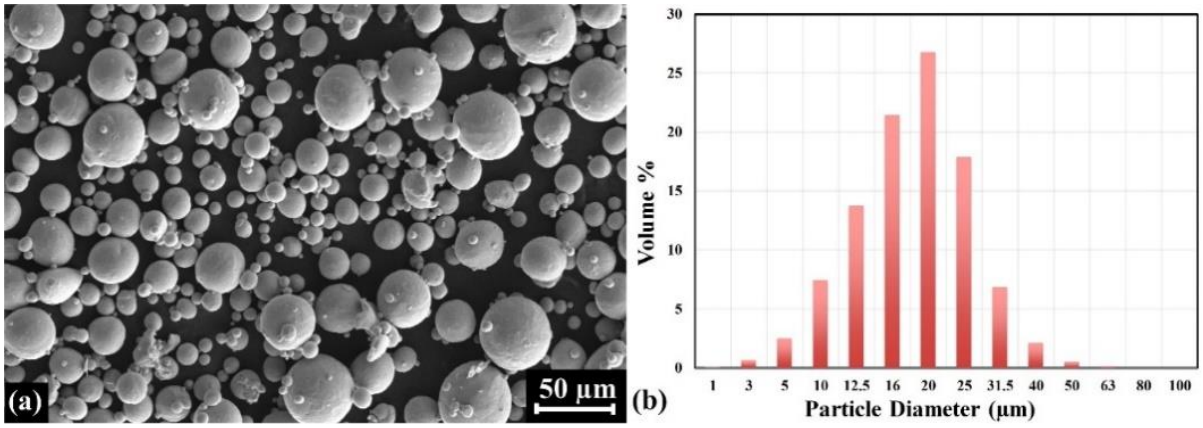

Fig. 8-1: a) SEM image of Al7075 powder; b) particle size distribution for Al7075.

8.3.2 Coating Process

A commercial supersonic spray technologies (SST) series P cold spray system (Centerline, Windsor, Canada) was used for depositing Al7075 on the magnesium alloy samples. Table 8-2 lists the coating processing parameters used for the experiments. To achieve tensile residual stress in the substrate surface (at the interface), the thermal energy of the system was increased by decreasing the nozzle speed and the substrate was situated on the insulated fixture. However, for obtaining the compressive residual stress, nozzle speed was increased to 10 mm/s, and the magnesium alloy substrate was placed on a water-cooling system during coating (Fig. 8-2a). To provide all coated samples with the same coating thickness and the minimum surface roughness, they were polished to achieve a 140µm thickness (see Fig. 8-2b).

Table 8-2: Cold Spray processing parameters

Costing Process	Carrier Gas	Gas Temperature	Gas Pressure	Powder Feed Rate	Nozzle Speed	Step Over	Stand-off Distance	Nozzle Length	Nozzle Orifice Diameter	Nozzle Exit Diameter	Fixture
Tensile Sample	N_2	400 °C	1.38 MPa	8gr/min	2mm/s	1.2 mm	12 mm	120 mm	2 mm	6.3 mm	insulated
Compressive sample	N_2	400 °C	1.38 MPa	8gr/min	10mm/s	1.2 mm	12 mm	120 mm	2 mm	6.3 mm	Water cooling

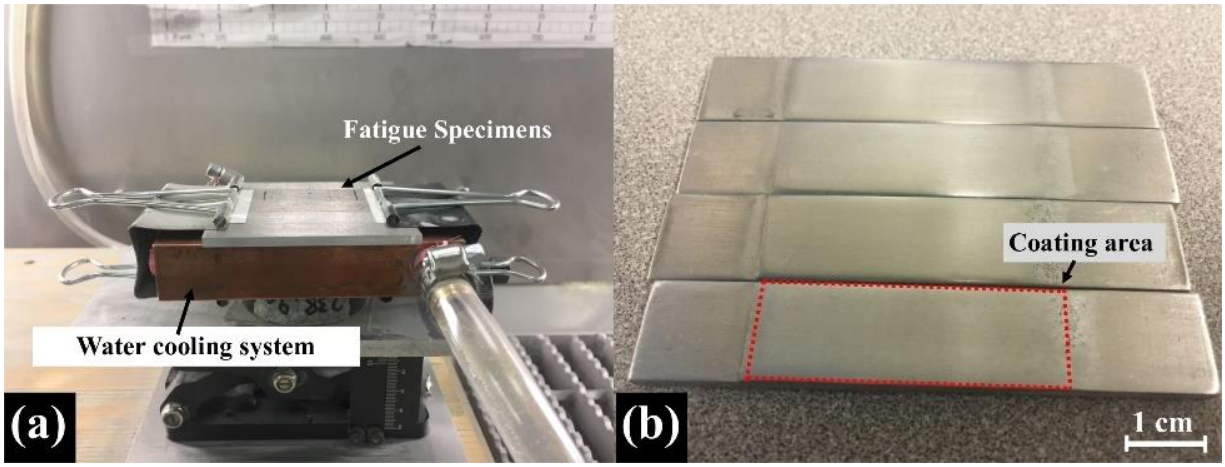

Fig. 8-2: a) AZ31B magnesium samples placed on water-cooling system during cold spray; b) fatigue coated samples.

8.3.3 Three-point Fatigue Bending Tests

An Instron 8872 servo-hydraulic axial test machine equipped with a 3-point bending fixture was employed for fatigue bending tests. The load capacity of the machine is 25KN, and the tests were conducted at ambient temperature. The supporting span distance was determined with respect to the samples' thickness, based on the ASTM D5947 test method. The bending tests were conducted with the R ratio of 0.1 and the frequency of 1Hz for low cycle and 2Hz for high cycle fatigue tests. Then, the three-point bending tests were performed for the three types of samples: stress-relieved magnesium alloy, coated tensile and coated compressive samples, all at the same stress level. The applied load was adjusted to keep constant the stress level of the coated samples and uncoated AZ31B. Fig. 8-3a shows the three-point fixture, and Fig. 8-3b shows the position of samples during the tests.

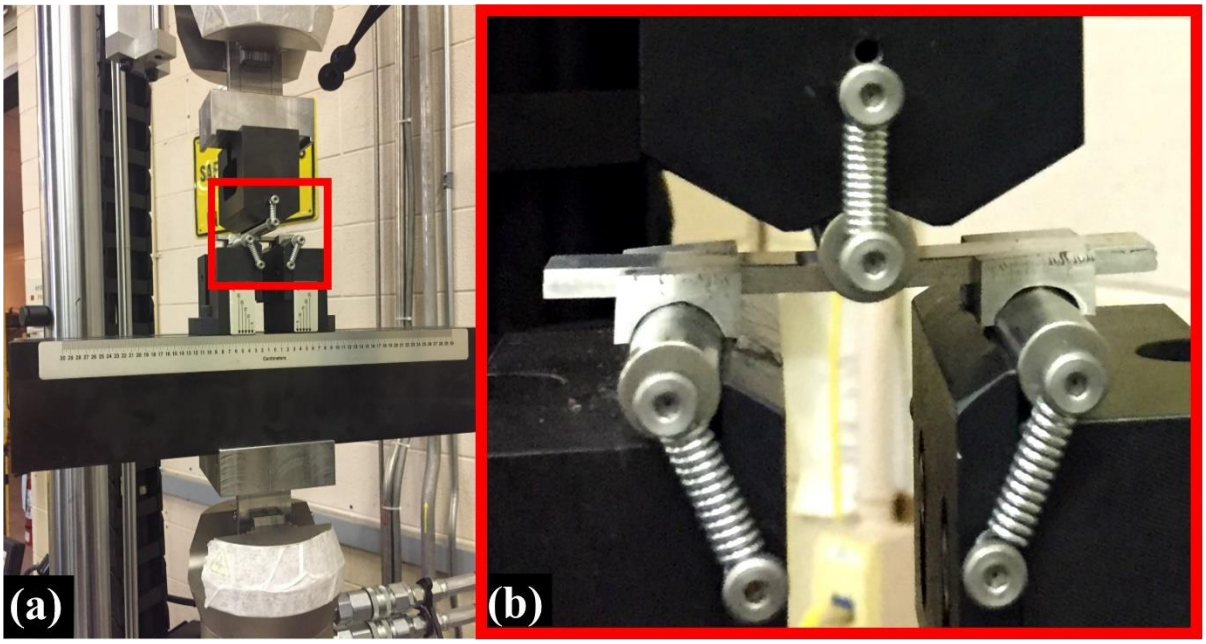

Fig. 8-3: a) Three-point bending setup; b) zoomed image of the sample.

8.3.4 Material Characterization

A scanning electron microscope TESCAN VEGA3 equipped with an e-Flash Bruker energy dispersive x-ray spectrophotometer (EDS) were employed for analyzing the fracture surface and to see the polished cross-section of coated samples. An EDS map of the fracture surfaces allowed the coating and substrate to be distinguished, and the position of the cracks specified. Moreover, X-ray computerized micro-scale tomography (CT) scans, were performed using a ZEISS Xradia 520 Versa 3D X-ray microscope (ZEISS, Oberkochen, Germany) to study crack locations prior to sample failure. A volume with dimensions of 1.8×1.3×3.26 mm was specified for the scanning to identify defects in the coated samples. A digital image correlation (DIC) camera (Correlated Solution co.) was used to capture the locations of crack initiation on the coated samples during the bending tests. In addition, to measure the residual stress after cold spray coating, a hole-drilling machine (Sint Technology, Restan MTS-3000) was employed. After installing conventional Fras-2 three-element strain gauge rosettes, the relaxation strain through the depth of coated samples was recorded during drilling. Then, the residual stress of the coated samples was measured using the ASTM E837-13 method [108].

8.4 Results and discussion

The residual stress profile of the tensile and compressive samples in the coating and substrate are shown in Fig. 8-4. The compressive residual stress was induced in the coating and substrate interface of the

compressive samples. However, the substrate interface of the tensile samples experienced positive residual stress, and lower compressive residual stress was induced in the coating of the tensile samples compared to the compressive ones. The maximum compressive residual stress (-60 MPa) was induced at around 100 µm below the coating surface of the tensile samples, whereas -150 MPa compressive residual stress was recorded at the coating surface of the compressive samples. At the interface of the tensile samples in the magnesium alloy substrate, a tensile residual stress of 11 MPa was developed, while the residual stress for compressive samples dropped to -53 MPa at the interface. Decreasing the coating temperature and increasing the heat transfer by water-cooling the substrate led to sustained induced compressive residual stress and reduced the detrimental effect of thermal mismatch in the compressive samples.

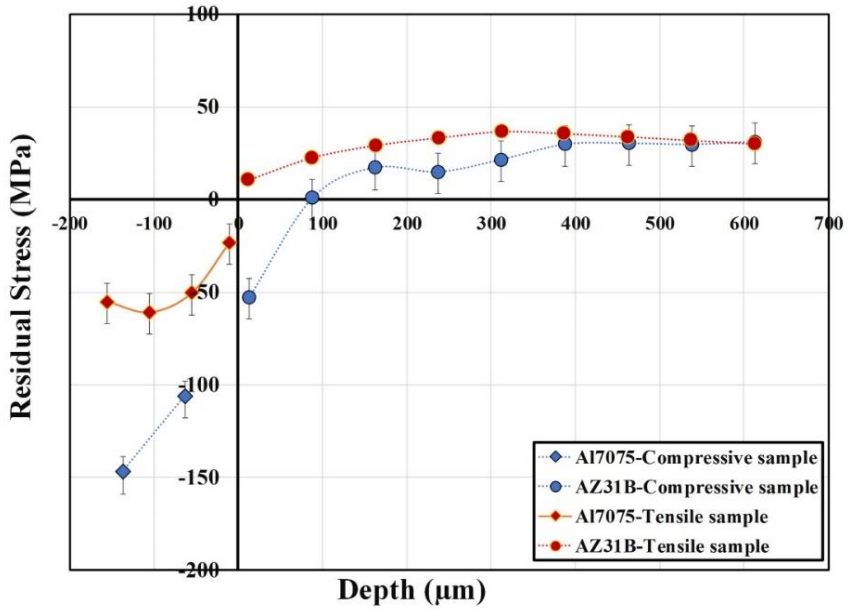

Fig. 8-4: Residual stress of tensile and compressive samples.

Fig. 8-5 shows the tensile and compressive samples after cold spray coating when placed on a flat surface. More bending can be observed in the tensile samples than in the compressive ones, which exhibit insignificant bending (almost none) (see Fig. 8-5a and Fig. 8-5b). This finding is compatible with the coating conditions of the samples. The coating setup and parameters of compressive samples were designed and chosen to keep the substrate temperature as low as possible during coating. However, for the tensile samples, the coating forms at a higher temperature and cools down afterward, inducing thermal tensile strain in Al7075 coating due to thermal mismatch. Despite the higher thermal expansion coefficient of the substrate compared to the coating, more thermal tensile strain is developed

in the coating, due to the lower substrate temperature than that of the coating during the process (Chapter 6). Hence, the higher coating temperature causes more bending to occur in the tensile samples compared to the compressive ones.

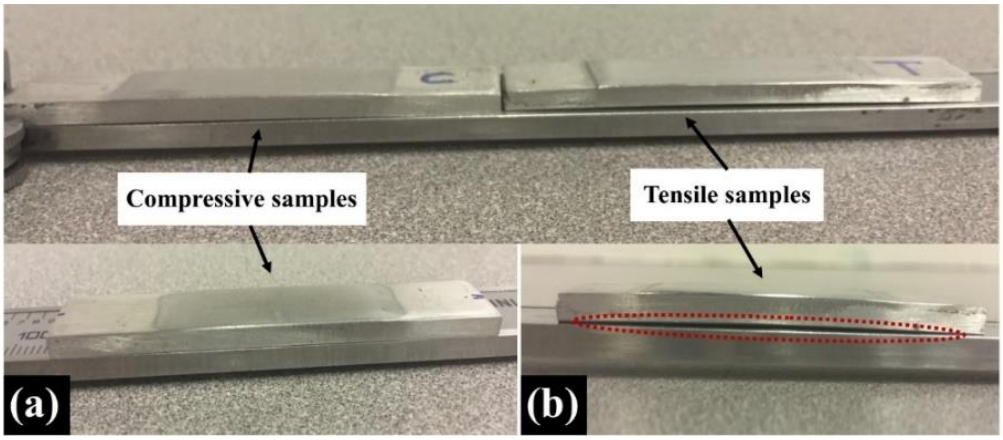

Fig. 8-5: Deflection of tensile and compressive samples after cold spray coating.

The three-point fatigue bending tests were performed for the prepared coated samples, both tensile and compressive, as well as for stress-relieved AZ31B. Fig. 8-6 depicts the fatigue life results obtained for the three types of samples. For comparison between the bare samples and coated samples, the stress levels have been selected in the range of the low and high cycle fatigue of AZ31B samples. The data presented in this S-N curve demonstrates that under a high cycle regime (stress amplitudes of 95-110MPa), the fatigue life of the tensile samples is less than that of the bare samples, while the compressive samples show significantly improved fatigue life at the same stress levels. For example, at the stress amplitude of 95MPa, the average fatigue life of the magnesium sample is 38,830 cycles, while the average fatigue life of tensile samples is 16,590, 57% reduction in fatigue life. However, the average fatigue life of the compressive samples in the high cycle regime is 89,237 cycles, which is an improvement of 130% compared to the AZ31B samples. Moreover, in the low cycle regime, different trends have been observed. The data presented in Fig. 8-6 shows the fatigue life of tensile and compressive samples in the low cycle regime reduced by 78% and 47% compare to the uncoated samples, respectively. In other words, regardless of the residual stress induced in the samples, the fatigue life of coated samples in a low cycle regime is decreased. Similar observation have been reported in the literature [193][69][194]. In the low cycle fatigue regime of this experiments, the stress applied to the samples was 164 MPa, which is high enough to provide a displacement range of 1.2 mm in the first cycle of testing (Fig. 8-7). The high level of applied load, plastic deformation, and defects

in the coating which reported in Fig. **6-8** might contribute to the cracking and failure of the coated samples earlier than uncoated Mg alloy samples.

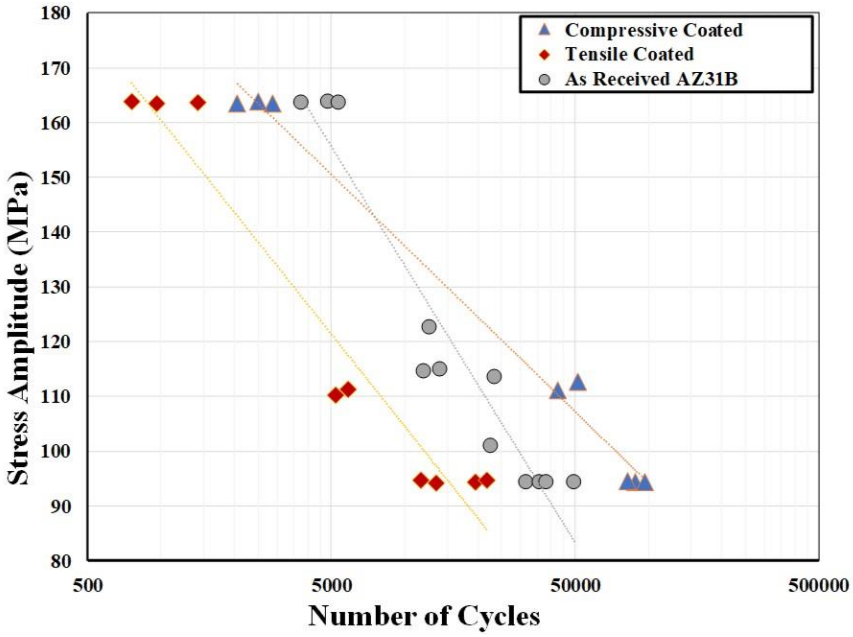

Fig. 8-6: Fatigue test results for magnesium AZ31B, tensile, and compressive sample.

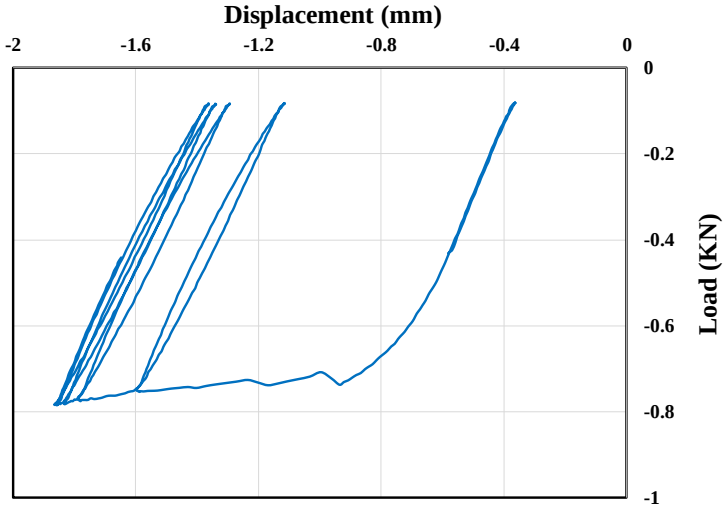

Fig. 8-7: Load versus displacement for the first five cycles of a tensile sample.

Fig. 8-8 shows the maximum and minimum displacement of a tensile and a compressive sample versus a normalized number of cycles, extracted from the data recorded in the three-point bending test. To

compare the displacement obtained from the two types of coated samples with different fatigue lives, the number of cycles was normalized through the following equation:

$$\boldsymbol{Normallized\ number\ of\ cycle} = \frac{\boldsymbol{cycle\ number}}{\boldsymbol{Cycle\ number\ at\ failure}} \times \mathbf{100} \qquad \textbf{(8-1)}$$

At the same stress amplitude of 95MPa, the maximum and minimum displacements of the tensile and compressive samples have different trends (see Fig. 8-8). Different behaviour can be observed for the tensile and compressive samples during failure. The displacement curves of the tensile sample start to increase when it reaches 90% of its life (point A). In this situation, fatigue cracks cannot be observed on the coating surface of the tensile sample, although the response of the sample to the applied load was changed. In contrast, the compressive sample did not show this relatively long-term degradation instead; it failed fast at the end of the experiment as is observable in Fig. 8-8 (point B). Interestingly, when the displacement response to the loading of the compressive samples started to change, immediately fatigue cracks appeared on the coating surface of the compressive samples. Fig. 8-9 shows an example of the fatigue cracks at the coating surface of compressive samples when the displacement response of the sample started to change. From this observation, it can be concluded that the fatigue failure behaviour of the tensile and compressive samples would differ.

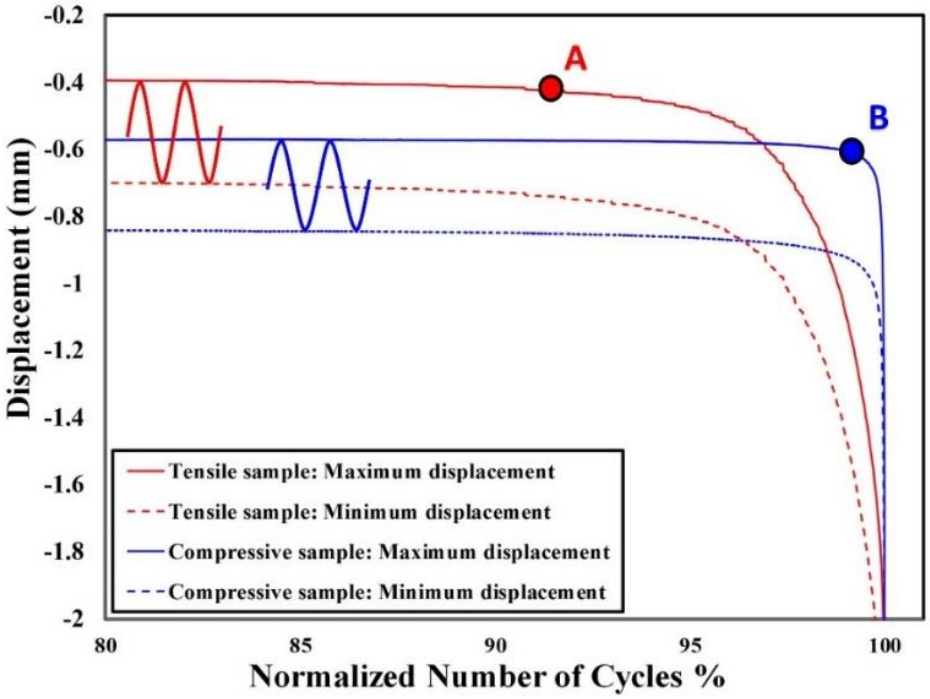

Fig. 8-8: Maximum and minimum displacements of coated samples during three-point bending tests versus the normalized number of cycles in the high cycle regime.

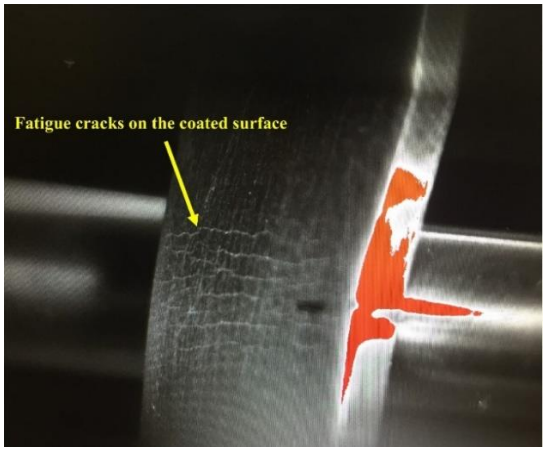

Fig. 8-9: Fatigue cracks nucleated on the coated surface of the compressive sample when the sample's displacement started to increase and the sample was about to fail (point B in Fig. 8-8).

To study the fatigue crack nucleation in the coated samples, the tests were immediately stopped after the displacement curves started to deviate from their steady state. Points A and B in Fig. 8-8demonstrate schematically where the three point bending experiments were stopped for the tensile and compressive samples, Fig. 8-10a shows the fatigue crack on the coating surface of the compressive sample before failure occurred. To illustrate the progress of the nucleated crack, the samples were cut perpendicular to the crack propagation direction and polished. Fig. 8-10b shows the cross-section of the coated sample which represents the fatigue crack that developed in the coating, crossed the interface, and grew in the substrate.

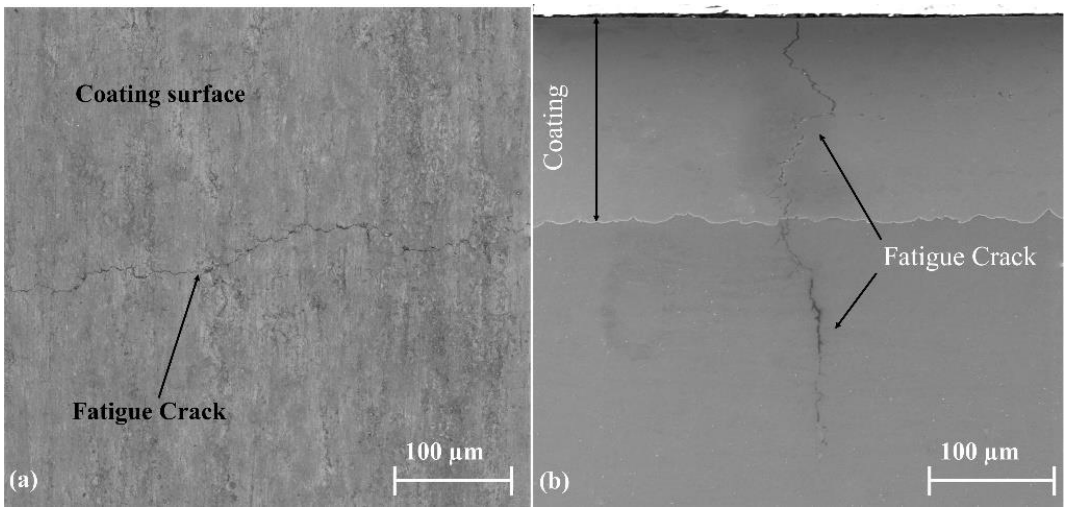

Fig. 8-10: a) Fatigue crack observed on the top surface of compressive sample; b) fatigue crack in the cross section of the compressive sample, cracks in the coating and substrate.

However, when the bending test of the tensile sample was stopped at the point A (Fig. 8-8), no crack was observed on the coating surface. A micro-CT scan was used to investigate the possibility of crack nucleation inside the sample before cutting it. The CT scan image shows evidence of the existence of the crack and void formation along the interface of the coating and substrate (Fig. 8-11a). To confirm the observation, a cross section of the tensile coated samples was prepared and polished. Fig. 8-11b shows the presence of cracks at the interface, which initiated from that area. Therefore, the existence of fatigue cracks at the interface of the tensile sample, when the displacement response started to deviate from the initial state (point A in Fig. 8-8) was confirmed by the SEM and CT scan images before failure of the samples.

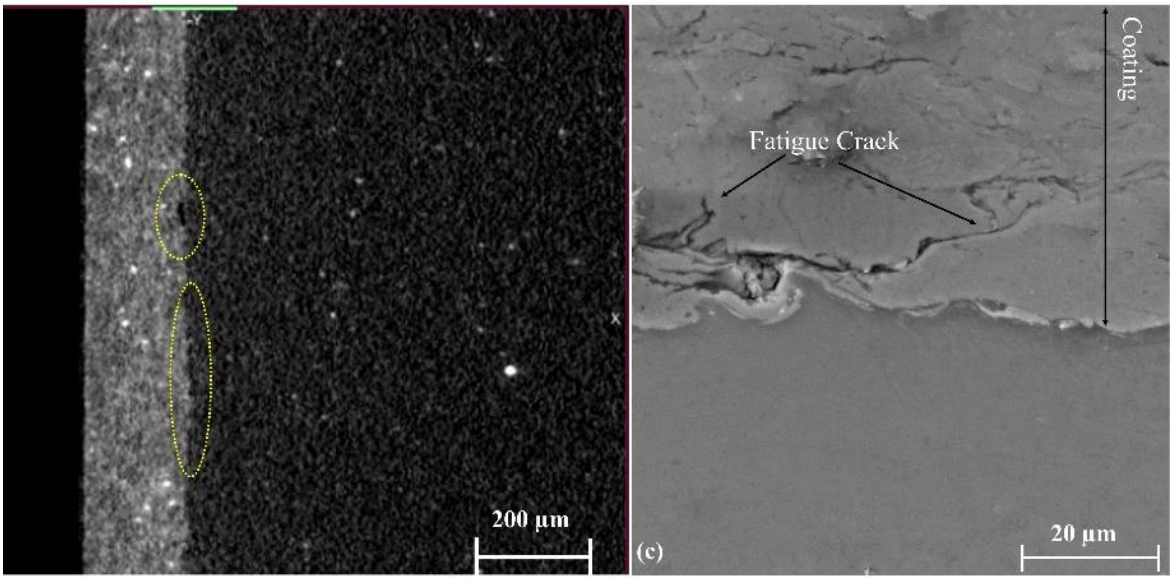

Fig. 8-11: a) CT scan image of a cross section of the tensile sample after 90% of its fatigue life; b) crack initiation at the interface in the cross section of tensile sample at the point A (Fig. 8-8).

After fatigue failure, the fracture surface of the tensile and compressive coated samples was studied. Fig. 8-12a shows the fracture surface of the tensile sample after fatigue failure. To distinguish the coating and substrate of the fracture surface, EDS elemental mapping of the coating and substrate was performed (Fig. 8-12b). These figures show the fatigue crack propagation in the coating across the interface and perpendicular to the interface in the substrate. This fractography images support the previous evidence of fatigue crack nucleation of the interface in the tensile sample (Fig. 8-8 and Fig. 8-11). In contrast, fractography of the interface area of the compressive sample (Fig. 8-12c and Fig. 8-12d), confirms that the interface of the coating and substrate remain intact during fatigue, and no cracks, delamination or defects are observed at this area in the fracture surface of the compressive

samples. Therefore, inducing tensile and compressive residual stress in the substrate interface through cold spray coating affects the fatigue behaviour of the coated samples, despite inducing compressive residual stress in the coating surfaces of both types of samples.

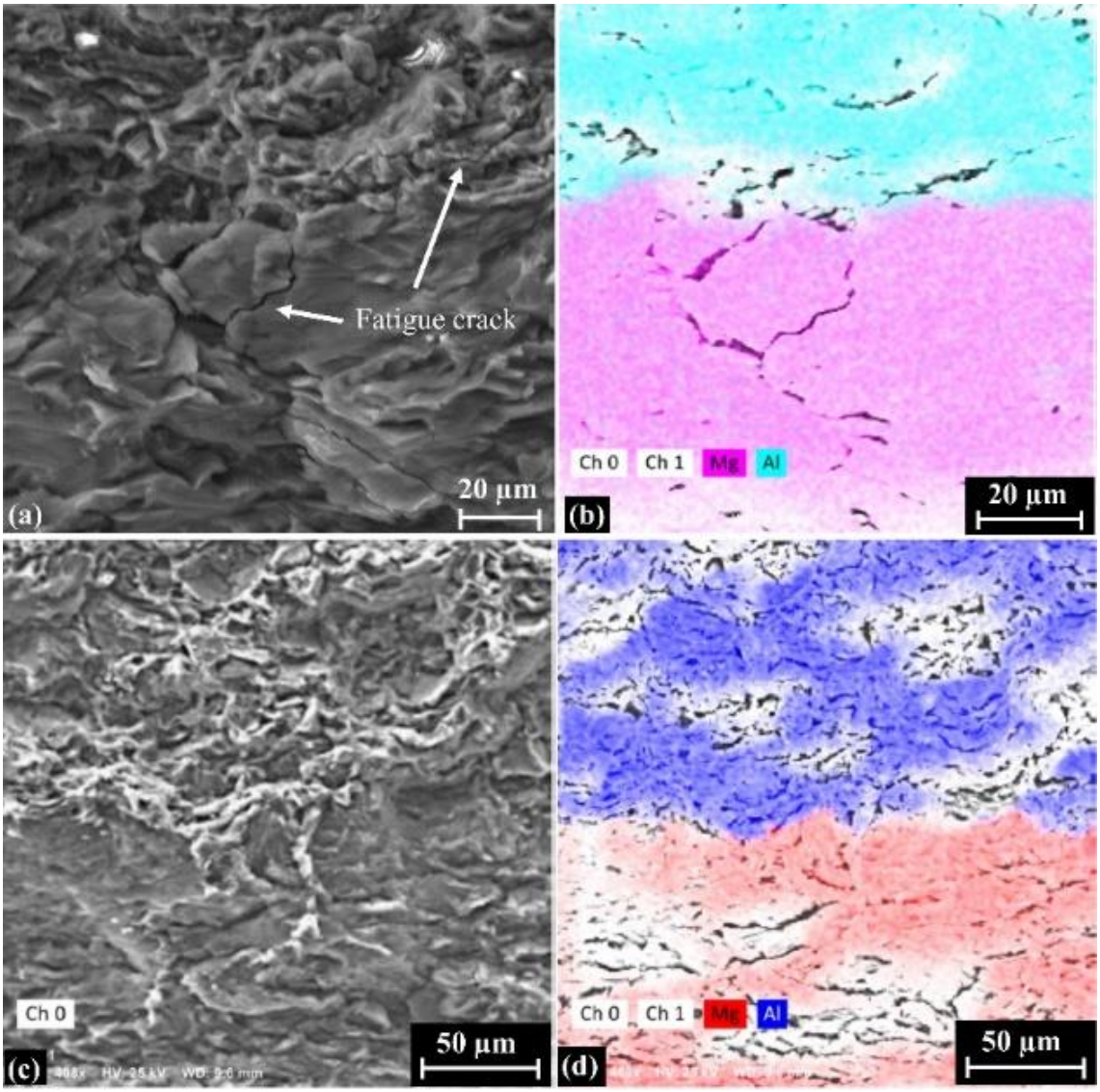

Fig. 8-12: a and b) Fracture surface of tensile sample demonstrating crack propagation along the interface and in the substrate, and EDS elemental mapping at the same area of SEM image; c and d) defect free interface between coating and substrate of compressive sample and EDS elemental mapping of the SEM image.

8.5 Conclusion

AZ31B magnesium sheets coated by Al7075 under two different cold spray coating conditions developed tensile and compressive residual stress in the substrate near the interface. The fatigue performance of the samples was assessed using three-point bending fatigue tests. The findings to emerge from this study can be summarized as follows:

1) The average fatigue life of the compressive samples under high cycle fatigue with a stress amplitude of 95MPa was greater by about 130% than that of the uncoated AZ31B samples at the same stress amplitude. However, the average fatigue life of the tensile sample showed 57% reduction compared to the stress-relieved AZ31B samples.
2) In the compressive samples, the fatigue cracks nucleated from the coating surface of the sample and propagated through the coating and substrate, leading to failure of the sample.
3) The fatigue crack in the tensile sample initiated from the coating-substrate interface and propagated along the interface and toward the substrate and coating.
4) This research shows that inducing compressive residual stress around the interface of cold spray coated samples enhances their fatigue performance. However, tensile residual stress around the interface had a negative impact on the fatigue performance of the magnesium AZ31B sample.

Chapter 9

Conclusions and Future work

9.1 Summary

Cold spray coating, a solid-state promising technique, has been developed for a wide range of manufacturing, repairing and coating technology. In recent years, many investigations have been performed into the amelioration of the coating conditions including quality, bonding and hardness. These studies have been distributed in a vast range of materials, respecting to the impressive features of the solid-state method mostly to improve the performance of corrosion and wear resistance of coated material. The most important advantage of this method compared to conventional coating is creation a dense layer of coating materials without evaporation, phase change and detrimental residual stress formation due to the relatively low process temperature. Hence, the characteristics of this coating process provides unique way to coat highly sensitive materials, such as Mg alloys. Besides, in-born peening effect phenomena of cold spray coating is likely to enhance fatigue performance of materials. Therefore, detail understanding of cold spray is critical to implement this technique successfully.

In this research, cold spray technique was employed to enhance the fatigue performance of AZ31B-H24 Mg alloy, with the aim of creating a high quality of hard coating material (Al7075), maximizing the compressive residual stress in coating and substrate surface, and minimizing the thermal effects. To achieve these goals, the effect of cold spray coating parameters on the induced residual stress of the Mg alloy substrate and the coated material were evaluated through in-situ monitoring and residual stress measurement. These results along with the other studies, such as microstructural observations and coating characterizations helped to find the optimum conditions for coating Mg alloys, to boost their fatigue life. The conclusions of the research work are summarized in the following section.

9.2 Conclusions

- The FBG sensors were embedded successfully into Mg substrate to monitor the thermo-mechanical behaviour of substrate during the cold spray process.
- To separate the thermal strain from mechanical strain, temperature versus wavelength shift calibration curves, for several embedded FBG sensors were extracted, while the mechanical strain was zero. The results showed a repeatable linear trend for the embedded sensors and the calculated squared R (0.996~1) represented negligible difference between the obtained data and the fitted curve. Then, the extracted calibration curve was used as a reference for thermal strain

measurements. Moreover, by employing thermocouples during the cold spray process, the temperature changes were recorded and used for distinguishing and calculating the mechanical strain.

- The in-situ observations obtained by FBG sensors uncovered that the interaction between thermal and mechanical strain induced during the process led to the release of compressive peening strain after a few seconds. Moreover, positive elastic strains were developed in the substrate near the interface after treatment due to the thermal mismatch.
- The residual stress measurements after cold spray coating through the hole-drilling and XRD are compatible with the results obtained from the FBG sensors. The results concluded that the high thermal energy generated by Al7075 particles during impact, as well as thermal energy input from carrier gas were sufficient for Mg substrate to recover the compressive residual stress in the range of experiments (T=400C, P=200, Nozzle speed=2 to 10 mm/s and Feed rate 25%, insulated fixture). The microstructural observations explored that the expected grain refinement changed particularly at the substrate interface due to the high thermal energy of the system, and low annealing temperature of Mg alloy.
- Statistical analysis declared the role of temperature and pressure of the carrier gas, and nozzle speed in the residual stress variation of coated samples.
- To maintain the induced compressive residual stress, the thermal energy of the system was reduced by decreasing the exposure time and reducing the substrate temperature. The optimum condition was provided for maximizing the compressive residual stress and minimizing thermal mismatch effects in the coating and the substrate. In this situation, the beneficial residual stress of the substrate near the interface was increased to about -40 MPa, -53MPa.
- Rising temperature during the coating process (with increasing the exposure time and decreasing the heat transfer) leads to creating greater coating thickness and increase the surface roughness of coated samples. Moreover, the quality and density of the coating under the higher deposition temperature process (“tensile sample”) was less than the density of coated samples under the low temperature treatment (“compressive sample”). In addition, the hardness of the coating and interface of the compressive samples was higher than that of the tensile samples.
- The similar interface microstructure was observed for the tensile and compressive samples through the TEM; however, higher thermal energy led to a thicker interfacial area and bigger columnar grains. Fine crystalline embryos could be detected in the fine grain interfacial zone by the selected area diffraction pattern in the samples and no detectable intermetallic phases observed in this

regime. In addition, the phase identification of tensile and compressive samples was performed through the XRD that confirmed no intermetallic phases could be formed within the cold spray temperature range used in this study.

- Optical microscopy and SEM observations demonstrated the formation of equiaxed grains near the interface in the tensile samples (due to dynamic recrystallization) and accumulation of twinning in a band around 140μm from the interface. However, decreasing the temperature resulted in finer grains in the compressive sample, and twin band was accumulated near the interface.
- The three-point bending fatigue tests were performed for three types of samples; stress relieved Mg samples, tensile-coated samples and compressive coated samples. The average fatigue life of the compressive samples under high cycle fatigue with a stress amplitude of 95MPa was greater about 130% than that of the stress-relieved Mg alloy samples at the same stress amplitude. However, the average fatigue life of the tensile samples showed 57% reduction compared to the stress-relieved Mg alloy samples.
- In the compressive samples, the fatigue cracks nucleated from the coating surface and propagated through the coating and substrate; however, the fatigue crack in the tensile samples initiated of the coating-substrate interface and propagated toward the substrate and coating.
- The effect of thermal mismatch on the residual stress distribution of coated samples was investigated. Pure zinc with a higher thermal expansion coefficient than Mg alloy and Al7075 was selected as an intermediate layer to decrease the detrimental effect of thermal mismatch. The results of this research affirmed the effectiveness of depositing zinc to increase the compressive residual stress in all three layers. However, various intermetallic phases were formed at the interface of zinc coating and Mg alloy substrate under different coating conditions. We explored a relation between the type of intermetallic phase formation at the interface and the thermal input energy. In addition, microhardness measurements showed a dependency between the hardness and intermetallic phase formation at the interface.
- Coating zinc on Mg alloys even under low temperature enabled the melting of zinc particles and thus spherical droplets were observed on the surface of the coated samples.
- The cold spray processing parameters influenced the microstructure of the zinc coating and Mg alloy substrate. At low coating temperature, an integrated dense coating was formed, whereas with an increase in carrier gas temperature defects such as porosity created in the coating.

- Based on these observations, deposition of a layer of zinc between substrate and Al7075 coating overcame the unfavourable thermal mismatch effects; however, intermetallic phase formation at the interface led to the weakness of the coated samples, decreasing the fatigue performance.

9.3 Future Work

1. Microstructural observations revealed that after cold spray coating, the grain size of substrate close to the interface became larger than the grain size after peening (coating at RT). Analyzing the structure of the magnesium grains next to the interface by EBSD would provide detailed information from the deformation of the grains, recovery, recrystallization and grain growth during the cold spray coating. This experiment will provide required information for identifying if recrystallization occur in the sample.

2. Defects such as pores could play detrimental effect on the fatigue performance of the coated samples. Based on the primary investigations in this research, decreasing the coating temperature decreases the defects in the sample. Continuation of this research would be necessary to optimize the deposition condition to minimize the defects in the coating and enhancing the fatigue life of the sample.

3. Since the effect of thermal mismatch leads to induce the tensile residual stress in the substrate (due to the lower CTE of Al7075 than Mg alloys), replacing Al7075 with another material, or spraying an intermediate layer of a material (analogous to the idea of re-autofrettage in cylinders for maximizing beneficial residual stress [195]) that has a CTE higher than Mg alloys can be beneficial to generate compressive residual stress. For this purpose, in this research the zinc coating has been examined, which successfully increased the level of compressive residual stress in the substrate and coating. However, poor mechanical performance of the zinc and formation of intermetallic phases at the interface of Zinc\AZ31B substrate is a barrier for using the multi-layer coated samples for cyclic loading services. Investigation into other proper materials to replace the zinc seems to be importance research topic for future.

4. Al7075 is a high fatigue resistance alloy, which was studied in this research. However, this material is not the best candidate in aluminum alloy family from corrosion-resistant point of view. The information and experiences of this research can be a good foundation for the future

research on another aluminum alloys (5000 series) as a high corrosion and fatigue resistance coating material.

5. Particle morphology and particle size have significant role in the particle velocity and thus directly affect the cold spray parameters, coating efficiency, and defect formation in the coating. Tailoring the particle size and morphology can enhance the quality of coating and increase the beneficial residual stress and hence increasing the fatigue life.

6. To the best of author's knowledge, this research for the first time illustrate the importance of in situ monitoring the cold spray coating process. In addition to the employed sensors, using a high resolution and precise thermal camera for recording the temperature during coating will provide supplementary information to the FBG and thermocouple sensors. Collected data from these three sensors help to tune the process parameters and setup to achieve the best quality of coating.

7. This research highlighted the capability of the FBG sensor for in situ monitoring of the cold spray deposition process. However, the mechanical output that measured by FBG sensor is elastic strain. Converting the strain data to stress be an important research topic, which may generate very informative data for future research.

8. Conducting further fatigue tests in various stress amplitudes is required for proving a clear picture of the effect of cold spray coating and the residual stress on the fatigue performance of the sample, finding the fatigue limit and life under various loading conditions.

9. More investigation requires to explain the detrimental effect of cold spray coating on the fatigue life of the coated sample in low cycle fatigue regime.

10. Optimizing the processing parameters and designing the setup to enhance the fatigue performance of AZ31B-H24 industrial parts through the cold spray deposition, would be expanded to load bearing industrial parts.

Bibliography

[1] Masson-Delmotte, P. Z. V., H.-O. Pörtner, D. Roberts, and J. Skea, “Global warming of 1.5°C,” IPCC, 2019.

[2] H. Friedrich and S. Schumann, “Research for a new age of magnesium in the automotive industry,” *J. Mater. Process. Technol.*, vol. 117, no. 3, pp. 276–281, 2001.

[3] W. S. Miller, L. Zhuang, J. Bottema, and A. J. Wittebrood, “Recent development in aluminium alloys for the automotive industry,” *Mater. Sci. Eng. A*, vol. 280, pp. 37–49, 2000.

[4] C. Blawert, N. Hort, and K. U. Kainer, “Automotive application of magnesium and its alloys,” *Trans. Indian Inst. Met.*, vol. 57, no. 4, pp. 397–408, 2004.

[5] D. Eliezer, E. Aghion, and F. H. Froes, “Magnesium science, technology and applications,” *Adv. Perform. Mater.*, vol. 5, no. 3, pp. 201–212, 1998.

[6] B. L. Mordike and T. Ebert, “Magnesium: Properties — applications — potential,” *Mater. Sci. Eng. A*, vol. 302, pp. 37–45, 2001.

[7] T. Kaneko and M. Suzuki, “Automotive applications of magnesium alloys,” *Mater. Sci. Forum*, vol. 419–422, no. I, pp. 67–72, 2003.

[8] S. M. Hassani-Gangaraj, A. Moridi, and M. Guagliano, “Critical review of corrosion protection by cold spray coatings,” *Surf. Eng.*, vol. 31, no. 11, pp. 803–815, 2015.

[9] Y. Xiong and M. X. Zhang, “The effect of cold sprayed coatings on the mechanical properties of AZ91D magnesium alloys,” *Surf. Coatings Technol.*, vol. 253, pp. 89–95, 2014.

[10] J. Cizek, O. Kovarik, J. Siegl, K. A. Khor, and I. Dlouhy, “Influence of plasma and cold spray deposited Ti Layers on high-cycle fatigue properties of Ti6Al4V substrates,” *Surf. Coatings Technol.*, vol. 217, pp. 23–33, 2013.

[11] W. Yang, J. Wang, D. Xu, P. Ke, and J. Li, “Microstructure and properties of duplex coatings on magnesium alloy,” *Surf. Eng.*, vol. 32, no. 8, pp. 601–606, 2016.

[12] Y. K. Wei, X. T. Luo, C. X. Li, and C. J. Li, “Optimization of In-Situ Shot-Peening-Assisted Cold Spraying Parameters for Full Corrosion Protection of Mg Alloy by Fully Dense Al-Based Alloy Coating,” *J. Therm. Spray Technol.*, vol. 26, no. 1–2, pp. 173–183, 2017.

[13] D. Dzhurinskiy, V. Leshchinsky, E. Strumban, E. Maeva, and R. G. Maev, “Protective coatings for mechanical aluminum-magnesium joints,” *Surf. Eng.*, vol. 31, no. 10, pp. 740–746, 2015.

[14] M. Diab, X. Pang, and H. Jahed, “The effect of pure aluminum cold spray coating on corrosion and corrosion fatigue of magnesium (3% Al-1% Zn) extrusion,” *Surf. Coatings Technol.*, vol. 309, pp. 423–435, 2017.

[15] Y. Hao, J. Wang, X. Cui, J. Wu, T. Li, and T. Xiong, “Microstructure characteristics and mechanical properties of Al-12Si coatings on AZ31 magnesium alloy produced by cold spray technique,” *J. Therm. Spray Technol.*, vol. 25, no. 5, pp. 1020–1028, 2016.

[16] L. Yuliang and Z. Qing, “Study on processing parameters of cold spray Al coating on magnesium alloy,” *International Conference on Materials, Environmental and Biological Engineering*. Atlantis Press, China, 2015.

[17] Q. Wang, N. Birbilis, and M. X. Zhang, “Process optimisation of cold spray Al coating on AZ91 alloy,” *Surf. Eng.*, vol. 30, no. 5, pp. 323–328, 2014.

[18] S. B. Dayani, S. K. Shaha, R. Ghelichi, J. F. Wang, and H. Jahed, “The impact of AA7075 cold spray coating on the fatigue life of AZ31B cast alloy,” *Surf. Coatings Technol.*, vol. 337, pp. 150–158, 2018.

[19] P. Cavaliere and A. Silvello, “Processing conditions affecting residual stresses and fatigue properties of cold spray deposits,” *Int. J. Adv. Manuf. Technol.*, vol. 81, no. 9–12, pp. 1857–1862, 2015.

[20] D. Knight, *Oxford Dictionary of National Biography*. Oxford University Perss, 2004.

[21] M. K. Kulekci, “Magnesium and its alloys applications in automotive industry,” *Int. J. Adv. Manuf. Technol.*, vol. 39, no. 9–10, pp. 851–865, 2008.

[22] M. Gupta and N. M. L. Sharon, *Magnesium, Magnesium alloys, and Magnesium Composites*. Wiley, 2011.

[23] M. M. Avedesian, H. Baker, M. M. Avedesian, and H. Baker, *ASM Specialty Handbook: Magnesium and Magnesium Alloys,*. Asm International, 1999.

[24] A. Gryguc, H. Jahed, B. Williams, and J. McKinley, “Mechanical Behaviour of Forged AZ31B Extruded Magnesium in Monotonic Compression,” *Mater. Sci. Forum*, vol. 828, pp.

291–297, 20156.

[25] D. Toscano, S. K. Shaha, B. Behravesh, H. Jahed, and B. Williams, “Effect of forging on the low cycle fatigue behavior of cast AZ31B alloy,” *Mater. Sci. Eng. A*, vol. 706, no. May, pp. 342–356, 2017.

[26] E. F. Emley, *Principles of Magnesium Technology*. Oxford Pergamon Press Inc., 1966.

[27] A. Luo, “Magnesium: Current and potential automotive applications,” *JOM J. Miner. Met. Mater. Soc.*, vol. 52, no. 2, 2002.

[28] C. S. Roberts, *Magnesium and its alloys*. Wiley, 1960.

[29] J. Casey and H. Jahedmotlagh, “The strength-differential effect in plasticity,” *Int. J. Solids Struct.*, vol. 20, no. 4, pp. 377–393, 1984.

[30] B. S. Behzad, J. Hamid, L. Steve, and M. Chengji, “Constitutive Modeling for Cyclic Behavior of AZ31B Magnesium Alloy and its Application,” *Adv. Mater. Res.*, vol. 891, no. 809–814, 2014.

[31] M. A. Khayamian, B. Behravesh, and H. Jahed, “Incorporation of asymmetric yield and hardening behaviour in axisymmetric elastoplastic problems,” *Mater. Des.*, vol. 99, pp. 490–499, 2016.

[32] A. Roostaei and H. Jahed, “A cyclic small-strain plasticity model for wrought Mg alloys under multiaxial loading: Numerical implementation and validation,” *Int. J. Mech. Sci.*, vol. 145, pp. 318–329, 2018.

[33] S. Graff, W. Brocks, and D. Steglich, “Yielding of magnesium: From single crystal to polycrystalline aggregates,” *Int. J. Plast.*, vol. 23, no. 12, pp. 1957–1978, 2007.

[34] M. A. Gharghouri, G. C. Weatherly, J. D. Embury, and J. Root, “Study of the mechanical properties of Mg-7.7at.% Al by in-situ neutron diffraction,” *Philos. Mag. A*, vol. 79, no. 7, pp. 1671–1695, 1999.

[35] C. H. Cáceres and P. Lukáč, “Strain hardening behaviour and the Taylor factor of pure magnesium,” *Philos. Mag.*, vol. 88, no. 7, pp. 977–989, 2008.

[36] A. Staroselsky and L. Anand, “A constitutive model for hcp materials deforming by slip and twinning,” *Int. J. Plast.*, vol. 19, no. 10, pp. 1843–1864, 2003.

[37] A. L. Oppedal, H. El Kadiri, C. N. Tomé, and G. C. Kaschner, “Effect of dislocation transmutation on modeling hardening mechanisms by twinning in magnesium,” *Can. J. Chem.*, vol. 30–31, pp. 41–46, 2012.

[38] M. Huppmann, M. Lentz, S. Chedid, and W. Reimers, “Analyses of deformation twinning in the extruded magnesium alloy AZ31 after compressive and cyclic loading,” *J. Mater. Sci.*, vol. 46, no. 4, pp. 938–950, 2011.

[39] I. Polmear, *Light Alloys: from Traditional Alloys to Nanocrystals*. Butterworth-Heinemann, 2006.

[40] K. U. Kainer, *Magnesium Alloys and Technologies* . Wiley-VCH, 2003.

[41] C. Bettles and M. Gibson, “Current Wrought Magnesium Alloys: Strengths and Weaknesses,” *JOM J. Miner. Met. Mater. Soc.*, vol. 57, no. 5, pp. 46–49, 2005.

[42] X. Y. Lou, M. Li, R. K. Boger, S. R. Agnew, and R. H. Wagoner, “Hardening evolution of AZ31B Mg sheet,” *Int. J. Plast.*, vol. 23, no. 1, pp. 44–86, 2007.

[43] D. Toscano, S. K. Shaha, B. Behravesh, H. Jahed, and B. Williams, “Effect of Forging on Microstructure, Texture, and Uniaxial Properties of Cast AZ31B Alloy,” *J. Mater. Eng. Perform.*, vol. 26, no. 7, pp. 3090–3103, 2017.

[44] S. M. H. Karparvarfard, S. K. Shaha, S. B. Behravesh, H. Jahed, and B. W. Williams, “Fatigue characteristics and modeling of cast and cast-forged ZK60 magnesium alloy,” *Int. J. Fatigue*, vol. 118, pp. 282–297, 2019.

[45] A. Gryguc *et al.*, “Monotonic and cyclic behaviour of cast and cast-forged AZ80 Mg,” *Int. J. Fatigue*, vol. 104, pp. 136–149, 2017.

[46] T. Shih, W. Liu, and Y. Chen, “Fatigue of as-extruded AZ61A magnesium alloy,” *Mater. Sci. Eng. A*, vol. 325, no. 1–2, pp. 152–162, 2002.

[47] Z. Zhihao, M. Yi, and C. Jianzhong, “Effect of Mn on microstructures and mechanical properties of Al-Mg-Si-Cu-Cr-V alloy,” *China Foundry*, vol. 9, no. 4, pp. 349–355, 2012.

[48] S. M. H. Karparvarfard *et al.*, “Characterization of Semi-Closed Die-Forged ZK60 Mg Alloy Extrusion,” in *Magnesium Technology*, 2017, pp. 329–334.

[49] ASTM, “Standard Practice for Codification of Unalloyed Magnesium and Magnesium-Alloys,

Cast and Wrought." 2011.

[50] ASTM-B296-03, "Standard Practice for Temper Designations of Magnesium Alloys, Cast and Wrought"," 2014.

[51] H. O. Fuchs and R. I. Stephens, *Metal Fatigue in Engineering*. New York: Wiley, 1980.

[52] M. Tsushida, K. Shikada, H. Kitahara, S. Ando, and H. Tonda, "Relationship between fatigue strength and grain size in AZ31 magnesium alloys," *Mater. Trans.*, vol. 49, no. 5, pp. 1157–1161, 2008.

[53] K. Tokaji, "Fatigue behaviour and fracture mechanism of a rolled AZ31 magnesium alloy," *Int. J. Fatigue*, vol. 26, no. 11, pp. 1217–1224, 2004.

[54] S. B. Behravesh, H. Jahed, and S. Lambert, "Characterization of magnesium spot welds under tensile and cyclic loadings," *Mater. Des.*, vol. 32, no. 10, pp. 4890–4900, 2011.

[55] S. B. Behravesh, "Fatigue Characterization and Cyclic Plasticity Modeling of Magnesium Spot-Welds," 2013.

[56] M. Kuffova, "Fatigue Endurance of Magnesium Alloys," *Magnes. Alloy. - Des. Process. Prop.*, 2011.

[57] A. Papyrin, V. Kosarev, S. Klinkov, A. Alkhimov, and V. Fomin, *Cold Spray Technology*, 1st ed. Amsterdam: Elsivier, 2006.

[58] Julio Villafuerte, Ed., *Modern Cold Spray; Materials, Process, and Applications*. Springer International Publishing, 2015.

[59] H. Assadi, F. Gärtner, T. Stoltenhoff, and H. Kreye, "Bonding mechanism in cold gas spraying," *Acta Mater.*, vol. 51, no. 15, pp. 4379–4394, 2003.

[60] S. Cadney, M. Brochu, P. Richer, and B. Jodoin, "Cold gas dynamic spraying as a method for freeforming and joining materials," *Surf. Coatings Technol.*, vol. 202, no. 12, pp. 2801–2806, 2008.

[61] J. Villafuerte, "Considering cold spray for additive manufacturing," *Adv. Mater. Process.*, vol. 172, no. 5, pp. 50–52, 2014.

[62] V. Luzin, K. Spencer, and M. X. Zhang, "Residual stress and thermo-mechanical properties of cold spray metal coatings," *Acta Mater.*, vol. 59, no. 3, pp. 1259–1270, 2011.

[63] H. Assadi, H. Kreye, F. Gärtner, and T. Klassen, “Cold spraying – A materials perspective,” *Acta Mater.*, vol. 116, pp. 382–407, 2016.

[64] M. Grujicic, J. R. Saylor, D. E. Beasley, W. S. DeRosset, and D. Helfritch, “Computational analysis of the interfacial bonding between feed-powder particles and the substrate in the cold-gas dynamic-spray process,” *Appl. Surf. Sci.*, vol. 219, no. 3–4, pp. 211–227, 2003.

[65] F. Wang and M. Zhao, “Simulation of Particle Deposition Behavior in Cold-Sprayed Mg Anticorrosion Coating,” *Mater. Manuf. Process.*, vol. 31, no. 11, pp. 1483–1489, 2016.

[66] Y. Ji, G. Bae, K. Kang, and C. Lee, “Influence of the interface temperature and strain gradients on the impact energy model of a soft particle on a hard substrate during kinetic spraying,” *Met. Mater. Int.*, vol. 17, no. 2, pp. 335–340, 2011.

[67] M. Saleh, V. Luzin, and K. Spencer, “Analysis of the residual stress and bonding mechanism in the cold spray technique using experimental and numerical methods,” *Surf. Coatings Technol.*, vol. 252, pp. 15–28, 2014.

[68] V. Lemiale, Y. Estrin, H. S. Kim, and R. O’Donnell, “Forming nanocrystalline structures in metal particle impact,” *Metall. Mater. Trans. A*, vol. 42, no. 10, pp. 3006–3012, 2010.

[69] A. Moridi, S. M. Hassani-Gangaraj, M. Guagliano, and M. Dao, “Cold spray coating: review of material systems and future perspectives,” *Surf. Eng.*, vol. 30, no. 6, pp. 369–395, 2014.

[70] W.-Y. Li, H. Liao, C.-J. Li, G. Li, C. Coddet, and X. Wang, “On high velocity impact of micro-sized metallic particles in cold spraying,” *Appl. Surf. Sci.*, vol. 253, no. 5, pp. 2852–2862, 2006.

[71] X.-T. Luo, C.-X. Li, F.-L. Shang, G.-J. Yang, Y.-Y. Wang, and C.-J. Li, “High velocity impact induced microstructure evolution during deposition of cold spray coatings: A review,” *Surf. Coatings Technol.*, vol. 254, pp. 11–20, 2014.

[72] Q. Wang, N. Birbilis, and M. X. Zhang, “On the formation of a diffusion bond from cold-spray coatings,” *Metall. Mater. Trans. A Phys. Metall. Mater. Sci.*, vol. 43, no. 5, pp. 1395–1399, 2012.

[73] A. Trinchi, Y. S. Yang, A. Tulloh, S. H. Zahiri, and M. Jahedi, “Copper surface coatings formed by the cold spray process: simulations based on empirical and phenomenological data,” *J. Therm. Spray Technol.*, vol. 20, no. 5, pp. 986–991, 2011.

[74] H. Bu, M. Yandouzi, C. Lu, and B. Jodoin, “Post-heat treatment effects on cold-sprayed aluminum coatings on AZ91D magnesium substrates,” *J. Therm. Spray Technol.*, vol. 21, no. 3–4, pp. 731–739, 2012.

[75] Z. B. Zhao, B. A. Gillispie, and J. R. Smith, “Coating deposition by the kinetic spray process,” *Surf. Coatings Technol.*, vol. 200, no. 16–17, pp. 4746–4754, 2006.

[76] L. F. Mondolfo, *Aluminum Alloys: Structure and Properties*. London ; Boston: Butterworths, 1976.

[77] M. V. Vidaller, A. List, F. Gaertner, T. Klassen, S. Dosta, and J. M. Guilemany, “Single impact bonding of cold sprayed Ti-6Al-4V powders on different substrates,” *J. Therm. Spray Technol.*, vol. 24, no. 4, pp. 644–658, 2015.

[78] B. S. Liu, Y. H. Wei, W. Y. Chen, L. F. Hou, and C. L. Guo, “Protective compound coating on AZ91D Mg alloy fabricated by combination of cold spraying with die casting,” *Surf. Eng.*, vol. 31, no. 11, pp. 816–824, 2014.

[79] B. S. DeForce, T. J. Eden, and J. K. Potter, “Cold spray Al-5% Mg coatings for the corrosion protection of magnesium alloys,” *J. Therm. Spray Technol.*, vol. 20, no. 6, pp. 1352–1358, 2011.

[80] Y. Tao *et al.*, “Microstructure and corrosion performance of a cold sprayed aluminium coating on AZ91D magnesium alloy,” *Corros. Sci.*, vol. 52, no. 10, pp. 3191–3197, 2010.

[81] K. Spencer, D. M. Fabijanic, and M. X. Zhang, “The use of Al–Al2O3 cold spray coatings to improve the surface properties of magnesium alloys,” *Surf. Coatings Technol.*, vol. 204, no. 3, pp. 336–344, 2009.

[82] P. J. Withers and H. K. D. . Bhadeshia, “Residual stress; Part 2 – nature and origins,” *Mater. Sci. Technol.*, vol. 17, no. 4, pp. 366–375, 2001.

[83] W. Liu, G. Wu, C. Zhai, W. Ding, and A. M. Korsunsky, “Grain refinement and fatigue strengthening mechanisms in as-extruded Mg–6Zn–0.5Zr and Mg–10Gd–3Y–0.5Zr magnesium alloys by shot peening,” *Int. J. Plast.*, vol. 49, pp. 16–35, 2013.

[84] G. Bae, J. Jang, and C. Lee, “Correlation of particle impact conditions with bonding, nanocrystal formation and mechanical properties in kinetic sprayed nickel,” *Acta Mater.*, vol. 60, no. 8, pp. 3524–3535, 2012.

[85] K. Kim, M. Watanabe, J. Kawakita, and S. Kuroda, “Grain refinement in a single titanium powder particle impacted at high velocity,” *Scr. Mater.*, vol. 59, no. 7, pp. 768–771, 2008.

[86] K. Kim, M. Watanabe, and S. Kuroda, “Thermal softening effect on the deposition efficiency and microstructure of warm sprayed metallic powder,” *Scr. Mater.*, vol. 60, no. 8, pp. 710–713, 2009.

[87] S. Yin, X. Wang, W. Y. Li, and H. Jie, “Effect of substrate hardness on the deformation behavior of subsequently incident particles in cold spraying,” *Appl. Surf. Sci.*, vol. 257, no. 17, pp. 7560–7565, 2011.

[88] Y. Y. Zhang and J. S. Zhang, “Recrystallization in the particles interfacial region of the cold-sprayed aluminum coating: Strain-induced boundary migration,” *Mater. Lett.*, vol. 65, no. 12, pp. 1856–1858, 2011.

[89] R. Ghelichi, D. MacDonald, S. Bagherifard, H. Jahed, M. Guagliano, and B. Jodoin, “Microstructure and fatigue behavior of cold spray coated Al5052,” *Acta Mater.*, vol. 60, no. 19, pp. 6555–6561, 2012.

[90] C. W. Ziemian, M. M. Sharma, B. D. Bouffard, T. Nissley, and T. J. Eden, “Effect of substrate surface roughening and cold spray coating on the fatigue life of AA2024 specimens,” *Mater. Des.*, vol. 54, pp. 212–221, 2014.

[91] A. Němcová, P. Skeldon, G. E. Thompson, S. Morse, J. Čížek, and B. Pacal, “Influence of plasma electrolytic oxidation on fatigue performance of AZ61 magnesium alloy,” *Corros. Sci.*, vol. 82, pp. 58–66, 2014.

[92] H. Assadi *et al.*, “On parameter selection in cold spraying,” *J. Therm. Spray Technol.*, vol. 20, no. 6, pp. 1161–1176, 2011.

[93] T. Schmidt, F. Gärtner, H. Assadi, and H. Kreye, “Development of a generalized parameter window for cold spray deposition,” *Acta Mater.*, vol. 54, no. 3, pp. 729–742, 2006.

[94] A. Moridi, S. M. Hassani-Gangaraj, M. Guagliano, and S. Vezzu, “Effect of cold spray deposition of similar material on fatigue behavior of Al 6082 alloy BT - The Society for Experimental Mechanics,” in *The Society for Experimental Mechanics*, 2013, pp. 51–57.

[95] S. Rech, A. Trentin, S. Vezzù, J.-G. Legoux, E. Irissou, and M. Guagliano, “Influence of Pre-Heated Al 6061 Substrate Temperature on the Residual Stresses of Multipass Al Coatings

Deposited by Cold Spray," *J. Therm. Spray Technol.*, vol. 20, no. 1–2, pp. 243–251, Jan. 2011.

[96] Y. C. Tsui and T. W. Clyne, "An analytical model for predicting residual stresses in progressively deposited coatings Part 1" Planar geometry," *Thin Solid Films*, vol. 306, pp. 23–33, 1997.

[97] G. Shayegan *et al.*, "Residual stress induced by cold spray coating of magnesium AZ31B extrusion," *Mater. Des.*, vol. 60, pp. 72–84, 2014.

[98] S. B. Dayani, "Improvement of fatigue and corrosion-fatigue resistance of AZ31B cast alloy by cold spray coating and top coating," University of Waterloo, 2017.

[99] S. B. Dayani, S. K. Shaha, R. Ghelichi, J. F. Wang, and H. Jahed, "The impact of AA7075 cold spray coating on the fatigue life of AZ31B cast alloy," *Surf. Coatings Technol.*, vol. 337, no. June 2017, pp. 150–158, 2018.

[100] S. K. Shaha, S. B. Dayani, H. Jahed, and T. M. M. Materials Society, "Influence of Cold Spray on the Enhancement of Corrosion Fatigue of the AZ31B Cast Mg Alloy," 2018, pp. 541–550.

[101] T. S. Price, P. H. Shipway, and D. G. McCartney, "Effect of cold spray deposition of a titanium coating on fatigue behavior of a titanium alloy," *J. Therm. Spray Technol.*, vol. 15, no. 4, pp. 507–512, 2006.

[102] G. S. Schajer, "Relaxation Methods for Measuring Residual Stresses: Techniques and Opportunities," *Exp. Mech.*, vol. 50, no. 8, pp. 1117–1127, 2010.

[103] X. Huang, Z. Liu, and H. Xie, "Recent progress in residual stress measurement techniques," *Acta Mech. Solida Sin.*, vol. 26, no. 6, pp. 570–583, 2013.

[104] K. Zhang, M. Yuan, and J. Chen, "General Calibration Formulas for Incremental Hole Drilling Optical Measurement," *Exp. Tech.*, vol. 41, no. 1, pp. 1–8, 2016.

[105] H. Jahed, M. R. Faritus, and Z. Jahed, "Residual Stress Measurements in an Autofrettage Tube Using Hole Drilling Method," *J. Press. Vessel Technol.*, vol. 134, no. 5, Aug. 2012.

[106] ASTM, "Standard Test Method for Determining Residual Stresses by the Hole-Drilling Strain-Gage Method," 2013.

[107] G. S. Schajer, "Measurement of non-uniform residual stresses using the hole-drilling method.

part i—stress calculation procedures," *J. Eng. Mater. Technol.*, vol. 110, pp. 338–343, 1988.

[108] G. S. Schajer, "Measurement of non-uniform residual stresses using the hole-drilling method. part ii—practical application of the integral method," *J. Eng. Mater. Technol.*, vol. 110, pp. 344–349, 1988.

[109] "X-RAY Diffraction Residual Stress Techniques," in *Metal Handbook*, American Society for Metals, 1986, pp. 380–392.

[110] B. D. Cullity and S. R. Stock, *Elements of X-Ray Diffraction*, Scholar's. USA: Eddison-Wesley P Inc, 2015.

[111] M. M. Werneck, R. C. S. B. Allil, B. A. Ribeiro, and F. V. B. de Nazaré, *A Guide to Fiber Bragg Grating Sensors*. InTech, 2013.

[112] J. M. Dockney and R. Tatam, "Simultaneous independent temperature and strain measurement using in-fiber Bragg grating sensors," *Electron. Lett.*, vol. 32, no. 12, 1996.

[113] R. Maron and A. Kersey, "Multi-parameter fiber optic sensor for use in harsh environments," 1999.

[114] B. Marzbanrad, F. Ahmed, H. Jahed, and E. Toyserkani, "Application Of FBG Optical Sensors To In-Situ Monitoring The Thermo-Mechanical Behaviour Of Cold Spray Coated Samples," pp. 1–5, 2018.

[115] M. Kreuzer, "Strain measurement with fiber Bragg grating sensors." Darmstadt, Germany.

[116] B. Marzbanrad, "Behaviour of Magnesium Alloy Under Load-Control Cyclic Testing," University of Waterloo, Waterloo, Canada, 2015.

[117] A. Pahlevanpour, B. Marzbanrad, S. B. Behravesh, and H. Jahed, "Application Of Fiber Bragg Grating Sensor For Strain Measurement At The Notch Tip Under Cyclic Loading," pp. 1–5, 2018.

[118] B. Marzbanrad, H. Jahed, and E. Toyserkani, "On the sensitivity and repeatability of fiber Bragg grating sensors used in strain and material degradation measurement of magnesium alloys under cyclic loads," *Int. J. Adv. Manuf. Technol.*, vol. 86, no. 9–12, 2016.

[119] B. Marzbanrad, E. Toyserkani, and H. Jahed, "Cyclic hysteresis of AZ31B extrusion under load-control tests using embedded sensor technology," *Fatigue Fract. Eng. Mater. Struct.*,

2016.

[120] R. I. Stephens, A. Fatemi, R. R. Stephens, and H. O. Fuchs, *Metal Fatigue in Engineering*, 2nd ed. Wiley, 2000.

[121] A. H. Mahmoudi, A. Ghasemi, G. H. Farrahi, and K. Sherafatnia, "A comprehensive experimental and numerical study on redistribution of residual stresses by shot peening," *Mater. Des.*, vol. 90, pp. 478–487, 2016.

[122] S. M. Hassani-Gangaraj, M. Carboni, and M. Guagliano, "Finite element approach toward an advanced understanding of deep rolling induced residual stresses, and an application to railway axles," *Mater. Des.*, vol. 83, pp. 689–703, 2015.

[123] H. Jahed and R. Ghelichi, "Residual Stresses and Fatigue Life Enhancement of Cold Spray," in *Modern Cold Spray: Materials, Process, and Applications*, J. Villafuerte, Ed. Cham: Springer International Publishing, 2015, pp. 225–252.

[124] R. N. Raoelison, C. Verdy, and H. Liao, "Cold gas dynamic spray additive manufacturing today: Deposit possibilities, technological solutions and viable applications," *Mater. Des.*, vol. 133, pp. 266–287, 2017.

[125] S. Yin, E. J. Ekoi, T. L. Lupton, D. P. Dowling, and R. Lupoi, "Cold spraying of WC-Co-Ni coatings using porous WC-17Co powders: Formation mechanism, microstructure characterization and tribological performance," *Mater. Des.*, vol. 126, pp. 305–313, 2017.

[126] F. Meng, D. Hu, Y. Gao, S. Yue, and J. Song, "Cold-spray bonding mechanisms and deposition efficiency prediction for particle/substrate with distinct deformability," *Mater. Des.*, vol. 109, pp. 503–510, 2016.

[127] K. Spencer, V. Luzin, N. Matthews, and M. X. Zhang, "Residual stresses in cold spray Al coatings: The effect of alloying and of process parameters," *Surf. Coatings Technol.*, vol. 206, no. 19–20, pp. 4249–4255, 2012.

[128] W. Li, K. Yang, D. Zhang, X. Zhou, and X. Guo, "Interface behavior of particles upon impacting during cold spraying of Cu/Ni/Al mixture," *Mater. Des.*, vol. 95, pp. 237–246, 2016.

[129] A. N. Ryabinin, "One-Dimensional Non-Isentropic Approach," *ARPN J. Eng. Appl. Sci.*, vol. 10, no. 6, pp. 2435–2439, 2015.

[130] V. K. Champagne, D. J. Helfritch, M. D. Trexler, and B. M. Gabriel, “The effect of cold spray impact velocity on deposit hardness,” *Model. Simul. Mater. Sci. Eng.*, vol. 18, no. 6, p. 65011, 2010.

[131] G. Bae, Y. Xiong, S. Kumar, K. Kang, and C. Lee, “General aspects of interface bonding in kinetic sprayed coatings,” *Acta Mater.*, vol. 56, no. 17, pp. 4858–4868, 2008.

[132] P. Cavaliere and A. Silvello, “Fatigue behaviour of cold sprayed metals and alloys: critical review,” *Surf. Eng.*, vol. 32, no. 9, pp. 631–640, 2016.

[133] D. Lehmhus *et al.*, “Taking a downward turn on the weight spiral – Lightweight materials in transport applications,” *Mater. Des.*, vol. 66, pp. 385–389, 2015.

[134] S. D. Wang, D. K. Xu, B. J. Wang, E. H. Han, and C. Dong, “Effect of corrosion attack on the fatigue behavior of an as-cast Mg–7%Gd–5%Y–1%Nd–0.5%Zr alloy,” *Mater. Des.*, vol. 84, pp. 185–193, 2015.

[135] *Metal Handbook: 4E: Heat Treating of Nonferrous Alloys*. ASM International, 2018.

[136] A. Feng, D. Chen, C. Li, and X. Gu, “Flat-cladding fiber Bragg grating sensors for large strain amplitude fatigue tests,” *Sensors (Basel)*, vol. 10, no. 8, pp. 7674–7680, 2010.

[137] E. Kalatehmollaei, H. Mahmoudi-Asl, and H. Jahed, “An asymmetric elastic–plastic analysis of the load-controlled rotating bending test and its application in the fatigue life estimation of wrought magnesium AZ31B,” *Int. J. Fatigue*, vol. 64, pp. 33–41, 2014.

[138] E. TECHNOLOGY, Ed., “EPO-TEK 353ND.” 2014.

[139] R. Kashyap, *Fiber Bragg Gratings*, Second Edi. United States of America: Elsevier, 2010.

[140] Z. Arabgol, H. Assadi, T. Schmidt, F. Gärtner, and T. Klassen, “Analysis of thermal history and residual stress in cold-sprayed coatings,” *J. Therm. Spray Technol.*, vol. 23, no. 1–2, pp. 84–90, 2013.

[141] S. Housh, B. Mikucki, and A. Stevenson, *Properties of Magnesium Alloys, Properties and Selection: Nonferrous Alloys and Special-Purpose Materials*, vol. 2. ASM International, 1992.

[142] A. Mishra, B. Kad, F. Gregori, and M. Meyers, “Microstructural evolution in copper subjected to severe plastic deformation: Experiments and analysis,” *Acta Mater.*, vol. 55, no. 1, pp. 13–28, 2007.

[143] D. C. Montgomery, *Design and Analysis of Experiments*, 8th ed. John Wiley & Sons, Inc., 2012.

[144] M. Hassani-Gangaraj, D. Veysset, V. K. Champagne, K. A. Nelson, and C. A. Schuh, "Response to Comment on 'Adiabatic shear instability is not necessary for adhesion in cold spray,'" *Scr. Mater.*, 2018.

[145] B. Marzbanrad, F. Ahmed, H. Jahed, and E. Toyserkani, "Application of FBG Optical Sensors To In-Situ Monitoring The Thermomechanical Behaviour of Cold Spray Coated Samples," *CSME International Congress 2018*. Toronto, On, Canada, 2018.

[146] B. Marzbanrad, H. Jahed, and E. Toyserkani, "On the evolution of substrate's residual stress during cold spray process: A parametric study," *Mater. Des.*, vol. 138, pp. 90–102, 2018.

[147] L. F. V. Qian, A. A. Roostaei, U. Dighrasker, G. Glinka, and H. Jahed, "Notch Plasticity and Fatigue Modelling of AZ31B-H24 Magnesium Alloy Sheet," in *SAE Technical Paper*, 2019.

[148] H. Assadi, F. Gartner, T. Klassen, and H. Kreye, "Comment on 'Adiabatic shear instability is not necessary for adhesion in cold spray,'" *Scr. Mater.*, vol. 162, pp. 512–514, 2019.

[149] K. Ogawa, *Cold spray coatings*, vol. 60, no. 5. 2017.

[150] M. Krystýnová, P. Doležal, S. Fintová, M. Březina, J. Zapletal, and J. Wasserbauer, "Preparation and Characterization of Zinc Materials Prepared by Powder Metallurgy," *Metals (Basel).*, vol. 7, no. 10, p. 396, 2017.

[151] G. K. Levy, J. Goldman, and E. Aghion, "The prospects of zinc as a structural material for biodegradable implants—a review paper," *Metals (Basel).*, vol. 7, no. 10, pp. 1–18, 2017.

[152] N. M. Chavan, B. Kiran, A. Jyothirmayi, P. S. Phani, and G. Sundararajan, "The corrosion behavior of cold sprayed zinc coatings on mild steel substrate," *J. Therm. Spray Technol.*, vol. 22, no. 4, pp. 463–470, 2013.

[153] N. B. Maledi, O. P. Oladijo, I. Botef, T. P. Ntsoane, A. Madiseng, and L. Moloisane, "Influence of cold spray parameters on the microstructures and residual stress of Zn coatings sprayed on mild steel," *Surf. Coatings Technol.*, vol. 318, pp. 106–113, 2017.

[154] J. G. Legoux, E. Irissou, and C. Moreau, "Effect of Substrate Temperature on the Formation Mechanism of Cold-Sprayed Aluminum, Zinc and Tin Coatings," *J. Therm. Spray Technol.*, vol. 16, no. 5–6, pp. 619–626, 2007.

[155] C.-J. Li, W.-Y. Li, and Y.-Y. Wang, “Formation of metastable phases in cold-sprayed soft metallic deposit,” *Surf. Coatings Technol.*, vol. 198, no. 1–3, pp. 469–473, 2005.

[156] T. Schmidt *et al.*, “From particle acceleration to impact and bonding in cold spraying,” *J. Therm. Spray Technol.*, vol. 18, no. 5–6, pp. 794–808, 2009.

[157] J. Pattison, S. Celotto, A. Khan, and W. O’Neill, “Standoff distance and bow shock phenomena in the Cold Spray process,” *Surf. Coatings Technol.*, vol. 202, no. 8, pp. 1443–1454, 2008.

[158] G. Mauer, R. Singh, K. H. Rauwald, S. Schrüfer, S. Wilson, and R. Vaßen, “Diagnostics of Cold-Sprayed Particle Velocities Approaching Critical Deposition Conditions,” *J. Therm. Spray Technol.*, vol. 26, no. 7, pp. 1423–1433, 2017.

[159] R. Ninomiya, H. Yukawa, M. Morinaga, and K. Kubota, “An electronic approach to the prediction of the mechanical properties of magnesium alloys,” *J. Alloys Compd.*, vol. 215, no. 1–2, pp. 315–323, 1994.

[160] C. C. Kammerer *et al.*, “Diffusion kinetics, mechanical properties, and crystallographic characterization of intermetallic compounds in the Mg-Zn binary system,” *Intermetallics*, vol. 67, pp. 145–155, 2015.

[161] B. Marzbanrad, E. Toyserkani, and H. Jahed, “Multi-Layer Cold Spray Coating: Strain Distribution,” *Key Eng. Mater.*, vol. 813, pp. 411–416, Jul. 2019.

[162] V. K. Champagne, *The Cold Spray Materials Deposition Process; fundamentals and applications*, 1st ed. Cambridge, England : CRC Press, 2007.

[163] S. Sampath, X. Y. Jiang, J. Matejicek, L. Prchlik, A. Kulkarni, and A. Vaidya, “Role of thermal spray processing method on the microstructure, residual stress and properties of coatings: An integrated study of Ni-5 wt. % Al bond coats,” *Mater. Sci. Eng. A*, vol. 364, no. 1–2, pp. 216–231, 2004.

[164] P. Bansal, P. H. Shipway, and S. B. Leen, “Residual stresses in high-velocity oxy-fuel thermally sprayed coatings - Modelling the effect of particle velocity and temperature during the spraying process,” *Acta Mater.*, vol. 55, no. 15, pp. 5089–5101, 2007.

[165] J. Matejicek and S. Sampath, “Intrinsic residual stresses in single splats produced by thermal spray processes,” *Acta Mater.*, vol. 49, no. 11, pp. 1993–1999, 2001.

[166] X. Song *et al.*, “Residual stresses in single particle splat of metal cold spray process – Numerical simulation and direct measurement,” *Mater. Lett.*, vol. 230, pp. 152–156, 2018.

[167] T. Suhonen, T. Varis, S. Dosta, M. Torrell, and J. M. Guilemany, “Residual stress development in cold sprayed Al, Cu and Ti coatings,” *Acta Mater.*, vol. 61, no. 17, pp. 6329–6337, 2013.

[168] D. Boruah *et al.*, “Evaluation of residual stresses induced by cold spraying of Ti-6Al-4V on Ti-6Al-4V substrates,” *Surf. Coatings Technol.*, vol. 374, pp. 591–602, 2019.

[169] R. Singh, S. Schruefer, S. Wilson, J. Gibmeier, and R. Vassen, “Influence of coating thickness on residual stress and adhesion-strength of cold-sprayed Inconel 718 coatings,” *Surf. Coatings Technol.*, vol. 350, no. June, pp. 64–73, 2018.

[170] Y. Xue, X. Pang, B. Jiang, and H. Jahed, “Corrosion and corrosion fatigue performances of micro-arc oxidation coating on AZ31B cast magnesium alloy,” *Mater. Corros.*, vol. 70, no. 2, pp. 268–280, 2019.

[171] M. Salarian and E. Toyserkani, “The use of nano-computed tomography (nano-CT) in non-destructive testing of metallic parts made by laser powder-bed fusion additive manufacturing,” *Int. J. Adv. Manuf. Technol.*, vol. 98, no. 9–12, pp. 3147–3153, 2018.

[172] A. W. Y. Tan *et al.*, “Effect of coating thickness on microstructure, mechanical properties and fracture behaviour of cold sprayed Ti6Al4V coatings on Ti6Al4V substrates,” *Surf. Coatings Technol.*, vol. 349, no. December 2017, pp. 303–317, 2018.

[173] Y. Watanabe, C. Yoshida, K. Atsumi, M. Yamada, and M. Fukumoto, “Influence of Substrate Temperature on Adhesion Strength of Cold-Sprayed Coatings,” *J. Therm. Spray Technol.*, vol. 24, no. 1, pp. 86–91, 2015.

[174] S. Ehrenberger, “Assessment of Magnesium Components in Vehicle,” 2013.

[175] P. Cavaliere, *Cold-Spray Coatings Recent Trends and Future Perspectives*. Switzerland: Springer Nature, 2018.

[176] W. Liu, G. Wu, C. Zhai, W. Ding, and A. M. Korsunsky, “Grain refinement and fatigue strengthening mechanisms in as-extruded Mg-6Zn-0.5Zr and Mg-10Gd-3Y-0.5Zr magnesium alloys by shot peening,” *Int. J. Plast.*, vol. 49, pp. 16–35, 2013.

[177] M. X. Zhang, H. Huang, K. Spencer, and Y. N. Shi, “Nanomechanics of Mg-Al intermetallic

compounds," *Surf. Coatings Technol.*, vol. 204, no. 14, pp. 2118–2122, 2010.

[178] H. Nie *et al.*, "A coupled EBSD/TEM study on the interfacial structure of Al/Mg/Al laminates," *J. Alloys Compd.*, vol. 781, pp. 696–701, Apr. 2019.

[179] S. K. Shaha and H. Jahed, "Characterization of nanolayer intermetallics formed in cold sprayed Al powder on Mg substrate," *Materials (Basel).*, vol. 12, no. 8, 2019.

[180] H. Mehmer, "Diffusion in solids," *Springer*, pp. 784–789, 2010.

[181] S. R. Agnew and O. Duygulu, "Plastic anisotropy and the role of non-basal slip in magnesium alloy AZ31B," *Int. J. Plast.*, vol. 21, pp. 1161–1193, 2005.

[182] J. Koike, "Enhanced deformation mechanisms by anisotropic plasticity in polycrystalline Mg alloys at room temperature," *Metall. Mater. Trans. A Phys. Metall. Mater. Sci.*, vol. 36, no. 7, pp. 1689–1696, 2005.

[183] H. Li, E. Hsu, J. Szpunar, H. Utsunomiya, and T. Sakai, "Deformation mechanism and texture and microstructure evolution during high-speed rolling of AZ31B Mg sheets," *J. Mater. Sci.*, vol. 43, no. 22, pp. 7148–7156, 2008.

[184] Y. N. Wamg and J. C. Huang, "Texture analysis in hexagonal material," *Mater. Chem. Phys.*, vol. 81, pp. 11–26, 2003.

[185] J. A. Del Valle, M. T. Pérez-Prado, and O. A. Ruano, "Deformation mechanisms responsible for the high ductility in a Mg AZ31 alloy analyzed by electron backscattered diffraction," *Metall. Mater. Trans. A Phys. Metall. Mater. Sci.*, vol. 36, no. 6, pp. 1427–1438, 2005.

[186] Y. N. Wang and J. C. Huang, "The role of twinning and untwinning in yielding behavior in hot-extruded Mg-Al-Zn alloy," *Acta Mater.*, vol. 55, no. 3, pp. 897–905, 2007.

[187] G. Zhou, M. K. Jain, P. Wu, Y. Shao, D. Li, and Y. Peng, "Experiment and crystal plasticity analysis on plastic deformation of AZ31B Mg alloy sheet under intermediate temperatures: How deformation mechanisms evolve," *Int. J. Plast.*, vol. 79, pp. 19–47, 2016.

[188] A. Khosravani, J. Scott, M. P. Miles, D. Fullwood, B. L. Adams, and R. K. Mishra, "Twining in magnesium alloy AZ31B under different paths at moderatly elevated temperature," *Int. J. Plast.*, vol. 45, pp. 160–173, 2013.

[189] Q. Yang and A. K. Ghosh, "Formability of ultrafine-grain Mg Alloy AZ31B at warm

temperatures," *Metall. Mater. Trans. A Phys. Metall. Mater. Sci.*, vol. 39, no. 11, pp. 2781–2796, 2008.

[190] I. Ulacia, N. V. Dudamell, F. Gálvez, S. Yi, M. T. Pérez-Prado, and I. Hurtado, "Mechanical behavior and microstructural evolution of a Mg AZ31 sheet at dynamic strain rates," *Acta Mater.*, vol. 58, no. 8, pp. 2988–2998, 2010.

[191] M. P. Brady, W. J. Joost, and C. D. Warren, "Insights from a recent meeting: Current status and future directions in magnesium corrosion research," *Corrosion*, vol. 73, no. 5, pp. 452–462, 2017.

[192] X. Yuming and Z. Ming-Xing, "The effect of cold sprayed coatings on the mechanical properties of AZ91D magnesium alloys," *Surf. Coatings Technol.*, vol. 253, pp. 89–95, 2014.

[193] A. Moridi, S. M. Hassani Gangaraj, S. Vezzu, and M. Guagliano, "Number of passes and thickness effect on mechanical characteristics of cold spray coating," *Procedia Eng.*, vol. 74, pp. 449–459, 2014.

[194] T. Proulx, *Fracture and Fatigue , Volume 7*, vol. 7. 2013.

[195] H. Jahed, B. A. Moghadam, and M. Shambooli, "Re-Autofrettage," *J. Press. Vessel Technol.*, vol. 128, no. 2, pp. 223–226, Dec. 2005.

Appendix A

Response of FBG sensor to the external thermo-mechanical strains

During the experiments, any mechanical and\or thermal strain changes can shift the reflected wavelengths of the FBG sensors, which can be recorded by an interrogator. In this research, Sm125-200 with one optical channel and wavelength range from 1520 nm to 1570 nm, and the wavelength with an accuracy of 10 pm was employed.

Fig A. 1a illustrates the reflected spectrum of one of the sensors, which demonstrates the initial center wavelength of 1560 nm before embedding the sensor. After embedding, the shape of the spectrum was completely rough-and-tumble and the peak broadening was also observed (Fig A. 1b). Moreover, the intensity of the peak was changed after curing process. Fig A. 1c shows the spectrum changes after cutting and polishing the extra part of the sensor. As seen, the spectrum became narrower after cutting in comparison to the same sensor after embedding.

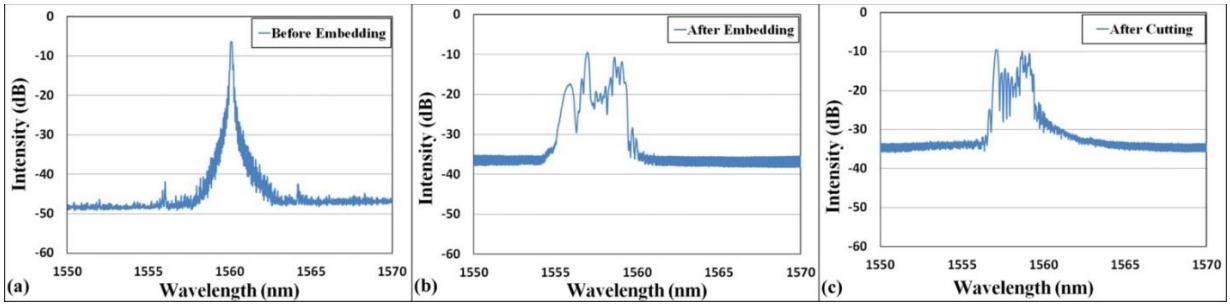

Fig A. 1: FBG spectrum, a) before embedding; b) after embedding with thermal epoxy; c) after cutting and polishing the sensor.

A.1 Repeatability of the Results

Fig A. 2 shows a set of critical spectra obtained at different nozzle positions during cold spraying for four different embedded samples. It should be noted that during the cold spray experiments, only the responses of sensors embedded at a 45º directions were recorded. The positions of the nozzle and sensors in four cold spray tests are shown schematically on the left side of Fig A. 2. In all of the tests as shown in Fig A. 2a, the first curves reveal the response of the sensors after embedding (before running the cold spray tests). As the nozzle approached the sensors (see schematic Fig A. 2b), peak broadening and spectral red shift were observed (Fig A. 2b). In this condition, thermal strain due to the

carrier gas temperature leads to the shifting and broadening of the spectrums. With decreasing the distance between nozzle and sensors, more stretching and shifting of spectrums were expected. However, with placing the nozzle exactly above the sensors (see schematic Fig A. 2c), in spite of higher predicted temperature due to the carrier gas temperature and the severe deformation of particles/substrate, the peaks narrowing were observed while the main peaks still showed more transition to the right (Fig A. 2c). This shape change of spectrum uncovers that a significant compressive residual stress is developed in the surface and as a consequence, a compressive strain is induced by peening and severe plastic deformation during the deposition, diminishing the effect of thermal expansion. This observation clarified the contrast between the peening effect and temperature deviation. After passing the nozzle (see schematic Fig A. 2d) the peaks became broaden and shifted even further to the right where the sign of compressive strains was no more observable. This indicates that the induced stress was weakened in the substrate in a few second. Fig A. 2e shows the shape of the spectrums after the cold spray tests were completed and the Mg alloy samples reached room temperature. The shapes of spectrums became narrow; however, the peaks were shifted to the right in comparison to the very initial spectrums (Fig A. 2a). For Test #2 before recording the spectrum after cold spray at room temperature, the FBG failed; hence, the spectrum was not recorded. Fig A. 3 shows the smart magnesium alloy sample embedded with two FBG sensors and thermocouple after conducting the cold spray coating tests.

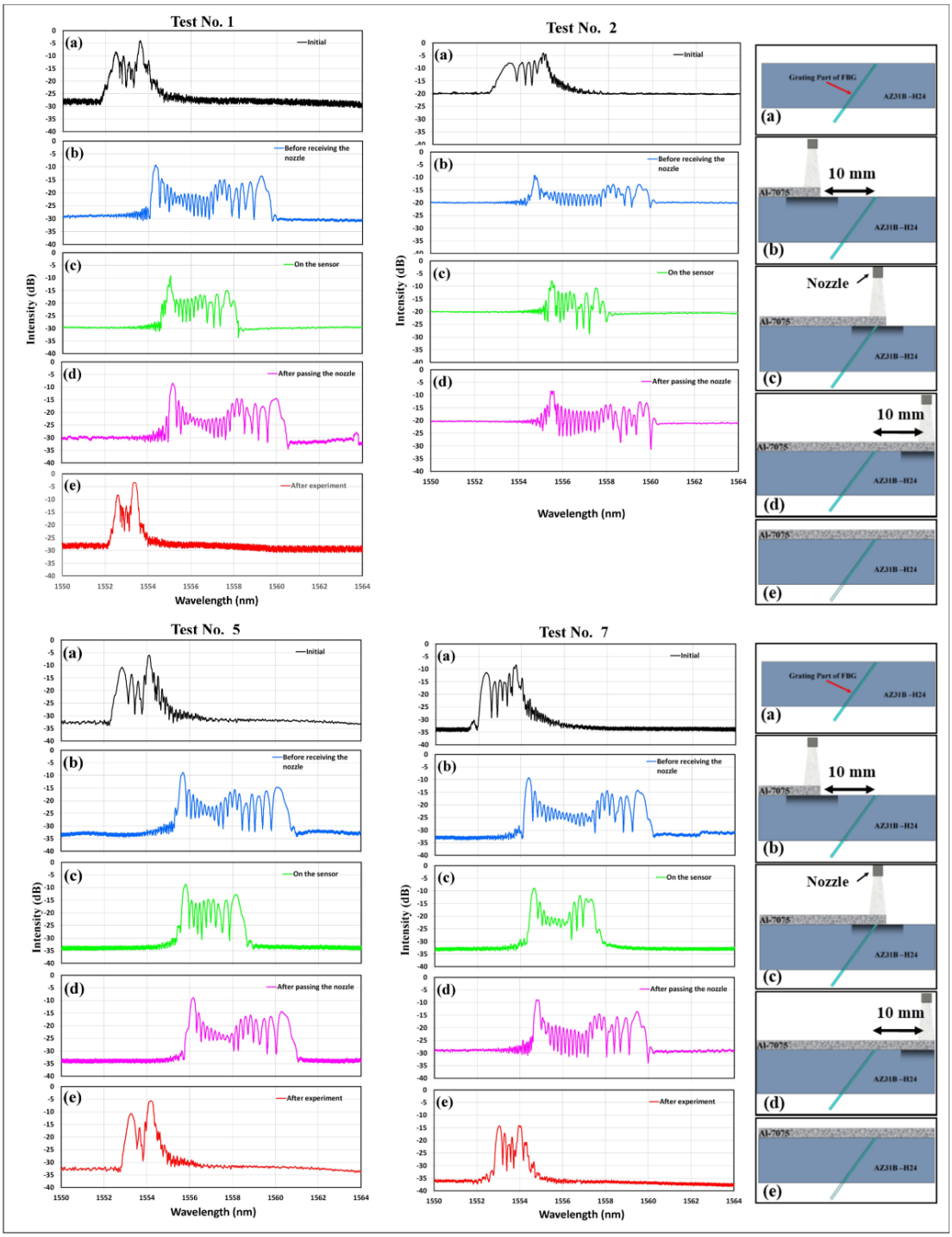

Fig A. 2: Schematic of the coating process and spectrums of FBG sensors for four different tests: a) after embedding sensor; b) during coating at 10mm distance from the nozzle; c) coating on the sensor; d) at 10 mm after passing the nozzle; e) after coating at RT.

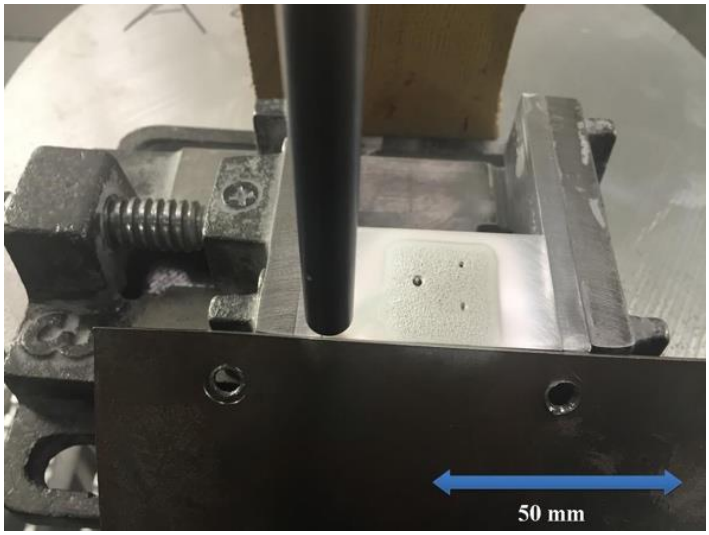

Fig A. 3: Embedded sample after the cold spray coating test.

For more clarification, the bandwidths and shifts of spectrums at different locations were measured: 1) before conducting the cold spray tests; 2) before receiving the nozzle on top of the sensors; 3) when the nozzle was on the sensors; 4) after passing the nozzle; and, 5) after the cold spray tests were completed and the part arrived at room temperature. The bar graphs in Fig A. 4 depict the changes of spectrum bandwidth during the experiments. Usually, the bandwidth of the reflection peak is defined with Full-Width-Half-Maximum (FWHM), which is the width of 50% of the main peak. In addition, the averages of the widths for all experiments in each situation were added to the bar graphs. Based on the measurements, for all experiments when the nozzle was on top of the sensor the bandwidths of spectra were decreased, significantly, while before and after receiving the nozzle during the cold spray the bandwidths were increased due to the raise in temperature.

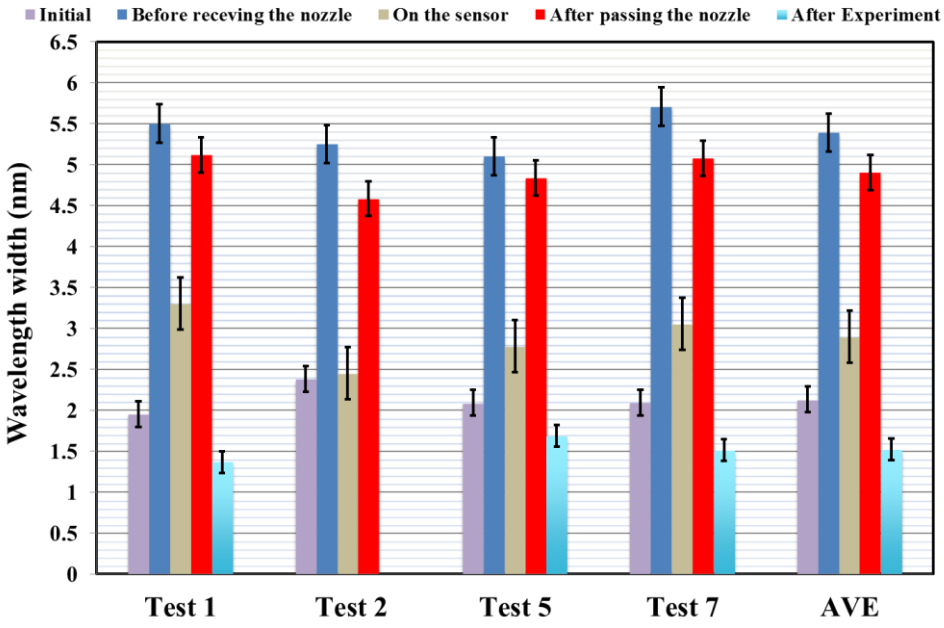

Fig A. 4: Wavelength width for different situations in the four tests.

In addition, the wavelengths shift during the experiments and after the cold spray tests at room temperature were measured (see Fig A. 5). Based on the observations, the wavelengths shifted to the right noticeably, during the experiments because of increased temperature; however, subtle shifts occurred at different situations during the tests. After the cold spraying tests, a significant amount of wavelengths shifts observed in all samples (purple bars in Fig A. 5), which indicates the existence of tensile strains. These results highlight the effect of temperature due to the carrier gas and adiabatic shear deformation on the evolution of tensile strains in the coated samples. It is noticeable that the stress relief process releases the residual elastic energy of the material while in these cases, not only the compressive stresses due to peening process were relieved, but also tensile residual strains were imposed in the substrates. This can be explained by considering the thermal mismatch strain of the Al7075 coating and AZ31B-H24 substrate, which created tensile residual strain during the cooling process (after coating).

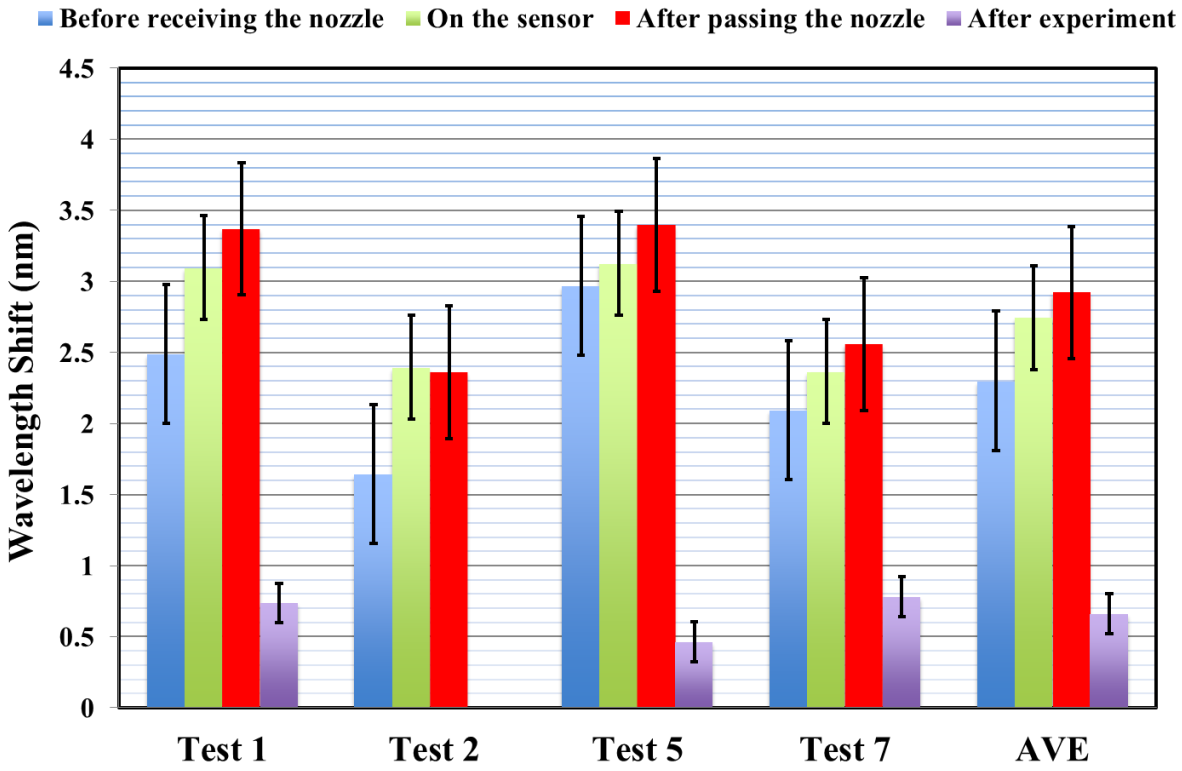

Fig A. 5: Wavelength shifts for different situations in the four tests.

Appendix B

Temperature calibration of FBG sensor

During the cold spray tests, both mechanical and thermal strains are induced in the sample, and the FBG sensor can record the induced strains as the wavelength changes. Hence, the FBG sensor responses include the mechanical and thermal changes. The correlation between the wavelength shifts and axial deformation of the FBG sensor due to the mechanical and\or thermal strains can be calculated by the following equations [115]:

$$\frac{\Delta\lambda}{\lambda_0} = \boldsymbol{k} \times \boldsymbol{\varepsilon} + \boldsymbol{\alpha_\delta} \times \Delta\boldsymbol{T} \quad \textbf{(B-1)}$$

$$\boldsymbol{\varepsilon} = \boldsymbol{\varepsilon_m} + \boldsymbol{\varepsilon_T} \quad \textbf{(B-2)}$$

$$\boldsymbol{\alpha_\delta} = \frac{\delta n/_n}{\delta T} \quad \textbf{(B-3)}$$

$$\boldsymbol{\varepsilon_T} = \boldsymbol{\alpha_{sp}} \times \Delta\boldsymbol{T} \quad \textbf{(B-4)}$$

$$\frac{\Delta\lambda}{\lambda_0} = \left(\boldsymbol{k} \times \boldsymbol{\alpha_{Sp}} + \frac{\delta n/_n}{\delta T}\right) \times \Delta\boldsymbol{T} + \boldsymbol{k}\,\boldsymbol{\varepsilon_m} \quad \textbf{(B-5)}$$

where, $\Delta\lambda$ is the wavelength shift, λ_0 is the initial wavelength of the sensor at the beginning of the experiment, k is the gauge factor which is equal to 0.78, ε is the total strain caused by force (ε_m) and temperature (ε_T), α_δ is defined by the change of the refractive index, and ΔT is the temperature change (K). α_{sp} is the expansion coefficient of the sample (1/K).

Based on equation (B- 5), if the temperature remains constant, the relation between wavelength changes and mechanical strain is simple and corresponds only to the gauge factor (k), which is a constant. However, any temperature changes add a complicated coefficient to equation (B-5), which introduces the effects of the sample's thermal expansion coefficient and the sensor's refractive index change to the peak's shift. Hence, calculating the effect of thermal strain on the wavelength shift of the FBG sensors is not as simple as calculating the mechanical strain. The change of refractive index is dependent on the reflectivity of the sensor and grating length, which can be calculated through the following equations:

$$\boldsymbol{R(L, \lambda_B)} = \boldsymbol{tanh^2(\Omega L)} \quad \textbf{(B-6)}$$

$$\boldsymbol{\Omega} = \frac{\boldsymbol{\pi \Delta n}}{\boldsymbol{\lambda}} \boldsymbol{M_p} \quad \textbf{(B-7)}$$

$$\boldsymbol{M_p} = \boldsymbol{1 - V^{-2}} \quad \textbf{(B-8)}$$

$$\boldsymbol{V = \frac{2\pi a}{\lambda}\sqrt{n_{co}^2 - n_{cl}^2}} \quad \textbf{(B-9)}$$

where a is the core radius and $n_{co}$and n_{cl} are the core and cladding refractive indices. Based on the specifications of the FBG sensors (Corning SMF-28) used, the relation between reflectivity and the change of refractive index are calculated by equation (B-10);

$$\boldsymbol{R(L, \lambda_B) = tanh^2\left(0.8\pi \frac{\Delta n}{\lambda}\right)} \quad \textbf{(B-10)}$$

By inserting Δn from equation (B-10) into equation (B-5), the relation between the temperature and wavelength changes can be obtained if the mechanical strain is known. However, in this configuration and during the cold spraying, the relation is also dependent on the mechanical strains corresponding to the peening process, the different embedding situations, and the distance between the sample and a sensor embedded in an epoxy-filled hole drilled in that sample. Increasing the distance aggravates the effect of the epoxy, adding another factor to equation (B-5); the thermal expansion coefficient of the epoxy. Reducing the complexity and boosting accuracy require that we find the relation between the wavelength changes and temperature by conducting experiments with the same embedding conditions but without applying the mechanical loads. To achieve the best correlation between temperature and wavelength with high precision the following experiments were conducted.

B.1 Sample preparation

In this study, two 3.16-mm thick AZ31B-H24 Mg alloy samples were used for temperature calibration tests. Three 300 μm diameter holes were drilled into the samples at a 45° angle. Since the maximum strains of substrate are developed very closely to the surface (less than 200 μm in depth) at the horizontal direction due to the peening process during the coating treatment, the grating needs to be embedded very closely to the surface for optimum outcome. However, when the sensor is embedded horizontally (parallel to the surface), the recorded strains are exactly restricted to the specific place, where the grating is accommodated, and this configuration does not meet the requirement for monitoring or recording the strain evolution of the substrate. Therefore, a 45° angle was considered to record the strain as a resultant of strains in two directions, vertical and horizontal. Fig B. 1a and Fig B. 1b show the shape and dimension of the sample and the positions of the embedding sensors. Fig B. 1c shows the position of grating and thermocouple, schematically.

Fig B. 1: a) Sample drawing and geometry of AZ31-H24 (all dimensions in mm); b) Position of FBG sensors; c) schematic of grating position and a thermocouple.

B.2 Preparation of the FBG sensors

Four acrylate-coated FBG sensors with an initial wavelength of around 1550nm and the reflectivity of about 80% were utilized. Three of them were embedded into the sample without removing the acrylate coating, and one of them was fixed on the surface of the AZ31B-H24 sample during the calibration temperature tests.

B.3 Embedding the FBG sensors

For this set of experiments, after cleaning the holes, the as-received FBG sensors with acrylate coating were dipped into the thermal epoxy and embedded inside the 300µm diameter of the holes without any support, and then cured using a hotplate (Torrey Pines Echo Therm HS40). The curing setup and embedding of sensors in the magnesium plate are shown in Fig B. 2a and Fig B. 2b. Fig B. 3 depicts top view of the sample after cutting off the protruding extra parts of the sensors and polishing the sample surface. It should be noted that during the temperature calibration tests, instead of embedding the thermocouple in the sample, it was placed and fixed on the sample surface using Kapton tape.

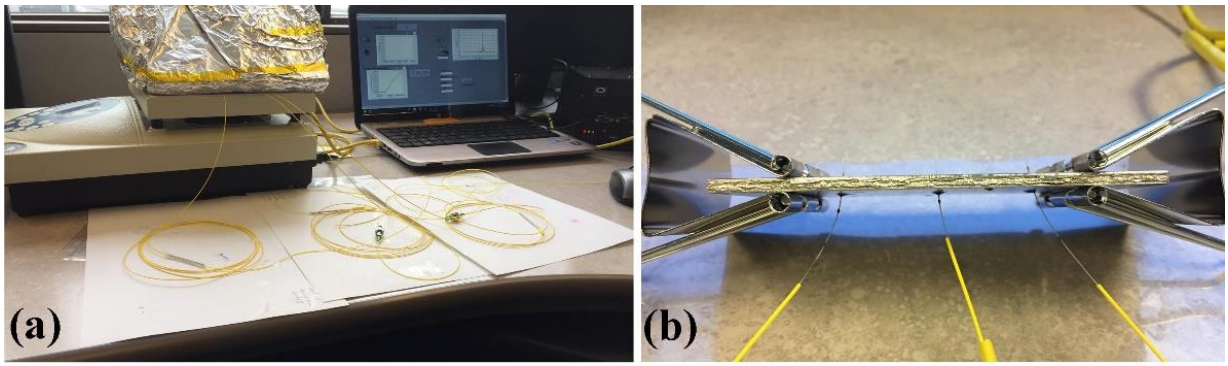

Fig B. 2: a) Curing using a hotplate; b) AZ31B-H24 magnesium alloy sample after curing.

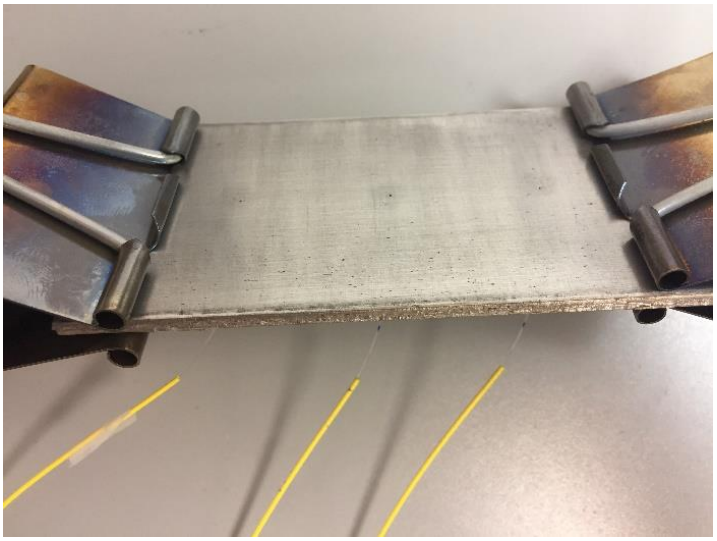

Fig B. 3: AZ31B-H24 magnesium alloy sample after polishing the surface (top view).

During sample preparation, the responses of the three FBG sensors were recorded by employing another interrogator (Sm125-500 with four optical channels and wavelength range from 1510 nm to 1590 nm and the wavelength accuracy of 1 pm) in different stages of embedding, such as before embedding, during curing, after curing and after cutting off the protruding extra part of the gratings. Fig B. 4 illustrates the spectra shapes for the different FBG sensors in the abovementioned situations. Comparing the spectra shifts in Fig B. 4, low spectrum movement can be seen only during curing, and low peak broadening happens only for FBG 3. However, the intensity changed after embedding and trimming of the FBG sensors. These results confirm that decreasing the hole diameter, decreased the effect of epoxy, and as a consequence, the spectrum response became more precise, with minimal deformation and peak broadening.

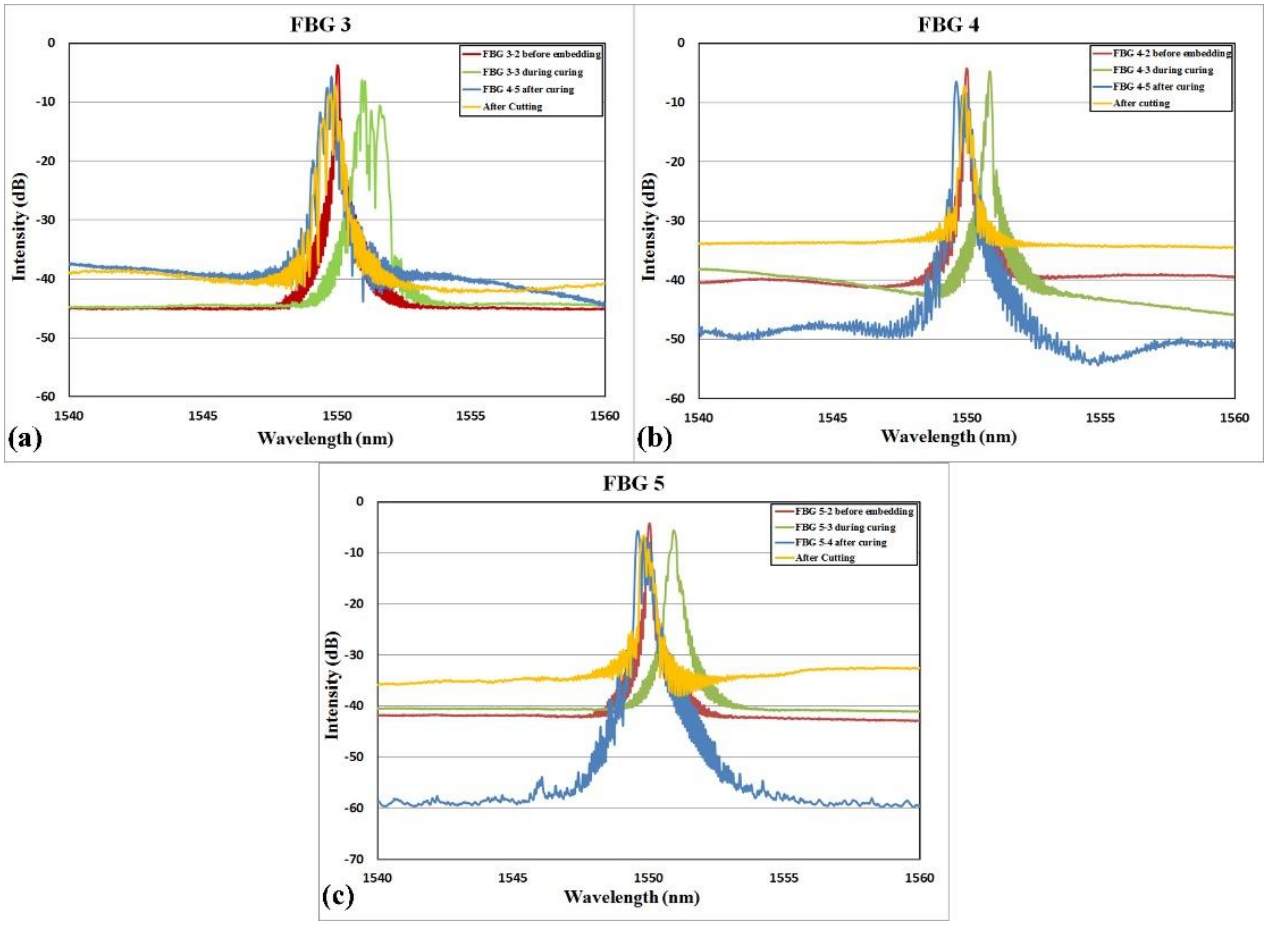

Fig B. 4: FBG spectrum changes before embedding, after embedding, after cutting and polishing for three different sensors.

B.4 Results and discussions

The responses of the three FBG sensors were recorded at 23 different temperatures, from room temperature (24°C) to 450°C, while the sensors were embedded in the AZ31B-H24 sample, and while a thermocouple was attached on the sample surface. The hotplate (Torrey Pines Echo Therm HS40) was employed to control the sample temperature during the tests. While the hotplate temperature was being increased, the thermocouple and the interrogator recorded the sample temperature and wavelengths changes, respectively. The temperature was increased incrementally and kept constant for a sufficient time until it stabilized at a certain temperature, and then the responses of the sensors and temperature of the sample were recorded. It is noted that the sample temperature was not the same as the hot plate temperature, since the sample was placed vertically on the hot plate, with only its edge in contact with direct heat. A small heat insulation tent, covered by aluminum foil, was put on the sample

to prevent heat transfer and stabilize its (Fig B. 2a). The spectra of three FBG sensors at four different temperatures of the sample are shown in Fig B. 5. As can be seen, no significant change can be observed in the spectra shapes at the different temperatures; however, all spectra shift to the right, proportional with increasing temperature (see Fig B. 5).

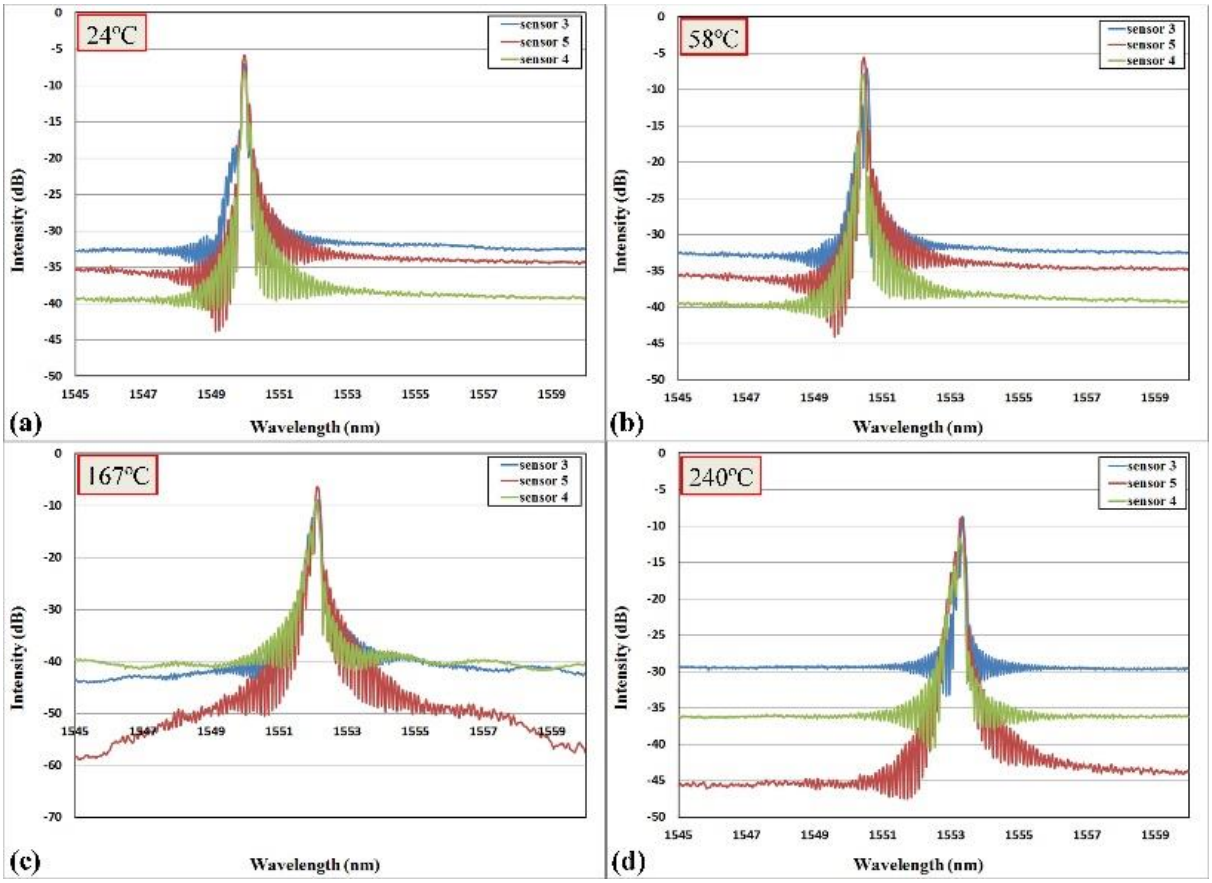

Fig B. 5: Response of three sensors at different temperatures; a) RT (24°C); b) 58°C; c) 167°C; d) 240°C.

During the experiments, the temperature of the sample increased up to 287°C, and at this relatively high temperature, the spectral shapes became non-uniform (see **Fig B. 6**). All these experiments were repeated twice, and the wavelength changes were recorded after stabilizing the temperatures for the three FBG sensors. Raising the temperature over about 280°C and keeping the sensors at the high level of temperature damaged the polymer jacket of the sensors, since this type of FBG sensor cannot tolerate prolonged high temperatures. **Fig B. 7** shows the embedded sensors after exposure to high temperatures; their acrylate coating has melted. Hence, the experiments halted at 287°C, as no more observations could be conducted at higher temperatures.

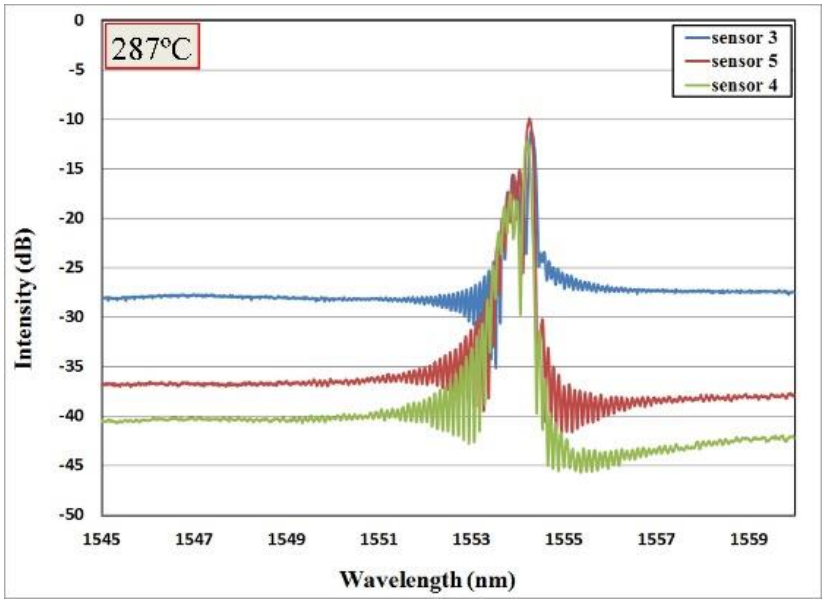

Fig B. 6: The changes of spectrums for three FBG sensors at 287°C.

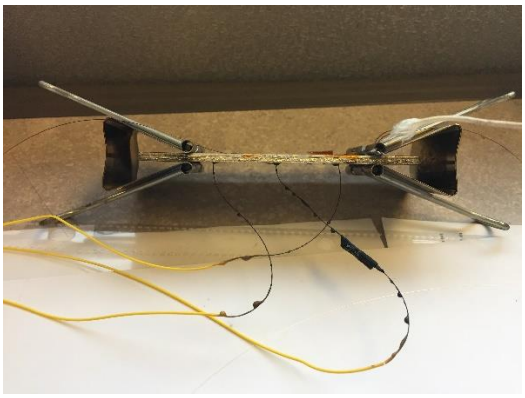

Fig B. 7: Embedded AZ31B-H24 Magnesium alloy sample after doing high temperature tests.

These experiments extracted the relation between the temperature changes and the wavelength shifts of the three FBG sensors. **Fig B. 8**a depicts the linear trend of the sensors with increasing temperature. The average of the three FBG sensors at different embedding positions demonstrated almost the same slopes with the linear trend of $\mathbf{0.0160 \pm 1 \times 10^{-4}}$ (**Fig B. 8**b). This linear trend value can be inserted into equation (B-5) instead of the expression $\left(\boldsymbol{k} \times \boldsymbol{\alpha_{Sp}} + \frac{\boldsymbol{\delta n/n}}{\boldsymbol{\delta T}}\right)$. However, the wavelength changes include the mechanical changes and thermal changes. To extract the mechanical strain from equation (B-5), the temperature changes should be measured by thermocouple or thermal camera for the same

smart magnesium alloy samples. Therefore, the same structures can be utilized in cold spray experiments, and then the mechanical strain can be separated from thermal strain during the tests, after recording the wavelength changes during the tests. In addition, the temperature changes during cold spraying can be measured without applying a mechanical load (cold spray without spraying powder).

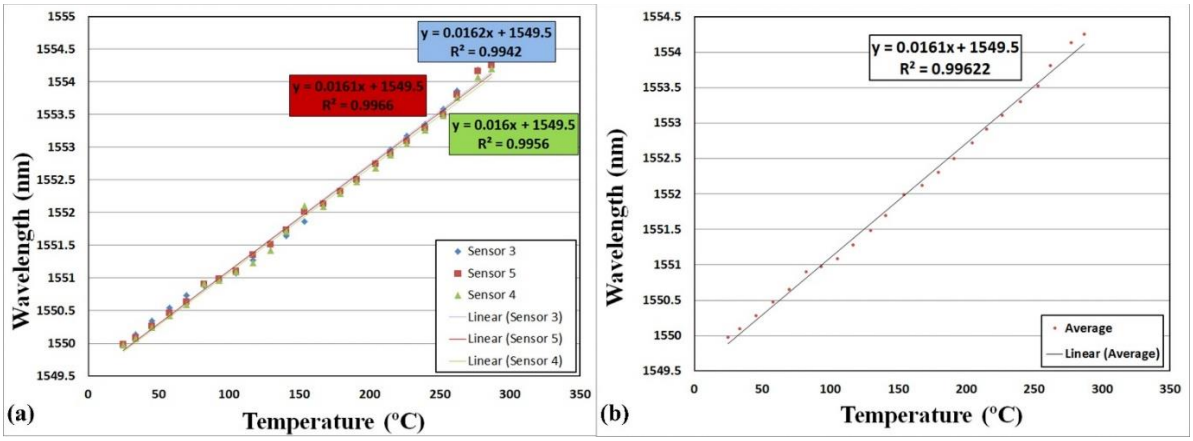

Fig B. 8: a) Temperature vs. wavelength for three FBG sensors; b) extracted temperature calibration curve.